University of Sussex

Search for supersymmetry in events with leptons (e, μ, τ), jets and missing transverse energy with the ATLAS detector at the LHC

Anthony Rose

Submitted for the degree of Doctor of Philosophy

University of Sussex

September 2012

Declaration

I hereby declare that this thesis has not been and will not be submitted in whole or in part to another University for the award of any other degree.

Signature:

Anthony Rose

UNIVERSITY OF SUSSEX

Anthony Rose, Doctor of Philosophy

Search for supersymmetry in events with leptons (e, μ, τ), jets and missing transverse momentum with the ATLAS detector at the LHC

Summary

Two searches for events containing τ-leptons, jets, large missing transverse momentum, and zero or one light leptons ($\ell = e, \mu$) in the final state have been performed using proton-proton collision data at $\sqrt{s} = 7$ TeV, recorded with the ATLAS detector at the Large Hadron Collider. The first search was performed using 2.05fb^{-1} of the ATLAS data collected in 2011, and focused on the final state containing two hadronically decaying τ-leptons. For the second search the dataset was extended to 4.7fb^{-1}, and four separate channels (1τ, 2τ, $\tau+e$, $\tau+\mu$) were combined for the final result. No excess above the Standard Model background expectation is observed and 95% CL visible cross-section upper limits for new phenomena are set. In the framework of gauge-mediated SUSY-breaking models (GMSB), exclusion limits on the GMSB mass scale Λ are set at 54 TeV in the regions where the lightest $\tilde{\tau}$ is the next-to-lightest SUSY particle ($\tan\beta > 20$). These limits provide the most stringent tests to date of GMSB models in a large part of the considered parameter space.

Acknowledgements

There are many people that have contributed to my studies over the past few years, and I would like to take this opportunity to thank them. First and foremost, I would like to thank my supervisor Dr. Fabrizio Salvatore, who has provided countless hours of advice, support and guidance throughout the course of both my MSc. and DPhil., and helped shape my knowledge of (and passion for) high energy physics. I would also like to say thank you to my second supervisor, Dr. Antonella De Santo, for her extremely valuable input throughout my time at the University of Sussex. I am extremely grateful to both of my supervisors for the opportunity to work on the ATLAS experiment, and the enormous influence that they have had on my research. The last four years have presented challenges both inside and outside of the academic environment, and I hope Dr. Salvatore and Dr. De Santo know how much I appreciate their support during this time.

Also at the University of Sussex, I would like to express sincere thanks to the rest of the ATLAS group. It has been a huge pleasure to work with you, and each of you has provided contributions during our time together. I would like to thank Dr. Valeria Bartsch for her vital support during my technical work, Dr. Tina Potter for answering *many* questions during my time at Sussex (particularly during the first year!), and Stewart Martin-Haugh, with whom I have been on this DPhil-journey since the beginning. He has often had the answer to a question, and has become a close friend. It is difficult to thank so many people in the detail that they deserve, but I'm grateful to Dr. Mark Sutton, Dr. Lisa Falk, Ed Leming, Nicky Santoyo, Yusufu Shehu and Zara Grout for valuable conversations and for making Sussex such a great place to spend several years. A special thanks also goes to Emyr James, for keeping things working despite my best efforts. A big "thank you" also goes to the other members of the department at Sussex. I'll never forget my time here. I am also grateful to the University of Sussex and to SEPnet for their generous financial support that made any of this possible in the first place.

I would also like to thank the other members of the "SUSY-with-taus" group at ATLAS. We have had many late nights together, rushing to complete a task before a deadline, and I'm very proud of the work that was achieved by this group. I would like to extend particular thanks to Dr. Dörthe Kennedy, Steffen Schaepe, Dr. Wolfgang Ehrenfeld, Till

Natterman, Dr. Aldo Saavedra, Alex Kastanas, Ørjan Dale, Wolfgang Liebig, Dr. Paul Jackson, and Martin Schultens. I am also extremely grateful to the wider ATLAS SUSY Working Group, and the members of the ATLAS collaboration in general. It has been a mixture of exciting, interesting and challenging to work with such an incredible group of people, at such an important time for high energy physics.

Outside of academia, many people have provided vital support throughout the past few years. Firstly, I would like to thank my wife Elizabeth, for everything that she has had to put up with over the past few years. You have been there through all of the highs and all of the lows, and I'll forever be grateful for your love, support, and sacrifice. My mother, grandmother, brother, and sister have each been there for me when times have been tough and I love you all, I hope you realise that this achievement would have been impossible without your input. I would also like to say thank you to Sandy, Jamie and the other members of Lizz's family, for their support and making me feel so welcome. A special thanks goes to Tom and Rosalind, whom I also consider family. Without Tom's suggestion 10 years ago I would have never even considered a career in physics. Armand, Dan, Duncan, Jamie, Brenham, Piglet, Dean, Killian, Brendon, Adam, Mat, Nicky: thanks for the good times that make the hard work seem easier.

To Elizabeth.

Contents

List of Tables **xiii**

List of Figures **1**

1 Introduction **1**

2 Theoretical background **3**

2.1 The Standard Model 4

2.1.1 Quantum chromodynamics 5

2.1.2 Quantum electrodynamics 7

2.1.3 From weak interactions to the electroweak theory 8

2.1.4 The Higgs mechanism 9

2.2 Limitations of the Standard Model 12

2.2.1 The hierarchy problem 12

2.2.2 Dark matter 12

2.2.3 Unification of gauge couplings 13

2.3 Supersymmetry 13

2.3.1 The hierarchy problem 14

2.3.2 Unification of gauge couplings 15

2.3.3 Dark matter 15

2.4 The Minimal Supersymmetric Standard Model 16

2.5 Gauge-Mediated Supersymmetry Breaking 19

2.5.1 Searching for GMSB at the LHC 20

3 The Large Hadron Collider and the ATLAS Detector **23**

3.1 The Large Hadron Collider 23

3.2 The ATLAS detector 27

3.2.1 The magnet system . . . 27
3.2.2 The inner detector . . . 28
3.2.3 The ATLAS calorimeter system . . . 32
3.2.4 The muon spectrometer . . . 34
3.3 The ATLAS trigger and data acquisition system . . . 36
3.3.1 Level 1 Trigger . . . 37
3.3.2 High Level Trigger . . . 37

4 Event Simulation and Reconstruction 39
4.1 Event generation . . . 39
4.1.1 Parton distribution functions . . . 39
4.1.2 Multi-jet production . . . 40
4.1.3 $W^{\pm}/Z$ boson+jets production . . . 41
4.1.4 Top quark and diboson production . . . 42
4.1.5 GMSB signal production . . . 42
4.1.6 Simulation of τ-lepton decay . . . 42
4.2 Detector simulation . . . 43
4.2.1 Full detector simulation . . . 43
4.3 Object reconstruction . . . 44
4.3.1 Electrons . . . 45
4.3.2 Muons . . . 47
4.3.3 Clustering algorithms . . . 47
4.3.4 Jets . . . 48
4.3.5 b-jets . . . 49
4.3.6 Taus . . . 50
4.3.7 Reconstruction of the missing transverse energy . . . 60
4.3.8 Removal of overlapping reconstructed objects . . . 61

5 Search for supersymmetry in final states with two τ-leptons, jets and missing transverse energy 62
5.1 Introduction . . . 62
5.2 Data and Monte Carlo samples . . . 63
5.2.1 ATLAS data samples . . . 63
5.2.2 Simulated Standard Model background samples . . . 64
5.2.3 Simulated signal samples . . . 64

5.3 Analysis strategy . . . 65
5.3.1 Kinematic variables used in the analyses . . . 68
5.4 Pre-selection and event cleaning . . . 68
5.5 Triggers used in the analysis . . . 70
5.6 Signal selection requirements . . . 70
5.7 Background estimation . . . 79
5.7.1 Introduction . . . 79
5.7.2 Multi-jet background estimation . . . 79
5.7.3 W+jets and top background estimation . . . 88
5.7.4 Signal Efficiency . . . 96
5.8 Systematic uncertainties . . . 97
5.8.1 Jet energy scale . . . 97
5.8.2 Jet energy resolution . . . 98
5.8.3 τ energy scale . . . 98
5.8.4 Missing transverse energy . . . 99
5.8.5 Event pile-up . . . 99
5.8.6 τ identification efficiency . . . 99
5.8.7 Luminosity . . . 100
5.8.8 Theory uncertainties on the signal cross-section predictions . . . 100
5.8.9 Theoretical uncertainties on the transfer factor . . . 102
5.8.10 Summary of the systematic uncertainties . . . 102
5.9 Analysis results . . . 104
5.10 The CL_S method . . . 108
5.11 Setting exclusion limits . . . 109

6 Search for supersymmetry in final states with one or more τ-leptons, zero or one light leptons, jets and missing transverse energy 115
6.1 Introduction . . . 115
6.2 Data and Monte Carlo samples . . . 116
6.2.1 ATLAS data samples . . . 116
6.2.2 Simulated Standard Model background samples . . . 117
6.2.3 Simulated signal samples . . . 117
6.3 Pre-selection and event cleaning . . . 118
6.4 Triggers used in the analysis . . . 119
6.5 Signal selection requirements . . . 120

6.6 Background estimation . . . 126
6.6.1 Estimation of the multi-jet background . . . 126
6.6.2 Estimation of W/Z+jets and top backgrounds . . . 134
6.6.3 1τ final state . . . 140
6.6.4 $\tau + \ell$ final states . . . 141
6.7 Systematic uncertainties . . . 144
6.7.1 Jet energy scale . . . 144
6.7.2 Jet energy resolution . . . 145
6.7.3 Missing transverse energy . . . 145
6.7.4 b-tagging efficiencies . . . 145
6.7.5 Generator uncertainties . . . 145
6.7.6 Summary of the systematic uncertainties . . . 146
6.8 Analysis results . . . 148
6.8.1 2τ final state . . . 148
6.8.2 1τ final state . . . 153
6.8.3 $\tau + \ell$ final states . . . 155

7 Statistical analysis of the results **157**

8 Conclusion **162**

A 2.05fb^{-1} analysis: data and MC samples **165**

B 4.7fb^{-1} analysis: data and MC samples **170**

C BDT input variables for τ-ID **176**

Bibliography **178**

List of Tables

2.1 The fermionic and bosonic sectors of the Standard Model 6
2.2 Chiral and gauge supermultiplets in the MSSM 17

3.1 Running conditions of the LHC from 2010 to 2012 26
3.2 General performance goals of the ATLAS detector 29
3.3 Main characteristics of the muon spectrometer sensors 35

4.1 Criteria for the three electron ID algorithm working points 46
4.2 τ-lepton BDT-ID input variables 53

5.1 Data-taking period details 63
5.2 Summary of the simulated Standard Model samples 65
5.3 Summary of the GMSB benchmark samples 66
5.4 Mass hierarchy for GMSB benchmark points 67
5.5 Monte Carlo signal selection, scaled to 2.05fb^{-1} 77
5.6 Number of events in the 0-τ multi-jet sideband 81
5.7 Number of events in the 1-τ multi-jet sideband 82
5.8 Data and MC events in the control region, per background channel 89
5.9 Observed and expected events and normalisation factors for the control regions 92
5.10 Number of events expected for the signal region 92
5.11 Normalisation factors after raising the $p_{\mathrm{T}}^{\mathrm{jet2}}$ threshold 95
5.12 Separate background systematic variations after the full signal selection . . 102
5.13 Combined background systematic variations after the full signal selection . 103
5.14 Expected number of events for each of the SM backgrounds 104
5.15 The expected number of events for the signal benchmark points, the sum of the different SM processes and 2011 data 105

6.1 Data-taking period details . . . 116
6.2 Summary of the simulated Standard Model samples . . . 117
6.3 Summary of the GMSB benchmark samples . . . 118
6.4 Triggers for 1τ and 2τ final states . . . 120
6.5 Triggers for $\tau + \ell$ final states . . . 120
6.6 Event selection for the four final states . . . 125
6.7 Number of events in the multi-jet control region . . . 127
6.8 Number of events in the "extra loose" 0 and 1τ regions . . . 130
6.9 Number of events in the 1τ sideband . . . 131
6.10 Definitions of the W/Z + jets and top control regions . . . 134
6.11 Background contributions for the 2τ W, Z, and top control regions . . . 136
6.12 Normalisation factors for the SM background, and correlations between the factors . . . 138
6.13 Normalisation factors and SM background predictions for varied control region definitions . . . 140
6.14 SM background in the 1τ signal region . . . 141
6.15 SM background in the $\tau + \ell$ signal regions . . . 142
6.16 Control region definitions for the four channels . . . 143
6.17 Systematic and statistical uncertainties for the 2τ channel . . . 146
6.18 Overview of the dominant uncertainties for the four final states . . . 147
6.19 Signal selection summary for the 2τ final state . . . 150
6.20 Signal prediction and uncertainties in the 2τ final state . . . 151
6.21 Signal prediction and uncertainties in the 1τ final state . . . 153
6.22 Signal prediction and uncertainties in the $\tau + \ell$ final states . . . 155
6.23 Expected background events and data yields in the four final states . . . 156

7.1 Summary of the results of the four channels . . . 161

A.1 Details of the GMSB benchmark samples . . . 165
A.2 Details of the $t\bar{t}$ and single t simulated samples . . . 166
A.3 Details of the W + jets simulated samples . . . 166
A.4 Details of the Z + jets simulated samples . . . 167
A.5 Details of the diboson simulated samples . . . 168
A.6 Details of the di-jet simulated samples . . . 168
A.7 Details of the Drell-Yan simulated samples . . . 169

B.1 Details of the $t\bar{t}$ and single t simulated samples 170
B.2 Details of $t\bar{t}$ simulated samples 171
B.3 Details of the W + jets simulated samples 171
B.4 Details of the Z + jets simulated samples 172
B.5 Details of the diboson simulated samples 173
B.6 Details of the alternative diboson simulated samples 173
B.7 Details of the di-jet simulated samples 174
B.8 Details of the Drell-Yan simulated samples 174
B.9 Details of the GMSB simulated samples 175

List of Figures

2.1 Mexican hat potential of the Higgs field . . . 11
2.2 Quantum corrections to m_H^2 . . . 13
2.3 Unification of gauge couplings in the MSSM . . . 14
2.4 SUSY cancellation of quadratic terms in m_H . . . 15
2.5 GMSB NLO cross-section in the Λ–$\tan\beta$ plane . . . 21
2.6 NLO cross-sections for SUSY production at the LHC . . . 21
2.7 Feynman diagrams for SUSY production at the LHC . . . 22
2.8 Feynman diagram for a typical GMSB event . . . 22

3.1 CERN accelerator complex . . . 25
3.2 Integrated luminosity and mean number of interactions . . . 26
3.3 The ATLAS detector . . . 28
3.4 The ATLAS inner detector . . . 30
3.5 Three main components of the inner detector . . . 30
3.6 The ATLAS calorimeter system . . . 32
3.7 The accordion structure of the ATLAS ECAL . . . 33
3.8 The ATLAS muon spectrometer . . . 36
3.9 The ATLAS trigger system . . . 38

4.1 HERA and CTEQ PDFs . . . 40
4.2 The ATLAS simulation software . . . 44
4.3 Example of the anti-k_t algorithm . . . 50
4.4 Schematic of a τ-lepton decaying hadronically . . . 51
4.5 Selection of τ-ID jet discriminating variables . . . 55
4.6 τ-ID jet BDT score . . . 56
4.7 Inverse background efficiency as a function of signal efficiency for τ-ID . . . 56
4.8 Selection of τ-ID electron discriminating variables . . . 57

4.9 τ-ID electron BDT score . . . 58
4.10 Inverse background efficiency as a function of signal efficiency for τ-ID . . . 59

5.1 Mass spectra for the "GMSB3020" and the "GMSB4030" benchmark point 66
5.2 τ-lepton production in the GMSB Λ–$\tan\beta$ plane . . . 68
5.3 The jet+$E_{\mathrm{T}}^{\mathrm{miss}}$ trigger efficiencies . . . 71
5.4 Jet multiplicity and p_{T} after the trigger plateau requirements and relevant p_{T} requirements . . . 72
5.5 τ multiplicity and p_{T} of leading and sub-leading τ candidates after $\ell = 0$ requirement . . . 73
5.6 $\Delta\phi(E_{\mathrm{T}}^{\mathrm{miss}}, \mathrm{jet}_{1,2})$ after requiring $\geq 2\tau$ . . . 74
5.7 m_{eff} and Asimov significance scan after $\Delta\phi$ requirement . . . 76
5.8 $m_{\mathrm{T}}^{\tau_1} + m_{\mathrm{T}}^{\tau_2}$ after requiring $m_{\mathrm{eff}} > 700\,\mathrm{GeV}$ . . . 78
5.9 $\Delta\phi(\mathrm{jet}_{1,2}, E_{\mathrm{T}}^{\mathrm{miss}})$ after $\ell = 0$ . . . 80
5.10 $E_{\mathrm{T}}^{\mathrm{miss}}/m_{\mathrm{eff}}$ in the multi-jet control regions . . . 83
5.11 $E_{\mathrm{T}}^{\mathrm{miss}}/m_{\mathrm{eff}}$ in the 1-τ sideband, using "τ-jet" shape change . . . 83
5.12 Kinematic variables in the 0 and 1-τ sidebands of the multi-jet control region 84
5.13 Kinematic variables in the multi-jet control region for the leading τ and τ-jet 85
5.14 $E_{\mathrm{T}}^{\mathrm{miss}}/m_{\mathrm{eff}}$ for the 0 τ, 1 τ-jet distribution in the multi-jet control region, varying the number of tracks associated to the τ-jet . . . 86
5.15 $E_{\mathrm{T}}^{\mathrm{miss}}/m_{\mathrm{eff}}$ for the 0- and 1-τ sidebands, varying τ-ID strength . . . 87
5.16 m_{eff} in the combined W+jets and top control region . . . 88
5.17 Kinematic variables in the W+jets top control region . . . 90
5.18 b-jet multiplicity and m_{eff} in separate W and top control regions . . . 91
5.19 The ratio of the number of signal events to the number of background events in the combined W and top CR . . . 93
5.20 True τ-lepton content of the signal and control regions . . . 94
5.21 The number of events in the GMSB grid. . . . 96
5.22 The p_{T} spectrum of the leading τ-candidates . . . 105
5.23 τ-candidate multiplicity and p_{T} . . . 106
5.24 Distributions of variables used for the signal region definition . . . 106
5.25 Distribution of some of the main kinematic variables . . . 107
5.26 True τ-lepton multiplicity in the signal region . . . 108
5.27 Distributions of the test variable q for CL_{s} method . . . 108
5.28 Relative systematic uncertainties over the GMSB parameter space . . . 111

5.29 Observed upper limit on the production cross-section 112
5.30 Expected and observed GMSB exclusion limit from 2τ analysis 113
5.31 Expected and observed GMSB exclusion limits from 2τ, 1τ and dilepton analyses 113
5.32 Event display for run 180400, event 58989646 114

6.1 $m_{\mathrm{T}}^{\tau_1} + m_{\mathrm{T}}^{\tau_2}$ after the $\Delta\phi$ requirement 121
6.2 H_{T} distribution and Asimov significance scan after $m_{\mathrm{T}}^{\tau_1} + m_{\mathrm{T}}^{\tau_2}$ requirement . 122
6.3 Distribution of m_{T} and H_{T} for the 1τ final state 123
6.4 Distribution of $m_{\mathrm{T}}^{e,\mu}$ for the τ+μ and τ+e final states 124
6.5 Distribution of m_{eff} for the τ+μ and τ+e final states 125
6.6 $\Delta\phi(\mathrm{jet}_{1,2}, E_{\mathrm{T}}^{\mathrm{miss}})$ after $\ell = 0$ 127
6.7 $E_{\mathrm{T}}^{\mathrm{miss}}/m_{\mathrm{eff}}$ in the multi-jet control region 128
6.8 Kinematic variables in the multi-jet control region 128
6.9 The rejection factor of the jet BDT requirement as function of the τ-candidate p_{T} 129
6.10 $E_{\mathrm{T}}^{\mathrm{miss}}/m_{\mathrm{eff}}$ in the "extra loose" multi-jets control region 131
6.11 Kinematic variables in the 0 and 1 "extra loose" τ sideband of the multi-jet control region 132
6.12 Validation plots for the jet BDT rejection method 133
6.13 $E_{\mathrm{T}}^{\mathrm{miss}}/m_{\mathrm{eff}}$ in the 1τ sideband 133
6.14 The leading jet p_{T} in the three 2τ control regions 135
6.15 Distributions of obtained normalisation factors and background predictions 137
6.16 $p_{\mathrm{T}}^{\tau 1}$ after the $\Delta\phi$ requirement 138
6.17 True τ-lepton composition in the control regions for the 2τ analysis 139
6.18 $m_{\mathrm{T}}^{\tau_1} + m_{\mathrm{T}}^{\tau_2}$ and H_{T} distribution for 2τ signal selection 148
6.19 Expected and observed 95% CL limits for the 2τ final state 149
6.20 Event display for 2τ analysis 151
6.21 Acceptance and Efficiency in the GMSB grid for the 2τ analysis 152
6.22 Expected and observed 95% CL limits for the 1τ final state 154
6.23 Expected and observed 95% CL limits for the $\tau + \ell$ final states 156

7.1 Expected and observed 95% CL limits for the full combination of channels . 158
7.2 CL_{s}, CL_{b}, and $CL_{\mathrm{s+b}}$ p-values as a function of different signal strength values 160

8.1 Expected and observed 95% CL limits for the combined analysis 164

1 Introduction

The Standard Model of particle physics [1–6] provides a unified description of the fundamental particles and interactions that make up the universe, and is one of the most significant achievements of modern science. It has required decades of work from both the theoretical and the experimental physics community to reach the level of precision that exists today, and the recent observation of a new boson by the ATLAS and CMS collaborations, consistent with the Standard Model Higgs boson [7, 8], could potentially be the missing piece of the Standard Model puzzle that physicists have been searching for since it was postulated in the 1970s.

Despite its success, the Standard Model is known to be incomplete and to suffer from several problems, leading to the assumption that it is a low-energy effective approximation of a more fundamental theory. These problems include the fact that many parameters of the theory are not generated spontaneously, and the model suffers from inconsistencies when extrapolated to higher energies[1].

Also, the Standard Model does not offer an explanation of the gravitational force, and neither does it contain a dark matter candidate. With the experiments at the Large

[1]Such as the scattering of longitudinally polarised vector bosons, via the process $W_L W_L \to W_L W_L$, which violates perturbative unitarity at centre-of-mass energy of 1.2 TeV [9].

Hadron Collider (LHC) it is now possible to probe a much higher energy scale than ever achieved before. The physics programme of the ATLAS experiment is designed to answer some of the questions that remain about the Standard Model, such as the mechanism of electroweak symmetry breaking, the nature of dark matter, and also the mechanism that resolves the so-called hierarchy problem, which is related to the sensitivity of the mass of the Higgs boson to radiative corrections from physics at high energies.

There are many candidates for theories to extend the Standard Model, and supersymmetry [10–18] is one of the leading options. It predicts a new "superpartner" particle for each of the Standard Model particles, sharing all of the same properties, other than spin (which differs by 1/2 a unit in $\hbar$) and mass. Supersymmetry provides a solution to the hierarchy problem, contains a natural dark matter candidate, and also unifies the gauge coupling constants, which is an important consideration if the SM is to be shown to be part of a larger, unifying theory.

An understanding of τ-leptons at ATLAS is important for a wide range of physics analyses, including precision electroweak measurements, searches for Higgs bosons, and searches for evidence of physics beyond the Standard Model (BSM), such as supersymmetry and more exotic models. This work focuses on the search for evidence of supersymmetry in events containing τ-leptons, jets, missing transverse momentum and zero or one light lepton ($\ell = e, \mu$).

This document is structured as follows: chapter 2 provides an overview of the theoretical considerations for these searches. The Standard Model is described, along with a discussion of its limitations, and the theory of supersymmetry is introduced in order to provide a possible explanation for these limitations. Potential experimental signatures of supersymmetry at the LHC are also discussed. Chapter 3 outlines both the Large Hadron Collider and the ATLAS experiment. Chapter 4 summarises the event generation, detector simulation and physics object reconstruction at the ATLAS detector, providing background information for the two searches for supersymmetry, which are presented in chapters 5 and 6. The method of setting exclusion limits from the results in chapters 5 and 6 is described in chapter 7. The work is concluded in chapter 8.

2

Theoretical background

The Standard Model of particle physics provides a unified description of the fundamental particles and interactions from which the universe is built, and is perhaps one of the most impressive achievements of human thought. It was first developed in the 1960s and 1970s, beginning with Sheldon Glashow's discovery of a way to combine the theories of the electromagnetic and weak interactions into a single theory of the *electroweak* interaction [1]. In 1967 the Higgs mechanism [2–4] was incorporated into the electroweak theory by Steven Weinberg [5] and Abdus Salam [6].

The Standard Model became widely accepted following the discovery at CERN in 1973 of neutral weak currents [19–21] (due to the exchange of Z bosons), and Glashow, Salam, and Weinberg shared the 1979 Nobel Prize in Physics for their contribution. The existence of the W and Z bosons was confirmed experimentally in 1981, and their masses were consistent with the Standard Model predictions. The theory of the strong interactions was formulated as it exists today around 1973–74, when it was confirmed experimentally at Stanford Linear Accelerator Center that hadrons were composed of fractionally charged quarks [22, 23].

Since its formulation the Standard Model has sucessfully provided an explanation for experimental results in particle physics to a very high degree of precision. A full

discussion of the details of the Standard Model is beyond the scope of this work, but this chapter will attempt to provide an overview of the theory, as well as a discussion of some of its limitations. One of the theoretically attractive extensions to the Standard Model is supersymmetry (SUSY) [10–18], which is able to offer a solution to some of these limitations, and this is also discussed, particularly in the context of its discovery potential at the LHC.

2.1 The Standard Model

The Standard Model (SM) provides a mathematical description, within the framework of quantum field theory (QFT), of the fundamental matter particles and the electromagnetic, weak, and strong interactions, via the exchange of gauge bosons. All of the SM particles are divided in two categories, according to their spin: *fermions* are those with half-integer spin, and *bosons* those with integer spin (tables 2.1(a) and 2.1(b), respectively). The fermions are further divided into two types: *leptons*, which interact via the weak and electromagnetic forces, and *quarks*, which also interact via the strong force. Leptons and quarks are arranged into doublets corresponding to three generations, of which the first generation comprises stable matter. The primary difference between the generations is the mass of the particles, as each successive generation is heavier than the previous. These masses differ by several orders of magnitude but the reason for this is not explained by the SM, and these are therefore free parameters of the theory.

The SM is based on a gauge principle, according to which all the forces of nature are mediated by an exchange of the gauge fields[1] of the corresponding local symmetry group. The SM is a non-Abelian[2] Yang-Mills relativistic QFT [24] of the topological group given in equation 2.1:

$$SU(3)_{\mathrm{C}} \otimes SU(2)_{\mathrm{L}} \otimes U(1)_{\mathrm{Y}} \tag{2.1}$$

Here the $SU(3)_{\mathrm{C}}$ group corresponds to the theory of quantum chromodynamics (QCD) [25, 26], which provides the description for the strong-nuclear force; $SU(2)_{\mathrm{L}} \otimes U(1)_{\mathrm{Y}}$ corresponds to the electroweak theory (in which the weak-nuclear force is unified with electromagnetism), but this group is broken spontaneously, leaving only $U(1)_{\mathrm{EM}}$ unbroken and

[1] A gauge field theory is one in which the Lagrangian is invariant under a continuous group of local transformations.

[2] An Abelian group is a group for which the result of applying the group operation to two elements of the group is not dependent on the order in which this is applied (this is the so-called *axiom of commutativity*). If this is not the case then a group is known as non-Abelian.

resulting in these forces manifesting very differently at everyday energies. C, L and Y correspond to the "colour charge", "left-handedness" and the "weak hypercharge", respectively, about which more will be said when each force is discussed in detail. The unified electroweak theory and quantum chromodynamics are both formulated as Yang-Mills theories, meaning that they are gauge QFTs based upon the symmetry groups given in equation 2.1. The construction of the SM requires the combination of the two QFT descriptions of the electroweak and the strong interactions. The former already unifies the relativistic theory of the electromagnetic force, known as quantum electrodynamics (QED), with the theory for weak interactions, as initially proposed by Glashow, Weinberg, and Salam.

All of the SM forces are mediated by the exchange of gauge bosons, corresponding to spin-1 vector fields. The strong force is mediated by gluons, which carry colour charge. The weak force is mediated by the exchange of Z^0 (*neutral-current interactions*) and $W^{\pm}$ bosons (*charged-current interactions*), and the electromagnetic force is mediated by the photon, γ. Each of these three forces are described in detail in the following sections. Gravity, which is not included in the SM, is thought to be mediated by the (as yet unobserved) graviton, corresponding to a spin-2 field.

2.1.1 Quantum chromodynamics

The strong interaction is a result of the gauge invariance under the $SU(3)$ transformation, and the colour charge is the associated conserved quantity. This is analagous to the electric charge of QED, with the difference that there are three colour eigenstates ("red", "green", "blue"), resulting in eight linear combinations of colour-anticolour pairs as one of the nine possible combinations results in a colourless state, which does not exist in nature. The gluons, which mediate the strong force and contain both a colour and an anticolour, are therefore arranged in an $SU(3)_C$ octet. This results in their coupling to other coloured particles, including other gluons. Quarks also interact via the strong force, as they are colour triplets of the QCD gauge group. There are six quarks, divided into three families of two, and each type of quark appears in three forms, corresponding to the three different colour charges.

Quantum chromodynamics, which describes the strong interactions of coloured quarks and gluons, is an $SU(3)$ gauge field theory described by the Lagrangian:

$$\mathcal{L}_{\mathrm{QCD}} = i \sum_f \bar{q}_f \gamma^\mu D_\mu q_f - \frac{1}{4} G^i_{\mu\nu} G^{\mu\nu}_i \ . \tag{2.2}$$

Table 2.1: (a) The three generations of the fermionic sector of the Standard Model, where Q is the electric charge, I_3 is the third component of the weak isospin and Y is the hypercharge, and (b) the bosonic sector of the Standard Model.

(a) The fermionic sector of the Standard Model.

			Q	I_3^W	Y
$\begin{pmatrix}\nu_e\\ e\end{pmatrix}_L$	$\begin{pmatrix}\nu_\mu\\ \mu\end{pmatrix}_L$	$\begin{pmatrix}\nu_\tau\\ \tau\end{pmatrix}_L$	0 -1	$\frac{1}{2}$ $-\frac{1}{2}$	$-\frac{1}{2}$ $-\frac{1}{2}$
ν_{eR}	$\nu_{\mu R}$	$\nu_{\tau R}$	0	0	0
e_R	μ_R	τ_R	-1	0	-1
$\begin{pmatrix}u\\ d\end{pmatrix}_L$	$\begin{pmatrix}c\\ s\end{pmatrix}_L$	$\begin{pmatrix}t\\ b\end{pmatrix}_L$	$\frac{2}{3}$ $-\frac{1}{3}$	$\frac{1}{2}$ $-\frac{1}{2}$	$\frac{1}{6}$ $\frac{1}{6}$
u_R	c_R	t_R	$\frac{2}{3}$	0	$\frac{2}{3}$
d_R	s_R	b_R	$-\frac{1}{3}$	0	$-\frac{1}{3}$

(b) The bosonic sector of the Standard Model.

	Force	Spin	Q
γ	electromagnetism	1	0
$\mathrm{W}^{\pm}, Z^0$	weak	1	± 1, 0
$\mathrm{g}_i, i \in 1,8$	strong	1	0

Here, q_f is a colour triplet of quarks with flavour f, γ^μ are the Dirac matrices, and D_μ is the covariant derivative, given by:

$$D_\mu = \partial_\mu - ig_3 \frac{\lambda_i}{2} G_\mu^i \ , \tag{2.3}$$

with the $SU(3)_\mathrm{C}$ coupling constants g_3. The field strength tensor for the gluon fields $G_i^{\mu\nu}$ (i=1...8) are defined as:

$$G_i^{\mu\nu} = \partial^\mu G_i^\nu - \partial^\nu G_i^\mu + g_s f_{ijk} G_j^\mu G_k^\nu \ , \tag{2.4}$$

where λ_i represents the generators of $SU(3)_\mathrm{C}$ (the Gell-Mann matrices), g_s represents the coupling from the strong charge of the quarks, and $f_{ijk} (i,j,k = 1 \ldots 8)$ are the structure constants of the group. The strong coupling constant α_s, which parameterises the strength of the strong interaction, is given by:

$$\alpha_s \equiv \frac{g_s}{4\pi} \approx 1 \quad (\text{for } Q \propto \Lambda_\mathrm{QCD}) \ , \tag{2.5}$$

The value of the strong coupling constant depends on the momentum transfer Q^2, which is the amount of momentum that one particle transfers to another, and a measure of

how "hard" an interaction is. For lower values of Q^2, corresponding to distances of $>$ $\mathcal{O}$(10–15 m), the value of α_s becomes large. This is the origin of *confinement* [27, 28] and is the reason that quarks and gluons are not observed in isolation, but exist as colourless bound states known as hadrons. These hadrons are either a doublet ($q\bar{q}$), known as a meson, or a triplet (qqq), known as a baryon, and have a total colour charge of zero. At larger values of Q^2, corresponding to distances of $<$ $\mathcal{O}$(10–15 m), α_s becomes smaller, leading to high-energy constituent quarks and gluons behaving as free particles. This phenomenon is known as *asymptotic freedom* [27].

2.1.2 Quantum electrodynamics

Quantum electrodynamics provides a description of the electromagnetic interaction, and is based on the $U(1)_Q$ symmetry group. The interaction of a charged fermionic field ψ with the electromagnetic field represented by the vector potential A_μ, is described by the Lagrangian:

$$\mathcal{L}_{QED} = \bar{\psi}(i\gamma^\mu D_\mu - m)\psi - \frac{1}{4}F_{\mu\nu}F^{\mu\nu} \ . \tag{2.6}$$

Here, m is the mass associated to the fermion field, and the tensor of the electromagnetic field strength is $F_{\mu\nu} = \partial_\mu A_\nu - \partial_\nu A_\mu$. This term is the Lagrangian for the free electromagnetic field. D_μ is the covariant derivative, which transforms in the same way as the field:

$$D_\mu\psi(x) \rightarrow e^{i\alpha(x)}D_\mu\psi(x) \tag{2.7}$$

Requiring the Lagrangian to be invariant under rotations of the $U(1)_Q$ results in the introduction of the photon field. $\mathcal{L}_{QED}$ is invariant under a local $U(1)$ phase transformation (equation 2.8a) and a gauge transformation (equation 2.8b):

$$\psi(x) \rightarrow e^{i\alpha(x)}\psi(x) \ , \tag{2.8a}$$

$$A_\mu(x) \rightarrow A'_\mu(x) = A_\mu(x) - \frac{1}{e}\partial_\mu\alpha(x) \ , \tag{2.8b}$$

where $\alpha(x)$ is a local phase. Adding an explicit mass term proportional to $A_\mu A^\mu$ destroys the gauge invariance, and therefore the photon field A_μ must be massless. The symmetry group $U(1)_Q$ is Abelian and therefore there is no self-interaction term for the photon.

2.1.3 From weak interactions to the electroweak theory

Experiments have shown that the weak charged vector bosons ($W^{\pm}$) only interact with left-handed chiral states[3] [30, 31]. When considering the theory of the weak interactions, the left-handed charged leptons and associated left-handed neutrino can therefore be grouped into a two component field:

$$\Psi_l = \begin{pmatrix} \nu_e \\ e \end{pmatrix}, \qquad \begin{pmatrix} \nu_\mu \\ \mu \end{pmatrix}, \qquad \begin{pmatrix} \nu_\tau \\ \tau \end{pmatrix} , \tag{2.9}$$

which transform under $SU(2)_{\mathrm{L}}$. The right-handed leptons are considered as singlets. The Lagrangian $\mathcal{L}_W$ is defined by:

$$\mathcal{L}_W = i\bar{\Psi}_l \gamma^\mu D_\mu \Psi_l + i\bar{e}_R \gamma^\mu \partial_\mu e_R \ . \tag{2.10}$$

This is invariant under $SU(2)_{\mathrm{L}}$ transformations, given by:

$$\Psi_l \rightarrow \Psi_l' = e^{[\frac{i}{2}\vec{\alpha}(x)\vec{\tau}]}\Psi_l \ , \tag{2.11}$$

if the covariant derivative D^μ transforms like:

$$D^\mu = \partial^\mu + i\frac{g}{2}\vec{\tau}\vec{W}_\mu(x) \ , \tag{2.12}$$

where $\vec{\tau}$ are the Pauli matrices and g is a coupling constant. Imposing local gauge invariance results in three vector fields W_1, W_2 and W_3. W_1 and W_2 mix to give the physical $W^{\pm}$ bosons:

$$W_\mu^{\pm} = \frac{1}{\sqrt{2}}(W_{1\mu} \mp W_{1\mu}) \tag{2.13}$$

Requiring that only the left-handed fermions are included in the Ψ_l doublets results in interaction terms that involve the W_3^μ and left-handed fermions, but no terms that involve interactions between W_3^μ and right-handed fermions. The Z boson interacts with both right and left-handed fermions, so the W_3 is not trivially the Z. This is confirmed by the fact that the Z and $W^{\pm}$ bosons are not mass degenerate, as they would be if the W_3 was the Z boson.

The electroweak force, $SU(2)_L \otimes U(1)_Y$, allows for a prediction of the mass of the Z, given the mass of the W. The conserved quantity of $SU(2)_{\mathrm{L}}$ is the third component of the weak isospin I_3, and the conserved quantity of $U(1)_{\mathrm{Y}}$ is the hypercharge Y. These are related by equation 2.14, where Q is the electric charge.

$$Q = \frac{Y}{2} + I_3 \tag{2.14}$$

[3]The chirality of a particle is determined by whether the particle transforms in a right or left-handed representation of the Poincaré group [29].

The electroweak Lagrangian, $\mathcal{L}_{EW}$, is still given by equation 2.10, but the covariant derivative is now:

$$D_\mu = \partial_\mu + ig\frac{\vec{\tau}}{2}\vec{W}_\mu + ig'\frac{Y}{2}B_\mu \ , \tag{2.15}$$

where g and g' are coupling constants. The three vector fields, W_μ, are the three $SU(2)_L$ isospin bosons and B_μ is the weak hypercharge boson. The Lagrangian is invariant under local gauge transformations of the form:

$$\Psi_l \rightarrow \Psi_l' = e^{i(\vec{\alpha}(x)\vec{\tau}+\beta(x)Y)/2}\Psi_l \tag{2.16a}$$

$$e_R \rightarrow e_R' = e^{\beta(x)Y/2}e_R \tag{2.16b}$$

These transformations result in the Lagrangian:

$$\mathcal{L}_{EW} = \Psi_l\gamma^\mu\left(i\partial_\mu - g\frac{1}{2}\vec{\tau}\vec{W}_\mu - g'\frac{Y}{2}B_\mu\right)\Psi_l\bar{e}_R\gamma^\mu\left(i\partial_\mu - g'\frac{Y}{B_\mu}\right)e_R - \frac{1}{4}\vec{W}_{\mu\nu}\vec{W}^{\mu\nu} - \frac{1}{4}\vec{B}_{\mu\nu}\vec{B}^{\mu\nu} \ , \tag{2.17}$$

where $B_{\mu\nu} = \partial_\mu B_\nu - \partial_\nu B_\mu$ and $W_{\mu\nu} = \partial_\mu\vec{W}_\nu - \partial_\nu\vec{W}_\mu + ig\vec{W}_\mu \times \vec{W}_\nu$. The first two terms describe the kinetic energy of the fermions and their interaction with the gauge fields, whilst the final two terms describe the kinetic energy of the gauge fields and their self-interaction. The Lagrangian involves fermions, three gauge fields $W_\mu^{1,2,3}$ for $SU(2)$ and one gauge field B_μ for $U(1)$. The mixing of the four gauge fields results in the physical fields of the SM, the photon field A_μ, the Z boson field Z_μ, and the charged $W_\mu^\pm$ boson fields. Equation 2.13 describes the mass of the $W_\mu^\pm$, and A_μ and Z_μ are given by:

$$A_\mu = \sin\theta_W W_\mu^3 + \cos\theta_W B_\mu \ , \tag{2.18a}$$

$$Z_\mu = \cos\theta_W W_\mu^3 + \sin\theta_W B_\mu \ , \tag{2.18b}$$

where θ_W is the so-called "weak mixing angle". The resulting particles and their electroweak quantum numbers are given in table 2.1(a). The right-handed quarks and leptons have zero isospin, and therefore they do not couple to the isospin bosons. Including an explicit mass term for the W and Z bosons in the Lagrangian destroys the gauge invariance, and therefore the Higgs mechanism is required.

2.1.4 The Higgs mechanism

In order to generate masses for the weak gauge bosons, the electroweak symmetry must be broken from $SU(2)_L \otimes U(1)_Y$ to $U(1)_Q$. Manually inserting an explicit mass term in the SM Lagrangian violates the chiral symmetry $SU(2)_L$, and breaks the local gauge invariance of the theory. Masses can be generated by introducing a complex scalar doublet, resulting

in "Spontaneous Symmetry Breaking". This is known as the "Higgs Mechanism", after Peter Higgs, and with this procedure particles can acquire mass via a coupling to the scalar Higgs field. This is a complex $SU(2)$ doublet with four degrees of freedom, and the Lagrangian is given by:

$$\mathcal{L}_{\text{Higgs}} = (\partial^\mu \phi^\dagger)(\partial_\mu \phi) - \mu^2 \phi^\dagger \phi - \lambda(\phi^\dagger \phi)^2 \ , \tag{2.19}$$

where the minimum of the potential is:

$$V(\phi) = \mu^2 \phi^\dagger \phi + \lambda(\phi^\dagger \phi)^2 \tag{2.20}$$

The values of μ^2 and λ in the Higgs potential are free real parameters. For the minimum (vacuum) energy to be bounded from below, λ is chosen to be positive. If $\mu^2 > 0$, the potential has a single minimum at $\phi = \phi_0 = 0$. If $\mu^2 < 0$, the minimum of the potential is a circle in the complex plane of radius $-\mu^4/4\lambda$. This minimum occurs when ϕ_0 is given by:

$$\phi_0 = \sqrt{\frac{\mu^2}{2\lambda}} e^{i\theta} \tag{2.21}$$

Therefore the state of minimum energy, the vacuum state, is not unique and there are an infinite number of degenerate minima. This is demonstrated by the so-called "Mexican hat potential", shown in figure 2.1. To obtain the equations of motion the Lagrangian is expanded around the selected minimum, which ia chosen such that $\theta = 0$. This leads to:

$$\phi_0 = \frac{\nu}{\sqrt{2}} \qquad \text{where } \nu = \sqrt{\frac{-\mu^2}{\lambda}} \ , \tag{2.22}$$

resulting in:

$$\phi(x) = \frac{1}{\sqrt{2}}(\nu + \sigma(x) + i\eta(s)) \ , \tag{2.23}$$

where σ and η are Hermitian fields with zero vacuum expectation values. Expanding the Lagrangian in terms of these fields results in equation 2.24, in which $\mathcal{L}_I$ represents the interaction terms.

$$\mathcal{L} = \frac{1}{2}(\partial^\mu \sigma)(\partial_\mu \sigma) - \frac{1}{2} m_\sigma^2 + \frac{1}{2}(\partial^\mu \eta)(\partial_\mu \eta) + \mathcal{L}_I + \text{const.} \tag{2.24}$$

This Lagrangian contains mass terms for the σ field, but the η field is massless. Therefore the introduction of the complex scalar field (two degrees of freedom) has resulted in one massive and one massless scalar boson. If instead a weak isospin doublet of complex scalar fields (four degrees of freedom) is added to the electroweak Lagrangian, then this process can generate the required masses for the gauge bosons. Three of the four degrees of freedom associated to the complex scalar fields generate the masses of the $W^\pm$ and Z

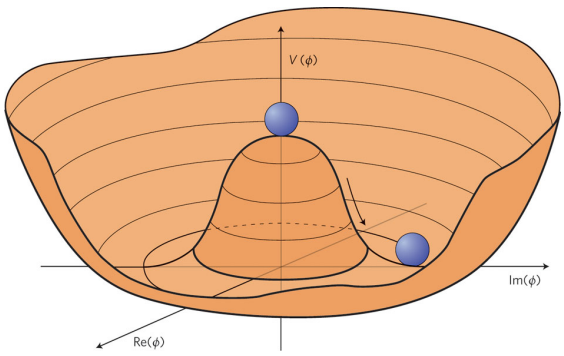

Figure 2.1: The vacuum is described by a randomly chosen point at the minimum of the potential (at the bottom of the hat). In a global symmetry, movements around the bottom of the hat correspond to a massless, spin-0, Nambu-Goldstone boson [32–34]. In the case of a local (gauge) symmetry, this boson combines with a massless spin-1 boson, resulting in a massive spin-1 particle [2–4]. The Higgs boson is a massive spin-0 particle corresponding to quantum fluctuations in the radial direction, oscillating between the centre and the side of the hat in the direction of the arrow [35].

bosons. The fourth results in one real scalar field, which manifests as the Higgs boson, and the photon remains massless.

After the inclusion of these complex scalar fields, the resulting electroweak Lagrangian includes a term of the form $\frac{1}{4}g^2\nu^2 W_\mu^\dagger W^\mu$, which corresponds to a mass m_W for the $W^\pm$ boson. $W_{3\mu}$ and B_μ only appear in the linear combination $\frac{1}{2}gW_{3\mu} - g'Y_H B_\mu$, resulting in this combination alone gaining a mass. If $Y_H = \frac{1}{2}$ (where Y_H is the weak hypercharge of the Higgs) then only the Z gains mass, given by $m_W/\cos\theta_W$.

This doublet can also be used to generate masses for the quarks and leptons. This requires introducing so-called "Yukawa" couplings of the Higgs field to fermions into the Lagrangian. An example of the Yukawa couplings, which describe the interaction between a scalar and a fermion field, can be seen in equation 2.25, where g is a coupling constant, ϕ the scalar Higgs field and Ψ_L and ψ_R the down quark fields.

$$\mathcal{L} = -g\bar{\Psi}_L\phi\psi_R \tag{2.25}$$

The result of this procedure is the generation of lepton masses that are proportional to the vacuum expectation value of the scalar field, and interactions between leptons and the Higgs field which are proportional to mass of the lepton.

The SM Higgs boson has not yet been experimentally confirmed, but on 4$^{\text{th}}$ July 2012 the ATLAS and CMS collaborations both reported the discovery of a new boson, with a mass of ∼125 GeV, the properties of which are currently consistent with the theoret-

ical predictions of the SM Higgs boson [7]. More precise measurements of this particle's properties are required to verify whether or not this is the SM Higgs boson.

2.2 Limitations of the Standard Model

Despite the success of the SM, the predictions of which have been verified by experimental data to a very high accuracy, there are still a number of problems that remain, and there are many hints that the SM is only a low-energy approximation to a more extensive theory. Some of the limitations of the SM will be discussed in the following sections.

2.2.1 The hierarchy problem

The hierarchy problem arises from the question as to why there is a vast difference between the weak and Planck scales. The weak scale m_W corresponds to energies around the mass of the weak vector bosons ($\sim$100 GeV), and the Planck scale m_P corresponds to $\sim 1.22 \times 10^{19}$ GeV, at which the quantum effects of gravity are no longer neglible, and the SM breaks down due to the apparent non-renormalisability of gravity. The Planck scale is considered to be a fundamental mass scale, at which point the gravitational interactions become comparable in magnitude to the other particle interactions. If it is assumed that the SM is valid when extrapolated to energies many orders of magnitude above the scale of electroweak symmetry breaking, then finely-tuned corrections to the Higgs mass are required for it to remain at the weak scale. This is because the Higgs field is sensitive to radiative contributions from any particle that couples to it. Figure 2.2 shows the radiative corrections to the Higgs mass from a Dirac fermion and a scalar particle, but these diagrams are quadratically divergent, which implies that:

$$\delta m_{H,W}^2 = \mathcal{O}\left(\frac{g^2}{16\pi^2}\right)\int^{\Lambda} d^4k \frac{1}{k^2} = \mathcal{O}\left(\frac{\alpha}{\pi}\right)\Lambda^2 \ , \tag{2.26}$$

where Λ represents the cut-off scale at which the SM is no longer valid [36]. If Λ is close to the Planck scale then the mass of the Higgs boson should be much larger than the mass of the W boson. This is the so-called hierarchy problem [37–40]. If these corrections are of the order m_P then the corrections for m_H^2 would exceed the value of m_H^2 by at least 30 orders of magnitude.

2.2.2 Dark matter

The first evidence for dark matter was from the observation that various astronomical objects (including stars, gas clouds and galaxies) move faster than is possible from only the

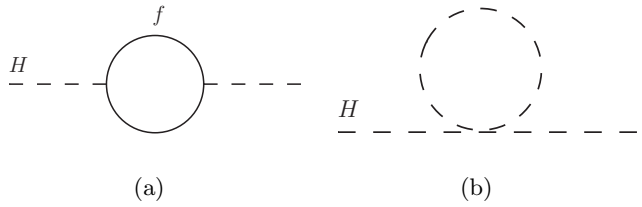

Figure 2.2: One-loop quantum corrections to the Higgs squared mass parameter m_H^2, from (a) a Dirac fermion f, and (b) a scalar particle [36].

gravitational attraction of other visible objects. The existence of dark matter (defined as non-luminous and non-absorbing) has been demonstrated by a number of experiments [29]. The Wilkinson Microwave Anisotropy Probe (WMAP) experiment performed precision measurements of the cosmic microwave background radiation, resulting in the discovery that baryonic matter comprises only ∼4% of the matter in the universe [41]. The remainder is comprised of dark energy[4] (∼73%) and dark matter (∼23%). The SM does not contain an dark matter candidate, with the neutrinos being too light, and new physics is required to explain this phenomena.

2.2.3 Unification of gauge couplings

The magnitudes of the gauge couplings of the three forces described by the SM are very different at the weak scale. However, the strength of these couplings is not constant, as they are linear functions of the logarithm of the energy scale [36]. The strength of the strong and weak couplings, both associated with non-Abelian groups, increases with the energy, whilst the electromagnetic coupling, associated to an Abelian group, decreases [36]. If these forces are aspects of a single, unifying group at a higher energy then it is necessary for them to be equal at this energy. These couplings have been measured precisely at the energies accessible to experiment, and can be evolved via the renormalisation group equations to higher energies. Following this procedure, for the SM there is no single point at which the three couplings converge [36].

2.3 Supersymmetry

Supersymmetry is a proposed extension to the SM, that offers a solution to some of the problems detailed in section 2.2, by providing a symmetry that relates fermions and bosons.

[4]Dark energy is a proposed form of energy that explains the acceleration of the expansion of the universe [41].

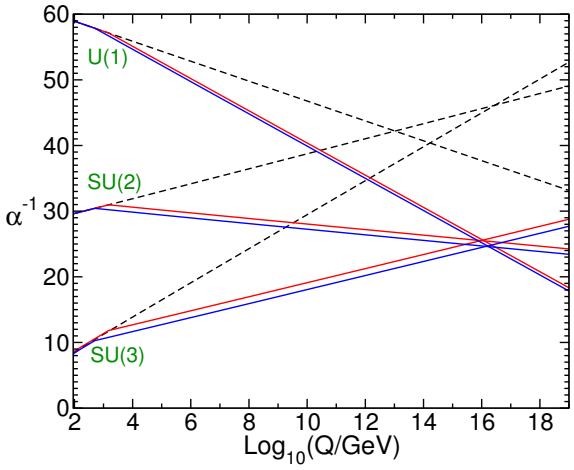

Figure 2.3: Two-loop renormalisation group evolution of the inverse gauge couplings $\alpha_a^1(Q)$ in the Standard Model (dashed lines) and the MSSM (solid lines). In the MSSM case, the sparticle masses are treated as a common threshold varied between 500 GeV and 1.5 TeV, and $\alpha_3(m_Z)$ is varied between 0.117 and 0.121 [36].

If Q is a generator of SUSY algebra, then:

$$\begin{aligned} Q|\text{fermion}\rangle &\propto |\text{boson}\rangle \\ Q|\text{boson}\rangle &\propto |\text{fermion}\rangle \end{aligned} \tag{2.27}$$

Fermions and bosons that are related via this transformation are known as "superpartners". If SUSY was an exact symmetry of nature then the SM particles and their superpartners would be degenerate in mass and share all quantum numbers, apart from a 1/2 unit difference in spin. As no superpartners have been experimentally observed this cannot be the case, and if SUSY is realised in nature then it must be a broken symmetry. The way this symmetry is broken has large implications for the phenomenology. It is possible to construct supersymmetric extensions of the SM and make precise phenomenological predictions. This allows for experimental searches for evidence of the supersymmetric particles, and these searches have been an important part of the physics programme of many particle colliders.

This section will provide more detail about the potential solutions to the problems of the SM, that makes SUSY an attractive theory for physics beyond the SM.

2.3.1 The hierarchy problem

The hierarchy problem is addressed in a natural way if there exist supersymmetric particles of mass $\lesssim 1$ TeV [36], and this also allows for the unification of gauge coupling constants. Supersymmetry is able to provide a cancellation of the contributions to Δm_H^2 by providing

a symmetry between fermions and bosons [42–47]. The contribution to Δm_H^2 from the boson loops cancels those from the fermion loops, due to a factor of -1 from Fermi statistics. The Feynman diagrams representing this process can be found in figure 2.4 [36]. As searches for evidence of supersymmetry have so far not resulted in the discovery of any SUSY particles much of the parameter space is constrained, and limits have been set on the masses of these particles. As these limits are pushed to higher masses the ability of SUSY to solve the hierarchy problem is reduced.

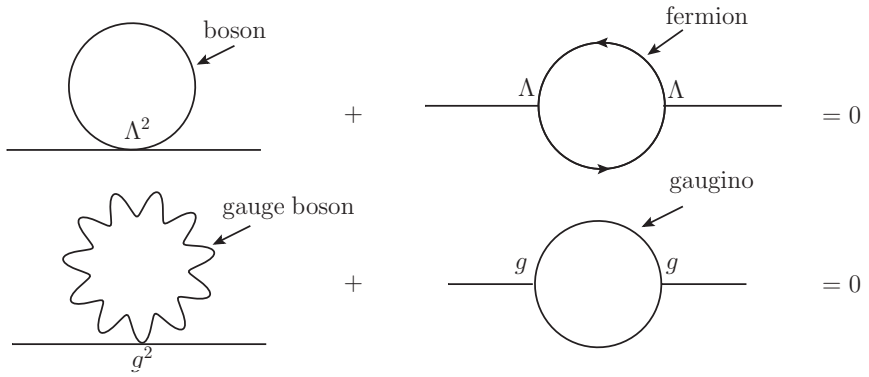

Figure 2.4: Cancellation of quadratic terms (divergences) in the Higgs mass via supersymmetry [48].

2.3.2 Unification of gauge couplings

For supersymmetric models it is possible for the gauge couplings to converge to a single point, at energies of $\sim 10^{15\text{–}16}$ GeV [46, 49–56]. The value of the gauge coupling constants as a function of the energy, for both the SM and the Minimal Supersymmetric Standard Model [42, 57–60] (MSSM), can be found in figure 2.3. The gauge coupling unification in the MSSM is due to extra loop contributions from the MSSM particles affecting the coefficients of the renormalisation group equations [36].

2.3.3 Dark matter

Many models of supersymmetry contain a natural dark matter candidate. If the SUSY quantum number known as *R-parity* (described in detail in section 2.4) is conserved, then the lightest supersymmetric particle (LSP) is stable and electrically neutral, interacting only weakly with baryonic matter, and is a dark matter candidate [61, 62]. Different models of SUSY-breaking result in different LSPs, and subsequently different experimental signatures, some of which will be accessible with the ATLAS detector. The results from the

analyses presented in this work are interpreted in the context of Gauge-Mediated SUSY Breaking, for which the LSP is the gravitino, $\tilde{G}$.

2.4 The Minimal Supersymmetric Standard Model

The Minimal Supersymmetric Standard Model is the minimal phenomenologically viable supersymmetric extension of the SM. In the MSSM, each of the SM particles is arranged in either a *chiral* or *gauge supermultiplet*, containing both fermion and boson states, which are superpartners of each other, and differ by half a unit of spin. The particle content of the MSSM can be found in table 2.2 [36].

The left-handed and right-handed components of the SM quarks and leptons are separate two-component Weyl fermions [63], with different gauge transformation properties in the SM (known as chiral fermions), and therefore each must have its own complex scalar supersymmetric partner. The so-called "chiral supermultiplets" are required to contain these fermions. The spin-0 partners of the quarks and leptons are prefixed with an "s", and known collectively as "squarks" and "sleptons", respectively. As an example, left-handed and right-handed components of the SM electron Dirac field have superpartners known as "selectrons", labelled $\tilde{e}_L$ and $\tilde{e}_R$, respectively. The chirality of these particles refers to that of the associated SM partner, as these are spin-0 particles. A similar naming convention is adhered to for the rest of the "sfermions". The gauge interactions and couplings of the sparticles are the same as those of their SM partners [36]. The naming convention for the supersymmetric partners of SM bosons is to suffix the particle name with "ino".

The MSSM contains two Higgs supermultiplets, which are required to prevent the introduction of anomalies. Each single Higgs supermultiplet contains higgsinos, which are chiral fermions, and contain anomalies that would break the chiral symmetry. To cancel these a second Higgs doublet with opposite hypercharge is required [48]. This results in eight degrees of freedom in the MSSM Higgs sector, manifesting in five physical states. These states correspond to five physical Higgs bosons: two neutral CP-even, one neutral CP-odd, and two charged [48]. In the MSSM one of these Higgs supermultiplets contains the Yukawa couping that is responsible for giving mass to the up-type quarks, and the other contains the coupling for the down-type quarks and the charged leptons. The vacuum expectation values of these are labelled v_u and v_d, respectively, and their ratio ($\tan\beta$) is an important parameter for the phenomenology of the model.

The superpartners of the SM gauge bosons are arranged into so-called *gauge supermultiplets*, and these do not correspond directly to the mass eigenstates. Neutral *winos*

Names		spin 0	spin $\frac{1}{2}$	mass eigenstates
		Chiral supermultiplets		
squarks, quarks	Q	$(\widetilde{u}_L \quad \widetilde{d}_L)$	$(u_L \quad d_L)$	$u, \tilde{u}_{\mathrm{L,R}}, d, \tilde{d}_{\mathrm{L,R}}$
($\times$3 families)	$\overline{u}$	$\widetilde{u}^*_R$	$u^\dagger_R$	$c, \tilde{c}_{\mathrm{L,R}}, s, \tilde{s}_{\mathrm{L,R}}$
	$\overline{d}$	$\widetilde{d}^*_R$	$d^\dagger_R$	$t, \tilde{t}_{1,2}, b, \tilde{b}_{1,2}$
sleptons, leptons	L	$(\widetilde{\nu} \quad \widetilde{e}_L)$	$(\nu \quad e_L)$	$e, \tilde{e}_{\mathrm{L,R}}, \mu, \tilde{\mu}_{\mathrm{L,R}}, \nu_{e,\mu}$
($\times$3 families)	$\overline{e}$	$\widetilde{e}^*_R$	$e^\dagger_R$	$\tau, \tilde{\tau}_{1,2}, \nu_\tau, \tilde{\nu}_\tau, \tilde{\nu}_{e,\mu}$
Higgs, higgsinos	H_u	$(H^+_u \quad H^0_u)$	$(\widetilde{H}^+_u \quad \widetilde{H}^0_u)$	$h, H, H^\pm, A$
	H_d	$(H^0_d \quad H^-_d)$	$(\widetilde{H}^0_d \quad \widetilde{H}^-_d)$	

Names		spin $\frac{1}{2}$	spin 1	mass eigenstates
		Gauge supermultiplets		
gluino, gluon		$\widetilde{g}$	g	$g, \tilde{g}$
winos, W bosons		$\widetilde{W}^\pm \quad \widetilde{W}^0$	$W^\pm, W^0$	
bino, B boson		$\widetilde{B}^0$	B^0	$W^\pm, Z, \gamma$

Table 2.2: Chiral and gauge supermultiplets in the MSSM. The spin-0 fields are complex scalars, and the spin-1/2 fields are left-handed two-component Weyl fermions. [36]

($\widetilde{\mathrm{W}}$), *binos* ($\widetilde{\mathrm{B}}$) (superpartners of the gauge boson fields) and *higgsinos* ($\widetilde{\mathrm{H}}^0$) mix to form neutral particles known as *neutralinos* ($\widetilde{\chi}^0$). The charged winos ($\widetilde{\mathrm{W}}^\pm$) and higgsinos ($\widetilde{\mathrm{H}}^\pm$) mix to form charged particles known as *charginos* ($\widetilde{\chi}^\pm$). Non-negligible Yukawa couplings result in a mixing between the electroweak eigenstates, which creates the mass eigenstates of the third generation sfermions (*stops* ($\widetilde{\mathrm{t}}$), *sbottoms* ($\widetilde{\mathrm{b}}$), *staus* ($\widetilde{\tau}$)). The $\tilde{\tau}_R$ usually mixes significantly with $\tilde{\tau}_L$, proportional to the Yukawa coupling of the τ. The resulting physical stop, sbottom and stau states are denoted by subscripts 1 and 2 instead of L and

R.

$$\tilde{B}^0, \tilde{W}^0, \tilde{H}_u^0, \tilde{H}_d^0 \rightarrow \tilde{\chi}_1^0, \tilde{\chi}_2^0, \tilde{\chi}_3^0, \tilde{\chi}_4^0 \qquad \text{neutralinos}$$

$$\tilde{W}^{\pm}, \tilde{H}_u^+, \tilde{H}_d^- \rightarrow \tilde{\chi}_1^{\pm}, \tilde{\chi}_2^{\pm} \qquad \text{charginos}$$

$$\tilde{\tau}_{\mathrm{L}}, \tilde{\tau}_{\mathrm{R}} \rightarrow \tilde{\tau}_1, \tilde{\tau}_2 \qquad \text{stau}$$

$$\tilde{t}_{\mathrm{L}}, \tilde{t}_{\mathrm{R}} \rightarrow \tilde{t}_1, \tilde{t}_2 \qquad \text{stop}$$

$$\tilde{b}_{\mathrm{L}}, \tilde{b}_{\mathrm{R}} \rightarrow \tilde{b}_1, \tilde{b}_2 \qquad \text{sbottom}$$

When formulating a supersymmetric model, terms that violate baryon number B or lepton number L are not explicitly forbidden (unlike in the SM). This in conflict with current experimental evidence, as B- and L-violating processes (such as proton decay) have not been observed. These terms can be forbidden by the inclusion of the multiplicative R-parity quantum number, given by:

$$R = (-1)^{3(B-L)+2S} \ , \tag{2.28}$$

where S is the particle spin. All of the SM particles have $R = +1$ and all of the supersymmetric particles have $R = -1$. If R-parity is a conserved quantity then superpartners will be created in pairs, and the LSP will be stable. In the MSSM, R-parity is assumed to be conserved.

Supersymmetry predicts that all particles in a given supermultiplet will be mass degenerate. As no supersymmetric particles have been observed experimentally, if SUSY is a real symmetry of nature then it must be broken. This breaking will allow the SUSY particles to be heavier than their SM partner. Supersymmetry can be broken in several ways, but in order for it to provide a solution to the hierarchy problem "soft" breaking mechanisms are required. The soft SUSY breaking term contains the gauge and Yukawa interactions and violates supersymmetry, but contains only mass terms and coupling parameters with positive mass dimension [36]. The effective Lagrangian of the broken MSSM then takes the form:

$$\mathcal{L} = \mathcal{L}_{\mathrm{SUSY}} + \mathcal{L}_{\mathrm{soft}} \tag{2.29}$$

None of the SM fields have non-zero vacuum expectation values and could break SUSY without destroying the gauge invariance, and therefore spontaneous supersymmetry breaking requires the inclusion of additional fields. The most common approach is to break SUSY in a so-called "hidden sector" [64–66]. This scenario states that there is a *visible-sector*, which contains the known SM particles, and a *hidden-sector*, that contains the fields responsible for breaking SUSY. The interaction between these two sectors is

mediated by so-called *messenger* fields, which communicate the SUSY breaking from the hidden to the visible sector [48]. There are four common approaches to the mediation of breaking SUSY in a hidden sector, known as gravity mediation, anomaly mediation, gaugino mediation and gauge mediation [48]. The two searches for evidence of supersymmetry that are presented in this work are both focused on models of Gauge-Mediated Supersymmetry Breaking [44, 67–73] (GMSB) which will be discussed in detail in this chapter. An overview of the other methods of SUSY breaking can be found in [36].

2.5 Gauge-Mediated Supersymmetry Breaking

In Gauge-Mediated SUSY breaking, the SUSY breaking effects are mediated to the visible sector **V** via flavor-blind gauge interactions [67, 73] with messenger **M** fields. **M** mediates the spontaneous symmetry breaking by overlapping with a *hidden sector* **H**:

$$\mathbf{V} \xleftarrow{SU(5),\, SU(10)} \mathbf{M} \leftarrow \mathbf{H} \tag{2.30}$$

In the minimal version of GMSB, on which the analyses in chapters 5 and 6 is focused, the messenger fields form complete representations of $SU(5)$ and preserve the unification of the coupling constants. The minimal GMSB model is highly predictive and fully determined by six parameters:

- Λ: the scale of the SUSY breaking; typically it has values of 10–100 TeV and sets the overall mass scale for all supersymmetric particles, which depends linearly on Λ;
- M_{mes}: the messenger mass scale; it has to be larger than Λ in order to prevent color and charge breaking in the messenger sector;
- N_5: the number of equivalent messenger fields; the gaugino masses depend linearly on N_5 while the sfermion masses are proportional to $\sqrt{N_5}$;
- $\tan\beta$: the ratio of the two Higgs doublet vacuum expectation values at the electroweak scale;
- $\text{sgn}\mu = \pm$: the sign of the Higgsino mass term appearing in the neutralino and chargino mass matrices or in the superpotential;
- C_{grav}: the ratio of the gravitino mass to its value for a breaking scale Λ; it determines the lifetime of the next-to-lightest SUSY particle (NLSP).

The phenomenology of GMSB is characterised by the presence of a very light gravitino $\widetilde{G}$ as the LSP. For SUSY particles heavier than the NLSP, the coupling to the $\widetilde{G}$ is very small, meaning that the NLSP plays an important role in the phenomenology of gauge

mediation models. Assuming that R-parity is conserved, all supersymmetric particles will decay via cascades leading to the NLSP, and, as this has no competing decays, it will always decay into its SM partner and a gravitino. The nature of the NLSP therefore determines the experimental signatures to be searched for.

In this work, the minimal GMSB parameters are fixed to ensure that the NLSP is the $\tilde{\tau}_1$ in the majority of the parameter space. This means that all supersymmetric decay chains terminate in the decay of the $\tilde{\tau}_1$ to a τ-lepton and a gravitino ($\tilde{\tau}_1 \to \tau\tilde{G}$). There is also a so-called "co-NLSP" region, where there can effectively be more than one NLSP. The co-NLSP region is where $m_{\tilde{e}_R} \approx m_{\tilde{\mu}_R} < m_{\tilde{\tau}_1} + m_\tau$. In this region the $\tilde{e}_R$ and $\tilde{\mu}_R$ cannot have three-body decays into the $\tilde{\tau}_1$ NLSP, without violating lepton flavour conservation [36]. As lepton flavour-changing interactions are very highly suppressed in GMSB [36], each of the right-handed sleptons decays only into their associated lepton and a gravitino. This results in the $\tilde{\tau}_1$, $\tilde{\mu}_R$, $\tilde{e}_R$ acting effectively as co-NLSPs. In this region of parameter space all supersymmetric decay chains will terminate in $\tilde{\tau}_1 \to \tau\tilde{G}$, $\tilde{e}_R \to e\tilde{G}$ or $\tilde{\mu}_R \to \mu\tilde{G}$.

Of the six GMSB model parameters, Λ and $\tan\beta$ have the strongest influence on phenomenology. In this work the minimal GMSB model is studied in a two dimensional plane, produced by varying Λ and $\tan\beta$, with the other parameters defined as $M_{\text{mes}} = 250\,\text{TeV}$, $N_5 = 3$, $\text{sgn}(\mu) = +$ and $C_{\text{grav}} = 1$. The selected parameter values ensure that promptly decaying NLSPs are produced. If C_{grav} is greater than 1 the lifetime of the NLSP is extended, and the $\tilde{\tau}_1$ can decay outside of the detector. For $N_5 \geq 2$ the NLSP is a slepton in a wide range of the parameter space, as indicated in figure 2.5, for the example of $N_5 = 3$. The NLSP is the $\widetilde{\tau}_1$ ($\widetilde{\ell}_R$) for large (small) values of $\tan\beta$ while for medium $\tan\beta$ values the $\widetilde{\tau}_1$ and the right-handed sleptons ($\widetilde{\text{e}}_R, \widetilde{\mu}_R$) are co-NLSPs. The region of small Λ and large $\tan\beta$ is theoretically excluded.

Figure 2.5 shows the overall NLO GMSB production cross-section in the Λ–$\tan\beta$ plane, where the other parameters are defined above.

2.5.1 Searching for GMSB at the LHC

Figure 2.6 shows the cross-section for various SUSY processes, as a function of the average SUSY particle mass, for a pp centre-of-mass energy of $\sqrt{s} = 7$ TeV and 8 TeV. The processes with the highest cross-section are due to strong production: $\tilde{q}\tilde{g}$, $\tilde{q}\tilde{q}$, $\tilde{q}\tilde{q}^*$ and $\tilde{g}\tilde{g}$. This is because the colliding particles are protons, and their constituent particles are coloured quarks and gluons. Feynman diagrams for some of the contributing processes can be found in figure 2.7. The next highest cross-section is for $\tilde{t}_1\tilde{t}_1^*$ production, followed

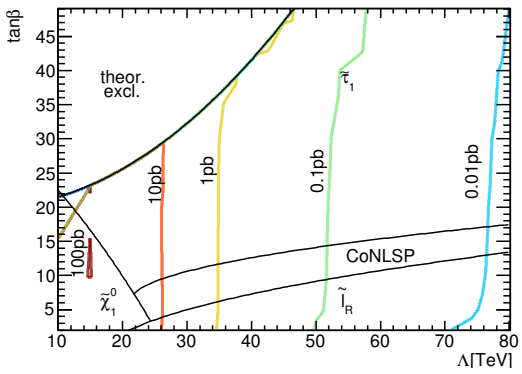

Figure 2.5: The GMSB NLO cross-section in the Λ–tan β plane for $M_{\text{mes}} = 250$ TeV, $N_5 = 3, C_{\text{grav}} = 1$. The black lines indicate the different NLSP regions. Some of the low Λ, high tan β region predicts the production of tachyons, and this region is therefore considered to be theoretically excluded.

by the weak-production of SUSY particles. The searches presented in this work are both optimised for strongly produced squarks and gluinos, in the context of GMSB. Figure 2.8 shows an example Feynman diagram for a GMSB final state to which these analyses are sensitive due to the large τ-lepton multiplicity, hadronic jets and missing transverse energy.

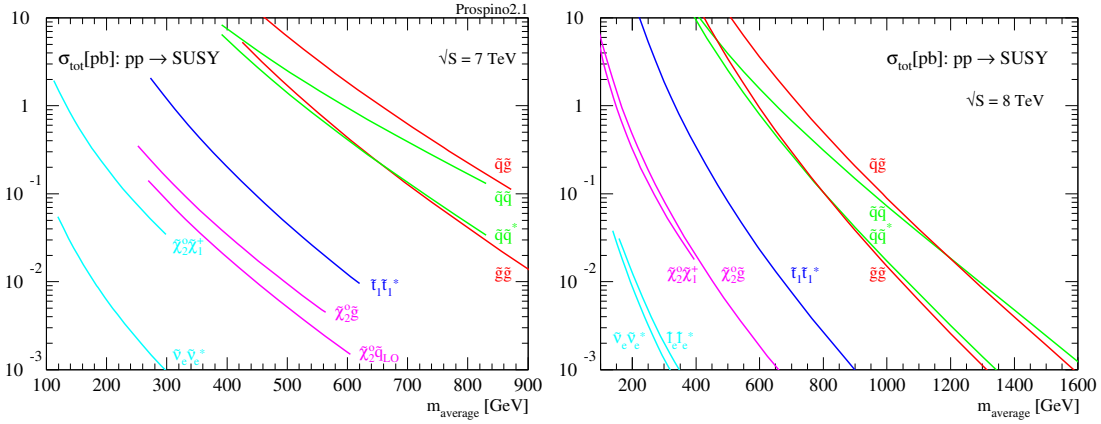

(a) (b)

Figure 2.6: Next-to-leading order cross-sections for SUSY production at the LHC, for 2.6(a) $\sqrt{s} = 7$ TeV or 2.6(b) $\sqrt{s} = 8$ TeV. These were calculated with `PROSPINO` (section 4.1.5) [74].

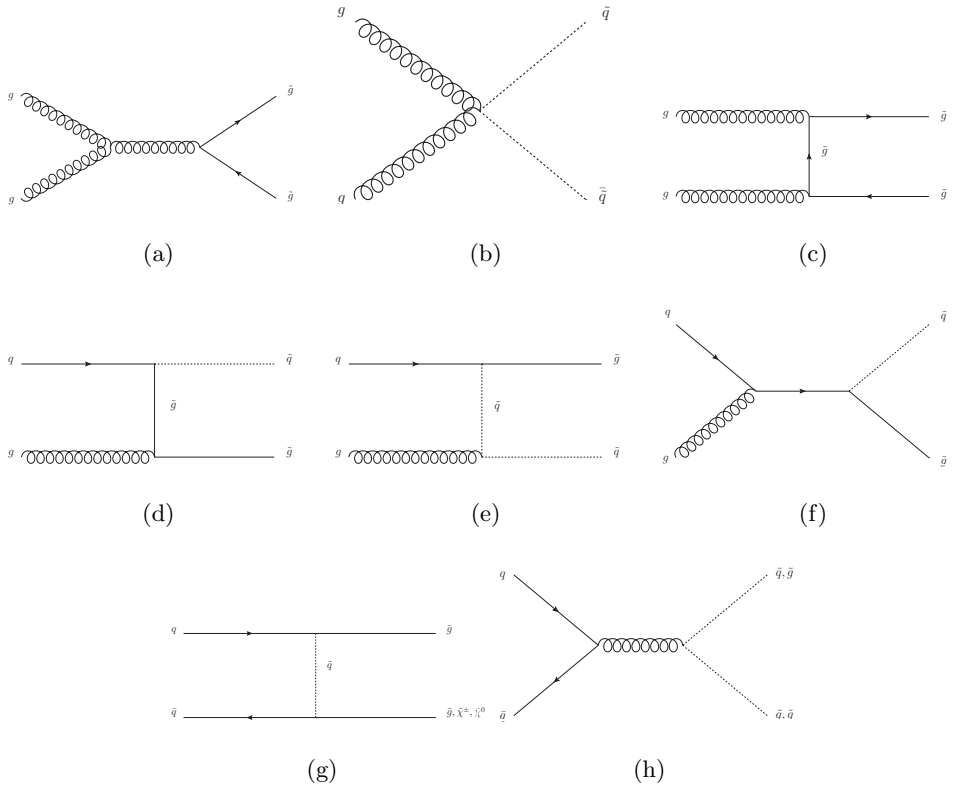

Figure 2.7: Feynman diagrams for gluino and squark production at hadron colliders from gluon-gluon and gluon-quark fusion [36].

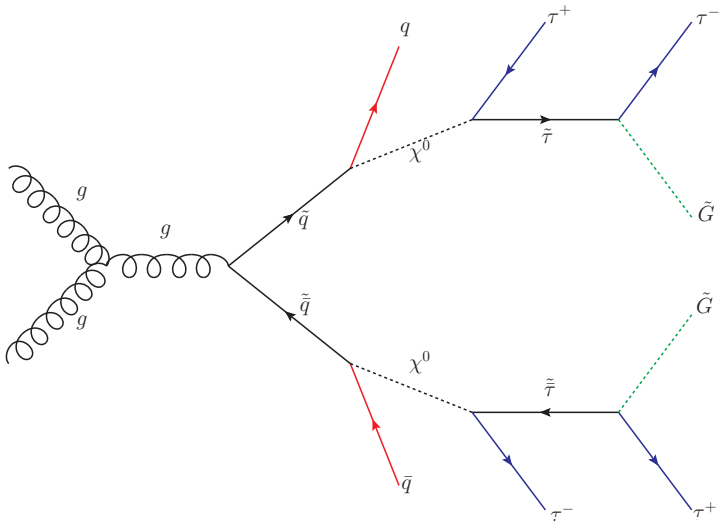

Figure 2.8: Feynman diagram for a typical event from the GMSB grid used in this work. In this example the $\tilde{\tau}_1$ is the NLSP.

3

The Large Hadron Collider and the ATLAS Detector

3.1 The Large Hadron Collider

The Large Hadron Collider (LHC) [75, 76] is a proton–proton (p–p) collider located at CERN (European Organisation for Nuclear Research). The protons collide inside a 27 km circular ring, approximately 100 m underground, and several experiments are positioned around this ring to analyse the result of these collisions.

The LHC is designed to collide protons at a centre-of-mass energy of $\sqrt{s} = 14$ TeV, with an instantaneous luminosity[1] of $\mathcal{L} = 10^{34}\,\mathrm{cm}^{-2}\,\mathrm{s}^{-1}$. It is also designed to collide lead ions at a centre-of-mass energy of $\sqrt{s}_{\mathrm{NN}} = 5.5$ TeV, and instantaneous luminosity of $\mathcal{L} = 10^{31}\,\mathrm{cm}^{-2}\,\mathrm{s}^{-1}$ [75].

A schematic representation of the full LHC complex can be found in figure 3.1. The protons are obtained by removing electrons from hydrogen atoms. These are then injected

[1] The instantaneous luminosity at the LHC is determined by $\mathcal{L} = f_{\mathrm{rev}} \frac{N_P^2 N_B}{A_{\mathrm{eff}}}$, where N_P represents the number of particles per bunch, N_B represents the number of circulating bunches, f_{rev} is the beam revolution frequency and the effective collision area is $A_{\mathrm{eff}} = 4\pi\sigma_x\sigma_y$.

into a linear accelerator (LINAC2), where they are accelerated to an energy of 150 MeV. They then enter the PS Booster, which is the first of a series of successive circular accelerators and accelerates the protons to 1.4 GeV. Following the PS Booster they are injected into the Proton Sychrotron (PS), which accelerates the protons to an energy of 26 GeV. Following the PS, the protons are injected into the Super Proton Synchrotron (SPS), where they are accelerated to 450 GeV, and are then finally injected into the ring of the LHC, where they are then accelerated to an energy of 7 TeV in 2011, and 8 TeV in 2012.

For the heavy ion runs, the lead ions begin as a source of vapourised lead and are accelerated through a linear accelerator (LINAC3), They then enter the Low Energy Ion Ring (LEIR), before entering the PS and following the same route to the LHC as the protons.

Inside the LHC ring, the two counter-rotating beams are contained inside an ultra-high vacuum of $\sim 10^{-10}$ mbar [76]. Radio Frequency cavities are used to accelerate the protons (or ions), and 1232 superconducting dipole magnets, operating at currents of 11850 A, provide a magnetic field of up to 8.3 T to achieve adequate beam bending power. An additional 392 quadrupole magnets are used to focus the beam and increase the probability of a collision at the interaction point. Liquid helium is used to cool the magnet system to the operating temperature of 1.9 K. For the p–p collisions, the beams contain "bunches" of protons, with a design value of 2808 bunches per beam, separated by intervals of 25 ns and each containing 10^{11} protons. This corresponds to a bunch crossing frequency of 40 MHz.

There are four beam collision points around the LHC ring, and each collision point corresponds to the location of a primary LHC experiment. Two of these experiments, ATLAS [78] (**A** **T**oroidal **L**HC **A**pparatu**S**) and CMS [79] (**C**ompact **M**uon **S**olenoid) are large general purpose detectors, designed to search for evidence of new physics in a wide range of final states. LHCb [80] (**L**arge **H**adron **C**ollider **b**eauty) is dedicated to b-physics, focused primarily on CP-violation and rare B meson decays. ALICE [81] (**A** **L**arge **I**on **C**ollider **E**xperiment) is primarily focused on the study of heavy ion collisions, with the aim of exploring the physics of strongly interacting matter at extreme energy densities. There are also two smaller experiments, LHCf [82] (**L**arge **H**adron **C**ollider **f**orward), which focuses on hadron interactions at high energies in the very forward region, and TOTEM [83] (**TOT**al cross-section and **E**lastic scattering **M**easurement), which will measure the total p–p cross-section and monitor the LHC's luminosity.

The LHC started single-beam operations in 2008 and first collisions were achieved in

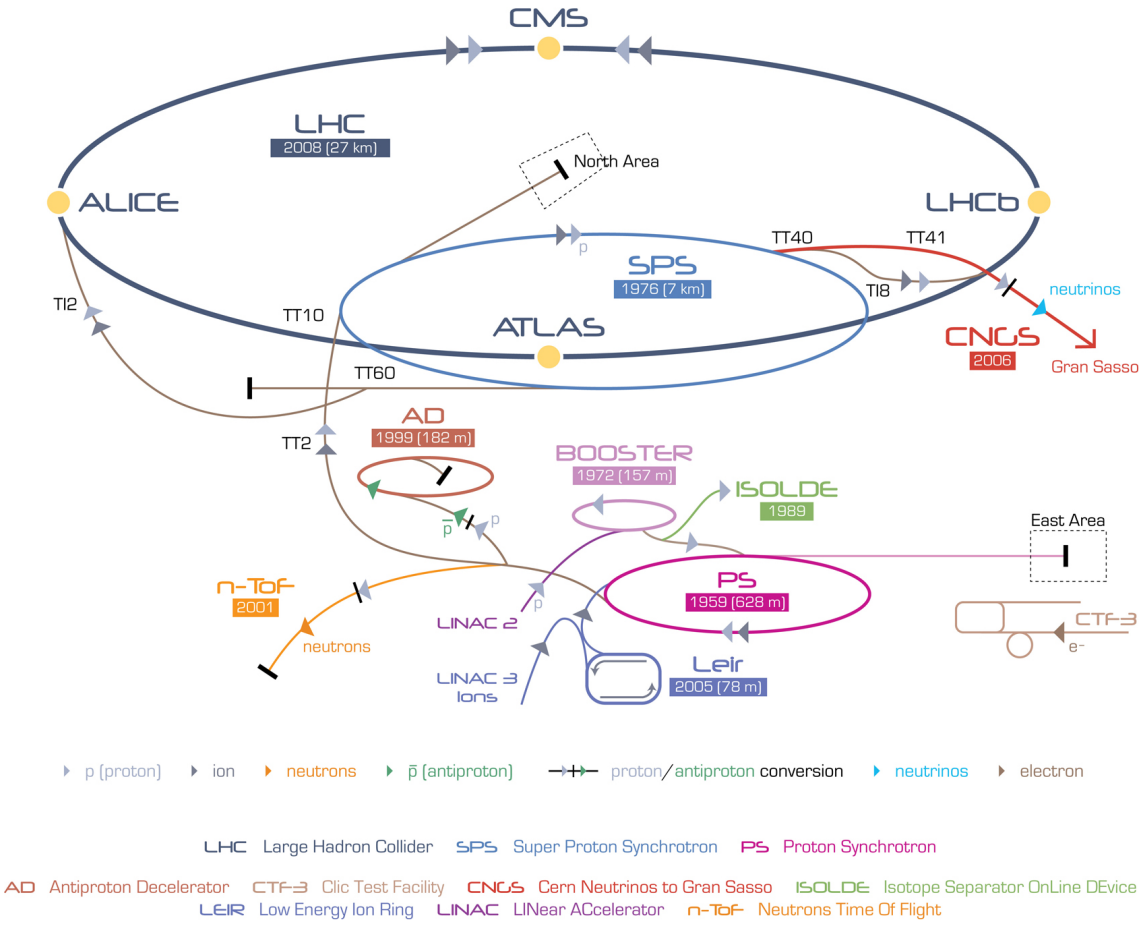

Figure 3.1: The CERN accelerator complex [77].

	2010	2011	2012	Design
Centre-of-mass energy, $\sqrt{s}$	7 TeV	7 TeV	8 TeV	14 TeV
Max. instantaneous luminosity ($\mathrm{cm}^{-2}\,\mathrm{s}^{-1}$)	2×10^{32}	3.6×10^{33}	7.7×10^{33}	10^{34}
Max. protons per bunch (10^{11})	1.2	1.3	1.5	1.15
Number of colliding bunches	$1 - 348$	$194 - 1332$	$194 - 1380$	2808
Collisions per bunch crossing	≤ 3	≤ 15	≤ 35	22

Table 3.1: Running conditions of the LHC from 2010 to 2012. More information can be found in the text.

2009. During the first run in 2010, the LHC reached a centre-of-mass energy of $\sqrt{s} = 7$ TeV and an instantaneous luminosity of between $9 \times 10^{26}\,\mathrm{cm}^{-2}\,\mathrm{s}^{-1}$ and $2 \times 10^{32}\,\mathrm{cm}^{-2}\,\mathrm{s}^{-1}$. The total integrated luminosity collected by ATLAS during this p–p run was $45\mathrm{pb}^{-1}$. The 2010 p–p run was followed by a short period of heavy ion collisions at $\sqrt{s}_{\mathrm{NN}} = 2.76$ TeV, during which ATLAS recorded $9.2\,\mu\mathrm{b}^{-1}$ of Pb–Pb collision data [84]. The p–p centre-of-mass energy of $\sqrt{s} = 7$ TeV continued through 2011, and was increased to $\sqrt{s} = 8$ TeV for the 2012 proton run. A summary of the LHC conditions from 2010 to 2012 can be found in table 3.1, and a summary of the integrated luminosity can be found in figure 3.2(a).

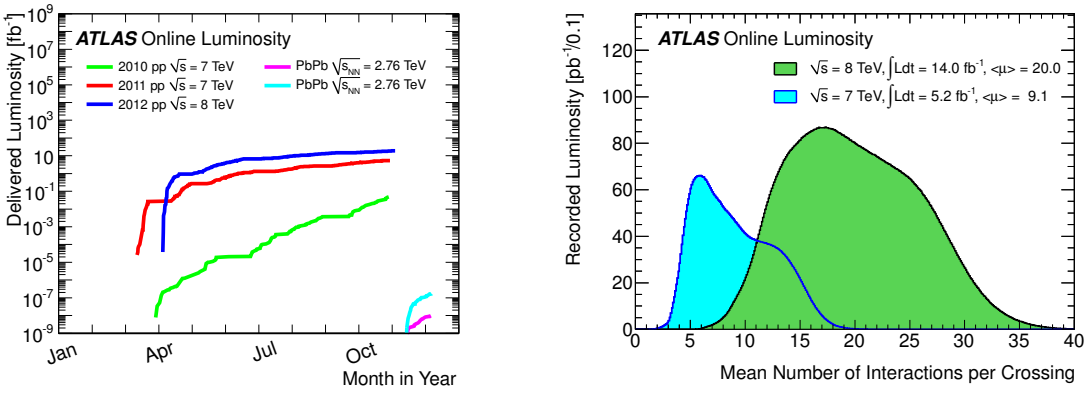

(a) (b)

Figure 3.2: (a) LHC delivered luminosity for p–p and Pb–Pb collisions, during the 2010 run (green for p–p, magenta for Pb–Pb), 2011 run (red for p–p, turquoise for Pb–Pb) and 2012 run (blue) [85]. (b) Luminosity-weighted distribution of the mean number of interactions per crossing, for the 2011 and 2012 data-taking [85–87].

Due to the high instantaneous luminosity of the LHC it is possible for multiple p–p interactions to occur in a single bunch crossing. This effect is known as *pile-up*. Figure 3.2(b)

shows the luminosity-weighted distribution of the mean number of interactions per bunch crossing for the 2011 and 2012 data. The mean number of interactions per bunch crossing (μ) is calculated from the instantaneous luminosity as $\mu = \mathcal{L}_{\text{bunch}} \times \sigma_{\text{inel}}/f_r$, where $\mathcal{L}_{\text{bunch}}$ is the instantaneous luminosity, σ_{inel} is the inelastic p–p cross-section (which is taken to be 71.5 mb for 7 TeV collisions and 73.0 mb for 8 TeV collisions), and f_r is the LHC revolution frequency [86, 87].

3.2 The ATLAS detector

The ATLAS experiment [78, 88, 89] is one of two general purpose detectors at the LHC (the other being CMS), and is the largest of the LHC experiments. The design of ATLAS was motivated by the desire for a wide physics program: from searches for the Higgs boson to new physics beyond the Standard Model.

ATLAS has a forward-backward symmetric cylindrical geometry and nearly 4π solid angle coverage. The inner tracking detector consists of a silicon pixel detector, a silicon microstrip detector and a transition radiation tracker. The inner detector is surrounded by a thin superconducting solenoid and by fine-granularity lead/liquid-argon (LAr) electromagnetic calorimeters. An iron/scintillator-tile calorimeter provides hadronic coverage in the central pseudorapidity[2] range. The end-cap and forward regions are instrumented with liquid-argon calorimeters for both electromagnetic and hadronic measurements. An extensive muon spectrometer system that incorporates large superconducting toroidal magnets surrounds the calorimeters. Each of these components will be discussed in the following sections.

3.2.1 The magnet system

The ATLAS superconducting magnet system [88] is a hybrid system consisting of three sub-systems: one barrel toroid, two end-cap toroids and a solenoid. The system is designed to provide a stable, precise magnetic field. The air-core barrel toroid covers the central region, and provides a magnetic field of 3–8 Tm for the muon spectrometer (described in section 3.2.4). The forward regions are covered by the end-cap toroids, which also provide

[2] ATLAS uses a right-handed coordinate system with its origin at the nominal interaction point (IP) in the centre of the detector and the z-axis along the beam pipe. The x-axis points from the IP to the centre of the LHC ring and the y-axis points upward. Cylindrical coordinates (r, ϕ) are used in the transverse plane, ϕ being the azimuthal angle around the beam pipe. The pseudorapidity is defined in terms of the polar angle θ as $\eta = -\ln\tan(\theta/2)$.

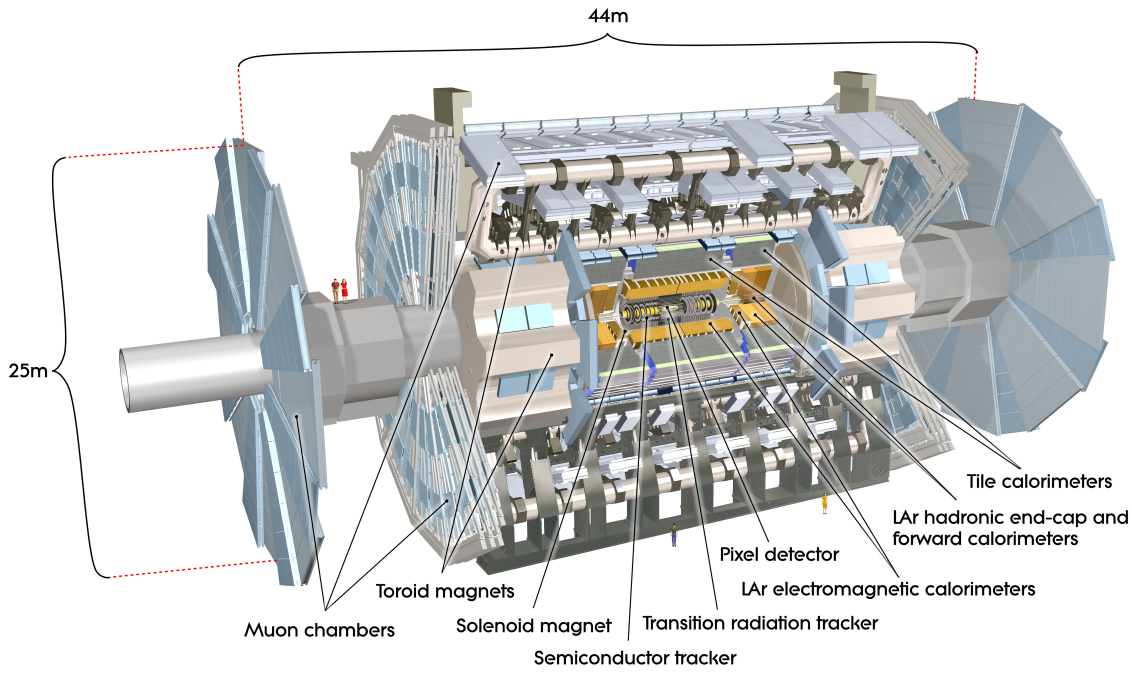

Figure 3.3: The ATLAS detector. [84]

3–8 Tm for the muon spectrometer. The solenoid, which is aligned along the beam pipe and placed between the inner detector and the barrel electromagnetic calorimeter, is designed to provide a 2 T axial magnetic field for the inner detector. The air-cooled end-cap and barrel toroids provide the muon spectrometers with an average of 1.0 and 0.5 T fields, respectively. All of these magnet systems are superconducting and cooled to 4.5 K by liquid helium, provided by a dedicated cryostat system.

3.2.2 The inner detector

The ATLAS inner detector (shown schematically in figure 3.5) is designed to perform precise charged particle momentum and vertex measurements close to the interaction point [90, 91]. At the LHC design luminosity of $10^{34}\,\mathrm{cm}^{-2}\,\mathrm{s}^{-1}$ a large number of particles will be produced at the interaction point every 25 ns, resulting in a challenging environment in which to make precision measurements. In order to meet this challenge, the inner detector comprises several different elements: pixel and silicon microstrip trackers are used along with the straw tubes of the transition radiation tracker in order to make high-granularity measurements. The inner detector surrounds the LHC beam pipe, and is positioned inside the solenoidal magnet, which provides a magnetic field strength of 2 T in the region $|\eta| < 2.5$. This allows for a measurement of the momenta of charged particles

Detector component	Required resolution	η coverage	
		Measurement	Trigger
Tracking	$\sigma_{p_T}/p_T = 0.05\% \, p_T \otimes 1\%$	± 2.5	
EM calorimeter	$\sigma_E/E = 10\%/\sqrt{E} \otimes 0.7\%$	± 3.2	± 2.5
Hadronic calorimeter			
Barrel and end-cap	$\sigma_E/E = 50\%/\sqrt{E} \otimes 3\%$	± 3.2	± 3.2
Forward	$\sigma_E/E = 100\%/\sqrt{E} \otimes 10\%$	$3.1 < \lvert\eta\rvert < 4.9$	$3.1 < \lvert\eta\rvert < 4.9$
Muon spectrometer	$\sigma_{p_T}/p_T = 10\%$ at $p_T = 1$ TeV	± 2.7	± 2.4

Table 3.2: General performance goals of the ATLAS detector. The "measurement" column corresponds to the regions of the detector in which particle properties can be recorded, and the "trigger" columns corresponds to the regions in which the triggers can be used to record the event. Note that, for high p_T muons, the muon spectrometer performance is independent of the inner detector system. The units for E and p_T are in GeV [78].

that traverse the inner detector. Each of the three sub-sections of the inner detector will be discussed separately in the following sections, and more details can be found in [88, 91]. A summary of the required resolution and η coverage for the inner detector, along with the other ATLAS detector components, can be found in table 3.2.

The Pixel Detector

The pixel detector [90] is a high precision tracking detector and covers the region $|\eta| < 2.5$. This is the highest granularity region of the ATLAS detector, and comprises three concentric cylinders of silicon pixels in the barrel region and two end-cap discs (perpendicular to the beam axis), each containing three layers of silicon pixels.

Ionising particles traversing the semiconductor material produce electron-hole pairs, which are subsequently channeled by an electric field and the resulting current is detected. The pixel layers are segmented in R–ϕ and z, with the innermost layer, known as the b-layer, located at $R = 50.5\,\text{mm}$. This is important when trying to identify jets that have originated from a b-quark (as will be explained in section 4.3.4), as it provides information about secondary vertices and impact parameter measurements. On average each track will cross three pixel layers. The minimum pixel size in (R–ϕ) is $50 \times 400\,\mu\text{m}^2$, and the pixels

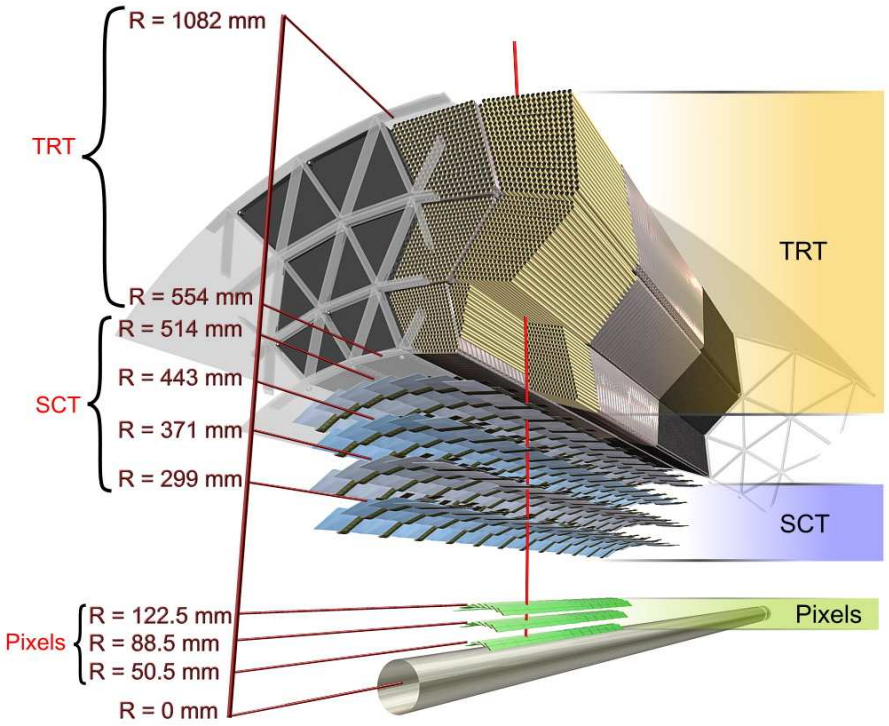

Figure 3.4: The ATLAS inner detector [92].

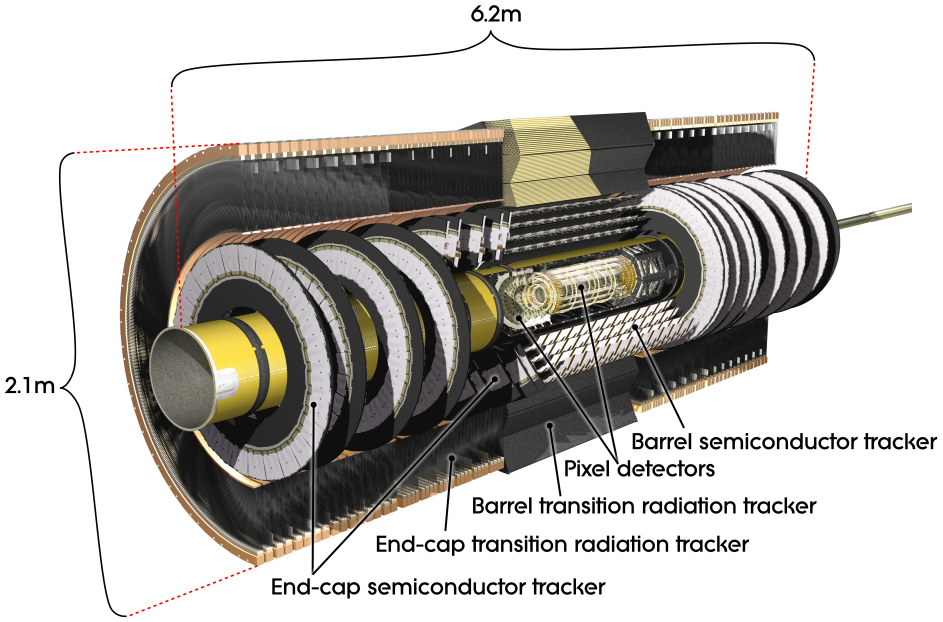

Figure 3.5: The three main components of the ATLAS inner detector: the semiconductor tracker, pixel detectors and transition radiation tracker [92].

have intrinsic measurement accuracies of 10 μm (R–ϕ) in the barrel and 115 μm (z) in the discs. The pixel detector contains approximately 80.4 million readout channels [90]. The position of the pixel layers with respect to the beam pipe and the rest of the inner detector can be seen in figure 3.4. A detailed description of the pixel detector can be found in [93].

The Semiconductor Tracker

The semiconductor tracker (SCT) [90] is another high precision tracking detector, also covering the region $|\eta| < 2.5$. It consists of two planes of silicon strip detectors, arranged in cylinders in the barrel region and discs in the end-cap region, similar to the design of the pixel detector.

The silicon is arranged into strips, which allows for the measurement of the track momenta, vertex position and the impact parameter. In the barrel region, the SCT uses stereo strips at a small angle (40 mrad) to provide a more accurate measurment of a particle's position in ϕ. In the end-cap region there is a set of strips positioned radially and another set of stereo strips, again at an angle of 40 mrad. The mean pitch of the SCT strips is $\sim$80 μm, and the spatial resolution of the silicon detectors is 17 μm (R–ϕ) and 580 μm (R). This resolution is not required to be as high that of the pixel detector, as there is a significantly lower particle density in the SCT. The total number of readout channels in the SCT is around 6.3 million [90].

The Transition Radiation Tracker

The transition radiation tracker (TRT) [90] is made of over 370,000 straw-like drift tubes. In the barrel region these are positioned parallel to the beam direction, and have a diameter of 4 mm and a length of 144 cm, with their wires divided into two halves, approximately at $\eta = 0$. In the end-cap region the straws are positioned radially, and are 37 cm long. The TRT only provides $R-\phi$ information, with an intrinsic accuracy of 130 μm per straw, significantly lower than that of the pixel detector and the SCT. The coverage is $|\eta| < 2.0$, lower than the $|\eta| < 2.5$ coverage of the pixel detector and SCT, but many more hits are recorded by the TRT. There are typically around 30 hits per track in the TRT, whereas this is around 3 for the pixel detector and 4 for the SCT in the barrel region [90]. The particle multiplicity decreases as the distance from the interaction point is increased, and the resolution provided by the TRT does not need to be as high.

Each TRT straw is coated on the inside with aluminium (a high voltage cathode), threaded with a gold-plated tungsten wire (the anode wire) and filled with a mixture of

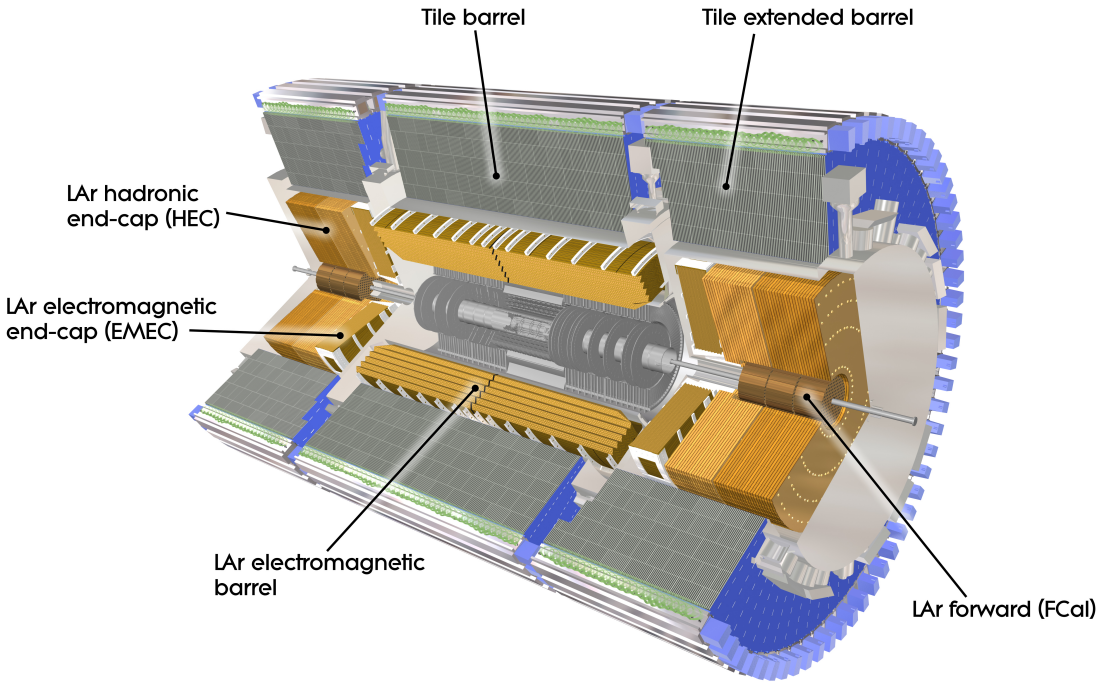

Figure 3.6: The ATLAS calorimeter system [92].

70% Xe, 27% CO_2 and 3% O_2. A more thorough description of the inner detector is given in the ATLAS Inner Detector Technical Design Report [91].

3.2.3 The ATLAS calorimeter system

The ATLAS calorimeter, shown in figure 3.6, is comprised of an electromagnetic calorimeter (ECAL), a hadronic calorimeter (HCAL) and a forward calorimeter (FCAL), and covers the range $|\eta| < 4.9$. These sub-detectors are located outside of the 2 T solenoid magnet. A comprehensive description of the ATLAS Calorimetery system can be found in the ATLAS Calorimeter Performance Technical Design Report [94], and the Liquid-Argon Calorimeter Technical Design Report [95]. A summary of the required resolution and η coverage for the calorimeters can be found in table 3.2.

The Electromagnetic Calorimeter

The ATLAS ECAL [88, 90] is required to efficiently identify electrons and photons over a wide range of energies (∼5–5000 GeV), and to measure their energies with a non-linearity of less than 0.5%. The ECAL, a schematic of which can be seen in figure 3.6, is a liquid-argon sampling detector with lead absorber plates, and comprises a barrel calorimeter ($|\eta| < 1.475$), and two end-cap calorimeters ($1.375 < |\eta| < 3.2$). An accordion-shaped

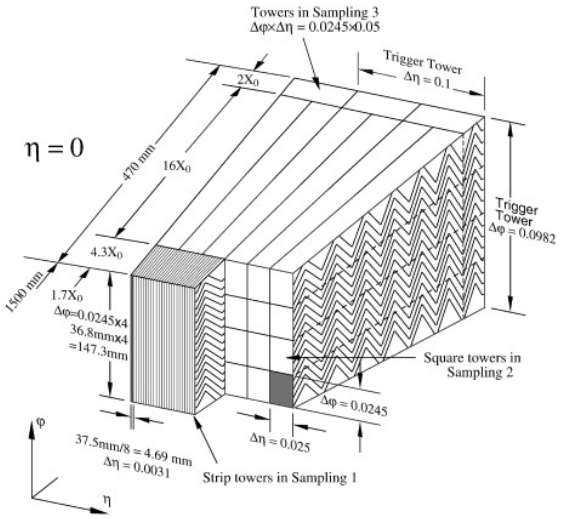

Figure 3.7: Schematic of the accordion structure of the ATLAS ECAL [95].

structure (shown schematically in figure 3.7), allows for a full coverage in ϕ without azimuthal cracks. The calorimeter is installed inside three cryostats, one for the barrel part ($|\eta| < 1.475$), and two for the two components of the end-cap ($1.375 < |\eta| < 3.2$).

Particles that interact electromagnetically will shower in the ECAL due to interactions with the absorber material. These interactions induce Bremsstrahlung, Compton scattering and conversion of photons to e^+e^- pairs. The resulting shower particles will ionise the LAr contained in the active regions, and the ionisation charges will be detected. Liquid argon was selected as the active material because it is radiation hard and it demonstrates both linear behaviour and a stable response over time.

In the pseudorapidity region $|\eta| < 2.5$, the ECAL is segmented into three layers, while in the regions of higher $|\eta|$, there are only two layers required. The layer of the precision region closest to the interaction point offers the highest granularity in $|\eta|$, making it possible to distinguish between π^0 and photons. The second layer collects the largest energy fraction, while the third collects only the tail of the electromagnetic shower. The total thickness of the ECAL is over 22 radiation lengths (X_0) in the barrel region and over 24 X_0 in the end-caps. In the region $|\eta| < 1.8$ there is a presampler, which is a thin layer of active liquid argon calorimeter inside the barrel cryostat. This is able to provide a measurement of the energy lost in the dead material of the support structure, such as the walls of the cryostat, upstream of the ECAL. The thickness of this layer is 1.1 cm in the barrel and 0.5 cm in the end-cap region [88].

The Hadronic Calorimeter

The hadronic calorimeters [88, 90] cover the range $|\eta| < 4.9$, and comprise several components depending on the specific requirements of the relevant region in η. The position of the various calorimeter components can be seen in figure 3.6. In the range $|\eta| < 1.7$, the hadronic calorimeter is made of iron, with a scintillating tile readout for the barrel ($|\eta| < 1.0$) and extended barrel ($0.8 < |\eta| < 1.7$). The tiles are 3 mm thick, positioned perpendicular to the beam axis, and are staggered in depth.

Liquid-argon calorimeters are used to cover the range $1.5 < |\eta| < 4.9$. The hadronic end-cap calorimeter extends to $|\eta| < 3.2$, and uses thick copper absorber plates which are separated by gaps filled with LAr. The range $3.1 < |\eta| < 4.9$ is covered by the high-density forward calorimeter (FCAL), which is made up of three sections: the first made of copper, and the other two made of tungsten. Each of these sections contains a matrix of regularly spaced longitudinal channels filled with concentric rods and tubes. These rods are at high, positive voltage, whilst both the tubes and matrix are grounded. Liquid argon fills the gaps between them.

The hadronic calorimeter has been designed to ensure that the thickness is sufficient to contain hadronic showers and minimise the punch-through of jets into the muon spectrometer. The thickness at $\eta = 0$ is 11 interaction lengths (Λ), which has been shown to adequately reduce the punch-through effect [88]. Around $10\,\Lambda$ of active calorimeter material is sufficient to provide good resolution for energetic jets, and together with the good η-coverage this allows for precise measurements of the missing transverse energy. A full description can be found in [88] and [90].

3.2.4 The muon spectrometer

The ATLAS muon spectrometer (MS) [88, 90, 96] is based on the magnetic deflection of muon tracks in large superconducting air-core toroid magnets, and a schematic can be seen in figure 3.8. The MS surrounds the calorimeters, and is designed to measure the momentum, direction and electric charge of charged particles that pass through the calorimeter system, as well as act as a stand-alone trigger for muons with p_{T} of the order of several GeV. The magnetic field is created by the barrel toroid for $|\eta| < 1.0$, and by the end-cap toroids for $1.4 < |\eta| < 2.7$. In the so-called "transition region" ($1.0 \leq |\eta| \leq 1.4$), the barrel and end-cap fields combine to deflect the trajectory of muons [88].

In the barrel region, the muon spectrometer consists of three cylindrical layers, arranged around the beam axis, whilst in the transition and end-cap regions the chambers

Characteristic	MDT	RPC	CSC	TGC
Coverage	$\|\eta\| < 2.7$	$\|\eta\| < 1.05$	$2.0 < \|\eta\| < 2.7$	$1.05 < \|\eta\| < 2.7$
# of chambers	1150	606	32	3588
# of channels	354000	373000	31000	318000
Function	Precision tracking	Triggering	Precision tracking	Triggering

Table 3.3: Main characteristics of the muon spectrometer sensors and their coverage region [96].

are installed vertically, also in three layers. The MS contains two precision measurement chamber designs: Monitored Drift Tubes (MDTs) are used for the majority of the η-range, and Cathode Strip Chambers (CSC), which have a higher granularity, are used for the innermost plane over $2 < |\eta| < 2.7$. The MDTs are aluminium tubes filled with gas, and provide momentum measurements in $|\eta| < 2.7$, with an average precision of $80\,\mu$m per tube and $35\,\mu$m per chamber. When a muon transverses these tubes it will result in the production of a trail of electrically charged ions and electrons, which can then drift to the sides and the centre of the tube. It is possible to determine the position of a muon in this region by measuring the drift time, which is the time it takes for these charges to drift from their initial point.

The precision chambers have a long charge collection time, which means that they cannot be relied upon for triggering purposes. After a muon has been detected with the precision chambers the other detector sub-components would no longer be storing the data from the corresponding bunch crossing due to the amount of time the precision chambers require to record data. For this reason, Resistive Plate Chambers (RPCs) and Thin Gap Chambers (TGCs), which are part of the stand-alone muon trigger system, are used to complement the precision chambers and to attach measured signals to certain bunch crossings. They provide a more coarse measurement of η and ϕ, but have a response time of less than 25 ns, making them appropriate for use in hardware trigger decisions. The RPCs provide the trigger for muons in the barrel region, whereas TGCs perform this role in the higher background region of the end-cap. Their location can be seen in figure 3.8.

A full description of the muon spectrometer system can be found in [96], and a summary of the main characteristics can be found in table 3.3.

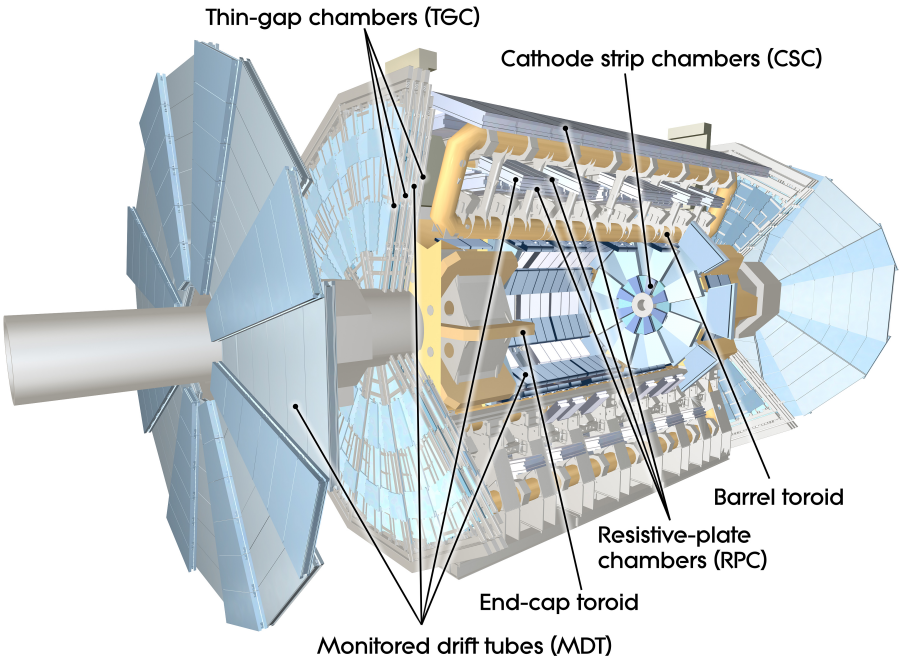

Figure 3.8: The ATLAS muon spectrometer [92].

3.3 The ATLAS trigger and data acquisition system

The ATLAS trigger and data acquisition (TDAQ) system [97, 98], shown schematically in figure 3.9, consists of three levels of online event selection: level-1 (L1), level-2 (L2) and the event filter (EF). The L2 and EF are known collectively as the "High Level Trigger" (HLT). The system is designed to select events of interest at around 200 Hz (determined by the computing requirements for the recording and offline processing of the data) from the 40 MHz bunch crossing rate at the interaction point. Each level of the system refines the decision from the previous level, and reduces the rate at which data is recorded for offline analysis by placing increasingly stringent requirements on the events.

The L1 trigger is a hardware-based system that uses information from the calorimeters and the muon spectrometer, and the L2 trigger and the EF are both software-based systems, and use information from all sub-detectors. The TDAQ system selects events by placing specific requirements on the physics objects that are reconstructed in each event, and combinations of different objects (e, μ, τ, jets, b-jets, γ or specific B-physics decay modes) correspond to different triggers. Triggers also exist to identify inelastic p–p collisions, known as minimum bias events, or events in which there is large missing transverse energy[3] ($E_{\mathrm{T}}^{\mathrm{miss}}$) or large total transverse energy ($\sum E_T$) [84]. The list of available triggers

[3]The missing transverse energy is defined as the momentum imbalance in the plane transverse to the beam axis. A detailed description can be found in section 4.4.

is known as the "trigger menu".

3.3.1 Level 1 Trigger

The L1 trigger, built from fast electronics, is responsible for quickly deciding if the event is potentially interesting enough for further analysis. It does this by considering reduced-granularity information from a subset of detectors. High p_{T} muons are identified using the trigger chambers (RPCs in the barrel region and TGCs in the end-caps). The calorimeter selections are based on reduced-granularity information from all of the ATLAS calorimeters. The L1 trigger considers the multiplicity of physics objects in the calorimeters (e, γ, jets, hadronically decaying τ-leptons) or the trigger chambers of the muon system (for high p_{T} muons). The total transverse energy and missing transverse energy are also considered. There are kinematic threshold requirements in place for each of these objects, with strengths that vary depending on the specific trigger requirements. At this stage of the TDAQ system there is is no information from the inner detector.

The signals recorded by the detector are stored in the memory of the "Front End Pipelines", which are contained in custom integrated circuits on or near the detector, until there is a decision from the L1 trigger. The L1 latency, which is measured from the time of the p–p collision until the L1 trigger decision is available to the front-end electronics, is required to be less than $2.5\,\mu$s.

The events that are selected by the L1 trigger are read out from the detector's front-end electronics systems into the so-called "Readout Buffers" (ROBs), pending the L2 decision. Following the application of the L1 trigger, the data rate is reduced to less than 75 kHz. The L1 triggers also identify $\Delta\eta \times \Delta\phi$ "Regions of Interest" (RoIs) within the detector to be investigated by the HLT.

3.3.2 High Level Trigger

The HLT exists in two stages: the L2 trigger involves high rejection power with fast, limited precision algorithms, and the EF involves modest rejection power with slower, high precision algorithms.

The "RoI Builder" combines the RoI information from the L1 trigger, and the resulting RoIs are analysed by the L2 algorithms. The L2 trigger has access to all of the event data if required, but typically only data from a small fraction of the detector, corresponding to the RoIs indicated by the L1 trigger, are required for the L2 decision to be made. This ensures that the algorithms select the region of the detector in which the interesting

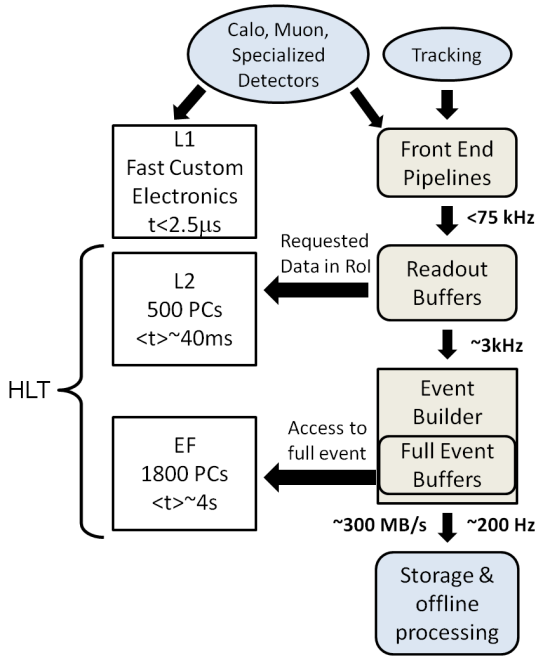

Figure 3.9: Schematic representation of the ATLAS trigger system [84]. More detail can be found in the text.

features reside, without having to readout the entire detector for every event. The latency for the L2 trigger is around 40 ms, which reduces the event rate to around 3 kHz.

The ROBs contain all of the data for the selected bunch crossing either until the event is rejected by the L2 trigger, resulting in the data being discarded, or, if the event passes the L2 trigger requirements, until the data have been successfully transferred to the storage associated with the EF. For an event that passes the L2 decision, all of the event fragments stored in the ROBs are assembled by the "Event Builder" into a single event, which is subsequently stored in memory accessible to the EF.

The EF runs the standard ATLAS offline reconstruction algorithms, and assigns events to one or more event streams, according to the trigger conditions satisfied by the event. The event streams separate events of interest for different analyses into different datasets. The EF reduces the rate to ∼200 Hz, with an average processing time of ∼4 s per event [84].

4

Event Simulation and Reconstruction

This chapter will discuss in detail the process of generating simulated Monte Carlo samples at ATLAS for individual physics processes, along with the detailed simulation of the detector response. Section 4.1 will discuss each of the MC generators used for the two analyses presented in chapters 5 and 6. Section 4.2 details the simulation of the ATLAS detector, and section 4.3 summarises the definition of the various physics objects that are used in the analyses.

4.1 Event generation

Monte Carlo simulations are used to evaluate the expected Standard Model backgrounds and the selection efficiencies for the GMSB models considered in this work. A range of generators is used to produce these samples, with different generators being selected for different production processes. Each of these will be discussed in detail in this section.

4.1.1 Parton distribution functions

Due to the composite nature of the proton, parton distribution functions (PDF) are required, which describe the probability density for observing a particle with a certain

longitudinal momentum fraction x, at momentum transfer Q^2. They provide a measure of the partonic structure of hadrons, which is important for any process which involves colliding hadrons. Parton distribution functions are extracted from a global analysis of hard scattering data, from a range of fixed-target and collider experiments. The HERA and CTEQ PDFs for u and d valence quarks, sea-quarks and gluons can be found in figure 4.1, for $Q^2 = 10\ \text{GeV}^2$.

When regarded as constituents of strongly interacting particles (such as a proton), the u and d quarks behave like quasi-particles with masses of ∼0.3 GeV. The corresponding "constituent-quark" masses of the s, c, and b quarks are ∼0.5, 1.5, and 4.9 GeV, respectively [29], using the $\overline{\text{MS}}$[1] renormalisation scheme [99, 100]. Various different PDFs are used by the MC generators used in this work.

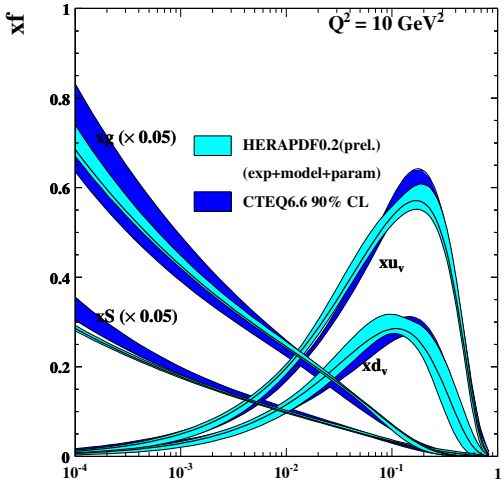

Figure 4.1: HERA and CTEQ proton parton distribution functions of valence quarks u_v, d_v , gluons g and sea-quarks S [101].

4.1.2 Multi-jet production

For the production of multi-jet events the `PYTHIA` [102] generator is used. `PYTHIA` is a general purpose event generator based on leading-order parton matrix elements, and has been used widely at ATLAS and other collider experiments. Event generation in `PYTHIA` begins with a hard scattering process, calculated to the lowest order in QCD. Additional QCD and QED radiation is subsequently added to this using a shower approximation. This shower approximation is designed to simulate higher-order corrections to the hard

[1]The modified minimal subtraction, $\overline{\text{MS}}$, scheme is a method of renormalisation to absorb the infinities that arise in pertubative calculations beyond leading order. These are absorbed into the so-called *counterterms*.

subprocess, due to partons in the event emitting radition. It is not possible to calculate these corrections directly so a method of approximation must be adopted.

PYTHIA makes use of a model for hard and soft scattering processes in order to accurately reproduce the underlying event[2]. The showering model describes this underlying event with multiple scatters, which are then augmented with the parton shower according to the hard scale of either the scatter or emission. A non-pertubative model of the hadronisation is used to combine the partons into hadrons and simulate the process of confinement. This model has been tuned using data from e^+e^-, $e-p$ and hadron colliders [102], with improvements obtained by including data from the ATLAS experiment, at $\sqrt{s} = 900$ GeV, 7 TeV and in 2012, 8 TeV [103].

For the analyses in this work, the production of simulated multi-jet events uses PYTHIA 6.4.25 [102], using either the so-called "AMBT1 tune" [104] or the "AUET2B tune" [105] for the analyses presented in chapters 5 and 6, respectively, and MST2007 LO* [106] PDFs. The AMBT1 tune [104] was the first tuning of PYTHIA to LHC data at $\sqrt{s} = 900$ GeV and $\sqrt{s} = 7$ TeV, and was tuned to the ATLAS minimum bias and underlying event data. The tune describes the majority of the minimum bias data and the high p_{T} plateau of the underlying event data to an accuracy of 10% [104]. This is approximately the accuracy of the leading order MC generators and at the time this was a significant improvement when compared with the pre-LHC data tunes. There was a remaining large deviation in the spectrum of charged particle multiplicities, with the predictions overestimating the data by up to 45% at $p_{\mathrm{T}} > 6$ GeV. To improve on this a new tune (AUET2) [103] was designed. For the ATLAS simulated samples used during the analysis of the full 2011 dataset the extension of this (AUET2B [105]) is used.

4.1.3 $W^{\pm}/Z$ boson+jets production

The $W^{\pm}$ and Z/γ^* samples (produced in association with jets) are simulated with ALPGEN [107], using CTEQ6L1 [108] PDFs. Z/γ^* events with $m_{\ell\ell} < 40$ GeV are referred to in this work as "Drell-Yan". The underlying event is simulated using JIMMY [109]. The hadronisation is performed with HERWIG [110], which includes both initial and final state QCD radiation, and events are simulated with between 0 and 5 partons.

[2]The underlying event constitutes the remainder of the parton–parton interaction that is not involved in the hard scattering process of interest.

4.1.4 Top quark and diboson production

The production of $t\bar{t}$, single top quark and diboson (WW, WZ, ZZ) samples is performed with MC@NLO [111–113]. This event generator makes use of hard scattering processes evaluated at next to leading order in QCD perturbation theory and includes corrections at the one-loop level. For the first analysis, presented in chapter 5, MC@NLO is used with the next-to-leading order (NLO) PDF set CTEQ6.6 [114], whilst for the analysis described in chapter 6 the next-to-leading-order PDF set CT10 [115] is used. As with the ALPGEN samples, the fragmentation and hadronisation is then performed with HERWIG, and the underlying event is simulated using JIMMY.

4.1.5 GMSB signal production

Simulated GMSB samples are used to optimise the signal selection, and to set exclusion limits on the GMSB parameter space. These samples represent points on the Λ–tan β plane for minimal GMSB, for which the mass spectra are calculated using ISAJET 7.80 [116]. The parameters of the generated signal grid were introduced in section 2.5. The simulated samples were produced with HERWIG++ 2.4.2 [117], with MRST2007 LO* PDFs. For the analysis presented in chapter 5, NLO cross sections are calculated using PROSPINO 2.1 [74, 118–122], using the CTEQ6.6 PDF. For the analysis presented in chapter 6, the signal cross-sections are calculated to next-to-leading order in the strong coupling constant, adding the resummation of soft gluon emission at next-to-leading-logarithmic accuracy (NLO+NLL) [118, 123–126]. The nominal SUSY production cross-sections and their uncertainties are taken from an envelope of cross-section predictions using different PDF sets and factorisation and renormalisation scales, as described in [127].

4.1.6 Simulation of τ-lepton decay

The decay of τ-leptons is simulated using TAUOLA [128, 129]. When simulating the decay, TAUOLA takes into account the τ helicities and helicity correlations, paying attention to the polarisation of the τ-lepton. In certain well-understood decays, such as $W^{\pm} \to \tau^{\pm}\nu_{\tau}$, the τ-lepton's polarisation is known. In others, such as $Z \to \tau^{+}\tau^{-}$, there is a correlation between the polarization of the two τ-leptons, which is taken into account by TAUOLA. PHOTOS [130] is used to handle the electromagnetic radiation, and is required by TAUOLA in order to improve the description of electromagnetic radiation in many decays, such as $W^{\pm} \to e^{\pm}\nu_{e}$, where the radiation results in a change to the final electron energy distribution.

4.2 Detector simulation

4.2.1 Full detector simulation

In addition to the generation of Monte Carlo samples for each of the Standard Model background processes, it is also necessary to produce a detailed simulation of the ATLAS detector to understand its response to these physics processes. This is integrated within the internal ATLAS software framework, known as ATHENA [131]. All levels of processing of ATLAS data, including the high-level trigger, event simulation, reconstruction and physics analysis, are performed within the ATHENA framework. This ensures that there is consistency between the detector geometry and conditions for all types of applications across the experiment. A schematic representation of the simulation process is presented in figure 4.2, where the algorithms and applications that must be run are represented by boxes with square corners whilst the data objects have rounded corners. The process of simulating data develops in three stages [132].

Event generation: this is the first stage, and uses the MC generators that have been detailed in section 4.1. Information about the particles that would propagate through the detector is stored. At this stage no information about detector geometry is required. A run number and individual event numbers are also generated at this stage.

Simulation: the event generation is followed by the simulation of the ATLAS detector and physics interactions, which is performed using GEANT4 [132]. The particles that traverse the detector will produce "hits", containing the total energy deposition, position, and time, and are written to a standard simulation output file known as a "hit file". Throughout this process the "truth" information is also recorded, which contains information about both the initial and final state particles from the generator. This is stored irrespective of whether or not the particle traversed the detector during the simulation.

Digitisation: this is the final step of the simulation, and involves the digitisation of the energy deposited in the detector into voltages and currents for comparison with the real output from the detector. At this stage of the process, Simulated Data Objects (SDOs) are built from the "truth" information. These contain information about the hits recorded in the detector and the corresponding MC particle that was responsible for depositing the given energy. The process takes the hit output from the MC events, including the hard

scattering signal, minimum bias[3], beam-halo[4], beam-gas[5] and cavern background[6] events. All of the different components of an event are overlaid prior to the detector signal being generated. The first level of the trigger is also simulated during digitisation, in a so-called "pass" mode that does not discard any events but does evaluate each trigger hypothesis. The digitisation constructs inputs, known as digits, to the read out drivers (RODs) in the detector electronics. The behaviour of the RODs is also simulated, and the output from this is a Raw Data Object (RDO) file.

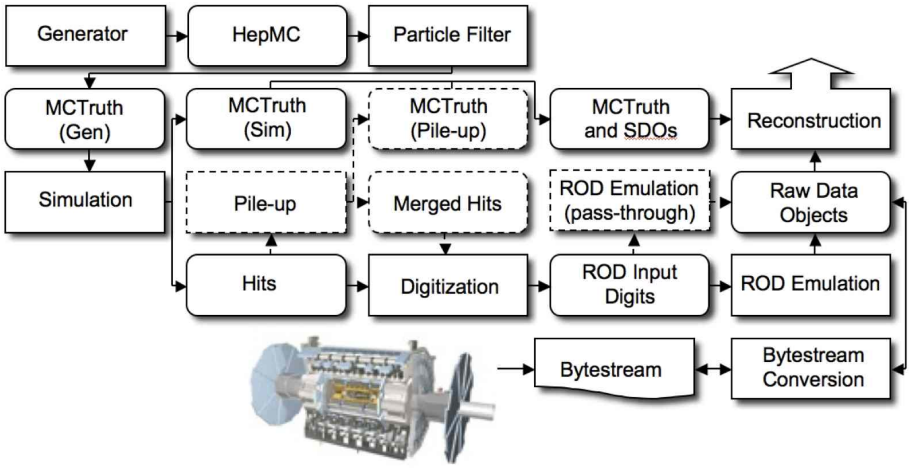

Figure 4.2: The procedure behind the ATLAS simulation software. This begins with the event generators (top left) and finishes with the object reconstruction (top right) [132]. More detail about this process is provided in the text.

4.3 Object reconstruction

The reconstruction and identification of the main physics objects used in the analyses described in this document (e, μ, τ, jets, and $E_{\mathrm{T}}^{\mathrm{miss}}$) are specified in this section. The object selection is based on an official ATLAS package, (SUSYTools [133]) that is maintained by the ATLAS Supersymmetry Working Group. This package is a collection of various tools provided by the ATLAS Collaboration for the reconstruction of physics objects and treatment of systematic uncertainties.

[3]The minimum bias interactions are inelastic, soft collisions of the two interacting protons.

[4]"beam-halo" refers to interactions in the tertiary collimators in the accelerator.

[5]"beam-gas" refers to the elastic and inelastic scattering of the beam protons on the residual gas in the detector.

[6]Cavern background events are primarily photons and neutrons generated from interactions in the cavern walls and shielding.

4.3.1 Electrons

Electrons produced in p–p collisions at ATLAS result in tracks in the inner detector before depositing energy in the electromagnetic calorimeter. Therefore, the electron reconstruction algorithm used to identify electron candidates makes use of a combination of tracking and calorimeter cluster information [134]. This is also designed to efficiently reject jets that may be incorrectly reconstructed as electrons.

The algorithm starts by selecting clusters in the electromagnetic calorimeter, with minimum transverse energy, $E_T > 2.5$ GeV. These are found using a so-called "sliding-window" algorithm [90]. This algorithm examines rectangular clusters with a fixed size, positioned to maximise the amount of energy within the cluster. The window size is 3×5 in units of 0.025×0.025 radians, in η–ϕ space, which corresponds to the granularity of the middle layer of the calorimeter. A matching track is then sought, with the distance between the track impact point and the cluster position required to satisfy $|\Delta\eta| < 0.05$, and is extrapolated to the calorimeter. In the case where there are multiple matching tracks the track that is closest in ΔR to the cluster is chosen, where $\Delta R = \sqrt{(\Delta\phi)^2 + (\Delta\eta)^2}$. Electron candidates are built with cluster sizes of $\Delta\eta \times \Delta\phi = 0.075 \times 0.175$ in the barrel calorimeter and 0.125×0.125 in the end-cap.

After reconstruction, an electron identification procedure is performed with a series of requirements on tracking and calorimeter variables, as well as a combination of such variables, in order to discriminate between isolated and non-isolated electrons, and jets faking electrons. Three levels of identification are defined, known as "loose", "medium" and "tight", which provide progressively stronger jet rejection (of the order of 500, 5000 and 50000 respectively), at the cost of lower identification efficiency [134]. A detailed breakdown of the variables used to select the different reference points can be found in table 4.1. The loose selection comprises requirements on shower shape variables in the middle layer of the EM calorimeter, along with hadronic leakage variables (defined as R_{had1} and R_{had} in table 4.1). For the medium selection, the loose selection is extended to include variables from the strip layer of the EM calorimeter, track quality requirements and track cluster matching. Finally, the tight selection includes both the loose and medium selection criteria, with additional requirements on E/p, particle identification using information from the TRT, a b-layer hit requirement and information about conversion vertices.

Type	Description	Name
Loose ID		
Acceptance	$\|\eta\| < 2.47$	
Hadronic leakage	Ratio of E_T in the first layer of the hadronic calorimeter to E_T of the EM cluster (used in range $\|\eta\| < 0.8$ and $\|\eta\| > 1.37$)	R_{had1}
	Ratio of E_T in the hadronic calorimeter to E_T of the EM cluster (used in range $\|\eta\| < 0.8$ and $\|\eta\| > 1.37$)	R_{had}
Middle layer of EM calorimeter	Ratio of the energy in 3×7 cells over the energy in 7×7 cells centred at the electron cluster position	R_η
	Lateral shower width, $\sqrt{(\sum E_i \eta_i^2)/(\sum E_i) - ((\sum E_i \eta_i)/(\sum E_i))^2}$, where E_i is the energy and η_i is the pseudorapidity of cell i and the sum is calculated within a window of 3×5 cells	$\omega_{\eta 2}$
Medium ID (includes loose)		
Strip layer of EM calorimeter	Shower width, $\sqrt{(\sum E_i (i - i_{\text{max}})^2)(\sum E_i)}$, where i runs over all strips in a window of $\Delta\eta \times \Delta\phi \approx 0.0625 \times 0.2$, corresponding typically to 20 strips in η, and i_{max} is the index of the highest energy strip	ω_{stot}
	Ratio of the energy difference between the largest and second largest energy deposits in the cluster over the sum of these energies	E_{ratio}
Track quality	Number of hits in the pixel detector (≥ 1)	n_{pixel}
	Number of total hits in the pixel and SCT detectors (≥ 7)	n_{Si}
	Transverse impact parameter ($\|d_0\| < 5$mm)	d_0
Track cluster matching	$\Delta\eta$ between the cluster position in the strip layer and the extrapolated track ($\|\Delta\eta\| < 0.01$)	$\Delta\eta$
Tight ID (includes medium)		
Track cluster matching	$\Delta\phi$ between the cluster position in the middle layer and the extrapolated track ($\|\Delta\phi\| < 0.02$)	$\Delta\phi$
	Ratio of the cluster energy to the track momentum	E/p
	Tighter $\Delta\eta$ requirement ($\|\Delta\eta\| < 0.005$)	$\Delta\eta$
Track quality	Tighter transverse impact parameter requirement ($\|d_0\| < 1$mm)	d_0
TRT	Total number of hits in the TRT	n_{TRT}
	Ratio of the number of high-threshold hits to the total number of hits in the TRT	f_{HT}
Conversions	Number of hits in the b-layer (≥ 1)	n_{BL}
	Veto electron candidates matched to reconstructed photon conversions	

Table 4.1: List of criteria for each of the three working points for the electron identification algorithm [134].

4.3.2 Muons

The process of identifying and reconstructing muons with the ATLAS detector involves the use of multiple sub-detectors, which provide complementary approaches and cover pseudorapidities up to $|\eta| = 2.7$ [135, 136]. There are several algorithms available for the reconstruction of muons, a "*stand-alone*" algorithm [135] that uses only information from the muon spectrometer, and "*combined*" and "*segment-tagged*" algorithms [135], which use muon spectrometer information along with tracking information from the inner detector. In the analyses presented in this work, the combined and segment-tagged algorithms are used for muon reconstruction, due to the higher purity of the selected muon sample. The combined algorithm works by associating a stand-alone muon spectrometer track to an inner-detector track. The tracks are reconstructed independently in both the inner detector and the muon spectrometer, and they are required to be well matched and have a compatible momentum measurement in both detectors. In order to prevent fake muons from jets "punching-through" the calorimeter and into the muon spectrometer, the muons within $\Delta R < 0.4$ of any jet are discarded. Further constraints are placed on the origin of the muon relative to the primary vertex of the event, which rejects muons originating from cosmic rays. These constraints ensure that muon tracks have a longitudinal impact parameter $|z_0| < 1\,\text{mm}$ and a transverse impact parameter of $|d_0| < 0.2\,\text{mm}$[7].

For segment tagged muons, an inner detector track is extrapolated and associated to a track segment in the muon spectrometer. This approach allows for the reconstruction of muons with an insufficient number of hits in the muon spectrometer. The resulting muon p_{T} is calculated by combining the inner detector track p_{T} with the information from the muon spectrometer, including any energy deposited by the muon candidate in the calorimeter.

4.3.3 Clustering algorithms

There are two calorimeter cell clustering algorithms used in the analyses presented in this work.

[7] The transverse impact parameter d_0 for a track is defined as the distance of closest approach to the beam-line, and the longitudinal impact parameter z_0 is defined as the $z-$ value of the point on the track that determines d_0.

Calorimeter towers

The calorimeter towers are built from a two-dimensional grid in η and ϕ. Each grid element has a size of $\Delta\eta \times \Delta\phi = 0.1 \times 0.1$, and the tower signal is the sum of the measured cell energies, calibrated at the EM scale[8] [90].

Topological clusters

The topological cell clusters attempt to reconstruct three-dimensional "energy blobs" that represent the showers developing for each particle traversing the calorimeter. The clustering process begins by selecting cells with a signal significance $\Gamma = E_{\text{cell}}/\sigma_{\text{noise, cell}} > 4$. All cells directly neighbouring these initial cells are added into the cluster. The neighbours of neighbours are added if $|\Gamma|$ computed for these cells is above 2. A final ring of cells is also added if the value of $|\Gamma|$ is greater than 0 [90].

4.3.4 Jets

Due to the principle of *colour confinement*, quarks and gluons involved in p–p collisions will hadronise and fragment into a large number of collimated particles ("jets") before they reach the ATLAS inner detector. The resulting hadrons will traverse the detector, depositing energy in the calorimeters. As the original partons are not physically observable objects, a procedure for associating these energy deposits to a single jet must be decided upon. There are several choices of jet reconstruction algorithm at ATLAS and the analyses presented in this work make use of the anti-k_t jet clustering algorithm [137], with radius parameter $R = 0.4$. The energy of the jets is calibrated to correct for calorimeter non-compensation[9], upstream material[10] and other effects [138]. Jets are required to have $p_{\text{T}} > 20$ GeV and $|\eta| < 2.5$, other than in the computation of the missing transverse momentum, where the requirements are instead $p_{\text{T}} > 20$ GeV and $|\eta| < 4.5$.

Anti-k_t algorithm

The procedure behind the anti-k_t algorithm is demonstrated by considering an example event in which there are several well separated energetic particles, with transverse momenta

[8] The EM scale is the basic signal scale for the ATLAS calorimeters. It accounts correctly for the energy deposited in the calorimeter by electromagnetic showers.

[9] For non-compensating calorimeters there is a higher response for electromagnetic particles ($EM/Had \neq 1$).

[10] This accounts for energy deposited in upstream material, such as the inner and outer walls of the cryostat.

k_{t1}, k_{t2}, ..., k_N and many other softer particles [137]. The smallest distance d_{1i} between hard particle 1 and soft particle i is given by:

$$d_{1i} = \min(\frac{1}{k_{t1}^2}, \frac{1}{k_{ti}^2})\frac{\Delta_{1i}^2}{R^2} \tag{4.1}$$

where $\Delta_{ij}^2 = (y_i y_j)^2 + (\phi_i \phi_j)^2$ and k_{ti}, y_i and ϕ_i are the p_{T}, rapidity, and azimuth of particle i, respectively. The value of d_{1i} is determined by the transverse momenta of the hard particle and the Δ_{1i} separation between the two. For soft particles with a similar separation the value of d_{ij} will be much larger. The result of this is that soft particles will more often cluster with hard ones, prior to clustering with other soft particles. If the hard particle is separated from other hard particles by a distance of at least $2R$ then it will acquire all of the soft particles within a circle of radius R and the final jet will be conical. However, if there is a second hard particle nearby, such that $R < \Delta_{12} < 2R$, then two hard jets will be produced. If $k_{t1} \gg k_{t2}$ then jet_1 will be conical and jet_2 will be missing the section that overlapped with jet_1. If $k_{t1} = k_{t2}$ neither jet will be conical and the overlapping region will be divided equally between both jets. In the case of $k_{t1} \sim k_{t2}$, neither jet will be conical and the boundary b between them will be given by $\Delta R_{1b}/k_{t1} = \Delta_{2b}/k_{t2}$. If $\Delta_{12} < R$ then both particles will be combined into a single jet. In the case where $k_{t1} \gg k_{t2}$ then the result will be centred on k_1, but if $k_{t1} \sim k_{t2}$ then the final shape will be the union of cones (radius $< R$) surrounding the two hard particles and another cone of radius R centred on the final jet. An important detail of the anti-k_t algorithm is that only hard particles are able to change the shape of the jet. The result of this is that the jet boundary is robust with respect to changes in the soft radiation and flexible with respect to hard radiation. An illustration of this algorithm is given in figure 4.3 [137].

4.3.5 *b*-jets

Jets originating from decays of b-quarks are identified in a process known as b-tagging [139], and used in the analyses presented in this work for separating the $W^{\pm}$ and $t\bar{t}$ background contributions, as will be described in chapters 5 and 6. For the analysis presented in chapter 5, the "JetFitterCombNN" algorithm [139] was used, whilst for the analysis in chapter 6, the "MV1" algorithm [139] was chosen. These are both neural-network-based algorithms, which combine information from the track impact parameters with a search along the jet axis for decay vertices [139]. Working points that correspond to a b-tagging efficiency of 60% and $< 1\,\%$ mis-identification of light-flavour or gluon jets are chosen [140]. The efficiencies and fake rates for identifying b-jets are dependent on the tagging algorithm

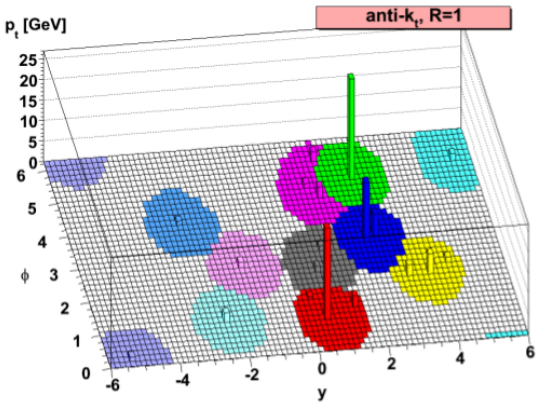

Figure 4.3: A sample parton-level event that includes several hard particles and many soft particles. The jets are clustered with the anti-k_t algorithm, illustrating the "active" catchment areas of the resulting hard jets [137].

used and these are not necessarily well modeled in the MC samples. An event weight is applied to the MC in order to ensure that there is a similar response for data and Monte Carlo. The re-weighting is done using a centrally provided calibration interface and measured efficiencies included in the SUSYTools package [133].

4.3.6 Taus

The τ-lepton has a mean lifetime of 2.9×10^{-13} seconds, which corresponds to a path length of 87 μm, meaning that they decay within the LHC beam pipe. The τ-lepton branching ratios for decays to either light leptons or hadrons are [29]:

$$\begin{aligned} \tau^- &\to e^-\bar{\nu}_e\nu_\tau \qquad (\mathcal{B} = 17.83 \pm 0.04\%) \\ \tau^- &\to \mu^-\bar{\nu}_\mu\nu_\tau \qquad (\mathcal{B} = 17.41 \pm 0.04\%) \\ \tau &\to \text{hadrons} \qquad (\mathcal{B} \approx 64.7\%) \end{aligned}$$

At ATLAS it is not possible to distinguish between a prompt light lepton ($\ell = e, \mu$) and τ-lepton decaying leptonically, so for the purposes of τ-identification at ATLAS only the hadronic decays are used. These decays are categorised by the number of charged decay products that they contain, which corresponds to the number of tracks (known as "prongs") reconstructed in the detector. The hadronic 1-prong decays are the most common, with a branching ratio, $\mathcal{B} = 49.5\%$, followed by 3-prong decays where $\mathcal{B} = 15.2\%$ [29]. A schematic of a 3 prong τ decay is shown in figure 4.4. The identification of τ-leptons at ATLAS is significantly more challenging than the identification of light leptons because the cross-section for the production of jets, which can be misidentified as

a τ-lepton, is many orders of magnitude larger than the cross-section for weakly-produced τ-leptons. It is also possible for electrons to be misidentified as 1-prong τ-leptons as they both result in a single charged track, and the τ-identification procedure must include separate steps to minimise this effect.

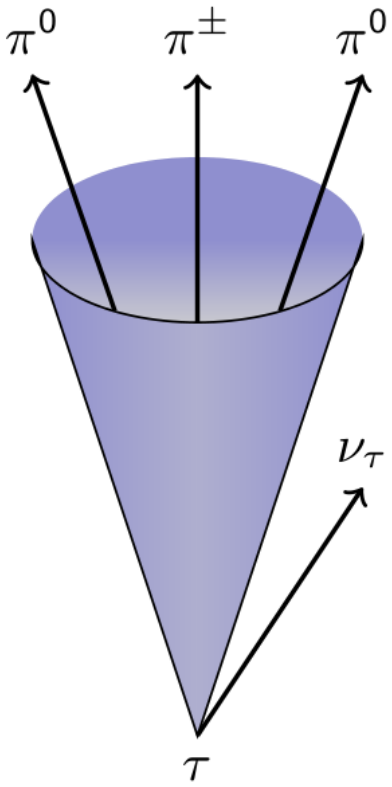

(a)

Figure 4.4: Schematic of a τ-lepton decaying hadronically.

The reconstruction of hadronic τ-candidates begins with the jets reconstructed with the anti-k_t algorithm already described, due to their similarity with collimated jets . All of the jets with $p_{\mathrm{T}} > 10$ GeV and $|\eta| < 2.5$ are considered as possible candidates for the τ-reconstruction algorithm [141]. The four-momenta of all visible decay products of the τ-candidate decay are combined to build the p_{T} of the τ-candidate. The η and ϕ of the candidate are taken from the sum of the four-vectors of the associated jet's topological clusters, where zero mass is assumed for each cluster.

These reconstructed τ-candidates are recorded as massless 4-vectors, and the track multiplicity for the τ-candidate is calculated by associating tracks to a candidate if they satisfy the condition $\Delta R \leq 0.2$ from the axis of the τ-candidate. The number of tracks associated to each candidate will categorise them as 1- or 3-prong τ-decays. Tracks in the region $0.2 < \Delta R < 0.4$ from the axis, known as the "isolation annulus", are also used

when defining the discriminating variables for τ-identification. All of these tracks must meet the following criteria:

- $p_{\mathrm{T}} > 1$ GeV
- number of pixel hits ≥ 2
- number of pixel hits + number of SCT hits ≥ 7
- $|d_0| < 1.0$ mm, where d_0 is the distance of closest approach of the track to the reconstructed primary vertex in the transverse plane.
- $|z_0 \sin\theta| < 1.5$ mm, where z_0 is the longitudinal distance of closest approach.

The calibration of the τ-energy scale is different from the general hadronic calibration (used for jet reconstruction), due to the fact that hadronic τ-lepton decays consist of a specific mix of charged and neutral pions. Extra p_{T} and η-dependent energy calibration factors are included for reconstructed τ-leptons to account for this [142].

The reconstruction stage alone is not adequate for a sufficiently pure identification of τ-leptons, and at this stage there is still a very large number of jets that are mis-reconstructed as τ-candidates. Further requirements are imposed on these candidates to improve the τ-lepton identification process. For the analyses presented in this work the boosted decision tree (BDT) identification algorithm, developed by the ATLAS Tau Combined Performance group, is used to discriminate between hadronically decaying τ-leptons and either quark or gluon-initiated jets, or electrons [141].

A BDT can be used as an event classifier as it can examine a range of input variables from predefined signal and background "training" samples, and via repeated yes or no decisions on each variable it is able to find the optimal cut value to maximise the signal significance. These decisions split the phase space into many regions, which are classified as either signal or background, depending on the majority of training events that end up in the region. The "boosting" of a decision tree refers to the reweighting of misclassified events, such as signal events that end up in a region of the phase space that is classified as background. These reweighted events are then used to build and optimise a new tree. Each of the trees is given a score that represents how succesful it is at discriminating between signal and background. Finally, all of these trees are combined into a single classifier, representing the average of all of the trees, with each tree's score used as a weight. This process stabilises the response of the decision trees with respect to fluctuations in the training sample [143].

For the τ-identification procedure, this multivariate technique makes use of a wide range of tracking and calorimeter based variables to attempt to discriminate between real

Variable	Jet BDT		Electron BDT
	1-prong	*3-prong*	
R_{track}	✓	✓	✓
f_{track}	✓	✓	✓
f_{core}	✓	✓	✓
$N_{\text{track}}^{\text{iso}}$	✓	✓	
R_{Cal}	✓	✓	
f_{iso}			✓
$m_{\text{eff. clusters}}$			✓
m_{tracks}		✓	
S_T^{flight}		✓	
$S_{\text{lead track}}$	✓	✓	
$f_{\text{3 lead clusters}}$	✓	✓	
ΔR_{max}		✓	
f_{EM}			✓
f_{HT}			✓
$f_{\text{Had}}^{\text{track}}$			✓
$E_{\text{T,max}}^{\text{strip}}$			✓
R_{Had}			✓

Table 4.2: Tracking and calorimeter variables that are used as an input for the τ-lepton BDT identification procedure [141]. Definitions of these variables can be found in appendix C.

and fake 1- and 3-prong τ-candidates. Three working points of this BDT identification are defined by the Tau Working Group at ATLAS ("loose", "medium" and "tight"), corresponding to signal efficiencies of $\approx 60\%$, 45% and 30%, respectively [141]. A complete list of the variables used by the identification algorithms can be found in table 4.3.6. The output of the BDT is known as a " score", which ranges from 0 to 1, where results closer to 1 correspond to more "τ-like" objects. Each of the working points has a corresponding value for the BDT score at which τ-candidates are accepted. A second BDT is used to discriminate between τ-leptons and electrons [141]. The jet and electron BDTs will both be discussed in more detail in the following, and a detailed discussion of the performance of the τ-lepton identification and reconstruction algorithms at ATLAS can be found in [141].

Jet BDT discriminant

The BDT used for the jet rejection is trained separately on 1-prong and 3-prong τ-candidates, and in separate categories depending on the number of reconstructed primary vertices, either 1–5 or ≥ 6. A ROOT [144] analysis toolkit package, TMVA [143], is used for training the BDTs. The three working points are defined based on the final jet BDT score, and these require p_{T}-dependent cuts to compensate for the p_{T}-dependence of the BDT distribution [141]. Distributions of a subset of the BDT input variables are shown in figure 4.5, and the final jet BDT score distributions can be seen in figure 4.6. A full list of the input variables for both the jet and electron BDTs can be found in appendix C. The signal and background efficiencies are defined as:

$$\epsilon_{\mathrm{sig}}^{\text{n-prong}} = \frac{\text{no. of } \tau\text{-candidates with } n \text{ reconstructed tracks, passing ID}}{\text{no. of true visible hadronic } \tau \text{ decays with } n \text{ prongs}} \tag{4.2}$$

$$\epsilon_{\mathrm{bkg}}^{\text{n-prong}} = \frac{\text{no. of } \tau\text{-candidates with } n \text{ reconstructed tracks, passing ID}}{\text{no. of } \tau \text{ candidates with } n \text{ reconstructed tracks}} \tag{4.3}$$

Distributions of the signal efficiency against the inverse background efficiency are presented in figure 4.7, where the jet BDT can be compared directly with two alternative τ-ID algorithms: the cut-based and likelihood based techniques. The jet BDT exhibits the best overall performance and was therefore chosen as the method of identification for the analyses presented in this work.

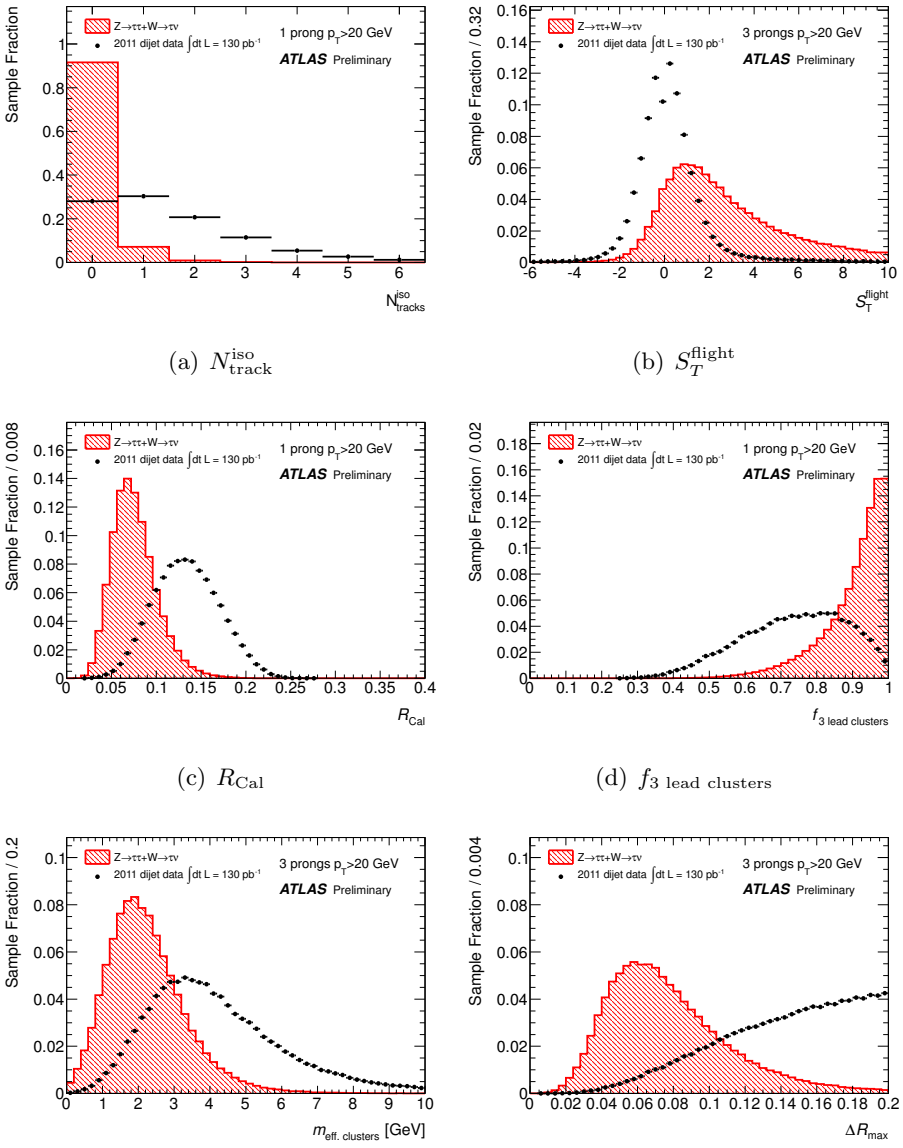

(a) $N_{\text{track}}^{\text{iso}}$ (b) S_T^{flight}

(c) R_{Cal} (d) $f_{3\text{ lead clusters}}$

(e) $m_{\text{eff. clusters}}$ (f) ΔR_{max}

Figure 4.5: Distributions of a selection of jet discriminating variables for MC simulated $Z \to \tau\tau$ and $W \to \tau\nu$ signal samples and a di-jet background sample selected from 2011 data. The distributions are normalised to unity [141].

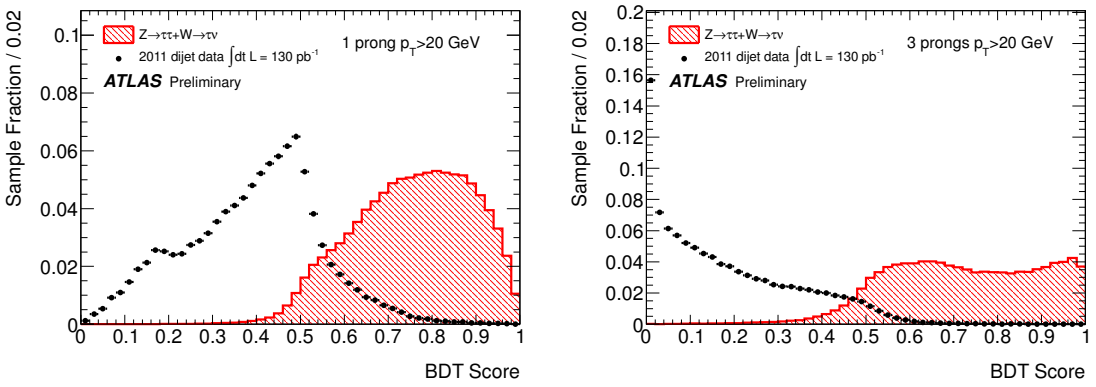

(a) (b)

Figure 4.6: (a) The jet BDT score for 1-prong and (b) 3-prong τ-candidates [141].

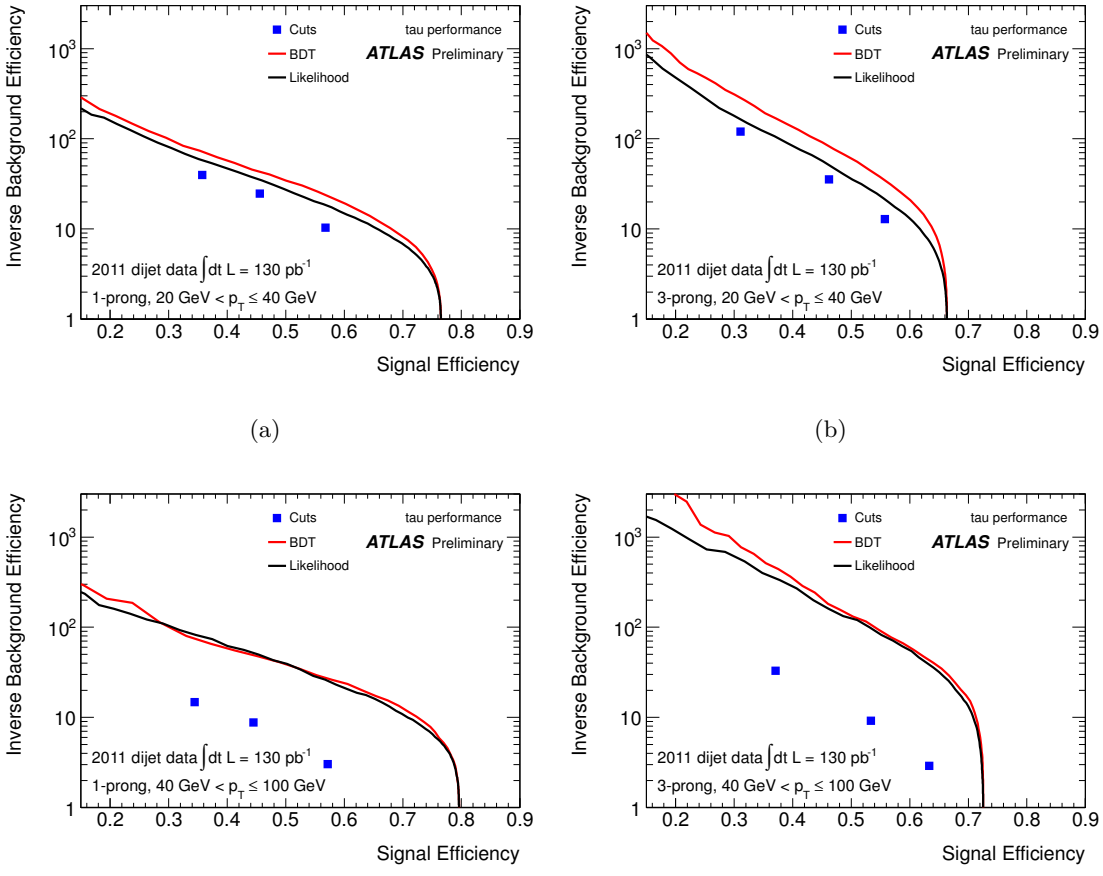

(a) (b)

(c) (d)

Figure 4.7: Inverse background efficiency as a function of signal efficiency for 1-prong (left) and 3-prong (right) candidates, in low (top) and high (bottom) p_{T} ranges, for all jet discriminants [141].

Electron BDT discriminant

Since it is possible for electrons to be incorrectly reconstructed as 1-prong τ-candidates, a second BDT is built to reduce fake τ-candidates from electrons [141]. There are several variables that can be used to discriminate between true 1-prong τ-candidates and electrons that are misidentified as τ-leptons. These include the emission of transition radiation from the electron track and the difference in the shower shape produced by a τ-lepton or an electron in the calorimeter. As with the jet BDT, "loose", "medium" and "tight" working points are defined which correspond to signal efficiencies of 95%, 85% and 75%, respectively. The variables that enter the BDT can be found listed in table 4.3.6 and several of the distributions are presented in figure 4.8 [141].

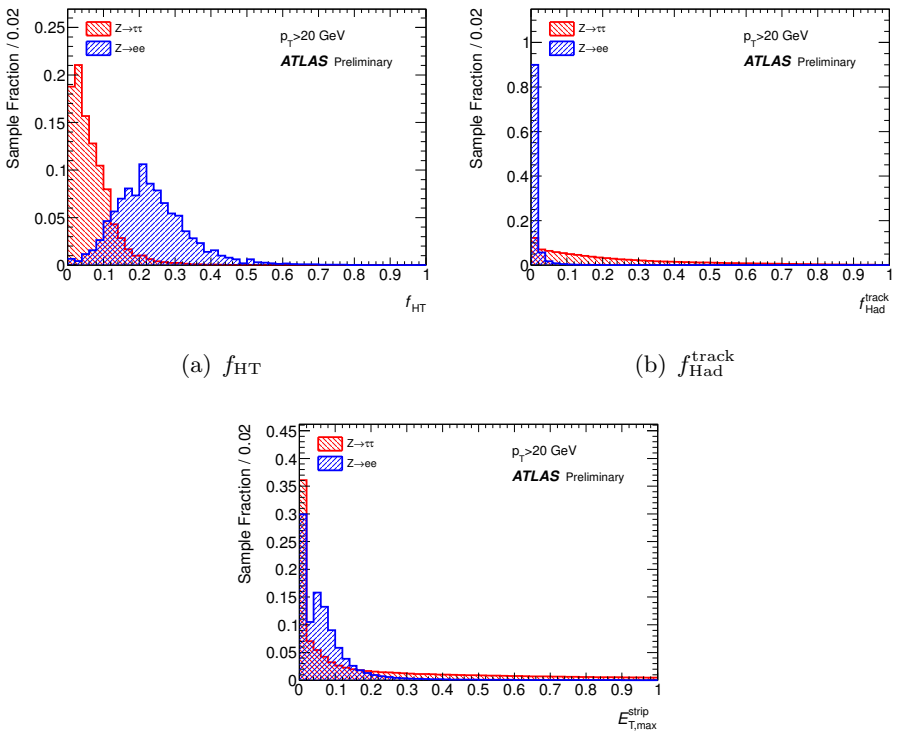

(a) f_{HT} (b) $f_{\mathrm{Had}}^{\mathrm{track}}$

(c) $E_{\mathrm{T,max}}^{\mathrm{strip}}$

Figure 4.8: Distributions of a selection of identification variables used in the electron BDT, for MC simulated $Z \to \tau\tau$ signal and $Z \to ee$ background events. The distributions are normalised to unity [141]

.

The final electron BDT score for electrons and hadronically decaying τ-leptons, selected using simulated samples can be found in figure 4.9. These objects are found to be well separated in MC, leading to a good signal and inverse background efficiency, which can be found in figure 4.10. Also shown in this figure is an alternative electron discriminant,

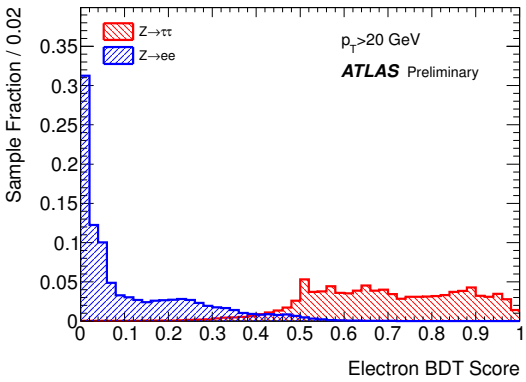

(a)

Figure 4.9: Score of the BDT-based electron veto for MC simulated electrons and hadronically decaying τ-leptons [141].

which employs a series of cuts to distinguish between 1 prong τ-candidates and tracks from electrons. The BDT-based electron discriminant is significantly better than the cut-based method, as can be seen in the figure. For a signal efficiency of $\sim 50\%$ the background rejection factor is in the range 100–1000. A full list of the input variables for the jet and electron BDTs can be found in appendix C.

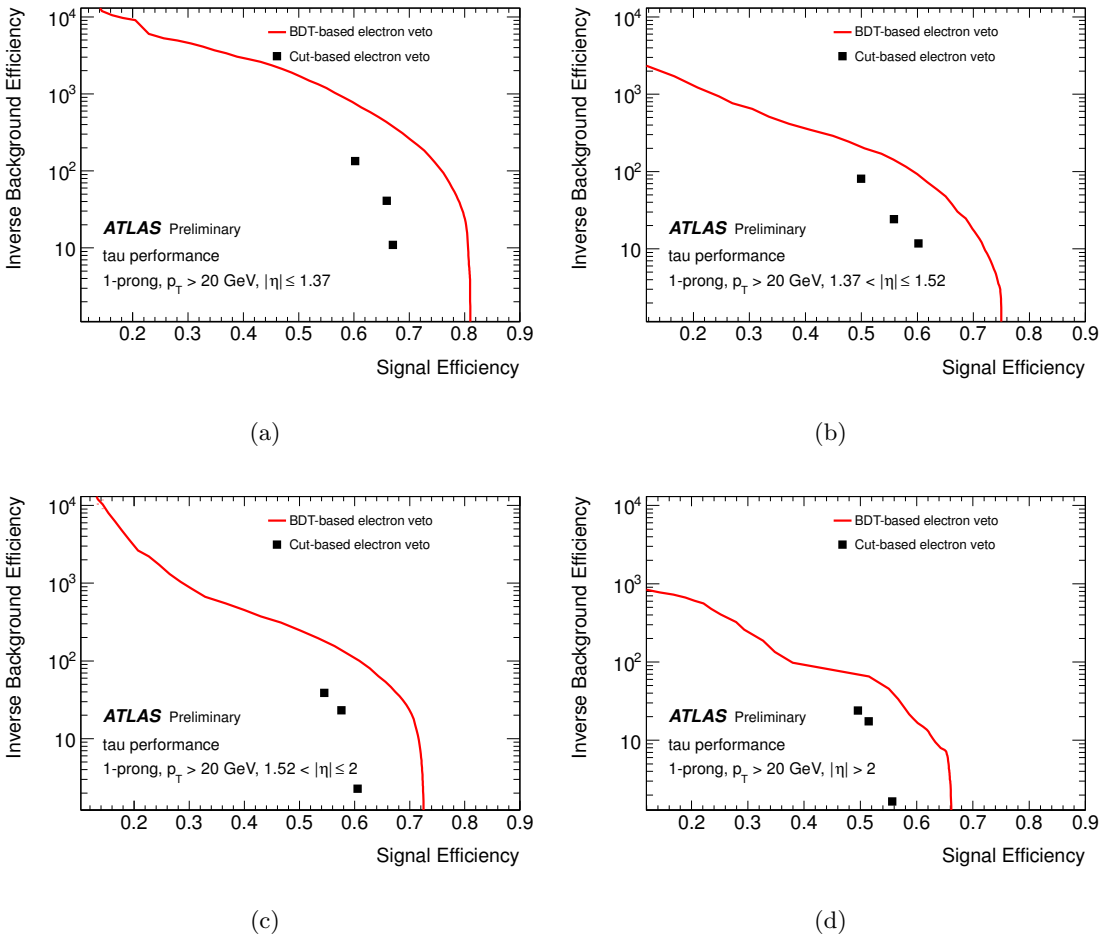

(a) (b)

(c) (d)

Figure 4.10: Inverse background efficiency as a function of signal efficiency for 1-prong reconstructed τ-candidates with $p_T > 20$ GeV, in four regions of $|\eta|$, for both electron discriminants [141].

4.3.7 Reconstruction of the missing transverse energy

The missing transverse momentum ($E_{\mathrm{T}}^{\mathrm{miss}}$) in an event is defined as the momentum imbalance in the plane transverse to the beam axis. Since it can be assumed that the inital partons involved in the collision have zero transverse momentum, the principle of conservation of momentum requires that momentum is conserved in this plane, and an imbalance may indicate the presence of undetected particles escaping the detector. These invisible particles could be neutrinos, or perhaps stable, weakly-interacting particles due to new physics processes. The measurement of the missing transverse momentum two-dimensional vector $\vec{p}_{\mathrm{T}}^{\mathrm{miss}}$ (and its magnitude $E_{\mathrm{T}}^{\mathrm{miss}}$) is based on the measurement of the transverse momenta of identified jets, electrons, muons and all calorimeter clusters with $|\eta| < 4.5$ not associated to such objects [145]. For the purpose of the measurement of $E_{\mathrm{T}}^{\mathrm{miss}}$, τ-candidates are not distinguished from jets.

The calculation of the $E_{\mathrm{T}}^{\mathrm{miss}}$ follows equation 4.4, and includes contributions from energy deposited in the calorimeters as well as muons that are reconstructed by the muon spectrometer.

$$E_{x(y)}^{\mathrm{miss}} = E_{x(y)}^{\mathrm{miss,calo}} + E_{x(y)}^{\mathrm{miss},\mu} \tag{4.4}$$

The values of $E_{\mathrm{T}}^{\mathrm{miss}}$ and ϕ^{miss}, the azimuthal component, are then given by:

$$\begin{aligned} E_T^{\mathrm{miss}} &= \sqrt{(E_x^{\mathrm{miss}})^2 + (E_y^{\mathrm{miss}})^2} \\ \phi^{\mathrm{miss}} &= \arctan(E_y^{\mathrm{miss}}, E_x^{\mathrm{miss}}) \end{aligned} \tag{4.5}$$

The computation of the $E_{\mathrm{T}}^{\mathrm{miss}}$ makes use of information from calibrated calorimeter cells associated to reconstructed objects (e, μ, τ, jets, γ).

The muon component of the $E_{\mathrm{T}}^{\mathrm{miss}}$ is calculated from the momenta of muon tracks reconstructed within $|\eta| < 2.7$:

$$E_{x(y)}^{\mathrm{miss},\,\mu} = -\sum_{\mathrm{muons}} p_{x(y)}^{\mu}$$

In order to appropriately account for the energy deposited by the muon in the calorimeters, the muon term $E_{x(y)}^{\mathrm{miss,calo},\mu}$ is calculated differently for isolated and non-isolated muons, with non-isolated muons defined as those within a distance $\Delta R < 0.3$ of a reconstructed jet in the event. For the isolated muons, the p_{T} is calculated from the combined measurement of the inner detector and muon spectrometer, taking into account the energy deposited in the calorimeters. In this case the energy lost by the muon in the calorimeters is not added to the calorimeter term, to avoid counting this twice. For non-isolated muons, the energy deposited in the calorimeter cannot be resolved from the calorimetric energy depositions

of the particles in the jet. The muon spectrometer measurement of the muon momentum after the energy loss in the calorimeter is therefore used, so the $E_{x(y)}^{\mathrm{miss,calo},\mu}$ term is added to the calorimeter term. In cases in which there is a significant mis-match between the spectrometer stand-alone and the combined measurement, the combined measurement is used and a parameterised estimation of the muon energy loss in the calorimeter is subtracted.

The full calorimeter term is given by:

$$E_{x(y)}^{\mathrm{miss,calo}} = E_{x(y)}^{\mathrm{miss},e} + E_{x(y)}^{\mathrm{miss},\gamma} + E_{x(y)}^{\mathrm{miss},\tau} + E_{x(y)}^{\mathrm{miss,jets}} + E_{x(y)}^{\mathrm{miss,softjets}} + (E_{x(y)}^{\mathrm{miss,calo}\mu}) + E_{x(y)}^{\mathrm{miss,CellOut}}$$

where $E_{x(y)}^{\mathrm{miss},e}$, $E_{x(y)}^{\mathrm{miss},\gamma}$, $E_{x(y)}^{\mathrm{miss},\tau}$ are reconstructed from energy deposited in the calorimeter cells associated to electrons, photons or τ-candidates, respectively. $E_{x(y)}^{\mathrm{miss,jets}}$ is reconstructed from cells in clusters associated to jets with calibrated $p_{\mathrm{T}} > 20$ GeV and $E_{x(y)}^{\mathrm{miss,softjets}}$ from cells in clusters associated to jets with 7 GeV $< p_{\mathrm{T}} < 20$ GeV. $E_{x(y)}^{\mathrm{miss,calo}\mu}$ is the contribution from energy lost by muons in the calorimeter and $E_{x(y)}^{\mathrm{miss,CellOut}}$ is calculated from the cells in the three-dimensional topoclusters which are not associated to a reconstructed object.

4.3.8 Removal of overlapping reconstructed objects

During the object reconstruction it is possible for a single physics object transversing the detector to be reconstructed by multiple algorithms, corresponding to different types of particle. This must be corrected for in order to avoid double counting elements in an event, and a chain of priorities is constructed to account for this:

- a τ-candidate is rejected if it overlaps with either an electron or a muon within $\Delta R < 0.2$, due to the higher efficiency and purity of the light lepton reconstruction algorithms;
- a jet is rejected if it overlaps with a reconstructed τ-candidate (which is seeded by the anti-k_t jet algorithm) or an electron within $\Delta R < 0.2$;
- a muon is rejected if it overlaps with a jet within $\Delta R < 0.2$, to prevent a "punch-through" effect in which jets deposit energy in the muon spectrometer;
- finally, an electron or a muon is rejected if it overlaps with a jet within $0.2 < \Delta R < 0.4$, since it is then assumed to be from a secondary decay within a jet.

5

Search for supersymmetry in final states with two τ-leptons, jets and missing transverse energy

This chapter details the search for evidence of supersymmetry in final states with two τ-leptons with the ATLAS detector, using the first $2.05\,\text{fb}^{-1}$ of the 2011 dataset. The analysis, published in Physics Letters B [146], focuses on final states containing at least two hadronically decaying τ-leptons, jets and $E_{\text{T}}^{\text{miss}}$. For this analysis I have contributed to the optimisation of the signal selection and the definitions the background control regions (in collaboration with colleagues from DESY and the University of Bonn). In particular, I have been solely responsible for the semi-data-driven estimate of the multi-jet background contribution to the signal region and the statistical interpretation of the result, including the setting of the 95% CL exclusion limit in the GMSB parameter space.

5.1 Introduction

Various SUSY models predict that the production of τ-leptons is enhanced with respect to the light leptons (e, μ) due to the large Yukawa coupling of the $\tilde{\tau}_1$. Assuming no lepton-flavour violation in the SUSY sector, the $\tilde{\tau}_1$ and the $\tilde{\tau}_2$ will contain τ-leptons in their decay

in the vast majority of cases. It is expected that very few SM processes will result in events with multiple τ-leptons, large $E_{\mathrm{T}}^{\mathrm{miss}}$ and energetic jets, and therefore a small background is expected to potential signals of new physics in this final state. The results of this analysis are interpreted in the context of the Gauge-Mediated SUSY Breaking scenario, which was introduced in section 2.5, but model independent limits on the visible cross-section are also produced.

5.2 Data and Monte Carlo samples

5.2.1 ATLAS data samples

The data used in this analysis were collected from p–p collisions at a centre-of-mass energy of $\sqrt{s} = 7$ TeV, recorded by the ATLAS detector between March 13$^{\mathrm{th}}$ and August 26$^{\mathrm{th}}$ 2011. The data periods and associated integrated luminosities are summarised in table 5.1.

Period	Run numbers	Runs	$\int \mathcal{L}\,\mathrm{dt}$ [pb^{-1}]
B	177986–178109	7	11
D	179710–180481	23	154
E	180614–180776	5	43
F	182013–182519	16	123
G	182726–183462	28	464
H	183544–184169	13	240
I	185353–186493	27	305
J	186516–186755	9	212
K	186873–187815	19	500
All		147	2053

Table 5.1: Details of the data-taking periods used in this analysis, along with corresponding run numbers and integrated luminosities. The stated integrated luminosity corresponds to the dataset after imposing detector quality conditions, described in detail in the text.

Data are pre-selected to ensure that the events analysed meet minimum detector quality requirements. These requirements are that all magnet systems were operating at their full field strength, and all of the detector subsystems were at their normal operating voltages when the data was recorded. The data are also required to be validated by the ATLAS Data Quality group, which studies a range of distributions in data to inspect it for deviations with respect to reference distributions from earlier, well understood runs. After applying these criteria, the total integrated luminosity available to be analysed is

2053 pb^{-1} [86, 87], with an uncertainty on the luminosity estimated to be 3.7% [87].

5.2.2 Simulated Standard Model background samples

In order to estimate the SM backgrounds to any potential signal of new physics, Monte Carlo background samples are used and compared to the data. The MC samples used in this analysis were produced as part of the official ATLAS MC production, for which details were provided in section 4.1. The MC samples have been scaled from leading-order (LO) cross-sections, as calculated by most of the generators, to next-to-next-leading-order (NNLO) cross-sections. The NNLO cross-sections are not avaliable for the diboson samples, so the next-to-leading order (NLO) cross-sections are used instead.

Table 5.2 contains a summary of the Monte Carlo background samples that have been used in this analysis, with the full details listed in appendix A, tables A.2–A.7. The dominant SM background processes to this search are $W+$jets and $t\bar{t}$, which have NNLO cross-sections of 31.4 nb and 165 pb, respectively. As the LHC is a hadron collider and the analysis selects hadronically decaying τ-leptons, multi-jet events are also considered as a potential background. This is because jets can be incorrectly reconstructed as τ-candidates and pass the signal selection criteria. These multi-jet processes have a large cross-section of $\sim$11 mb. The background contribution from multi-jet events is estimated using a semi-data-driven technique, in order to be less dependent on the Monte Carlo modeling of the exact cross-section, for which there is a reasonably large uncertainty. Other SM processes that may contribute to the total background in this analysis include $Z+$jets, where the Z boson decays to a pair of τ-leptons, which has a NNLO cross-section of 4.22 nb, and the production of dibosons: WW, WZ, and ZZ.

In order to accurately simulate the pile-up conditions in the data, a re-weighting procedure is applied to all of the MC samples to ensure that the distribution of the number of primary interactions per bunch crossing in MC is consistent with the data. The distribution in data is shown in figure 3.2(b).

5.2.3 Simulated signal samples

The GMSB signal Monte Carlo samples used in this analysis are summarised in table 5.3. The minimal GMSB model in which the results of this analysis are presented was introduced in section 2.5. In order to optimise the signal selection two GMSB points were chosen as benchmarks. These are defined with the parameters $\Lambda = 30$ TeV, $\tan\beta = 20$ and $\Lambda = 40$ TeV, $\tan\beta = 30$, and are referred to in the text as "GMSB3020" and "GMSB4030",

Name	Generator	Cross-section [pb]	Number of events
$t\bar{t}$ and single top	MC@NLO +JIMMY	0.47–89.35	3.0×10^5–1.5×10^7
$W \to e\nu/\mu\nu/\tau\nu + 0$–5 partons	ALPGEN +JIMMY	8.30–8305.92	6.3×10^4–3.7×10^6
$Z \to ee/\mu\mu/\tau\tau/\nu\nu + 0$–5 partons	ALPGEN +JIMMY	0.96–835.85	7.0×10^3–6.6×10^6
Multi-jets	PYTHIA	6.2×10^{-6}–9.86×10^9	1.4×10^6–1.6×10^7
Diboson (WW, ZZ, WZ)	MC@NLO +JIMMY	6.17–1688.9	2.5×10^4–2.0×10^5
Drell-Yan ($Z \to ee/\mu\mu/\tau\tau + 0$–5 partons, 10 GeV $< m_{\ell\ell} <$ 40 GeV)	ALPGEN +JIMMY	0.58–3819	1.0×10^3–1.0×10^5

Table 5.2: A summary of the simulated Standard Model samples used in this analysis, and corresponding generator, cross-section and number of simulated events. The stated cross-section is NNLO where possible, otherwise the NLO value is used. A full list can be found in appendix A, in tables A.2–A.7

respectively. These benchmark points were chosen because their kinematics are representative of a wide range of the considered parameter space, they offer relatively large inclusive τ-lepton production cross-sections, and have the advantage of not being excluded by previous experiments or precision measurements, such as constraints from measurements of $b \to s\gamma$ and $(g_\mu - 2)/2$ [147].

The mass hierarchy of the two benchmark points is displayed in figure 5.1(a) and 5.1(b), with more detailed values provided in tables 5.3(a) and 5.3(b). The gravitino, with a mass of 1.8 (2.4) eV for GMSB3020 (GMSB4030), is not shown graphically, and the $\tilde{\tau}_1$, with a mass of 88.0 (101.3) GeV for GMSB3020 (GMSB4030), is the NLSP in both cases. In both models the mass of the $\tilde{\ell}_R$ is close to that of the $\tilde{\tau}_1$. Figure 5.2 provides some details of the phenomenology of the GMSB signal grid, and the average number of true τ-leptons produced per event can be seen as a function of Λ and $\tan\beta$ in figure 5.2(a). Figure 5.2(b) shows the branching fraction to events that contain at least one τ-lepton in the final state. Black lines are included in both plots to indicate the various regions of parameter space, of which the most important for this analysis is the large region in which the $\tilde{\tau}_1$ is the NLSP.

5.3 Analysis strategy

This section details the signal selection criteria for the analysis, in which events containing jets, $E_{\mathrm{T}}^{\mathrm{miss}}$, and at least two hadronically decaying τ-leptons are selected. The approach of the analysis is to identify a minimal set of kinematic requirements that provide sensitivity to signals from new physics processes, without focusing explicitly on a single model. Although the results are interpreted in the context of GMSB, this analysis is also sensitive

Sample ID	Name	Generator	LO [pb]	NLO [pb]
137931	GMSB3020 ($\Lambda = 30, \tan\beta = 20$)	HERWIG++	1.95	2.35
137940	GMSB4030 ($\Lambda = 40, \tan\beta = 30$)	HERWIG++	0.41	0.45
137921–	GMSB grid	HERWIG++	0.006	0.005
–137975	GMSB grid	HERWIG++	15.8	21.7

Table 5.3: The GMSB benchmark samples with sample IDs, event generator, LO and NLO cross-sections. The LO cross-sections are taken from the generator, and the NLO cross-sections are calculated using PROSPINO. The GMSB grid ranges from 10–80 TeV in Λ and 2–50 in $\tan\beta$.

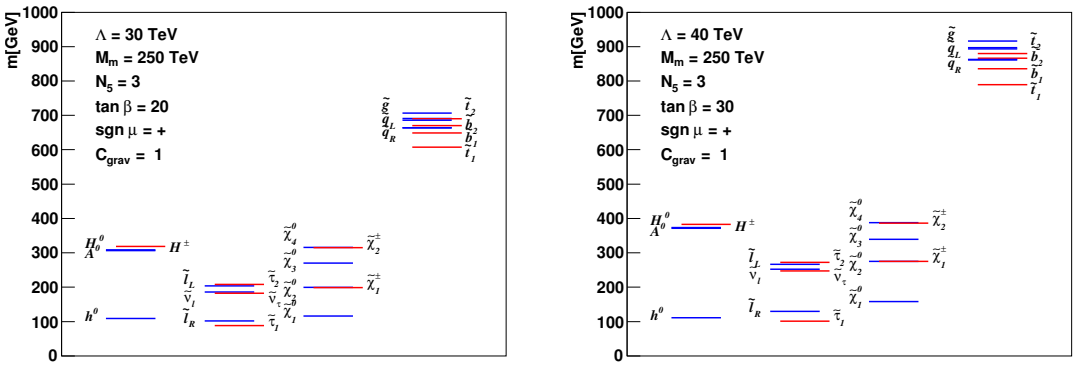

Figure 5.1: (a) Mass spectra for the GMSB3020 benchmark point and (b) for the GMSB4030 benchmark point. The almost massless gravitino ($m_{\tilde{G}} = 1.8\,\text{eV}$) is not depicted.

(a) Mass hierarchy for "GMSB3020"

$\widetilde{\mathrm{g}}$	706.5	$\widetilde{\chi}_1^0$	115.9	$\widetilde{\nu}_e$	185.8	h	108.9
$\widetilde{\mathrm{u}}_L$	686.2	$\widetilde{\chi}_2^0$	199.4	$\widetilde{\mathrm{e}}_L$	204.0	H	308.3
$\widetilde{\mathrm{u}}_R$	664.1	$\widetilde{\chi}_3^0$	270.4	$\widetilde{\mathrm{e}}_R$	101.6	A	306.2
$\widetilde{\mathrm{d}}_L$	691.2	$\widetilde{\chi}_4^0$	315.7	$\widetilde{\nu}_\tau$	182.7	$\mathrm{H}^\pm$	318.7
$\widetilde{\mathrm{d}}_R$	663.5	$\widetilde{\chi}_1^\pm$	198.6	$\widetilde{\tau}_1$	88.0		
$\widetilde{\mathrm{b}}_1$	648.9	$\widetilde{\chi}_2^\pm$	314.7	$\widetilde{\tau}_2$	207.8	$\widetilde{\mathrm{G}}$	1.8 eV
$\widetilde{\mathrm{b}}_2$	669.9						
$\widetilde{\mathrm{t}}_1$	607.7						
$\widetilde{\mathrm{t}}_2$	690.0						

(b) Mass hierarchy for "GMSB4030"

$\widetilde{\mathrm{g}}$	916.4	$\widetilde{\chi}_1^0$	158.4	$\widetilde{\nu}_e$	252.3	h	111.3
$\widetilde{\mathrm{u}}_L$	893.4	$\widetilde{\chi}_2^0$	274.8	$\widetilde{\mathrm{e}}_L$	266.7	H	373.7
$\widetilde{\mathrm{u}}_R$	862.8	$\widetilde{\chi}_3^0$	339.5	$\widetilde{\mathrm{e}}_R$	130.0	A	371.2
$\widetilde{\mathrm{d}}_L$	897.2	$\widetilde{\chi}_4^0$	387.9	$\widetilde{\nu}_\tau$	247.3	$\mathrm{H}^\pm$	382.7
$\widetilde{\mathrm{d}}_R$	861.1	$\widetilde{\chi}_1^\pm$	275.3	$\widetilde{\tau}_1$	101.3		
$\widetilde{\mathrm{b}}_1$	835.5	$\widetilde{\chi}_2^\pm$	386.7	$\widetilde{\tau}_2$	272.4	$\widetilde{\mathrm{G}}$	2.4 eV
$\widetilde{\mathrm{b}}_2$	866.6						
$\widetilde{\mathrm{t}}_1$	789.3						
$\widetilde{\mathrm{t}}_2$	879.6						

Table 5.4: Detailed mass hierarchy for the GMSB benchmark points (a) "GMSB3020" and (b) "GMSB4030". All masses are in GeV unless otherwise specified.

to any new physics process that results in large $E_{\mathrm{T}}^{\mathrm{miss}}$, energetic jets and at least two τ-leptons.

It is possible to consider the event selection for the analysis in three stages: pre-selection and event cleaning, multi-jet background and fake $E_{\mathrm{T}}^{\mathrm{miss}}$ rejection, and the final kinematic requirements to allow for the discrimination between possible signal events and the remaining background. Section 5.4 describes the pre-selection and event cleaning, including the treatment of the dead region in the liquid argon calorimeter that is present in the data recorded during 2011. Section 5.5 details the trigger used to select the data, and section 5.6 describes the final signal selection requirements. Section 5.7 describes the background estimation procedure, in which scaling factors for MC are obtained in dedicated control regions to correct for possible discrepancies with the data.

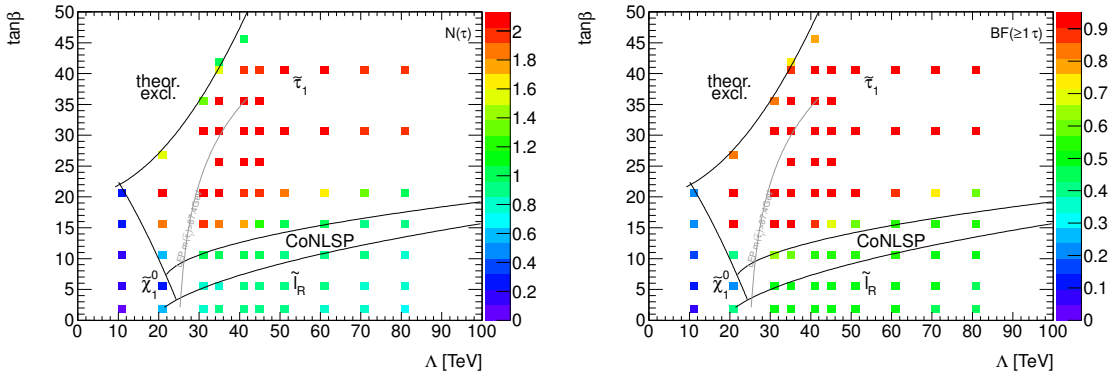

(a) Average number of true τ-leptons per event

(b) Branching fraction to $\geq 1\tau$-lepton

Figure 5.2: τ-lepton production in the GMSB Λ–$\tan\beta$ plane. (a) The average number of τ-leptons produced per event and (b) the branching fraction to events that contain at least one τ-lepton in the final state.

5.3.1 Kinematic variables used in the analyses

Several kinematic variables are used throughout this work to distinguish SUSY signals from SM backgrounds. The most important of these are defined below:

- the transverse scalar sum of the p_{T} of the jets and τ-candidates in the event: $H_{\mathrm{T}} = \sum p_{\mathrm{T}}^{\tau} + \sum p_{\mathrm{T}}^{\mathrm{jet}}$
- the effective mass $m_{\mathrm{eff}} = H_{\mathrm{T}} + E_{\mathrm{T}}^{\mathrm{miss}}$;
- the ratio $E_{\mathrm{T}}^{\mathrm{miss}}/m_{\mathrm{eff}}$;
- $\Delta\phi_{\mathrm{min}}$, the smallest of the two angles in the azimuthal plane between each of the two leading jets and the $E_{\mathrm{T}}^{\mathrm{miss}}$ vector.
- the transverse mass is formed by $E_{\mathrm{T}}^{\mathrm{miss}}$and the p_{T} of the τ-candidate

$$m_{\mathrm{T}} = \sqrt{m_{\tau}^2 + 2 \cdot p_{\mathrm{T}}^{\tau} \cdot E_{\mathrm{T}}^{\mathrm{miss}} \cdot \left(1 - \cos\Delta\phi(\tau, E_{\mathrm{T}}^{\mathrm{miss}})\right)} \tag{5.1}$$

When considering the separation of physics objects in η–ϕ space the variable ΔR is used, where:

$$\Delta R = \sqrt{(\Delta\eta)^2 + (\Delta\phi)^2} \tag{5.2}$$

5.4 Pre-selection and event cleaning

The primary interaction vertex of an event is identified as the vertex with the largest scalar sum of the transverse momenta of the associated tracks. In order to suppress non-collision

backgrounds, in this analysis the primary vertex is required to have at least five tracks associated to it.

Events where jets that are not associated to genuine physics objects, but instead to noise in the detector or calorimeter malfunction (known as "bad jets") are carefully identified and removed. Jets are labelled as "bad" if they have $p_{\mathrm{T}} > 20$ GeV and meet one of the following criteria:

- $f_{\mathrm{EM}} > 0.95$ and $|Q_{\mathrm{LAr}}| > 0.8$ and $|\eta| < 2.8$; where f_{EM} is the fraction of jet energy reconstructed in the EM calorimeter and Q_{LAr} is a jet-quality variable based on LAr pulse shapes, normalised such that $|Q| = 0$ (1) corresponds to high-(low-) quality jets; or
- $f_{\mathrm{HEC}} > 0.5$ and $|Q_{\mathrm{HEC}}| > 0.5$; where f_{HEC} is the fraction of jet energy in the HEC[1] and Q_{HEC} is a jet-quality variable based on HEC pulse shapes, normalised in the same way as Q_{LAr}; or
- $|\mathrm{neg.E}| > 60$ GeV; where neg.E denotes the sum of negative cell energies[2] within the jet; or
- $|t| > 25$ ns; where t is the measured jet time; or
- $f_{\mathrm{EM}} < 0.05$ and $f_{\mathrm{Charge}} < 0.05$ and $|\eta| < 2$; where f_{Charge} denotes the ratio of the sum of p_{T} of tracks associated to the jet to the transverse energy measured in the calorimeter; or
- $f_{\mathrm{EM}} < 0.05$ and $|\eta| > 2$; or
- $F_{\mathrm{max}} > 0.99$ and $|\eta| < 2$; where F_{max} is the maximum energy fraction in any one calorimeter layer.

During the 2011 data taking run there was a temporary failure in the electronics associated to the LAr barrel in the ECAL. This failure created a dead region in the second and third layers of the ECAL, corresponding to $\sim 1.4 \times 0.2$ radians in $\Delta\eta \times \Delta\phi$. Events containing electron or τ-candidates that are reconstructed in this region are discarded because it is impossible to be confident that the reconstruction of the energy and momentum was sufficiently accurate. For jets that transverse this region, however, it is possible to apply a p_{T} correction to account for potential mis-measurements of the energy deposited in the calorimeter.

[1] Hadronic end-cap calorimeter (HEC).

[2] Cell energies can be negative due to the electronic shaping function used in the LAr calorimeters. This is set up in such a way that noise contributions will fluctuate around zero, thus cell energies can obtain negative values.

5.5 Triggers used in the analysis

The data used in this analysis are selected with combined jet+$E_{\mathrm{T}}^{\mathrm{miss}}$ triggers. These triggers require the leading jet in the event to have $p_{\mathrm{T}} > 75\,\mathrm{GeV}$, measured at the EM scale, and $E_{\mathrm{T}}^{\mathrm{miss}} > 45\,\mathrm{GeV}$ [84]. A different trigger was used in the data-taking period labelled as "B" with respect to the later data-taking periods, to take into account the changes in the available online triggers. Additional requirements are imposed on the leading jet p_{T} ($p_{\mathrm{T}}^{\mathrm{jet1}}$) and the $E_{\mathrm{T}}^{\mathrm{miss}}$ to ensure that the selected events are in a kinematic regime where the trigger is fully efficient. The trigger selection has an efficiency of greater than 98% when requiring $p_{\mathrm{T}}^{\mathrm{jet1}} \geq 130$ GeV and $E_{\mathrm{T}}^{\mathrm{miss}} \geq 130$ GeV (known as the "trigger plateau requirements"), and the relevant trigger efficiency plot, showing the so-called "turn-on curves", can be found in figure 5.3.

5.6 Signal selection requirements

Once the pre-selection, event cleaning and the trigger plateau requirements have been applied, events are required to have a second jet with $p_{\mathrm{T}}^{\mathrm{jet2}} > 30$ GeV. This requirement suppresses a considerable fraction of the multi-jet background, without removing a significant number of signal events, which tend to have higher jet multiplicities. This can be seen in figure 5.4(a), which shows the jet multiplicity after the trigger plateau requirements and the $p_{\mathrm{T}}^{\mathrm{jet2}}$ requirement have been applied. The distributions of the p_{T} for the leading and sub-leading jets, after the requirement on their respective p_{T}, can be seen in figures 5.4(b) and 5.4(c), respectively.

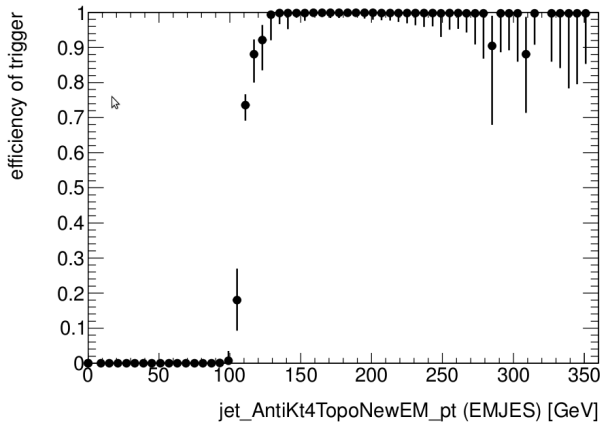

(a)

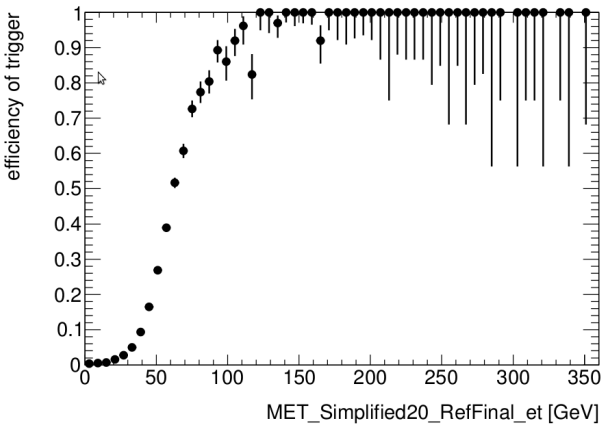

(b)

Figure 5.3: Projections of the jet+$E_{\mathrm{T}}^{\mathrm{miss}}$ (EF_j75_a4tc_EFFS_xe45_loose_noMu) trigger efficiencies onto the jet p_{T} axis following a cut of $E_{\mathrm{T}}^{\mathrm{miss}} > 130$ GeV (5.3(a)), and onto the $E_{\mathrm{T}}^{\mathrm{miss}}$ axis following a cut of $p_{\mathrm{T}}^{\mathrm{jet1}} > 130$ GeV (5.3(b)). The data used was from period D [148]

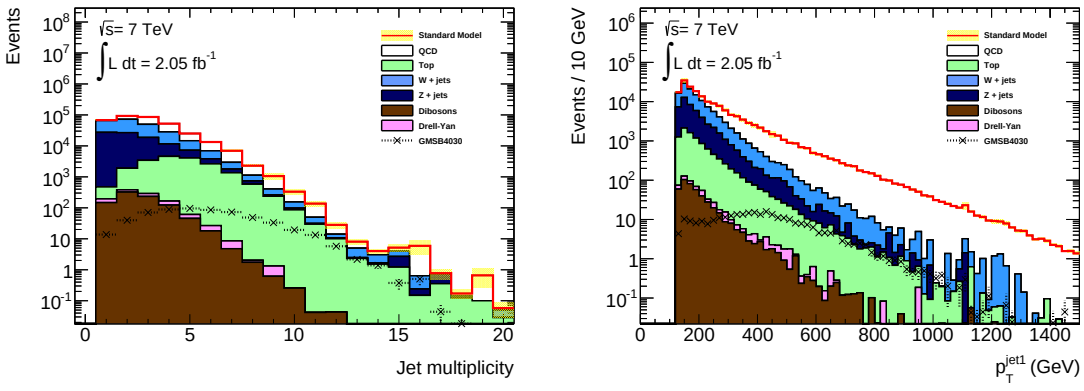

(a) (b)

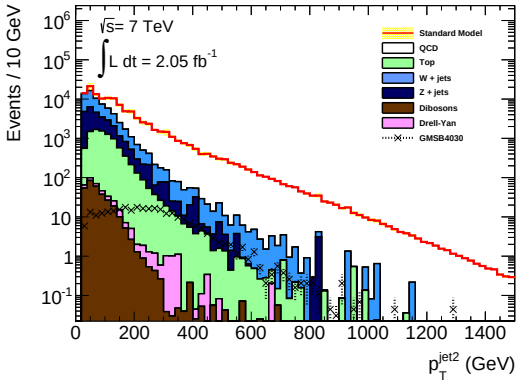

(c)

Figure 5.4: (a) The number of jets after the trigger plateau requirements have been applied. Figures (b) and (c) show the p_{T} of the leading ($p_{\mathrm{T}}^{\mathrm{jet1}}$) and sub-leading ($p_{\mathrm{T}}^{\mathrm{jet2}}$) jets, following the requirement on their respective p_{T}.

To avoid an overlap with other τ-based SUSY searches, in which one of the τ-leptons decays leptonically, events are rejected if either an electron or a muon is selected, with $p_{\mathrm{T}} \geq 20$ GeV and $|\eta| < 2.47$ or 2.4, respectively. This requirement also helps to suppress some of the SM backgrounds that result in the production of light leptons, including W+jets and $t\bar{t}$ events..

Figure 5.5 shows the reconstructed τ-candidate multiplicity and the leading and sub-leading τ-candidate p_{T} after the events containing light leptons have been removed. The τ-candidates are selected using the "loose" BDT ID (see section 4.3.6) and are required to have $p_{\mathrm{T}} > 20$ GeV. After requiring the presence of at least two reconstructed τ-candidates almost all of the MC background due to multi-jet events is rejected, with the remaining multi-jet background consisting of collimated jets that meet the τ-ID requirements, and are therefore incorrectly reconstructed as τ-leptons.

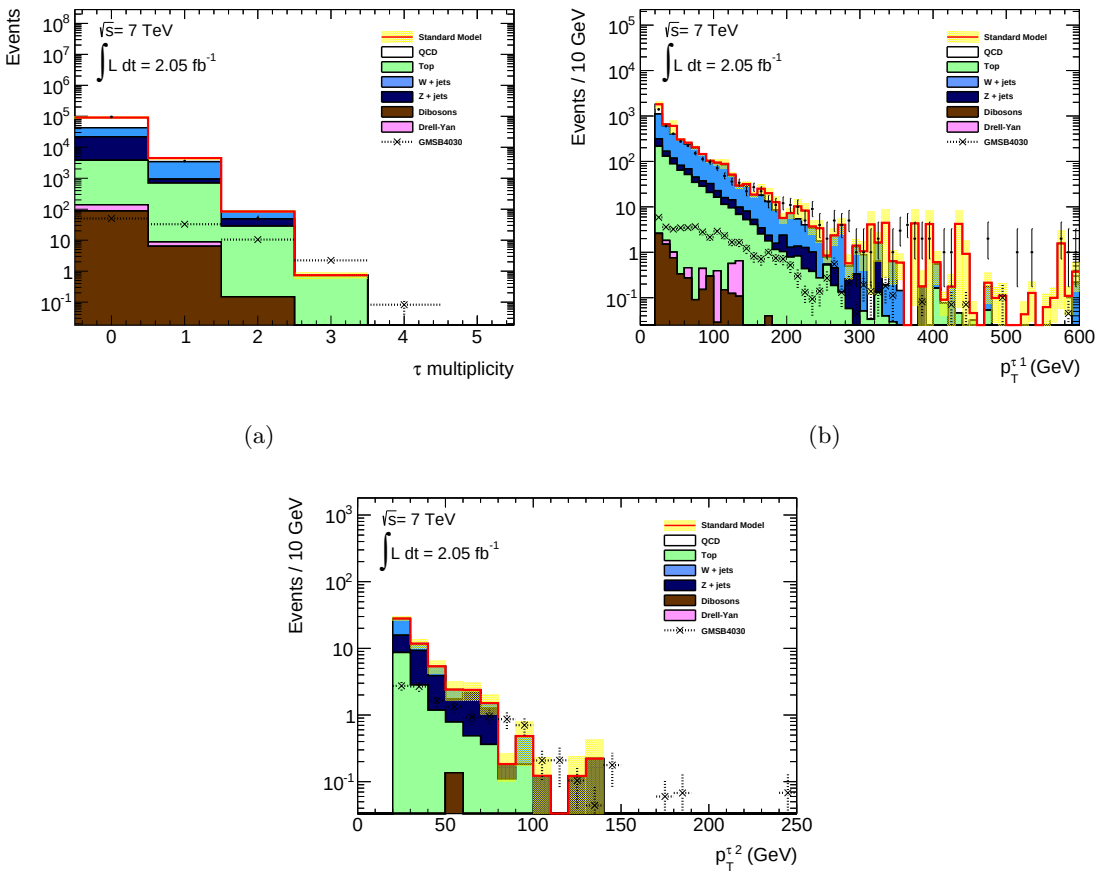

Figure 5.5: (a) The τ-candidate multiplicity and p_{T} of (b) leading and sub-leading (c) τ-candidates. after rejecting events containing a light lepton.

In order to further reduce any remaining contribution from multi-jet events, or events

in which the $p_{\mathrm{T}}^{\mathrm{jet1}}$, $p_{\mathrm{T}}^{\mathrm{jet2}}$ or $E_{\mathrm{T}}^{\mathrm{miss}}$ are incorrectly measured, events are rejected if the distance in ϕ between the leading or sub-leading jets and the $E_{\mathrm{T}}^{\mathrm{miss}}$ is less than 0.4. This is because fake, instrumental $E_{\mathrm{T}}^{\mathrm{miss}}$ is often the result of a mismeasurement of the jet p_{T}, and is therefore aligned with the direction of the leading jets. The distributions of these variables, after the selection of two or more τ-candidates, can be seen in figure 5.6. Following this requirement the remaining SM background consists primarily of W+jets, Z+jets and top events. As the multi-jet MC has been entirely rejected at this stage, a semi-data-driven estimate of this background is made to ensure that this background is correctly taken into account.

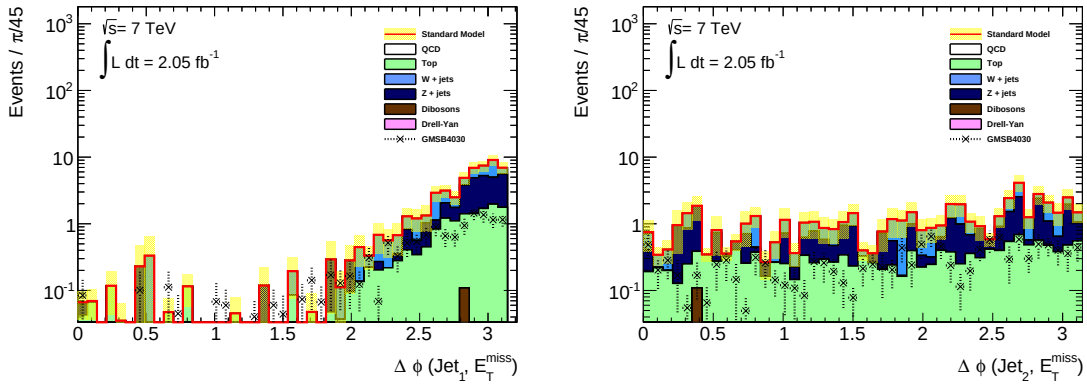

(a) (b)

Figure 5.6: (a) The $\Delta\phi$ between the $E_{\mathrm{T}}^{\mathrm{miss}}$ and the (a) leading and (b) the sub-leading jet after requiring at least two τ-candidates.

For the final signal selection, two quantities characterising the kinematic properties of the event are used to suppress the remaining background processes. These quantities are:

- the effective mass, m_{eff}, formed from the scalar sum of the p_{T} of τ-candidates, the two highest p_{T} jets and the $E_{\mathrm{T}}^{\mathrm{miss}}$ in the event: $m_{\mathrm{eff}} = \sum p_{\mathrm{T}}^{\tau} + \sum_{i=1,2} p_{\mathrm{T}}^{\mathrm{jet_i}} + E_{\mathrm{T}}^{\mathrm{miss}}$
- the sum of the transverse masses, $m_{\mathrm{T}}^{\tau_1} + m_{\mathrm{T}}^{\tau_2}$, formed by $E_{\mathrm{T}}^{\mathrm{miss}}$and the p_{T} of the two τ-candidates, using equation 5.1 for each of the candidates.

These quantities have been studied in detail in order to optimise the signal to background ratio. Using the Asimov approximation of the discovery significance, z_A, a requirement on these two variables is defined by maximising this quantity [149]:

$$z_A \equiv \sqrt{2\left[(N_{\mathrm{Sig}} + N_{\mathrm{BG}})\ln\left(1 + \frac{N_{\mathrm{Sig}}}{N_{\mathrm{BG}}}\right) - N_{\mathrm{Sig}}\right]}\,, \tag{5.3}$$

where N_{Sig} corresponds to the number of signal events for the sample under investigation, and N_{BG} is the sum of all SM background samples. As detailed later in the chapter,

the background estimation procedure calculates scaling factors to correct for any mis-modelling of the data in the simulated samples, and for the optimisation of the analysis the relevant MC scaling factors have been applied, prior to calculating the significance. The background estimation process, from which these scaling factors are derived, is described in section 5.7.3 for top and W+jets events, and section 5.7.2 for multi-jet events. The value of z_A for each of the GMSB points is highly dependent on the cross-section of the signal process, which falls sharply with increasing values of Λ. The shape of the optimisation curves, however, does not vary significantly across the samples, and the values selected are well motivated for the vast majority of the considered parameter space. Less sensitivity is expected in the co-NLSP and $\tilde{\ell}_{\mathrm{R}}$ NLSP regions due to the presence of fewer τ-leptons from $\tilde{\tau}_1$ decays. The quantity z_A reduces to $N_{\mathrm{Sig}}/\sqrt{N_{\mathrm{BG}}}$ if the event yield is high, but provides a better description of the Poisson fluctuations for low event yields.

Figure 5.7(a) shows the distribution of the effective mass for both signal and background, following the $\Delta\phi$ requirement. The background and signal are reasonably well separated, with the SM processes concentrated below about 700 GeV. The m_{eff} distribution tends towards higher values for the signal samples due to the high mass of the squarks and gluinos, which increase with Λ. This variable is scanned in increments of 1 GeV in order to maximise the value of z_A, and the result of this can be seen in figure 5.7(b). The required value is chosen to balance the value of z_A with the inevitable loss in the number of remaining events, and 700 GeV is the start of a plateau region beyond which no significant gain would be made until about 1100 GeV, at which point the event yield would be extremely limited and the statistical uncertainty on the predicted number of signal and background events would be unacceptably large. At this stage of the signal selection the dominant SM backgrounds still consists of Z+jets, W+jets and top production.

For the final signal selection requirement, the sum of the transverse mass of the two τ-candidates is considered. The $Z \to \tau\tau$ events will have a small combined transverse mass value, as the $E_{\mathrm{T}}^{\mathrm{miss}}$ is primarily a result of the neutrinos in the decays of the τ-leptons. For the top and W+jets events a higher $E_{\mathrm{T}}^{\mathrm{miss}}$ is possible due to the additional neutrinos from the decay of the W boson. For the GMSB signal samples, however, the $E_{\mathrm{T}}^{\mathrm{miss}}$ is a result of undetected SUSY particles escaping the detector, resulting in a larger value for the combined transverse mass. The requirement of $m_{\mathrm{T}}^{\tau_1} + m_{\mathrm{T}}^{\tau_2} \geq 80$ GeV is chosen as it provides a reasonable separation between the SM and signal samples, as can be see in figure 5.8. This requirement is most effective at suppressing the background from Z+jets events, and following this requirement the remaining SM backgrounds are primarily from

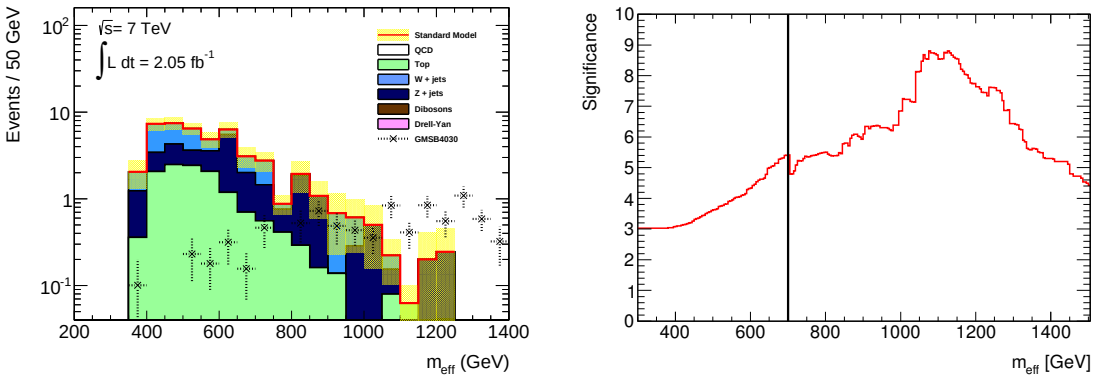

(a) (b)

Figure 5.7: (a) m_{eff} after the $\Delta\phi$ requirment, and (b) a scan of the Asimov significance as a function of the m_{eff} cut for the GMSB4030 benchmark point. The requirement that is placed on the value of m_{eff} is indicated with a black line.

W+jets, Z+jets and top events. Following the application of all of these requirements the region of parameter space selected is identified as the "signal region" (SR). The number of events for the various backgrounds at each stage of the signal selection are listed in table 5.5. The full list of the signal selection requirements is:

- Pre-selection and event cleaning;
- Trigger (data only);
- Trigger plateau requirements ($E_{\text{T}}^{\text{miss}} \geq 130$ GeV and $p_{\text{T}}^{\text{jet1}} \geq 130$ GeV);
- $p_{\text{T}}^{\text{jet2}} \geq 30$ GeV;
- $N_e + N_\mu = 0$;
- $N_\tau \geq 2$;
- $\Delta\phi(E_{\text{T}}^{\text{miss}}, \text{jet}_{1/2}) \geq 0.4$;
- $m_{\text{eff}} \geq 700$ GeV;
- $m_{\text{T}}^{\tau_1} + m_{\text{T}}^{\tau_2} \geq 80$ GeV.

	Total SM MC	Drell-Yan	Dibosons	Multi-jets	Z+jets	W+jets	Top
Pre-selection	$4.56 \cdot 10^9 \pm 3.91 \cdot 10^6$	24134882 ± 20059	19395 ± 56	$4.47 \cdot 10^9 \pm 3.91 \cdot 10^6$	8239809 ± 3228	387522 ± 304	61667097 ± 25114
$E_{\mathrm{T}}^{\mathrm{miss}} > 130\,\mathrm{GeV}$	258903 ± 5956	178 ± 10	436.8 ± 8.4	59750 ± 5897	65427 ± 486	17681 ± 33	115431 ± 682
$p_{\mathrm{T}}^{\mathrm{jet1}} > 130\,\mathrm{GeV}$	174165 ± 4340	115.0 ± 8.4	241.0 ± 6.6	53300 ± 4287	40021 ± 378	9146 ± 25	71342 ± 555
$p_{\mathrm{T}}^{\mathrm{jet2}} > 30\,\mathrm{GeV}$	116967 ± 4280	73.3 ± 5.2	163.0 ± 5.8	51446 ± 4266	18566 ± 258	8700 ± 23	38019 ± 244
Lepton Veto	95534 ± 4258	53.6 ± 4.4	53.4 ± 3.7	49660 ± 4245	18059 ± 258	4376 ± 17	23331 ± 205
$N_\tau \geq 1$	4038 ± 172	2.41 ± 0.81	10.0 ± 1.0	472 ± 162	353 ± 25	690.3 ± 6.3	2511 ± 51
$N_\tau \geq 2$	53.0 ± 6.7	0 ± 0	0.81 ± 0.14	0.034 ± 0.015	19.9 ± 3.3	14.6 ± 3.5	17.6 ± 4.7
$\Delta\phi(E_{\mathrm{T}}^{\mathrm{miss}}, \mathrm{jet1/2}) > 0.4$	46.7 ± 6.2	0 ± 0	0.68 ± 0.13	0 ± 0	16.4 ± 3.0	13.2 ± 3.1	16.4 ± 4.4
$m_{\mathrm{eff}} > 700\,\mathrm{GeV}$	10.2 ± 2.1	0 ± 0	0.193 ± 0.062	0 ± 0	5.6 ± 1.8	1.87 ± 0.49	2.5 ± 1.0
$m_{\mathrm{T}}^{\tau_1} + m_{\mathrm{T}}^{\tau_2} > 80\,\mathrm{GeV}$	5.3 ± 1.3	0 ± 0	0.135 ± 0.054	0 ± 0	1.08 ± 0.70	1.57 ± 0.42	2.5 ± 1.0

Table 5.5: The numbers for the individual MC contribution after each signal selection requirement, scaled to 2.05fb^{-1}. All MC predictions from the $\mathrm{N}_\tau \geq 2$ stage onward have been scaled by the relevant factors obtained in the appropriate control regions. Quoted statistical uncertainties include the statistical uncertainties on the scaling factors

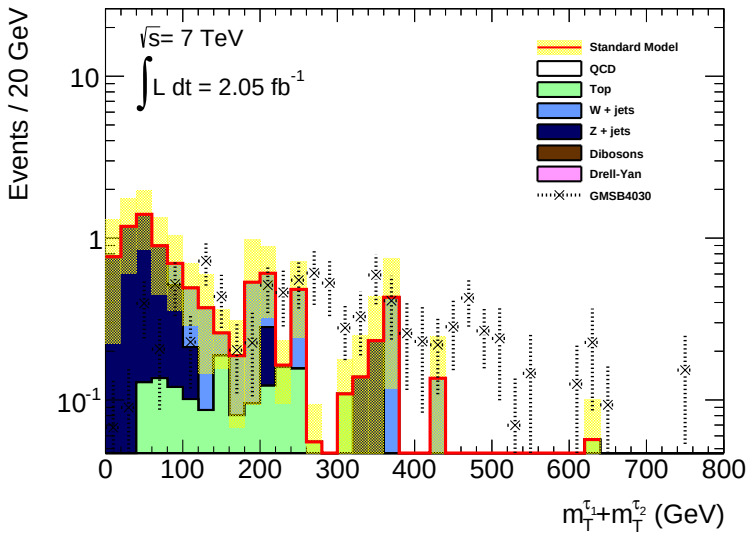

Figure 5.8: The sum of the transverse mass of the two leading τ-candidates after requiring $m_{\text{eff}} > 700$ GeV.

5.7 Background estimation

5.7.1 Introduction

In this section, the semi-data-driven techniques for estimating the background contributions in the signal region are described. After the full event selection has been applied, the backgrounds that dominate in the signal region are due to the production of either top quarks or a W boson that is produced in association with jets, as can be seen in table 5.5. In the majority of these events one of the τ-candidates is found to be a real τ-lepton, and the other is a jet that is misidentified as a τ-lepton. As there are very few true τ-leptons in multi-jet events, a semi-data-driven approach is also performed for this background, even though this has a sub-dominant contribution. The remaining background processes (Z + jets, diboson and Drell-Yan) were found to be either well described by MC due to the presence of two true τ-leptons (such as Z + jets), or only contributing a negligible number of events, and therefore the expected contribution to the signal region was taken from MC.

The process of estimating the backgrounds begins with defining a "control region" (CR), which is a region of the parameter space enriched with events from a single background process. The control regions are defined to be disjoint from the signal region, but with similar kinematic constraints. A normalisation factor is calculated in the CR to scale the number of MC events in this region to the number of observed events in data. This factor can then be used to scale the number of background MC events in the signal region for the final background estimate.

5.7.2 Multi-jet background estimation

The number of real τ-leptons produced in multi-jet events is very small, and the observed multi-jet background events contain jets that have been misidentified as a τ-lepton. As a negligible contribution to the signal region is expected from multi-jet events, a semi-data-driven estimation is made for this background to verify that this is the case.

A multi-jet enhanced control region is defined and the normalisation obtained from this region is used to estimate jet fake rates in the signal region. This control region is dominated by events with large instrumental $E_{\mathrm{T}}^{\mathrm{miss}}$, and is defined by requiring that the $E_{\mathrm{T}}^{\mathrm{miss}}$-vector points in the direction of one of the two leading jets. This is obtained by inverting the $\Delta\phi$ cut between $E_{\mathrm{T}}^{\mathrm{miss}}$ and the two leading p_T jets in the event. In order to further separate the multi-jet control region from the signal region, the m_{eff} requirement

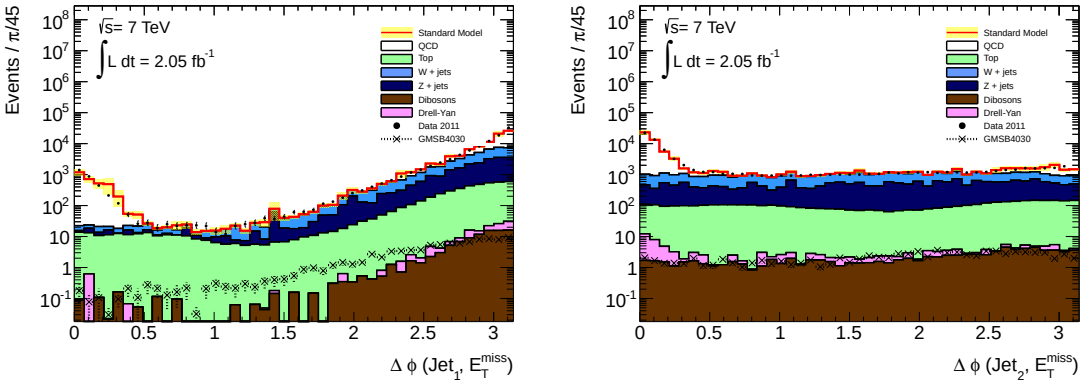

(a) (b)

Figure 5.9: $\Delta\phi(\text{jet}, E_{\text{T}}^{\text{miss}})$ for the (a) leading and (b) sub-leading jet after the lepton veto requirement in the nominal signal selection.

is also inverted, and an additional requirement on the variable $E_{\text{T}}^{\text{miss}}/m_{\text{eff}}$ is introduced. The full list of requirements used to define this control region are:

1. Pre-selection, event cleaning and trigger requirement;
2. $p_{\text{T}}^{\text{jet2}} \geq 30$ GeV;
3. Light lepton veto (no τ-lepton requirement);
4. $\Delta\phi(\text{jet}_1, E_{\text{T}}^{\text{miss}})$ or $\Delta\phi(\text{jet}_2, E_{\text{T}}^{\text{miss}}) < 0.4$;
5. $m_{\text{eff}} < 700$ GeV;
6. $E_{\text{T}}^{\text{miss}}/m_{\text{eff}} < 0.4$.

The distribution of $\Delta\phi$ between the two leading jets and the $E_{\text{T}}^{\text{miss}}$ are shown in figure 5.9 for the SM processes and the ATLAS data, for events surviving all of the signal selection requirements, up to and including the rejection of events containing light leptons. The shape of the two $\Delta\phi$-distributions is well described in MC, and the regions dominated by the the multi-jet contribution are found to satisfy $\Delta\phi < 0.4$.

There are three stages to the multi-jet background estimation process. The first stage is to define an overall scale factor (ω_o) for the normalisation of the multi-jet background, and this is computed from events in the control region where no τ-candidates are identified (*0-τ sideband*). The second stage is to calculate the correction factor, f, to correct for a possible mis-modelling of the jet fake rate in MC. This is computed from events that contain 1 τ-candidate (*1-τ sideband*). These factors can then be used to calculate the scaling factor ω_2, which is applied to the MC contribution in the signal region to estimate the contribution from multi-jet events. Due to the limited number of multi-jet MC events containing a τ-candidate, large fluctuations are observed in the multi-jet distributions in

	Events
$N_{0\tau}^{\text{QCD}}$	23360 ± 3030
$N_{0\tau}^{\text{nonQCD}}$	3710 ± 270
$N_{0\tau}^{\text{data}}$	27570 ± 350

Table 5.6: Number of events in the 0-τ sideband. Uncertainties are statistical only.

the 1-τ sideband. The final stage of the background estimation process is to estimate the shape of the multi-jet contribution in the 1-τ sideband, and reduce the effect of statistical fluctuations.

For the first stage of this process, ω_o is calculated in the 0-τ sideband by normalising the number of events in MC to the number of events in data, after subtracting from this the number of non-multi-jet MC events:

$$\omega_0 = \frac{N_{0\tau}^{\text{data}} - N_{0\tau}^{\text{nonQCD}}}{N_{0\tau}^{\text{QCD}}} \ , \tag{5.4}$$

where $N_{0\tau}^{\text{data}}$ is the number of data events in the 0-τ sideband, $N_{0\tau}^{\text{QCD}}$ is the number of multi-jet events in the sideband, and $N_{0\tau}^{\text{nonQCD}}$ the number of MC events for non-multi-jet processes. These numbers can be found in table 5.6, and ω_0 is found to be 1.02 ± 0.13. The $E_{\text{T}}^{\text{miss}}/m_{\text{eff}}$ distribution after the application of this scale factor to the multi-jet MC can be seen in figure 5.10(a), and a range of kinematic distributions in this sideband can be found in figure 5.12.

The correction factor, f, to take into account the mis-modelling of the jet fake rate in MC, is obtained from the 1-τ sideband. Figure 5.10(b) shows the $E_{\text{T}}^{\text{miss}}/m_{\text{eff}}$ distribution in this region, where the multi-jet contribution has been scaled with ω_0. The value of f is obtained from this region using the equation:

$$f = \frac{N_{1\tau}^{\text{data}} - N_{1\tau}^{\text{nonQCD}}}{\omega_0 \cdot N_{1\tau}^{\text{QCD}}} \tag{5.5}$$

The number of events in the 1-τ sideband used to compute the correction factor are listed in table 5.7, and this factor is found to be 0.46 ± 0.34. This is in good agreement with the scaling factors obtained in a contemporary $H \rightarrow \tau\tau$ analysis [150] and Z$\rightarrow \tau\tau$ analysis [141]. The multi-jet scale factor to be applied to the signal region is then calculated from the product of ω_0 and f^2, which is applied once for each τ-candidate:

$$\omega_2 = \omega_0 \cdot f^2 \tag{5.6}$$

This scaling factor, ω_2, is found to be 0.21 ± 0.22.

	Events
$N_{1\tau}^{\text{QCD}}$	614 ± 465
$N_{1\tau}^{\text{nonQCD}}$	188 ± 37
$N_{1\tau}^{\text{data}}$	471 ± 46

Table 5.7: Number of events in the 1-τ sideband. Uncertainties are statistical only.

Due to the limited event yield in the multi-jet sample after requiring one τ-candidate, statistical fluctuations are seen in the shape of the multi-jet MC distribution, as can be seen in figure 5.10(b). In order to improve the shape of the $E_{\text{T}}^{\text{miss}}/m_{\text{eff}}$ distribution in MC, a higher event yield sample of multi-jet events is created, where the τ-candidate requirement is replaced by selecting a jet which has similar kinematic properties to a real hadronically decaying τ-lepton ("τ-jet"). The kinematic requirements on the τ-jet are:

- $|\eta| < 2.5$
- $p_{\text{T}} > 20$ GeV
- Number of tracks associated to the jet < 7

The shape of the multi-jet contribution to the $E_{\text{T}}^{\text{miss}}/m_{\text{eff}}$ distributions is replaced with the shape from the τ-jet distributions, without altering the event yield. This method is used purely to allow a comparison of the shape of the distributions in data and MC after the scaling factors have been applied, and is not used in the calculation of ω_0 or f. The $E_{\text{T}}^{\text{miss}}/m_{\text{eff}}$ distribution in the 1-τ sideband, after the multi-jet shape change has been applied, can be found in figure 5.11(a). The shape of the distribution is significantly improved with respect to figure 5.10(b), without affecting the overall normalisation. The $E_{\text{T}}^{\text{miss}}/m_{\text{eff}}$ distribution in the 1-τ sideband after the application of ω_o, f and the shape change can be seen in figure 5.11(b), and several kinematic distributions in this region can be seen in figure 5.12.

As the definition of the 0-τ sideband depends on the τ-ID (and is therefore sensitive to the fake rate in MC), there will be a bias introduced into the calculation of ω_0. A conservative upper limit on this fake rate of 10% is taken from the published value of the inverse background efficiency [141], which leads to a bias in the signal region of approximately 15%. This effect is negligible in this analysis as there is no multi-jet MC contribution in the signal region.

In order to confirm that the method of replacing τ-candidates with τ-jets is robust, the kinematics of the selected τ-candidates and τ-jets are compared. Figure 5.13 shows

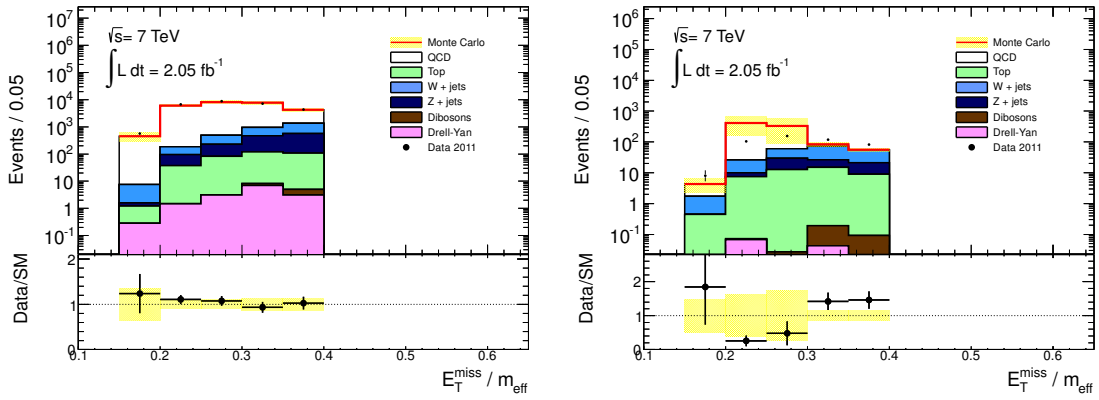

(a) 0-τ sideband (b) 1-τ sideband

Figure 5.10: Distributions of the $E_{\mathrm{T}}^{\mathrm{miss}}/m_{\mathrm{eff}}$ in the multi-jet control regions. The multi-jet contribution in the 1-τ sideband has been scaled with ω_0.

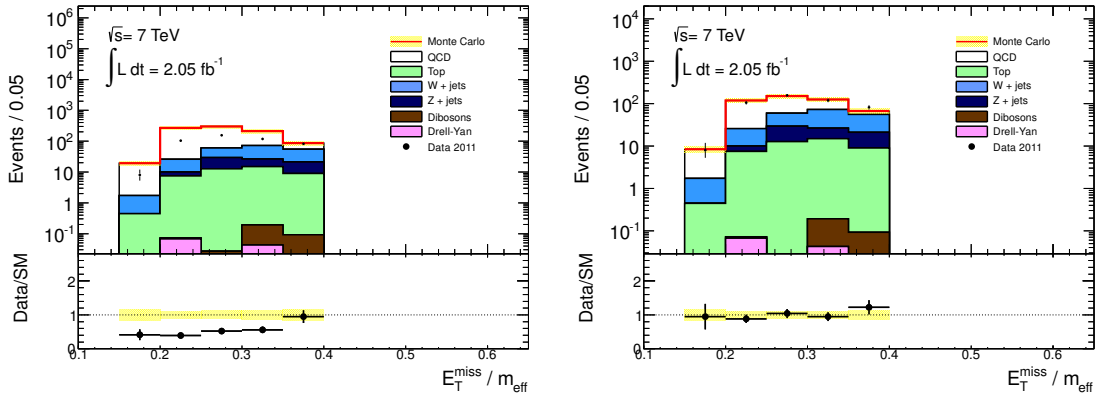

(a) (b)

Figure 5.11: (a) The 1-τ sideband, after the shape of the multi-jet contribution has been changed via the "τ-jet" shape change. (b) 1-τ sideband, after multi-jet correction factor f has been applied. In both plots the multi-jet contribution has been scaled according to the factor obtained from the 0-τ sideband.

the p_{T} and $|\eta|$ distributions for the leading τ-candidate, and leading τ-jet in the multi-jet control region. The τ-jet distributions show a reduction in the fluctuations in the multi-jet MC, with respect to the τ-candidate distributions, and the shapes are comparable. It is also checked that the shape of the 1-τ multi-jet contribution, after the application of the τ-jet shape change, is robust against variation in the number of tracks associated to the τ-jet. Figure 5.14 shows the $E_{\mathrm{T}}^{\mathrm{miss}}/m_{\mathrm{eff}}$ distributions when there are a maximum of 3, 7 or 15 tracks associated to the selected τ-jet. No significant shape changes are observed for the different track selections, and the < 7 track requirement is imposed in this method to ensure these objects are similar to the τ-candidates.

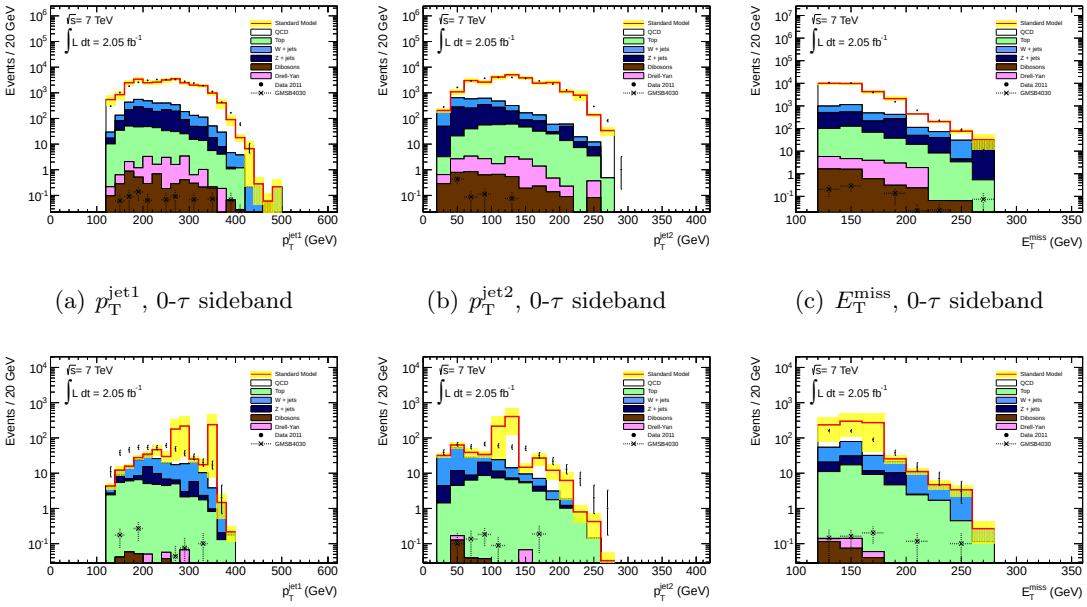

(a) $p_{\mathrm{T}}^{\mathrm{jet1}}$, 0-$\tau$ sideband (b) $p_{\mathrm{T}}^{\mathrm{jet2}}$, 0-$\tau$ sideband (c) $E_{\mathrm{T}}^{\mathrm{miss}}$, 0-$\tau$ sideband

(d) $p_{\mathrm{T}}^{\mathrm{jet1}}$, 1-$\tau$ sideband (e) $p_{\mathrm{T}}^{\mathrm{jet2}}$, 1-$\tau$ sideband (f) $E_{\mathrm{T}}^{\mathrm{miss}}$, 1-$\tau$ sideband

Figure 5.12: Kinematic variables in the 0 and 1-τ sidebands of the multi-jet control region.

The method of replacing a τ-candidate with a τ-jet is also studied under changes to the strength of the chosen τ-ID. The value of ω_0 for both the medium and tight τ-ID is found to be 1.02 ± 0.13, in agreement with the one found for the loose ID. The relevant $E_{\mathrm{T}}^{\mathrm{miss}}/m_{\mathrm{eff}}$ distributions can be seen in figures 5.15(a) and 5.15(b). The jet fake correction factor, f, for the medium ID is found to be 0.53 ± 0.48, and for the tight selection it is 0.28 ± 0.31. These are consistent within the large statistical uncertainties. The value of the scaling factor for the signal region, ω_2, is found to be 0.28 ± 0.51 for the medium ID, and 0.08 ± 0.17 for the tight ID. The scaling and MC correction factors are found to be consistent, within the given statistical uncertainties, and the results for the loose and medium selection are similar. There are considerably less fake τ-candidates with the tight selection, but the event yield is also significantly reduced.

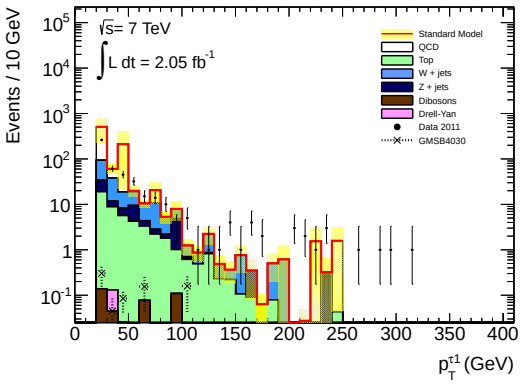

(a) Leading τ p_T

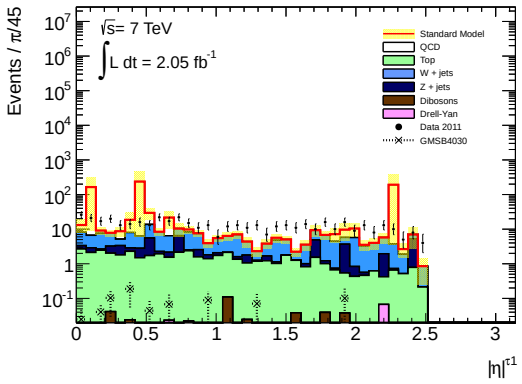

(b) Leading τ η

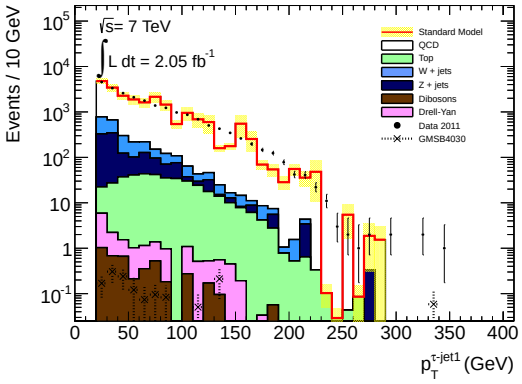

(c) Leading τ-jet p_T

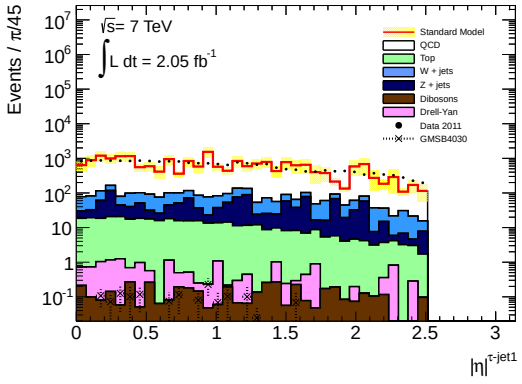

(d) Leading τ-jet η

Figure 5.13: Kinematic variables in the multi-jet control region for the leading τ, and leading τ-jet, used in the shape change procedure.

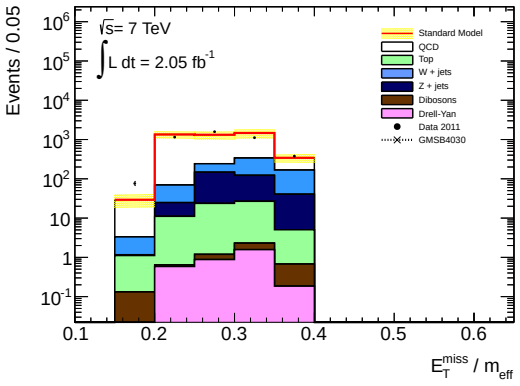

(a) τ-jet with ≤ 3 associated tracks

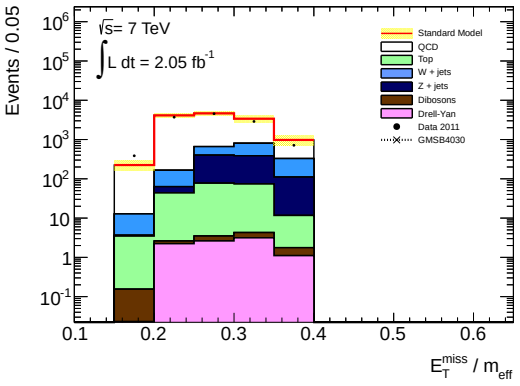

(b) ≤ 7 associated tracks

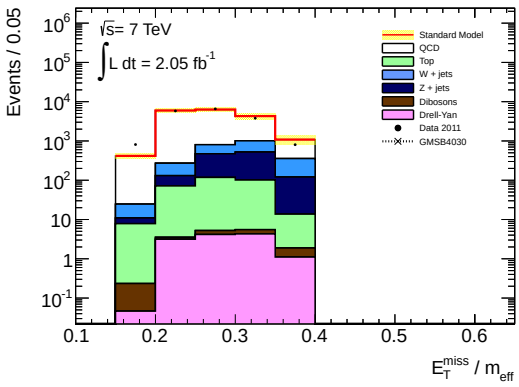

(c) ≤ 15 associated tracks

Figure 5.14: $E_{\mathrm{T}}^{\mathrm{miss}}/m_{\mathrm{eff}}$ for the 0-τ, 1 τ-jet distribution in the multi-jet control region, varying the number of tracks associated to the τ-jet.

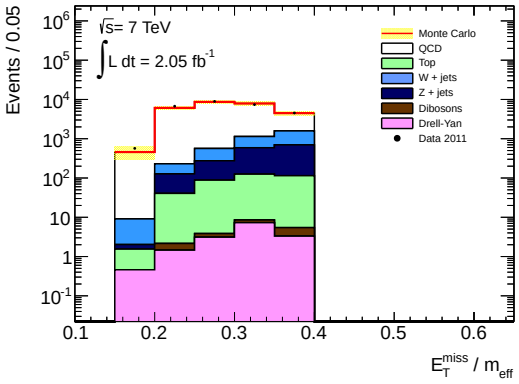

(a) 0-τ sideband, medium τ-ID

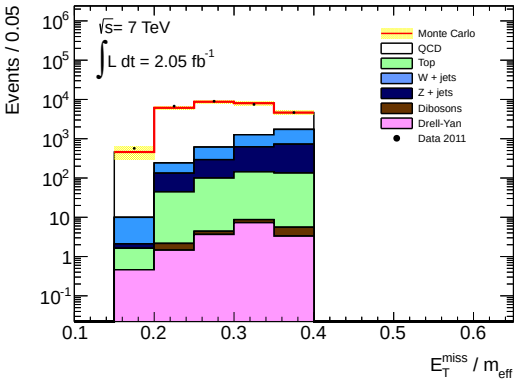

(b) 0-τ sideband, tight τ-ID

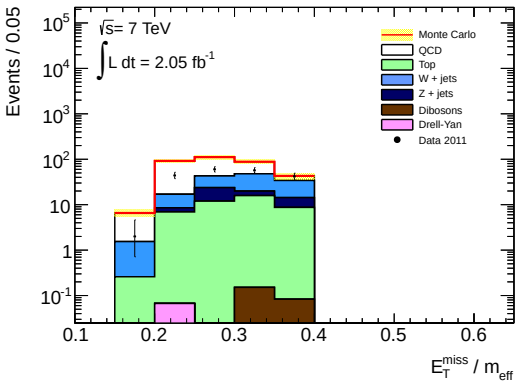

(c) 1-τ sideband, medium τ-ID

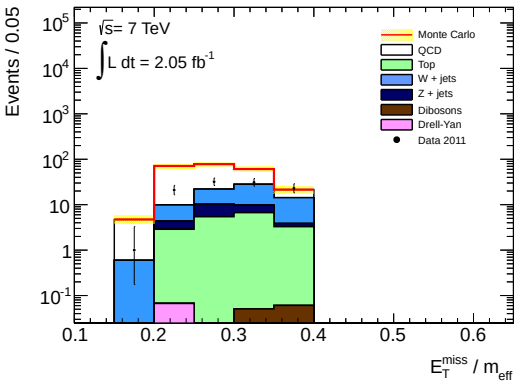

(d) 1-τ sideband, tight τ-ID

Figure 5.15: $E_{\mathrm{T}}^{\mathrm{miss}}/m_{\mathrm{eff}}$ for the 0- and 1-τ sidebands, requiring either medium (left) or tight (right) τ-ID

5.7.3 W+jets and top background estimation

The estimation of the W and top background has been carried out in collaboration with other members of ATLAS. For this section I have reproduced some of their plots that were not published as part of the paper detailing this analyis [146].

The CR used to estimate the W and top background normalisation is defined by inverting the 700 GeV m_{eff} requirement used for the signal region, whilst keeping all of the other signal selection cuts as previously described. The top contribution is dominated by $t\bar{t}$ production, but there is a non-negligible contribution from single top quark production. For the sake of estimating this background, these processes are both combined and referred to as *top* events. The m_{eff} distribution in this control region can be seen in figure 5.16(a), and the contribution to this region from each of the individual background samples can be found in table 5.8.

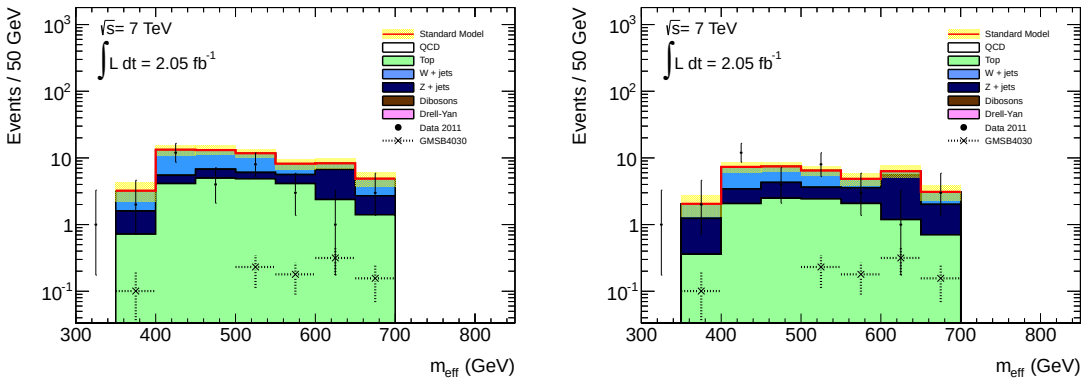

(a) unscaled m_{eff} (b) scaled m_{eff}

Figure 5.16: The effective mass distribution in the combined W+jets and top control region, (a) unscaled and (b) with the computed normalisation factor applied.

There is only a small contamination from Z+jets in this CR, and little to no contribution from diboson production, Drell-Yan or multi-jet events. A comparison of the number of events in data and simulation in this control region reveals that the MC overestimates the number of events observed in the data.

The normalisation factor to be applied to the MC prediction in the signal region (f_{Wtop}) is calculated with the following equation:

$$f_{\text{Wtop}} = \frac{N_{\text{Wtop}}^{\text{data}} - N_{\text{Wtop}}^{\text{otherMC}}}{N_{\text{Wtop}}^{\text{topMC}} + N_{\text{Wtop}}^{\text{WMC}}} \ , \tag{5.7}$$

where $N_{\text{Wtop}}^{\text{data}}$ represents the number of events observed in data in the CR, $N_{\text{Wtop}}^{\text{top}(W)\text{MC}}$ represents the number of top (W) MC events in the same region, and $N_{\text{Wtop}}^{\text{otherMC}}$ represents

	Number of events
Data	25
Diboson	0.27 ± 0.08
Drell-Yan	0
Multi-jet	0
Top	21.19 ± 1.01
W+jets	24.88 ± 3.65
Z+jets	1.59 ± 0.85

Table 5.8: Number of data and MC events per background channel observed in the control region. No normalisation factor has been applied to the MC and the uncertainties are statistical only.

the small contribution from diboson, Drell-Yan and multi-jet MC events. The value of f_{Wtop} is found to be 0.50 ± 0.12. The expected contribution from W+jets and top events to the signal region, $N_{SR}^{\text{Wtop,predicted}}$, is subject to statistical uncertainties from both the limited number of events in data and in MC. The uncertainty on the number of MC events is taken from the event yield and the data are assumed to be Poisson distributed. All of these uncertainties are propagated using uncorrelated Gaussian error propagation, and the result is taken as the statistical uncertainty on the estimated background.

After the MC normalisation factor has been applied to the distributions in the CR, the agreement between data and MC is significantly improved, as can be seen in the m_{eff} distribution in figure 5.16(b). Some discrepancy still remains, despite the data and MC agreeing within the statistical uncertainties, and in order to attempt to identify the source of this discrepancy the individual components that enter the effective mass calculation are studied. These kinematic distributions for the control region can be seen in figure 5.17. Reasonable agreement is observed between data and MC in the jet p_{T} distributions, although fluctuations due to the limited event yield are seen in the distributions associated to the τ-candidates and the $E_{\text{T}}^{\text{miss}}$. This is not considered to be a problem for the calculated value of f_{Wtop} because this factor makes no use of the shape information.

In order to further investigate this control region an attempt is made to separate the W+jets contribution from the top contribution. The ability of the ATLAS detector to identify jets that originated from b-quarks is used in order to distinguish between these two classes of events, as top events will usually contain at least one identified b-jet. This control region is therefore further divided, based on the b-jet multiplicity: events that are

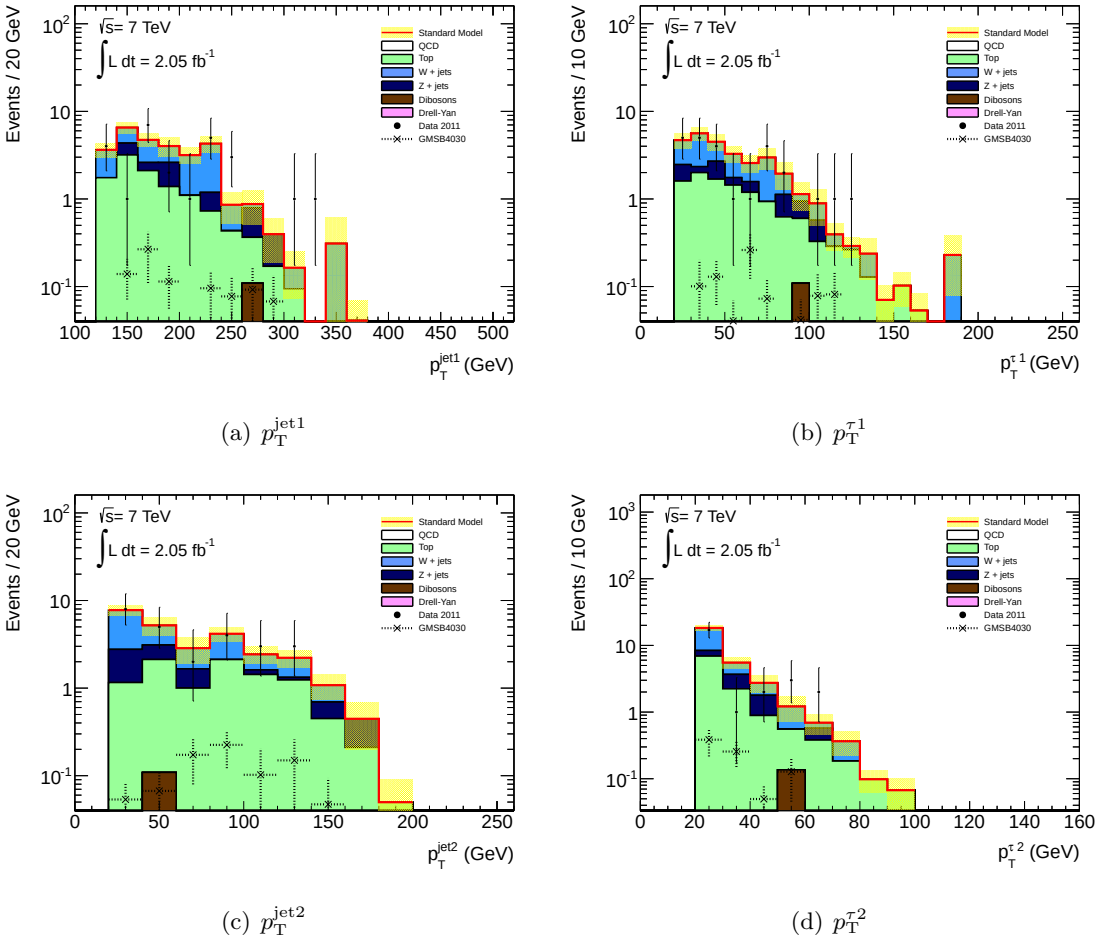

(a) $p_{\mathrm{T}}^{\mathrm{jet1}}$ (b) $p_{\mathrm{T}}^{\tau 1}$

(c) $p_{\mathrm{T}}^{\mathrm{jet2}}$ (d) $p_{\mathrm{T}}^{\tau 2}$

Figure 5.17: Distribution of the (a) leading and (c) sub-leading jet p_{T} and the leading (b) and sub-leading (d) τ-candidate p_{T}, in the W+jets top control region. The appropriate normalisation factors are applied to all distributions.

found to have at least one tagged b-jet define the top control region, and those without b-jets define the W+jets control region. Figure 5.18(a) shows the b-jet multiplicity in the combined W+jets and top region.

Once the separate control regions are defined, the process of calculating the normalisation factor is repeated individually in these regions. The m_{eff} distribution in these two regions before and after the individual normalisation factors have been applied can be seen in figures 5.18(b), 5.18(c), 5.18(d) and 5.18(e). The top control region exhibits a high level of purity and, despite the limited event yield, good agreement is observed between data and MC. The W+jets enriched region does not show the same level of purity and there is a non-negligible contribution from top production. For this region the top contribution in the W+jets control region is scaled with the normalisation factor obtained in the top

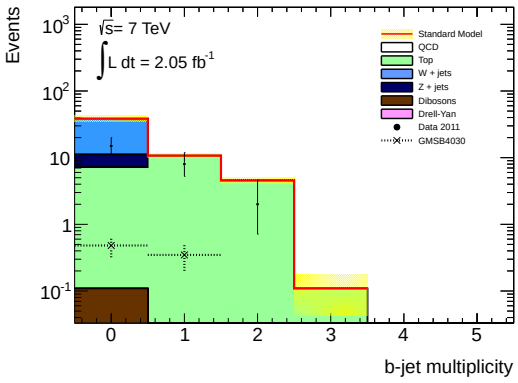

(a) N_{bjets} in W/top CR unscaled

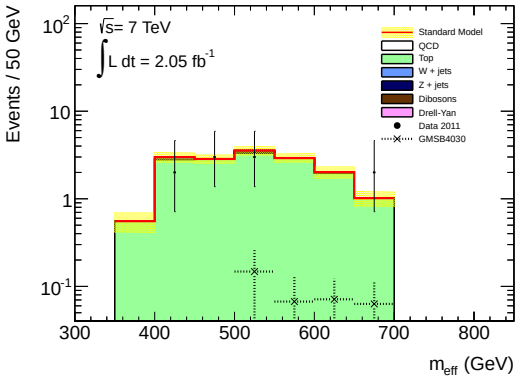

(b) Top CR: unscaled

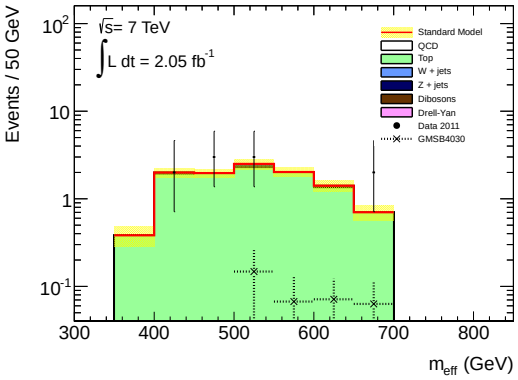

(c) Top CR: scaled

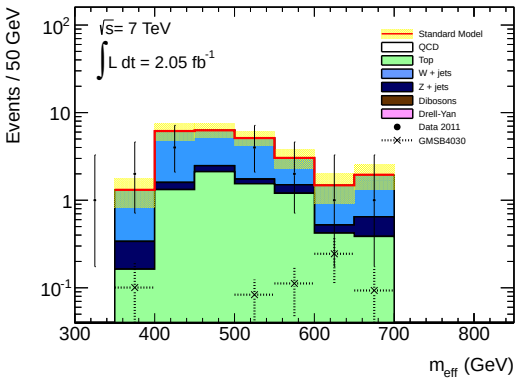

(d) W CR: unscaled

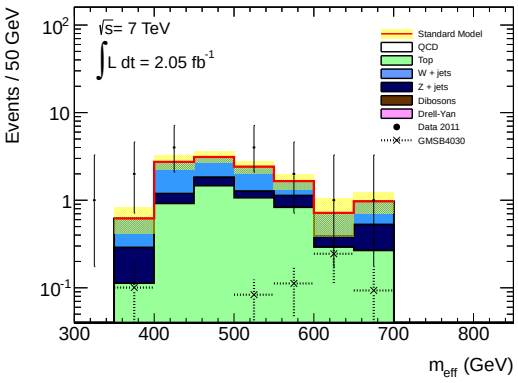

(e) W CR: scaled

Figure 5.18: (a) The number of b-jets prior to separating the W and top control regions, and (b)-(d) the m_{eff} distribution in the separate W and top control regions, shown with and without the respective scale factors applied.

	$\text{Data}^{\text{corr}}$	MC	Normalisation Factor	Rel. stat. uncert.
W+top control region	23±5	46.10±3.80	0.50±0.12	24%
Top control region	10±3	14.46±0.81	0.69±0.22	32%
W control region	8 ±3	24.83±3.65	0.34±0.16	47%

Table 5.9: Number of observed and expected events, and resulting normalisation factors, for the combined and separate control regions. $\text{Data}^{\text{corr}}$ is the number of observed data events minus the number of MC events from background channels not under study in the respective control region.

CR, before the W+jets normalisation factor is calculated:

$$f_W = \frac{N_{CRW}^{\text{data}} - f_{top} \cdot N_{CRW}^{\text{top}} - N_{CRW}^{\text{nonW,nontop}}}{N_{CRW}^{W}} \tag{5.8}$$

A summary of the scale factors in each of the three regions, along with the number of events from which they were calculated, can be found in table 5.9. The normalisation factors are consistent across the three regions, within the quoted statistical uncertainties, and are also consistent with contemporary measurements in the $H \to \tau\tau$ analysis [150].

Once the scale factors have been calculated the contribution from each of these backgrounds to the signal region can be estimated, and these can be found in table 5.10. For the other background processes (Z+jets, diboson and Drell-Yan production) the values presented in this table are obtained directly from MC.

	Expected SM background	Relative uncertainty
Without normalisation	$9.46 \pm 1.81^{\text{stat}}$	19.1%
Combined normalisation	$5.31 \pm 1.29^{\text{stat}}$	24.3%
Separate normalisation	$5.14 \pm 2.18^{\text{stat}}$	42.5%

Table 5.10: Number of events expected for the signal region with and without normalisation.

Both of the approaches to the calculation of the normalisation factor yield results that are consistent with each other, within the quoted statistical uncertainties. For the final background estimation the normalisation obtained in the combined W/top CR is used, due to the smaller relative statistical uncertainty. The variation between the scale factors calculated in the combined region and the separated regions is taken as an additional 30% systematic uncertainty on the W and top normalisation.

In order to ensure that the scale factors are not affected by signal contamination in

the control region, the signal contribution from each of the GMSB MC samples is checked in all three control regions. In the region of the GMSB parameter space where the 95% CL exclusion limit is expected (in the case of no observed signal in data), the signal contribution to the CR is around 1–2%, and therefore considered as negligible. In the region of low Λ and $\tan\beta$, the contribution is found to be more significant, as can be seen in figure 5.19, but this region of parameter space has been independently excluded by other experiments, so this is not a concern for this analysis.

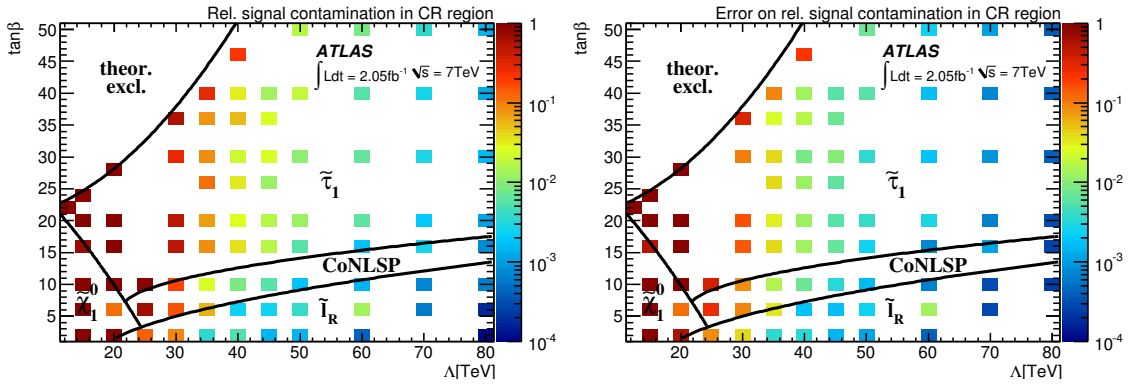

(a) Ratio of signal events to background events

(b) Statistical error on this ratio

Figure 5.19: (a) The ratio of the number of signal events to the number of background events in the combined W and top CR and (b) the statistical error on this ratio [146].

In order to ensure that the normalisation factors are safe to apply in the signal region, it is necessary to verify that the composition of true and fake τ-candidates is similar in the SR and CR. As the normalisation factor is highly dependant on the mis-modelling of the τ fake rate, any variation in the composition across the two regions will result in the MC in the SR being scaled incorrectly. Figure 5.20 shows the fraction of events containing true hadronically decaying τ-leptons in the signal and the W/top control region. The signal region and the combined control region are both dominated by events containing one true τ-lepton ($\approx$75%). Also shown in the figure is the fraction of events containing true hadronically decaying τ-leptons that are matched to reconstructed τ-candidates in the two regions. The similarity of the two distributions shows that the reconstructed τ-candidates almost always correspond to the presence of true τ-leptons in the event.

In order to validate the scale factors against changing the kinematic constraints, the requirement on $p_{\mathrm{T}}^{\mathrm{jet2}}$ is raised from 30 to 50 GeV, and the background estimation process is repeated. The results of this procedure can be seen in table 5.11. The combined normalisation factor calculated from the W+jets and top control region is stable with respect to this change, although changes are seen for the scale factors calculated in the

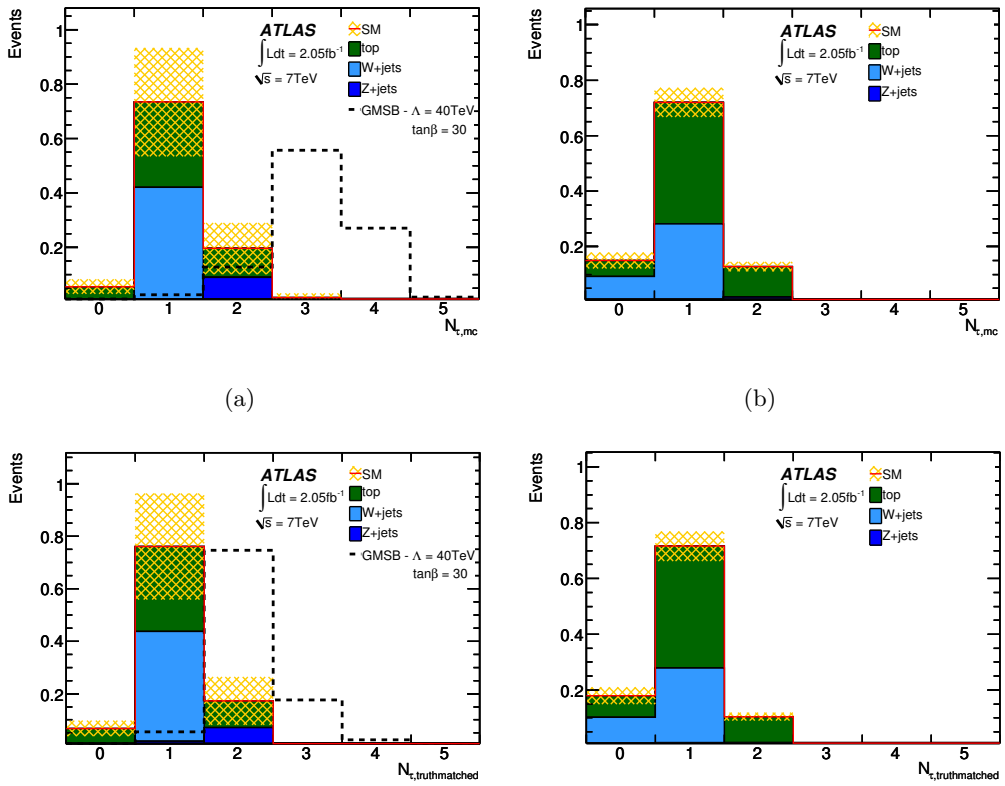

Figure 5.20: (a) The fraction of events containing true hadronically decaying τ-leptons in the signal and (b) the W/top control region. (c) The fraction of events containing true hadronically decaying τ-leptons matched to reconstructed τ-candidates in the SR and (d) the W/top CR. The yellow band corresponds to the statistical uncertainty.

separate control regions. This is primarily due to the increased statistical uncertainty due to the raised p_{T} requirement, and the new values are consistent with the nominal scale factors, within the large associated uncertainties.

Further studies are performed to check the effect of changing the strength of the ID requirement for the τ-candidates. The nominal selection for this analysis is the "loose" BDT ID, and a range of combinations are explored, including tightening the ID for only the leading τ, or both τ-candidates simultaneously. There is no significant difference observed in the nominal value of the calculated scale factors for the different ID strengths, although the statistical uncertainties are increased due to a more limited event yield.

Control Region	Nominal Selection	$p_{\mathrm{T}}^{\mathrm{jet2}} > 50$ GeV
W/top	0.50±0.12	0.55±0.14
top	0.69±0.22	0.76±0.26
W	0.34±0.16	0.27±0.22

Table 5.11: Normalisation factors and their respective statistical uncertainty obtained for the different control regions when increasing the requirement on the $p_{\mathrm{T}}^{\mathrm{jet2}}$.

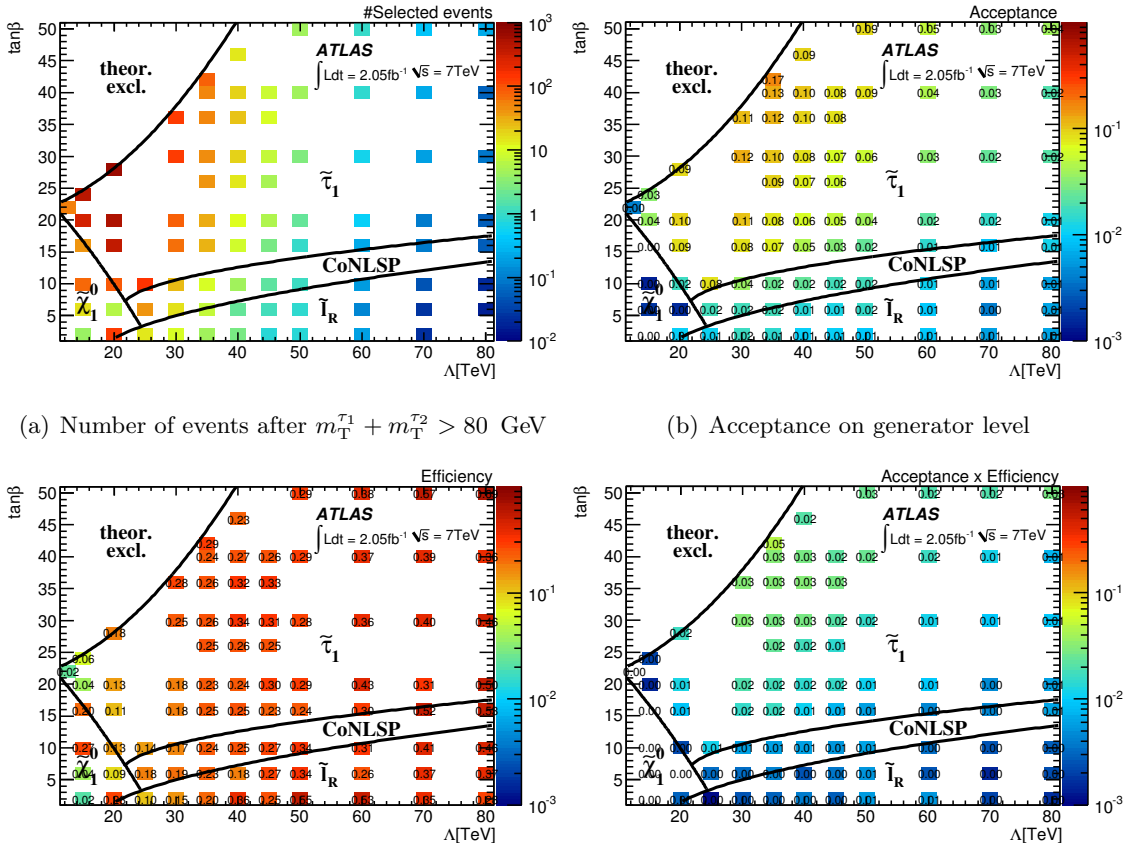

(a) Number of events after $m_{\mathrm{T}}^{\tau 1} + m_{\mathrm{T}}^{\tau 2} > 80$ GeV

(b) Acceptance on generator level

(c) Signal selection efficiency after $m_{\mathrm{T}}^{\tau 1} + m_{\mathrm{T}}^{\tau 2} > 80$ GeV

(d) Acceptance and efficiency folded

Figure 5.21: (a) The number of events and (b) the acceptance of the event selection on generator level, (c) the signal selection efficiency, and (d) the acceptance and the efficiency folded in the GMSB grid after the final selection cut [146].

5.7.4 Signal Efficiency

Several studies are performed to check the signal efficiency of the full selection requirements across the GMSB grid. Figure 5.21(a) shows the number of expected signal events across the Λ–$\tan\beta$ plane, after all of the signal selection requirements have been applied. The expected number of events in the signal region decreases as Λ increases, due to the significant dependence of the GMSB production cross-section on Λ. Also shown in figure 5.21 is the acceptance of the signal selection at generator level, the selection efficiency at the detector level and the combination of these two. In regions of low $\tan\beta$ the expected sensitivity of the analysis decreases, due to the fact that there are more SUSY particles decaying through a $\tilde{\ell}_{\mathrm{R}}$ NLSP. This results in more events containing light leptons in the final state, and subsequently being rejected by the signal selection requirements. The efficiency is relatively constant over the entire grid except for very low values of Λ, due to

the lower squark masses and therefore the lower p_{T} of the leading jets. Many of the events in the region with very low Λ and $\tan\beta$ will fail to pass the trigger plateau requirements. This region corresponds to the NLSP being a $\tilde{\chi}_1^0$, and therefore there are also fewer events containing τ-leptons in the final state. The selection efficiency is highest ($\approx 3\%$) for high $\tan\beta$ and lower Λ values, including in the region of the GMSB4030 reference point. It drops to 0.2% in the non-$\tilde{\tau}_1$ NLSP regions and for high Λ values. This is primarily a consequence of the rejection of events containing a light lepton and the requirement of two hadronically decaying τ-leptons, respectively.

5.8 Systematic uncertainties

There are a wide range of systematic uncertainties that affect the variables used in this analysis, and therefore affect the estimates of the background and signal yields. To calculate the effect of a systematic uncertainty on a given variable, this is modified in MC so as to deviate from its nominal value by the size of its systematic uncertainty, for which the value is provided by the relevant ATLAS combined performance group. The entire signal selection process is then repeated and any change in the result with respect to the nominal selection is taken as a systematic uncertainty. The same procedure is performed for the estimation of the MC normalisation factors obtained in the data-driven estimation of the SM backgrounds. The full list of the systematic uncertainties considered is:

- jet and τ energy scale
- jet and τ energy resolution
- $E_{\mathrm{T}}^{\mathrm{miss}}$calculation
- influence of event pile-up
- τ reconstruction efficiency
- τ fake rate
- signal and background MC predictions and cross-sections
- luminosity

In the following, a detailed description is given of the individual components and their treatment to obtain quantified systematic uncertainties.

5.8.1 Jet energy scale

The systematic uncertainty in the jet energy measurement is due to the fact that the relation between the energy measurement made in the detector and the corresponding true

jet energy is not known precisely. This jet energy scale (JES) uncertainty is dependent on the p_{T} and η of the jet, so its value is parameterised as a function of these variables [151]. Studies performed by the ATLAS Jet/Etmiss Combined Performance group compared the results from the nominal MC samples to those with different hadronic shower and physics models, alternative detector configurations, and the jet response as function of η [151], in both data and MC. The JES uncertainty in the central calorimeter region ($|\eta| < 0.8$) is lower than 2.5% for jets with $60 < p_{\mathrm{T}} < 800\,\mathrm{GeV}$, and less than 4.6% for the full p_{T} range ($p_{\mathrm{T}} > 20\,\mathrm{GeV}$). In the end-cap ($0.8 < |\eta| < 2.8$) and forward ($2.8 < |\eta| < 4.5$) regions, the uncertainty for jets with $p_{\mathrm{T}} > 50\,\mathrm{GeV}$ is below 4% and 6% respectively. The uncertainty is the largest for jets in the range $20 < p_{\mathrm{T}} < 30\,\mathrm{GeV}$ in the very forward region $3.2 < |\eta| < 4.5$ where it amounts to 14% [151]. The results of this study are used to define an analysis tool, known as `JESUncertaintyProvider` [152], which is employed to rescale the energies of all jets by this systematic uncertainty. Changes in the jet energies are then propagated to the variables used in the analysis, and the entire signal selection is repeated on both data and MC, to obtain new values for the event yields. The correction to the JES is applied once in the positive direction, scaling relevant quantities up, and once in the negative direction, scaling these quantities down. The difference between the final background estimation obtained with the nominal signal selection, and that after applying the JES uncertainty, is taken as the systematic uncertainty from the JES for the analysis.

5.8.2 Jet energy resolution

Within the GEANT4 detector simulation the jet energy resolution (JER) is only simulated with finite precision. The agreement between the JER in data and MC has been studied using the spread of the p_{T} imbalance in di-jet events [153] and with different in-situ techniques [154], with deviations having been found to be of the order of 10%. The jet resolution and its uncertainty are provided in bins of p_{T} and η and, as with the JES, the modified jet energies are propagated to the variables used in the signal selection. The difference between the nominal selection and the selection after modifying the JER by its uncertainty is taken as the systematic uncertainty.

5.8.3 τ energy scale

The origin of the systematic uncertainty on the τ energy scale (TES) is similar to the JES systematic discussed previously. The effect of this uncertainty is studied by the ATLAS

Tau Combined Performance group using MC samples in which the parameters affecting the τ energy reconstruction are varied and the effect on the energy scale analysed [141]. Some of these parameters are the MC event generator and underlying event model; the hadronic shower model; the amount of detector material; the electromagnetic energy scale; the topological clustering noise thresholds; and the event pile-up. The resulting uncertainty is dependent on the p_{T}, η, and the number of charged tracks associated to the τ-candidate, and it ranges from 3.5% up to 9.5% [141]. As with the JES and JER, the difference between the nominal selection and the selection after varying the TES is taken as the systematic uncertainty.

5.8.4 Missing transverse energy

The calculation of the $E_{\mathrm{T}}^{\mathrm{miss}}$ takes the objects in the event as input variables and is therefore sensitive to a large range of systematic uncertainties. Variations in the jet or τ energies are propagated to the $E_{\mathrm{T}}^{\mathrm{miss}}$ calculation, and the resulting systematic uncertainty is evaluated as in the previous cases.

5.8.5 Event pile-up

When the MC is re-weighted in order to reproduce the pile-up conditions in data, the overall number of events in each sample changes slightly due to a very small number of events ending up with an event weight of zero when reproducing the tails of the pile-up distribution. This effect has been examined and, although found to be smaller than 0.5%, a correction is applied to each MC sample. The effect of the pile-up re-weighting also depends on the model assumed for the determination of the pile-up conditions in the data. The nominal selection makes use of a measurement that averages the mean number of interactions per bunch crossing in the LHC over a period of 60 seconds, for data recorded in 2011, and uses this number as an input for the re-weighting. An alternative approach, in which the mean number of interactions for each bunch crossing is determined on an individual event basis, results in a slightly different distribution when combined for the entire dataset. The relative deviations between the two methods is taken as the size of the systematic uncertainty related to the pile-up uncertainty.

5.8.6 τ identification efficiency

The ATLAS Tau Combined Performance group has also studied the effect of systematic uncertainties on the τ-ID efficiency and fake rate [141]. These uncertainties are dependent

on both the particular τ-ID algorithm that is used, as well as the kinematics of the τ-candidate, and the number of associated tracks. In order to quantify these uncertainties two studies have been performed, one using $Z \rightarrow \tau\tau$ events and one using $W \rightarrow \tau\nu$ events [141]. The relative uncertainty on the τ-ID is calculated to be 4.3% [141], whilst for the probability a jet will be misidentified as a τ-lepton, a statistical uncertainty of 9.4% has been determined and is taken as the misidentification uncertainty [141]. In order to quantify the effect of the systematic uncertainty associated to the τ-ID efficiency, the MC samples are re-weighted in both the positive and negative direction, to simulate the changes of the the τ-ID efficiency by the reported values. This re-weighting is only applied to true τ candidates. The systematic effect on the τ fake rate is taken into account by re-weighting the MC events by the given systematic uncertainty, and this procedure is only applied to τ-candidates not matched to a real τ-lepton.

5.8.7 Luminosity

The systematic uncertainty on the integrated luminosity is dependent on the total uncertainty of the luminosity measurement in ATLAS, and details are provided by the Luminosity Working Group. For the first 2.05fb^{-1} of the 2011 data this uncertainty is determined to be 3.7% [86, 87].

5.8.8 Theory uncertainties on the signal cross-section predictions

There are three sources of uncertainty that contribute to the overall theory uncertainty. These are the uncertainties on the PDF, the strong coupling constant and the factorisation and renormalisation scales used in the generation of the MC. The dominant uncertainties are due to the PDF and the scale ($\approx 10\%$), with the uncertainty due to the strong coupling constant considerably smaller ($\approx 1\%$). The combined theory uncertainty, shown in figure 5.28(b), is relatively constant at around 15% across the GMSB parameter space.

PDF

The uncertainties associated to the PDF are represented by 22 sets of eigenvectors, which were used in the PDF global fit. The 44 error PDF sets included in the CTEQ6.6m are the 90% CL upper and lower bound variations of the PDF with respect to each of the eigenvectors. The uncertainty can be evaluated by the Hessian method [155], which takes the envelope of the deviations from the central value with these uncertainties. This is

defined as the maximum positive and negative errors on the observable X by,

$$\begin{aligned} \triangle X_+ &= \frac{1}{1.645}\sqrt{\sum_{i=1}^{22}\left(max[(X_i^+ - X_0),(X_i^- - X_0),0]\right)^2}, \\ \triangle X_- &= \frac{1}{1.645}\sqrt{\sum_{i=1}^{22}\left(max[(X_0 - X_i^+),(X_0 - X_i^-),0]\right)^2}, \end{aligned}$$

where X_i^+, X_i^-, X_0 are the upper, lower and nominal values of the eigenvector X_i. The factor 1.645 is used to convert the 90% CL uncertainty to 68% CL (1σ) one. The total PDF uncertainty is obtained by averaging $\triangle X_+$ and $\triangle X_-$.

Strong coupling constant

For the strong coupling constant α_s, the associated theoretical uncertainties are represented by two extreme CTEQ6.6AS variations, known as "AS-2" and "AS+2". The actual uncertainty is estimated as half of the difference between the cross-sections calculated using both PDFs:

$$\Delta\sigma(\alpha_s) = \frac{1}{2}\frac{1}{1.645}\left|\sigma[AS-2] - \sigma[AS+2]\right|,$$

where σ is the NLO cross-section using the specified PDF. The factor 1.645 is used to convert the 90% CL uncertainty to 68% CL (1σ) one.

Scale

In order to quantify the uncertainty on the scale, the factorisation and renormalisation scales are changed by factor of 2 or 1/2 in the `PROSPINO` calculations. The nominal scale is found from $Q = m_{\widetilde{p}}$, which is a solo scale factor in the process used. These uncertainties are estimated by comparing `PROSPINO` NLO cross-section values obtained with or without the scale variations included.

Combination

Calculating the uncertainty on α_s with the CTEQ6.6AS variations ensures an independent treatment of the α_s and PDF uncertainties, although some correlation between the α_s and PDF parameters could potentially still exist. Therefore, when combining the PDF and α_s uncertainties the recommendations from [156] are followed. The scale uncertainty is then added in quadrature.

Systematic Variation	Diboson		Z+jets		W+jets / Top	
	Events	Rel. Deviation	Events	Rel. Deviation	Events	Rel. Deviation
Nominal	0.135		1.08		4.09	
Theory	0.135	0.0%	1.08	0.0%	4.93	20.6%
Scaling	0.135	0.0%	1.08	0.0%	5.32	30.0%
JER	0.136	0.1%	1.08	0.0%	3.13	-24.0%
JES	0.147	8.5%	1.51	39.3%	5.59	13.2%
Pile-up	0.146	7.6%	1.09	1.3%	4.11	-0.1%
τ-ID	0.145	7.1%	1.17	7.9%	4.13	0.2%
τ fake rate	0.140	3.6%	1.10	1.9%	4.04	-1.9%
TES	0.145	6.7%	1.28	18.0%	5.64	6.3%
Luminosity	0.140	3.7%	1.12	3.7%	4.09	0.0%
Total		19.1%		58.0%		47.8%

Table 5.12: Effect of the systematic variations, studied for all separate background channels with non-zero contributions to the SR, after the full event selection.

5.8.9 Theoretical uncertainties on the transfer factor

The theoretical uncertainty on the extrapolation from the control region to the signal region for the W and top background estimates is obtained by using alternative MC samples with the same generator, but varied renormalisation and factorisation scales, along with the functional form of the factorisation scale, and the matching threshold in the parton shower process. This is studied in detail by a contemporary ATLAS SUSY search, which focuses on final states containing a single light lepton, described in [157]. The methods and data from this single lepton search are used in this analysis to estimate the theoretical uncertainty on the extrapolation of the MC normalisation factors from the W/top control region to the signal region, with some minor changes. The data files that are used do not include τ-leptons, so the selection instead requires one muon and one jet, in order to represent one true τ-candidate and one fake τ-candidate. An uncorrelated worst-case combination is performed for the different scale variations studied, whilst the uncertainties for the two background channels are combined in a fully correlated fashion.

5.8.10 Summary of the systematic uncertainties

The systematic uncertainties on each of the seperate backgrounds that contribute to the signal region can be found in table 5.12. In order to calculate the total systematic uncertainty on the final SM background prediction in the signal region, all of these backgrounds are combined, and the result can be found in table 5.13, with the relative uncertainty with respect to the nominal value. For this calculation all variations due to individual systematics have been combined, with correlations taken into account where appropriate. The

Systematic Variation	Number of events	Relative deviation
Nominal	5.31	
Theory	6.15	15.9%
Scaling	6.53	23.1%
JER	4.34	-18.1%
JES	6.24	17.6%
Pile-up	5.35	0.9%
τ-ID	5.44	2.5%
τ fake rate	5.28	-0.5%
TES	5.65	6.6%
Luminosity	5.35	0.8%
Total		41.4%

Table 5.13: Effect of the systematic variations studied for all backgrounds combined after the full event selection.

JES and TES show asymmetries between the "up" and "down" variations (which correspond to varying the relevant values with the systematic uncertainty in either the positive or negative direction, respectively), so the average value is used. The averaged values are shown in tables 5.12 and 5.13. The JES and TES are considered to be fully correlated when combined because both are susceptible to mismeasurements in the calorimeter and biased calibrations, but the remaining systematics are combined uncorrelated, as can be seen in equation 5.10.

$$\sigma_{\text{JES/TES}} = \frac{|\sigma_{\text{JES up}}| + |\sigma_{\text{TES down}}|}{2} + \frac{|\sigma_{\text{TES up}}| + |\sigma_{\text{JES down}}|}{2} \,, \tag{5.9}$$

$$\sigma^{\text{Tot}}_{\text{Syst}} = \sqrt{\sigma^2_{\text{Scaling}} + \sigma^2_{\text{JER}} + \sigma^2_{\text{TauID}} + \sigma^2_{\text{TauFake}} + \sigma^2_{\text{Pileup}} + \sigma^2_{\text{Lumi}} + \sigma^2_{\text{JES/TES}}} \tag{5.10}$$

5.9 Analysis results

After the full signal selection has been applied, 3 data events are observed in the signal region, which is in good agreement with the expected SM background of $5.3 \pm 1.3^{\text{stat}} \pm 2.2^{\text{syst}}$ events. The expected contribution to the signal region from each of the SM background processes can be found in table 5.14. Table 5.15 shows the number of events in the data, the expected SM contribution and the expected GMSB contribution, for each stage of the signal selection process. The agreement between data and MC at various stages of this signal selection can be found in figures 5.22, 5.23, 5.24. An event display for one of the three signal events can be found in figure 5.32.

	Expected SR contribution
Drell-Yan	0
Dibosons	$0.135 \pm 0.054 \pm 0.026$
Multi-jets	$0 \pm 0 \pm 0.0012$
Z+jets	$1.08 \pm 0.70 \pm 0.63$
W+jets	$1.57 \pm 0.42 \pm 0.75$
Top	$2.5 \pm 1.0 \pm 1.2$
Full SM	$5.3 \pm 1.3 \pm 2.2$

Table 5.14: A summary of the expected number of events in the signal region, for each of the individual SM backgrounds, along with associated statistical and sytematic uncertainty [146].

A range of kinematic distributions are presented in figure 5.25, after requiring at least two τ-candidates, with all of the relevant scaling factors applied to the MC. Small fluctuations between data and MC are observed, although they are consistent within the statistical uncertainties. Figure 5.24 shows the final signal selection variables, m_{eff} and $m_{\text{T}}^{\tau_1} + m_{\text{T}}^{\tau_2}$, prior to the relevant selection requirement being applied. Reasonable agreement between data and MC is seen in both distributions. The number of true τ-leptons and the number of true τ-leptons matched to reconstructed τ-candidates in the signal region can be seen in figure 5.26.

	Total SM MC	Data	GMSB4030
$E_{\mathrm{T}}^{\mathrm{miss}} > 130\,\mathrm{GeV}$	258903 ± 5956	509069	462 ± 12
$p_{\mathrm{T}}^{\mathrm{jet1}} > 130\,\mathrm{GeV}$	174165 ± 4340	440351	407.4 ± 9.5
$p_{\mathrm{T}}^{\mathrm{jet2}} > 30\,\mathrm{GeV}$	116967 ± 4280	116655	400.0 ± 9.5
Light lepton veto	95534 ± 4258	99078	123.6 ± 6.4
$N_\tau \geq 1$	4038 ± 172	3647	71.6 ± 5.7
$N_\tau \geq 2$	53.0 ± 6.7	52	25.1 ± 3.5
$\Delta\phi(E_{\mathrm{T}}^{\mathrm{miss}}, \mathrm{jet1/2}) > 0.4$	46.7 ± 6.2	43	22.2 ± 3.4
$m_{\mathrm{eff}} > 700\,\mathrm{GeV}$	10.2 ± 2.1	10	21.7 ± 3.4
$m_{\mathrm{T}}^{\tau_1} + m_{\mathrm{T}}^{\tau_2} > 80\,\mathrm{GeV}$	$5.3 \pm 1.3 \pm 2.2$	3	$20.8 \pm 3.4 \pm 5.4$

Table 5.15: A comparison between the expected number of events from the signal benchmark point, the sum of the SM processes and the data. Where possible, the MC predictions have been scaled by the factors obtained for the given background, obtained from the respective control regions. For the full signal selection the systematic uncertainties have also been given [146].

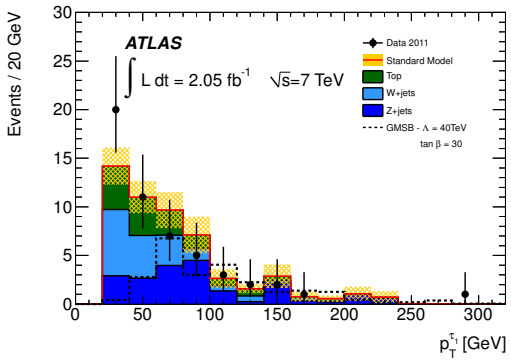

Figure 5.22: The p_{T} spectrum of the leading τ-candidates in data and the estimated SM background after the pre-selection of candidate events, soft multi-jet rejection and the requirement of two or more taus and no light leptons. The band centered around the total SM background indicates the statistical uncertainty. Also shown is the expected signal contribution from the GMSB4030 benchmark point [146].

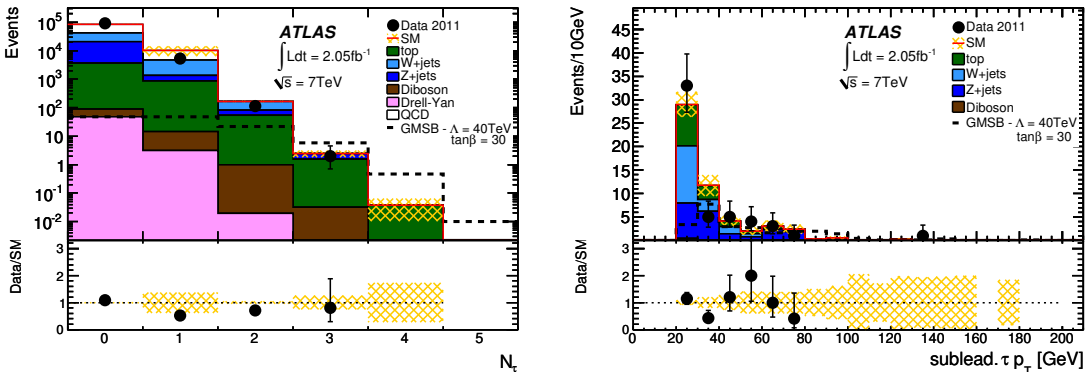

(a) N_τ after the light lepton veto

(b) Sub-leading p_{T}^{τ} after $N_\tau \geq 2$

Figure 5.23: (a) Number of selected τ-candidates after the lepton veto; (b) sub-leading p_{T}^{τ} after requiring at least two τ-candidates. The yellow band on the MC distribution corresponds to the statistical uncertainty. The background scaling factors computed in the analysis have been applied here and in all following plots. Also shown is the expected signal contribution from the GMSB4030 benchmark point [146].

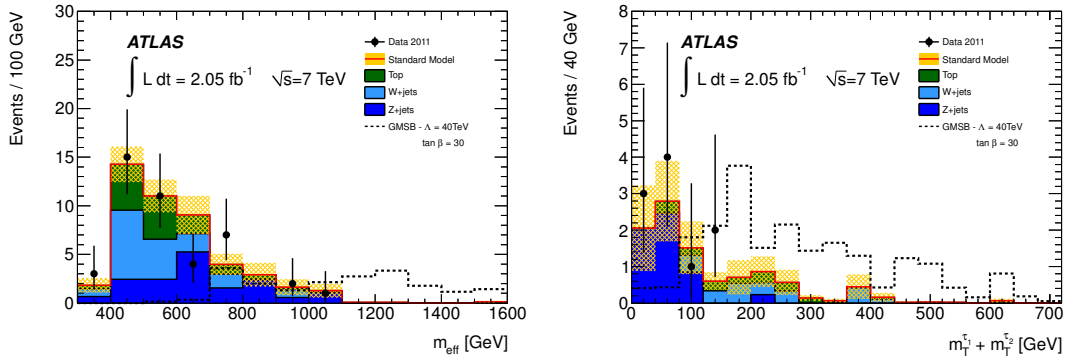

(a) m_{eff} distribution after the $\Delta\phi$ requirement

(b) $m_{\mathrm{T}}^{\tau 1} + m_{\mathrm{T}}^{\tau 2}$ distribution after the m_{eff} requirement

Figure 5.24: Distributions of variables used for the signal region definition in data and the estimated SM background after the pre-selection of candidate events, soft multi-jet rejection and the requirement of two or more τ-candidates, and no light leptons. The yellow band centered around the total SM background indicates the statistical uncertainty. Also shown is the expected signal contribution from the GMSB4030 benchmark point [146].

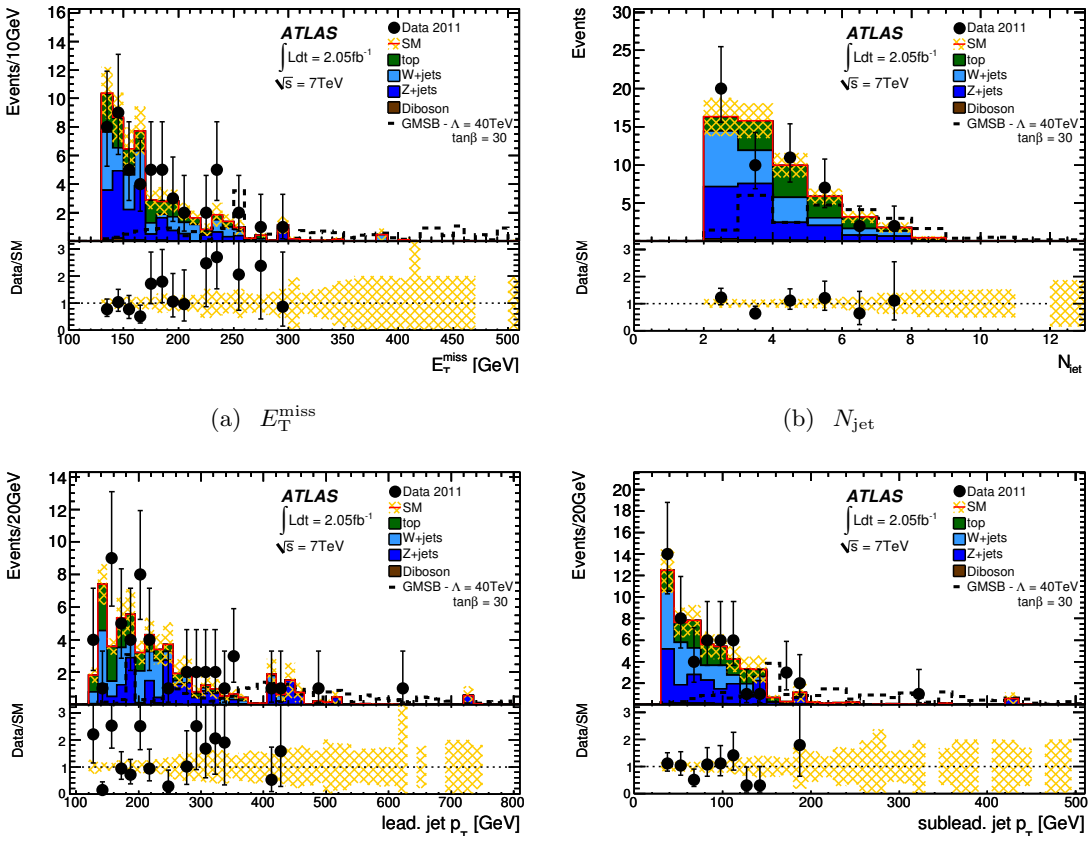

(a) $E_{\mathrm{T}}^{\mathrm{miss}}$ (b) N_{jet}

(c) $p_{\mathrm{T}}^{\mathrm{jet1}}$ (d) $p_{\mathrm{T}}^{\mathrm{jet2}}$

Figure 5.25: Distribution of some of the main kinematic variables after requiring two τ-candidates with the scaling factors from the control region applied to the MC background. The yellow band on the MC distribution corresponds to the statistical uncertainty. Also shown is the expected signal contribution from the GMSB4030 benchmark point [146].

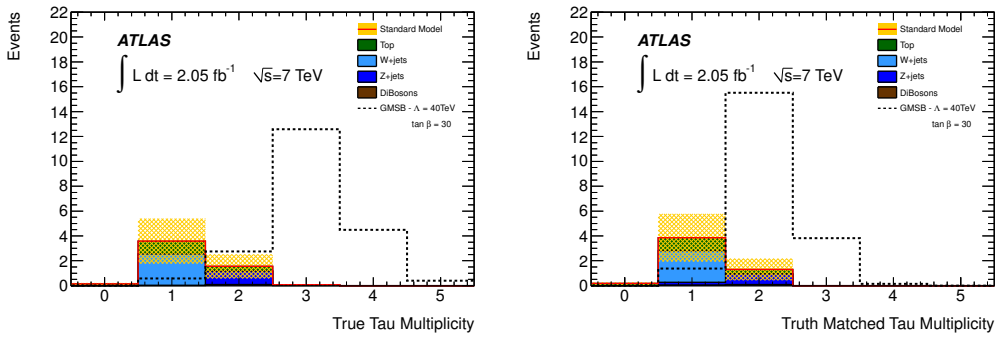

Figure 5.26: (a) Number of true τ-leptons and (b) number of true τ-leptons matched to reconstructed τ-candidates in the signal region. The yellow band corresponds to the statistical uncertainty.

In order to produce exclusion limits on the GMSB parameter space, the CL_s method [158, 159] is used. A detailed discussion of the procedure can be found in the following section, and further detail can be found in [158]. The ATLAS COMBINATION package [160] is used to set the exclusion limits for this analysis.

5.10 The CL_s method

The CL_s method is used to distinguish the hypothesis that the analysed data contains both signal and background contributions $(s + b)$, from the background-only hypothesis (b). This is used to set 95% CL exclusion limits on the GMSB parameter space.

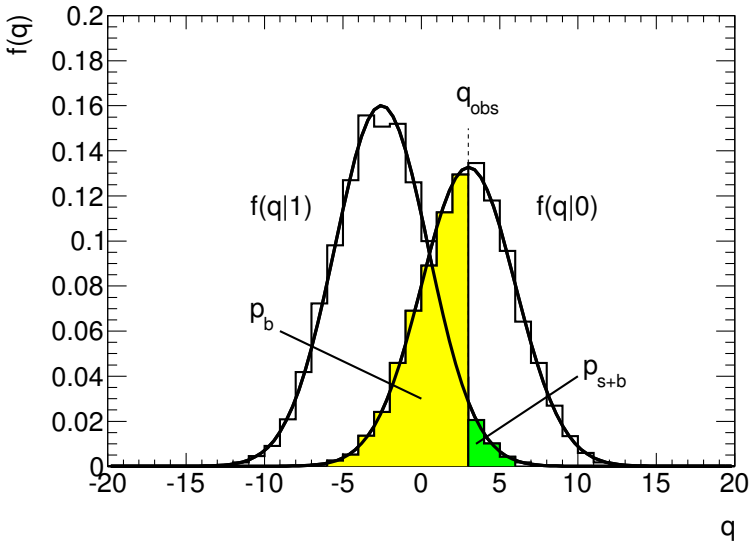

Figure 5.27: Distributions of the test variable q under the $s + b$ and b hypotheses, represented by $f(q|1)$ and $f(q|0)$ respectively. More details can be found in the text.

The CL_S method begins with the construction of a test statistic, q, which is a function of the observables and the model parameters. This test statistic is used to distinguish between two hypotheses. These are represented in figure 5.27 by the distributions $f(q|1)$, for the $s+b$ hypothesis, and $f(q|0)$, for the b hypothesis. In this figure, $q_{\rm obs}$ represents the value of the test variable observed in data, and the p-values of the two hypothesis are also shown. The p-value is the probability of obtaining a test statistic at least as extreme as the observed test statistic, under the assumption that the null hypothesis is true. The resulting p-value for the $s+b$ hypothesis is defined as the probability of observing a value of q with equal or lesser compatibility with this hypothesis, relative to $q_{\rm obs}$. This is represented in figure 5.27 by the green region of the distribution, and described by:

$$p_{\rm s+b} = P(q \geq q_{\rm obs}|s+b) = \int_{q_{\rm obs}}^{\infty} f(q|s+b)\, dq \tag{5.11}$$

The p-value of the background only hypothesis can be found by:

$$p_{\rm b} = P(q \leq q_{\rm obs}|b) = \int_{-\infty}^{q_{\rm obs}} f(q|b)\, dq \tag{5.12}$$

For the $CL_{\rm s}$ method, a signal model is regarded as excluded at a confidence level of $1-\alpha$ if equation 5.13 is satisfied:

$$CL_{\rm s} \equiv \frac{p_{\rm s+b}}{1-p_{\rm b}} < \alpha \ , \tag{5.13}$$

where $\alpha = 0.05$ for 95% CL. In equation 5.13 the $s+b$ p-value is divided by $1-p_{\rm b}$ in order to prevent the exclusion of signal models to which the analysis has little to no sensitivity. If the distributions of the two hypothesis are well separated, then the value of $1-p_{\rm b}$ will be close to 1, and the exclusion will be similar to the result from using the p-value alone to set the exclusion ($p_{\rm s+b} < \alpha$). If these two distributions are not well separated, then $1-p_{\rm b} < 1$, preventing signal models from being incorrectly excluded.

In these analyses a signal strength parameter (μ) is defined, where $\mu = 0$ corresponds to the background-only model, and $\mu = 1$ corresponds to the full number of signal events being considered. The value of μ depends on the GMSB signal model under investigation, and if $p_\mu < 0.05$, then this value of μ is excluded at 95% CL. The upper limit on μ is found by solving the equation $p_\mu = 0.05$ for μ.

5.11 Setting exclusion limits

For setting the 95% CL exclusion limits in the analyses described in both this chapter and in chapter 6 a likelihood function, $\mathcal{L}(n_S)$, is used as the test statistic, q. This likelihood function, which is the product of a Poisson distribution describing the signal region, and

a probability density function that describes the systematic uncertainties, is defined for each individual channel as:

$$\mathcal{L}(n_S|\mu, \mathbf{b}, \boldsymbol{\theta}) = P(n_S|\lambda_S(\mu, \mathbf{b}, \boldsymbol{\theta})) \times P_{\text{syst}}(\boldsymbol{\theta}^0, \boldsymbol{\theta}) \ , \tag{5.14}$$

where n_S is the number of events observed in data, $P(n_S)$ is a Poisson distribution modelling the expected event count in the signal region (based on the background $\mathbf{b}$, and the nuisance parameters[3] $\boldsymbol{\theta}$, which parameterise the systematic uncertainties), with an expectation λ_S. The $\boldsymbol{\theta^0}$ parameter is the nominal value around which $\boldsymbol{\theta}$ is varied, and the parameter μ is the GMSB signal strength. P_{syst} is the product of the constraints on the systematic uncertainties, which are described by Gaussian distributions with $\sigma = 1$, in the case that they are uncorrelated.

The p-value for each point on the GMSB grid is calculated to determine if the observed results exclude the point, and the exclusion contour represents the threshold of the excluded GMSB points. The p-value is obtained from profile log likelihood ratio tests, given by:

$$\Lambda(\mu) \equiv \Lambda(\mu, n_S, \boldsymbol{\theta^0}) \equiv -2\left(\ln \mathcal{L}(n_S, \boldsymbol{\theta^0}|\mu, \hat{\hat{\mathbf{b}}}, \hat{\hat{\boldsymbol{\theta}}}\,) - \ln \mathcal{L}(n_S, \boldsymbol{\theta^0}|\hat{\mu}, \hat{\mathbf{b}}, \hat{\boldsymbol{\theta}})\right) \ , \tag{5.15}$$

where $\hat{\boldsymbol{\mu}}$, $\hat{\boldsymbol{b}}$ and $\hat{\boldsymbol{\theta}}$ maximise the likelihood function, and $\hat{\hat{\mathbf{b}}}$, $\hat{\hat{\boldsymbol{\theta}}}$ maximise the likelihood for the specific fixed value of the signal strength μ, and the data n_S, $\boldsymbol{\theta^0}$ [158]. The χ^2 distribution for the log likelihood ratio test (equation 5.15) is then calculated, giving the one-sided p-value. This results in the test statistic for upper limits being defined as:

$$q_\mu \equiv \begin{cases} P_{\chi^2}(\Lambda(\hat{\mu})), & \hat{\mu} \geq \mu \\ 1 - P_{\chi^2}(\Lambda(\hat{\mu})), & \hat{\mu} < \mu \end{cases} \tag{5.16}$$

All of the systematic uncertainties described in the previous section are included in the limit setting procedure. Energy scale uncertainties are treated as correlated over the GMSB parameter space, whilst all other uncertainties are treated as uncorrelated. In the case of asymmetric "up" and "down" uncertainties the larger value is used. The sum of these uncertainties across the GMSB parameter space is shown in figure 5.28(a). The theory uncertainties on the PDF, α_s, and scale uncertainties are included, and are correlated across the GMSB parameter space. The sum of the theory uncertainties is shown in figure 5.28(b). The uncertainty from the limited number of MC events in the samples used is shown in figure 5.28(c). Figure 5.28(d) shows the total signal uncertainty

[3] A nuisance parameter is a parameter which is not of immediate interest to the analysis, but which must be accounted for to correctly calculate the parameters of interest.

over the GMSB parameter space. Figure 5.30 shows the 95 % CL exclusion limit across the GMSB grid. For $10 < \tan\beta < 40$, the region $\Lambda < 40$–50 TeV is excluded. For lower values of $\tan\beta$, this is due to the NLSP changing from $\tilde{\tau}_1$ to $\tilde{e}_R$ and $\tilde{\mu}_R$. For most of the excluded region, the NLSP is the $\tilde{\tau}_1$, as expected.

It is also possible to use the estimated SM background and associated uncertainty to set a 95 % CL upper limit on the number of events in the signal region from any new physics that would contribute events to this region. This limit is found to be 5.6 events. The 95 % CL upper limits on the effective cross-section in the signal region are also derived, by including the systematic uncertainty on the signal and the uncertainty from the limited MC signal sample size. This limit is found to be $\sigma < (3 - 25)$ fb. Figure 5.29 shows the observed upper limit on the production cross-section across the GMSB grid.

Figure 5.31(a) shows the expected and observed 95 % CL exclusion limit on the GMSB model parameters Λ and $\tan\beta$ for the published ATLAS dilepton search [161], and $\geq$

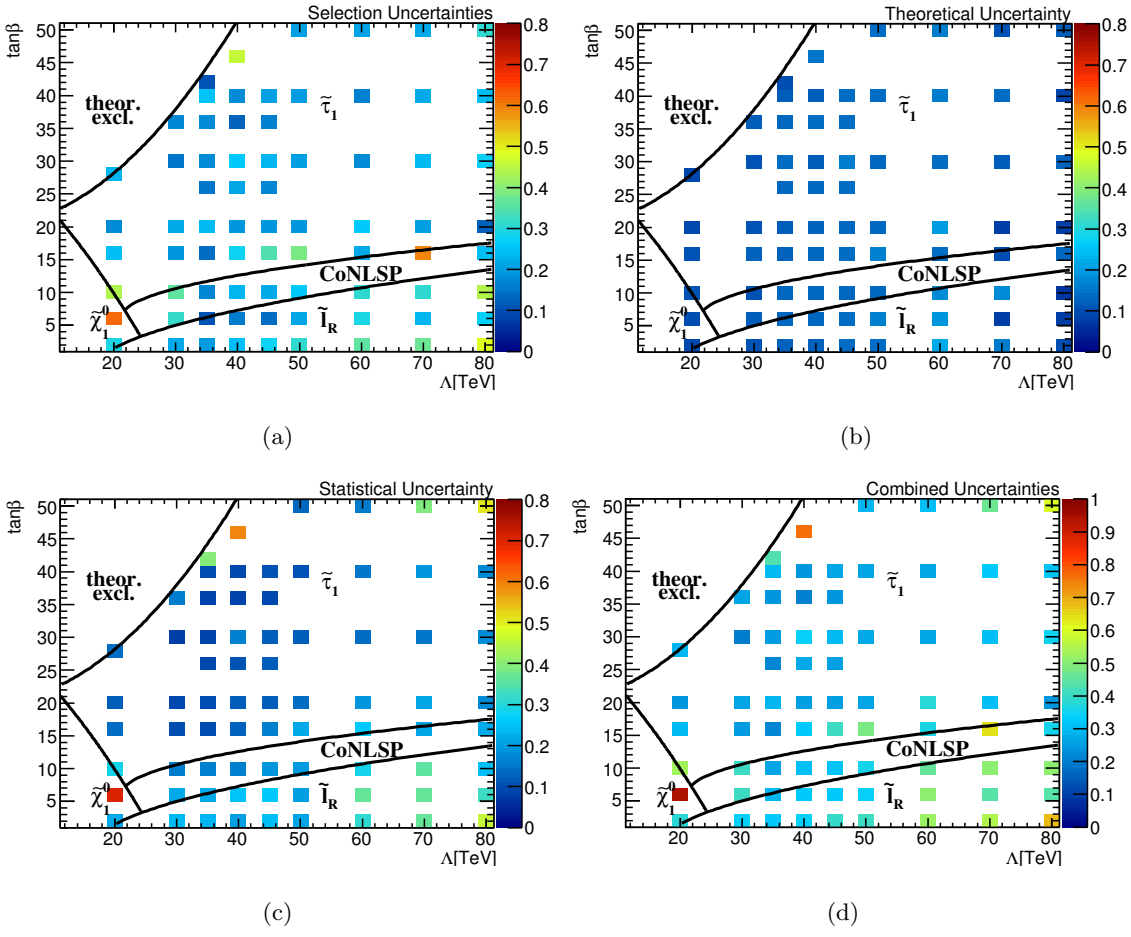

Figure 5.28: Relative systematic uncertainties from (a) selection, (b) theory and (c) statistical uncertainties and (d) including all systematic uncertainties over the GMSB parameter space [146].

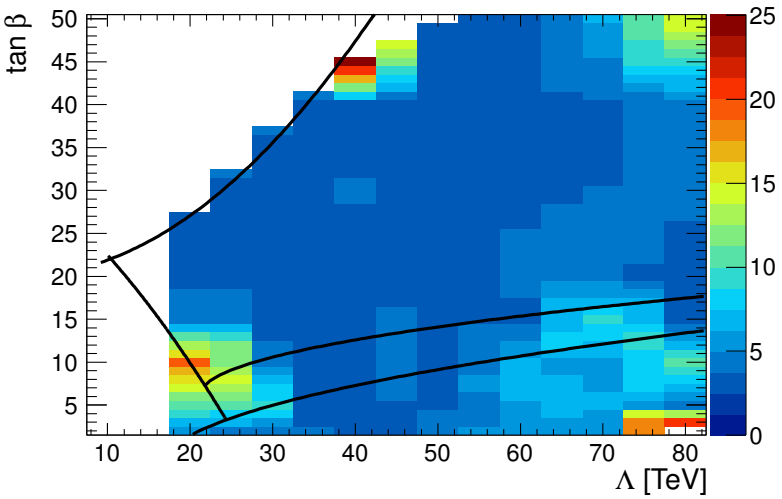

Figure 5.29: Observed upper limit on the production cross-section from the 2τ channel result in the GMSB plane. The grey lines indicate the different NLSP regions determining the phenomenology [146].

1τ-lepton search results [162], along with the 2τ search presented in this chapter. The exclusion contour obtained in this analysis has a significantly wider reach than the 1τ search in all regions of the considered GMSB parameter space. The 2τ search also excludes a larger area of the $\tilde{\tau}_1$ NLSP region than the dilepton search, which has to rely on leptonic τ-decays in the $\tilde{\tau}_1$ region. In the $\tilde{\ell}_R$ NLSP region the dilepton search excludes higher values of Λ, despite only using an integrated luminosity of $1\,\text{fb}^{-1}$.

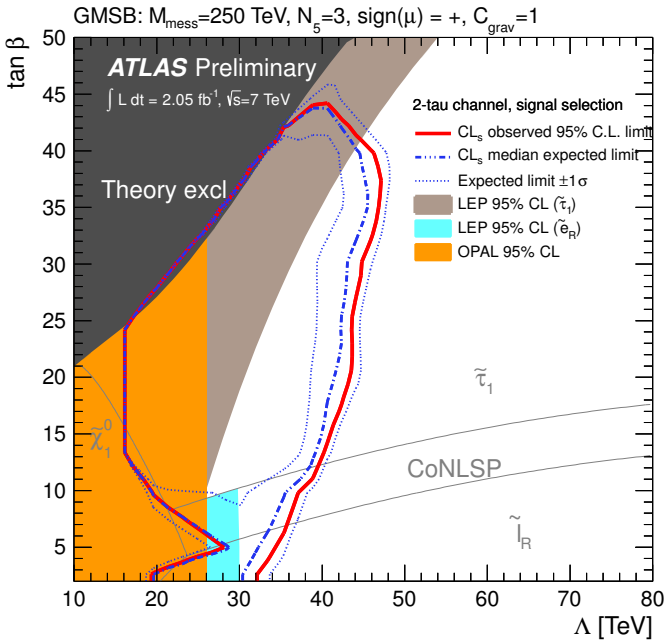

Figure 5.30: Expected and observed exclusion limit from the 2τ channel result in the GMSB plane. The grey lines indicate the different NLSP regions determining the phenomenology [146].

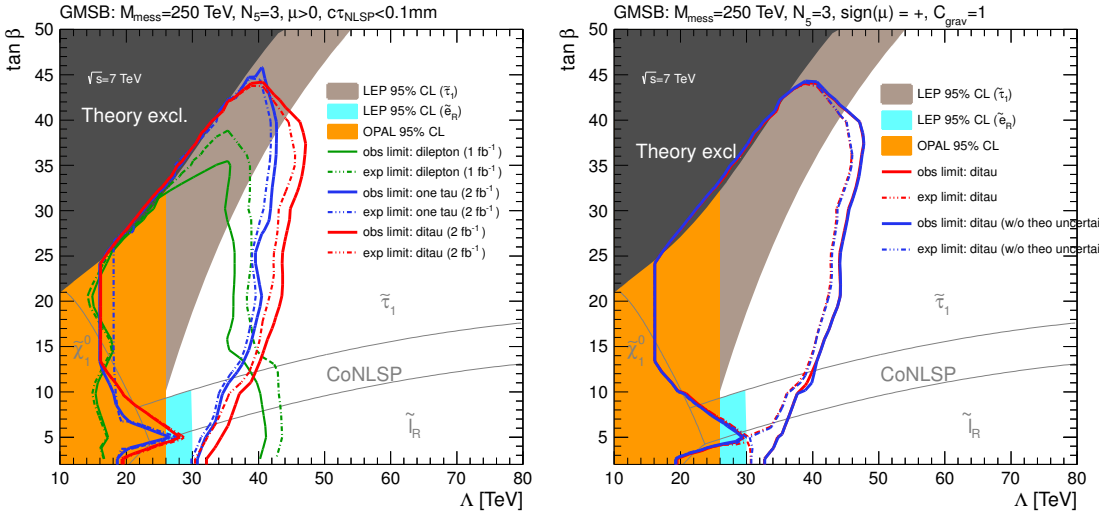

(a) (b)

Figure 5.31: Expected and observed exclusion limits in the GMSB plane, from (a) the dilepton [161], 1τ and 2τ searches, (b) the 2τ search (with and without signal theory uncertainties). The grey lines indicate the different NLSP regions determining the phenomenology [146].

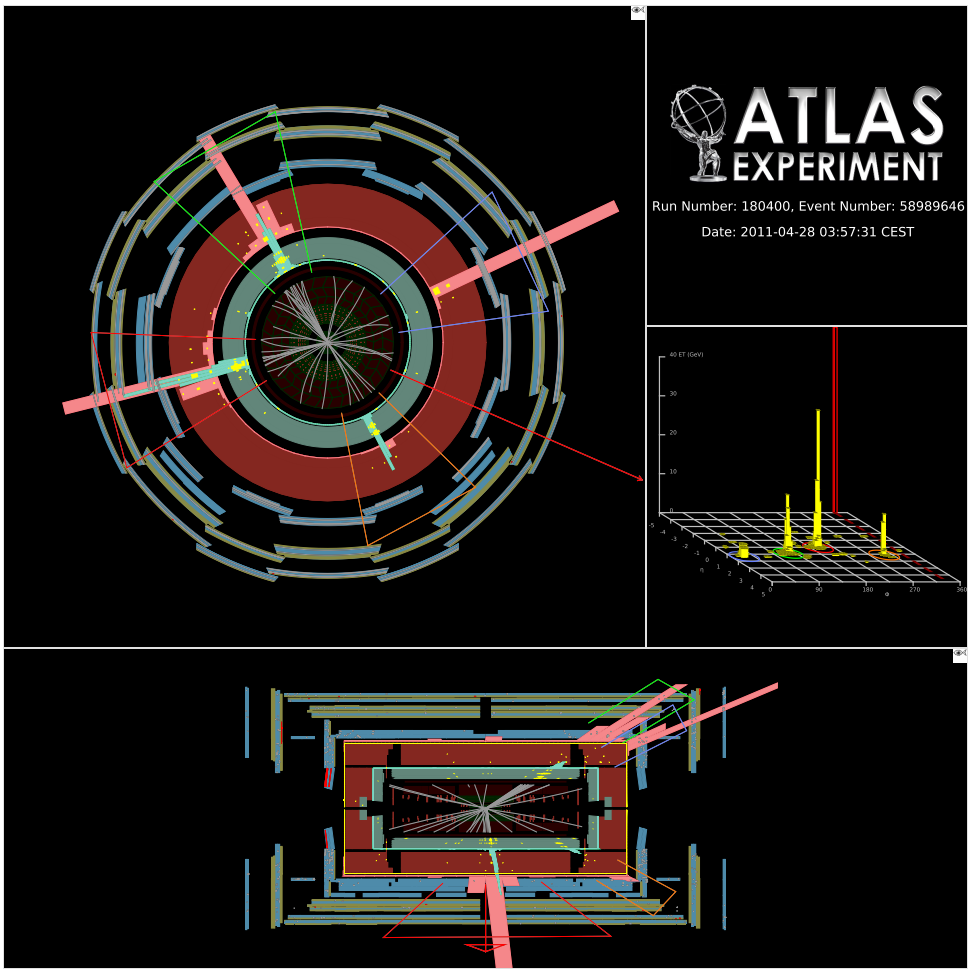

Figure 5.32: Event display for one of the data events in the signal region (run 180400, event 58989646). The $p_{\mathrm{T}}^{\mathrm{jet1}}$ (red cone) is 214.0 GeV, $p_{\mathrm{T}}^{\mathrm{jet2}}$ (green cone) is 177.2 GeV, $p_T^{\tau 1}$ (orange cone) is 66.2 GeV, $p_T^{\tau 2}$ (blue cone) is 48.1 GeV and the $E_{\mathrm{T}}^{\mathrm{miss}}$(red arrow) is 202.7 GeV [146]

6

Search for supersymmetry in final states with one or more τ-leptons, zero or one light leptons, jets and missing transverse energy

6.1 Introduction

This chapter describes an update to the search for supersymmetry at ATLAS in final states with at least one τ-lepton, where the full 2011 dataset is used. In this analysis, final sates with one τ-lepton and zero light leptons, or at least one τ-lepton and one light lepton are considered in addition to the two τ-lepton final state described in chapter 5. The light lepton channels were included to provide sensitivity to GMSB events in which one of the τ-leptons decays leptonically. A full statistical combination of the four final states is performed in order to maximise the sensitivity to new physics. The results of this analysis are published in European Physical Journal C [163].

Whilst this chapter will focus on my contribution to this analysis, there will inevitably be times where it will be necessary to present the work of others, and I will endeavour to make the author of each section clear. I worked exclusively on the 2τ final state, where

I have been responsible for the optimisation of the signal selection and the definition of the control regions (in collaboration with a collegue from the University of Bonn). I have also been the sole author for the multi-jet background estimation. I have been solely responsble for the statistical combination of the results obtained in the four final states, including the calculation of the expected and observed exclusion limits obtained from each of the individual final states, and from the full combination. Given that my main contribution to this analysis is in the 2τ final state, in this chapter I will provide full details for this channel, with a brief overview of the other channels. The discussion of the full statistical combination of these channels, including the final published results, is presented in chapter 7.

6.2 Data and Monte Carlo samples

6.2.1 ATLAS data samples

The data used in this analysis were recorded by the ATLAS detector at a centre-of-mass energy of $\sqrt{s} = 7\,\text{TeV}$ from Mar 22$^{\text{nd}}$ to Oct 30$^{\text{th}}$ 2011. As with the analysis documented in chapter 5, the data is required to meet minimum detector quality requirements (section 5.2.1), and the total integrated luminosity after the quality requirements is $(4.7 \pm 0.1)\,\text{fb}^{-1}$ [87, 164]. The data periods used in this analysis are summarised in table 6.1.

Periods	Run numbers	Runs	$\int \mathcal{L}\,\text{dt}$ [pb^{-1}]	$\int \mathcal{L}\,\text{dt}$ [pb^{-1}] corrected
B2	178044–178109	3	12.0	11.7
D–I	179710–186493	109	1490	1453
J–K	186516–187815	28	839	817
L–M	188902–191933	76	2487	2432
			Total:	4713.7

Table 6.1: Details of the 2011 p–p collision data at $\sqrt{s} = 7$ TeV used in this analysis. The corrections to the integrated luminosity take into account effects of the trigger live fraction and the dead channels in the LAr calorimeter [87, 164].

Name	Generator	Cross-section [pb]	Number of events
$t\bar{t}$ and single top	MC@NLO +JIMMY	0.22–90.57	2.5×10^4–1.5×10^7
$W \to e\nu/\mu\nu/\tau\nu + 0$–5 partons	ALPGEN +JIMMY	1.73–8288.878	6.5×10^4–3.8×10^6
$Z \to ee/\mu\mu/\tau\tau/\nu\nu + 0$–5 partons	ALPGEN +JIMMY	0.95–832.61	4.5×10^4–1.0×10^7
Multi-jets	PYTHIA	6×10^{-6}–1.2×10^{10}	1.0×10^6
Diboson (WW, ZZ, WZ)	MC@NLO +JIMMY	0.0065–1.695	2.5×10^4–5.0×10^5
Drell-Yan ($Z \to ee/\mu\mu/\tau\tau + 0$–5 partons, 10 GeV $< m_{\ell\ell} <$ 40 GeV)	ALPGEN +JIMMY	0.57–3798.62	1.0×10^4–1.0×10^6

Table 6.2: A summary of the simulated Standard Model samples used in this analysis, and corresponding generator, cross-section and number of simulated events. The stated cross-section is NNLO where possible, and NLO if this is not available. A full list can be found in appendix B, in tables B.1–B.8.

6.2.2 Simulated Standard Model background samples

The SM background samples that are used in this analysis are summarised in table 6.2, with a detailed list in appendix B, tables B.1–B.8. The majority of these samples are introduced in section 5.2.2, in the context of the $2.05\,\text{fb}^{-1}$ analysis. For the $t\bar{t}$ and diboson backgrounds alternative samples, built using different generators, have been studied (details can be found in the appendix, in tables B.2 and B.6). These samples are used to cross check results that are susceptible to mis-modelling of some aspects of the simulation. The difference between the nominal and alternative samples are treated as an additional systematic uncertainty.

In order to increase the number of available Monte Carlo events for this analysis, additional samples for the W+jets background were generated. These samples are generated with at least one jet with $p_{\text{T}} \geq 100$ GeV, and $E_{\text{T}}^{\text{miss}} \geq 100$ GeV. A list of these samples can be found in table B.3, where they are suffixed with "susyfilt".

6.2.3 Simulated signal samples

Two new benchmark points in the GMSB Λ–$\tan\beta$ plane are defined, and used to optimise the signal selection for this analysis. These points are referred to in the text as "GMSB5020" and "GMSB5040", where the defining parameters are $\Lambda = 50$ TeV, $\tan\beta = 20$ and $\Lambda = 50$ TeV, $\tan\beta = 40$ respectively. These points have been selected because they are positioned beyond the 95% CL exclusion limit from the previous analysis, and their kinematic properties are representative of a wide range of the GMSB parameter space, where the $\tilde{\tau}_1$ is the NLSP. A summary of the GMSB signal samples, including the two benchmark points, can be found in table 6.3, with more detail available

Sample ID	Name	Generator	NLO σ [pb]
137948	GMSB5020 ($\Lambda = 50, \tan\beta = 20$)	Herwig++	0.114
137950	GMSB5040 ($\Lambda = 50, \tan\beta = 40$)	Herwig++	0.133
137915–	GMSB grid	Herwig++	552.595
–137975	GMSB grid	Herwig++	0.0101

Table 6.3: The GMSB benchmark samples with sample IDs, event generator and NLO cross-sections.

in appendix B, table B.9.

The cross-sections for the signal samples have been calculated to NLO in the strong coupling constant, including the resummation of soft gluon emission at next-to-leading-logarithmic accuracy (NLO+NLL). This NLL correction is used for both squark and gluino production, in the case of their masses being in the range 200 GeV–2 TeV. In this context the mass of the squark is defined as the average mass of the first two generation squarks, as is the convention employed by the NLO calculators. For gluino pair production the upper limit of the mass range is extended to 4.5 TeV, and for associated squark-gluino production this value is 3.5 TeV. For masses that fall outside this range and for other types of production processes the NLO cross-sections that have been obtained with `PROSPINO` 2.1 are used. An envelope of cross-section predictions is defined using the 68% CL ranges of the CTEQ (including the α_S uncertainty) and MSTW [165] PDF sets, together with independent variations of the factorisation and renormalisation scales by factors of 2 or $\frac{1}{2}$. The nominal cross-section value is taken to be the midpoint of the envelope and the uncertainty assigned is half the full width of the envelope, closely following the recommendations of PDF4LHC [166].

6.3 Pre-selection and event cleaning

As with the previous analysis, there are several requirements that are applied to ensure that the data is of sufficient quality for physics analysis and also to reject the dominant sources of noise. These are described in detail in section 5.4, and enumerated below. These conditions are consistent for all four final states.

- Detector quality requirements are imposed to reject collision data that was recorded without the necessary detector conditions.

- Each event is required to have a primary vertex that contains at least 4 tracks.
- Events are rejected if they contain jets that have been categorised as "bad jets".
- For events in data the LAr calorimeter must not have reported any errors whilst recording the event. Infrequently the LAr calorimeter does suffer from error conditions, but these act only on individual events. If an error is recorded then the event is rejected.
- Electron candidates are required to satisfy $p_{\mathrm{T}} > 20$ GeV and $|\eta| < 2.47$, and meet the `Medium++` identification condition [167]. Electrons are rejected if they are touching a dead OTX module[1] or if they traverse the dead region in the second and third layers of the ECAL. Muon candidates are required to satisfy $p_{\mathrm{T}} > 10$ GeV and $|\eta| < 2.4$, and must be identified as a combined or segment-tagged muon [168]. For the 1τ and 2τ final states, events that contain light leptons are rejected, in order to ensure that they remain orthogonal with the $\tau+\ell$ final states. In the $\tau+e$ channel only electrons with $p_{\mathrm{T}} > 25$ GeV are selected.

6.4 Triggers used in the analysis

As with the previous analysis, the 1τ and 2τ final states both use data that were recorded with a combined jet+$E_{\mathrm{T}}^{\mathrm{miss}}$ trigger, which selects events containing at least one high p_T jet and large $E_{\mathrm{T}}^{\mathrm{miss}}$. This is chosen as the GMSB signal models predict final states containing high $E_{\mathrm{T}}^{\mathrm{miss}}$ due to the escaping LSP, and high p_{T} jets created in the cascade decay of the coloured squarks or gluinos.

A summary of the triggers used to select events in data can be found in table 6.4, with a detailed description in section 5.5. The LHC beam conditions changed for periods J–M and the trigger requirement on the $E_{\mathrm{T}}^{\mathrm{miss}}$ is raised from 45 to 55 GeV. Additional kinematic constraints are imposed on the leading jet p_{T} and the $E_{\mathrm{T}}^{\mathrm{miss}}$ in both data and MC to ensure the trigger is fully efficient. These conditions require the selection of a jet with $p_T > 130$ GeV and $E_{\mathrm{T}}^{\mathrm{miss}} > 130$ GeV. For periods L–M the $E_{\mathrm{T}}^{\mathrm{miss}}$ requirement is raised to 150 GeV. As with the analysis in chapter 5, a second jet with $p_T > 30$ GeV is also required in the 1τ and 2τ final states to suppress the multi-jet background.

In the $\tau + \ell$ final states the light lepton is always used to trigger the event, as the reconstruction efficiency of light leptons is higher than for τ-leptons, and a leptonic trigger provides the optimal acceptance. The $\tau+e$ channel uses a single lepton trigger for the

[1] OTX modules are custom-made optical transmitters for the Liquid Argon Calorimeter front-end electronics readout system.

Channel	Data-periods	Trigger	Offline trigger requirements
1τ, 2τ	B2–I	EF_j75_a4tc_EFFS_xe45_loose_noMu	$p_{\mathrm{T}}^{\mathrm{jet1}} > 130$ GeV, $E_{\mathrm{T}}^{\mathrm{miss}} > 130$ GeV
	J–M	EF_j75_a4tc_EFFS_xe55_loose_noMu	$p_{\mathrm{T}}^{\mathrm{jet1}} > 130$ GeV, $E_{\mathrm{T}}^{\mathrm{miss}} > 150$ GeV

Table 6.4: The triggers used in the 1τ and 2τ final states for different data-taking periods, and the corresponding trigger plateau requirements. Further details can be found in section 5.5.

entire 2011 dataset, but for the $\tau+\mu$ channel the recommended single muon trigger was changed during the later data-periods due to a higher instantaneous luminosity at the LHC. For the runs during this period a combined $\mu + \text{jet}$ trigger is used instead. A summary of the triggers used in the $\tau + \ell$ final states can be found in table 6.5.

Channel	Runs	Trigger
$\mu + \tau$	178044 – 186493	EF_mu18
	186516 – 191933	EF_mu18_L1J10
$e + \tau$	177968 – 186873	EF_e20_medium
	186873 – 188902	EF_e22_medium
	188902 – 191933	EF_e22vh_medium1 or EF_e45_medium1

Table 6.5: The triggers used in the $\tau+e$ and $\tau+\mu$ final states.

To avoid effects due to mis-modelling of the trigger efficiency in the simulated samples, requirements are placed on the light leptons to ensure that they are in the plateau region of the trigger efficiency. For both the single muon and the combined $\mu + \text{jet}$ triggers the muon is required to satisfy $p_{\mathrm{T}} > 20$ GeV. Additionally, in the case of the combined trigger, at least one jet with $p_{\mathrm{T}} > 50$ GeV is also required.

6.5 Signal selection requirements

After the application of the pre-selection, event cleaning and trigger requirements, the channels are defined by requiring the appropriate physics objects. For the 2τ channel at least two τ-candidates with $p_{\mathrm{T}} > 20$ GeV, selected with the "loose" BDT τ-ID, are required. Following this requirement the multi-jet background is almost entirely rejected, apart from an almost negligible contribution from highly collimated jets that are suffi-

ciently similar to hadronically decaying τ-leptons to satisfy the τ-ID conditions. The dominant contributions to the Standard Model background are events from W+jets, Z+jets and $t\bar{t}$ production.

In order to suppress events containing mis-measured jets and $E_{\mathrm{T}}^{\mathrm{miss}}$ coming from instrumental effects, it is required that the leading and sub-leading jets both have a minimal distance from the $E_{\mathrm{T}}^{\mathrm{miss}}$ of $|\Delta\phi| > 0.4$, since it can be assumed that hard jets aligned with the $E_{\mathrm{T}}^{\mathrm{miss}}$ have been mis-measured. This is consistent with the analysis presented in chapter 5, and further suppresses the remaining multi-jet background.

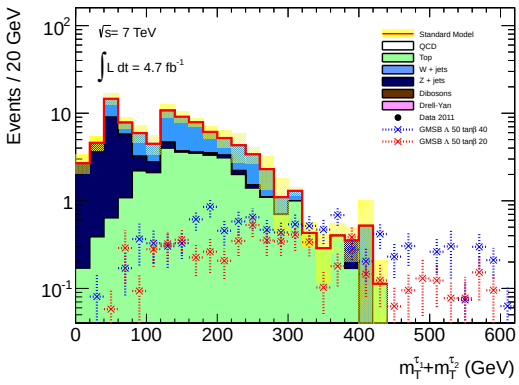

Figure 6.1: $m_{\mathrm{T}}^{\tau_1} + m_{\mathrm{T}}^{\tau_2}$ after requiring that $|\Delta\phi(\mathrm{jet}_{1,2}, E_{\mathrm{T}}^{\mathrm{miss}})| > 0.4$.

The Asimov approximation of the discovery significance is used when optimising the signal selection, with requirements designed to maximise ${z_A}^2$ (described in section 5.6). The first of the signal selection requirements is on the sum of the transverse mass of the two leading τ-leptons, $m_{\mathrm{T}}^{\tau_1} + m_{\mathrm{T}}^{\tau_2}$. For the 2.05fb^{-1} analysis this variable was required to be $\geq$ 80 GeV, but this is re-optimised for the full 2011 dataset. A requirement of $m_{\mathrm{T}}^{\tau_1} + m_{\mathrm{T}}^{\tau_2} > 100$ GeV is chosen, and the distribution of $m_{\mathrm{T}}^{\tau_1} + m_{\mathrm{T}}^{\tau_2}$ prior to imposing this requirement can be seen in figure 6.1. This requirement mainly suppresses Z+jets events.

For this analysis H_{T} contains the scalar sum of the p_{T} of the leading and sub-leading jets, and all of the τ-candidates in the event:

$$H_{\mathrm{T}} = \sum p_{\mathrm{T}}^{\tau} + \sum_{i=1,2} p_{\mathrm{T}}^{\mathrm{jet_i}}$$

Figure 6.2 shows the H_{T} distribution following the $m_{\mathrm{T}}^{\tau_1} + m_{\mathrm{T}}^{\tau_2}$ requirement, as well as a scan of the Asimov significance for the GMSB benchmark points. The cut value of 650 GeV has been chosen to be at the start of the plateau indicated by the significance scan. These requirements defined the signal region for the 2τ final state.

[2] $z_A \equiv \sqrt{2\left[(N_{\mathrm{Sig}} + N_{\mathrm{BG}})\ln\left(1 + \frac{N_{\mathrm{Sig}}}{N_{\mathrm{BG}}}\right) - N_{\mathrm{Sig}}\right]}$

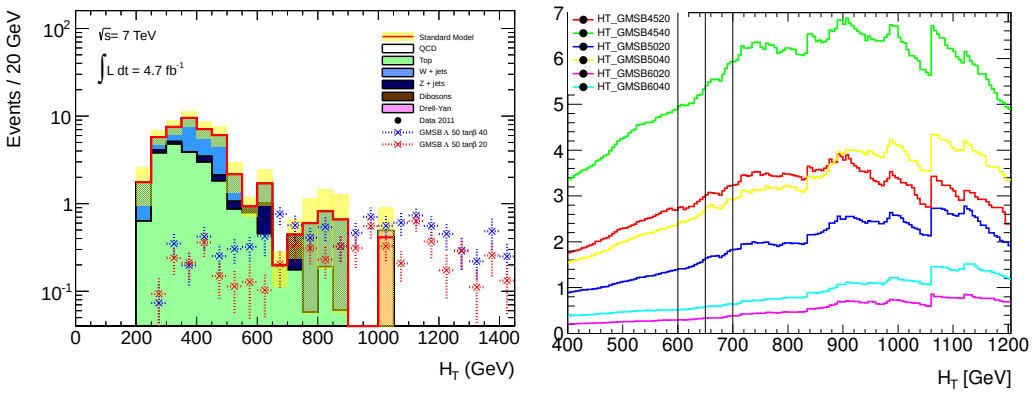

(a) H_{T} distribution (b) Significance scan

Figure 6.2: (a) H_{T} distribution after requiring the transverse mass cut, and (b) a scan of the discovery significance for the two benchmark points. Additional GMSB points for lower and higher values of Λ are displayed for comparison. Black lines indicate possible cuts at 600 GeV , 650 GeV and 700 GeV.

For the 1τ channel, exactly one τ-candidate with the "medium" BDT τ-ID is required. To avoid overlap with the 2τ channel, events are rejected if they contain a second τ-candidate, identified with the "loose" τ-ID. The following requirements are then applied as signal selection and background rejection:

- $\Delta\phi_{\mathrm{min(jet_{1,2},E_T^{miss})}} > 0.3$;
- $E_{\mathrm{T}}^{\mathrm{miss}}/m_{\mathrm{eff}} > 0.3$;

} Designed to suppress multi-jet background

- $m_T > 110$ GeV;
- $H_T > 775$ GeV,

where the definitions of m_{eff}, m_T and H_T are given in section 5.3.1. In the calculation of m_{eff} only the two leading jets are included, whilst for H_{T} the τ-candidate is also included, and the sum includes all jets with $p_{\mathrm{T}} > 30$ GeV. The $\Delta\phi_{\mathrm{min}}$ and $E_{\mathrm{T}}^{\mathrm{miss}}/m_{\mathrm{eff}}$ requirements suppress the background from multi-jet events, where a hadronic jet is mis-identified as a τ-candidate. The m_T requirement mainly suppresses events containing $W \to \tau\nu$, produced in association with jets, which is the dominant non-multi-jet background for the 1τ channel. The m_T distribution after all of the preceding event selection requirements have been applied can be seen in figure 6.3(a). Good agreement is observed between the data and the Monte Carlo background samples, and the m_T requirement also suppresses a large number of background events from W + jets or top production.

The H_{T} distribution, following the m_{T} requirement, is presented in figure 6.3(b). Requiring $H_T > 775$ GeV suppress much of the remaining Standard Model background,

which at this stage primarily consists of $Z \to \nu\nu$, dibosons, W+jets and top events.

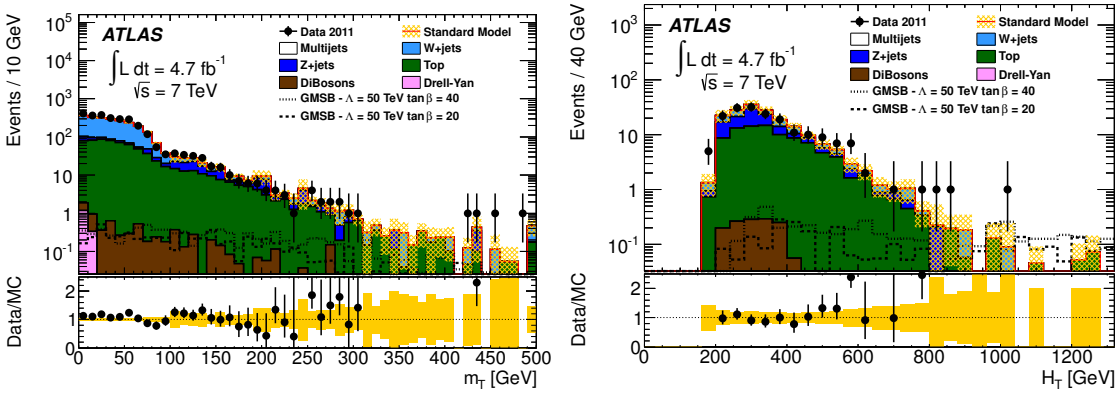

(a) m_{T} distribution for the 1τ final state.

(b) H_{T} distribution for the 1τ final state.

Figure 6.3: Distribution of (a) m_{T} and (b) H_{T} for the 1τ final state after all preceding analysis requirements have been applied. Data is represented by the points, with statistical uncertainty only. The SM prediction includes the data-driven corrections discussed in the text. The band centred around the total SM background indicates the uncertainty on the background expectation due to finite MC sample sizes [163].

For the $\tau + \ell$ final states, each channel rejects events that contain a light lepton of opposite flavour, to avoid any overlap between them. For both channels, events containing a second light lepton ($p_T^e > 10$ GeV or $p_T^\mu > 10$ GeV) of the same flavour are also rejected, to avoid overlap with the dilepton GMSB search published by ATLAS[3] [169]. Each of the three BDT τ-ID strengths are studied in order to select the one that results in the optimal signal sensitivity, and the "medium" τ-ID is selected for both $\tau + \ell$ final states.

The optimisation of the signal selection for the $\tau + \ell$ final states is again performed with the Asimov definition of significance. For these channels, the m_{eff} is defined as the scalar sum of the p_{T} of the two leading jets with $p_{\mathrm{T}} > 25$ GeV, the light lepton p_{T} and the $E_{\mathrm{T}}^{\mathrm{miss}}$. A balance between optimising the signal sensitivity whilst retaining an adequate Monte-Carlo event yield is achieved by defining the signal region for both channels with the requirements:

$$\begin{aligned} m_T^{e,\mu} &> 100 \text{ GeV} \\ m_{\mathrm{eff}} &> 1000 \text{ GeV} \end{aligned}$$

Figure 6.4 shows the distribution of $m_{\mathrm{T}}^{e,\mu}$ for both of the $\tau + \ell$ final states, where all of the preceding selection requirements are in place. In the region $m_{\mathrm{T}}^{e,\mu} < 100$ GeV

[3] A comparison of the results from this analysis and the dilepton analysis can be found in chapter 7.

the Standard Model background contains a large contribution from W/Z + jets and top production, which is many orders of magnitude above the contribution from the GMSB benchmark points. The m_{eff} distribution following the application of the $m_{\text{T}}^{e,\mu}$ requirement can be found in figure 6.5. The selected value of 1000 GeV suppresses the vast majority of the remaining Standard Model background, with the benchmark signal points tending to higher values due to the comparatively large squark and gluino masses. For both final states the dominant background processes in the signal region are W+jets and top production.

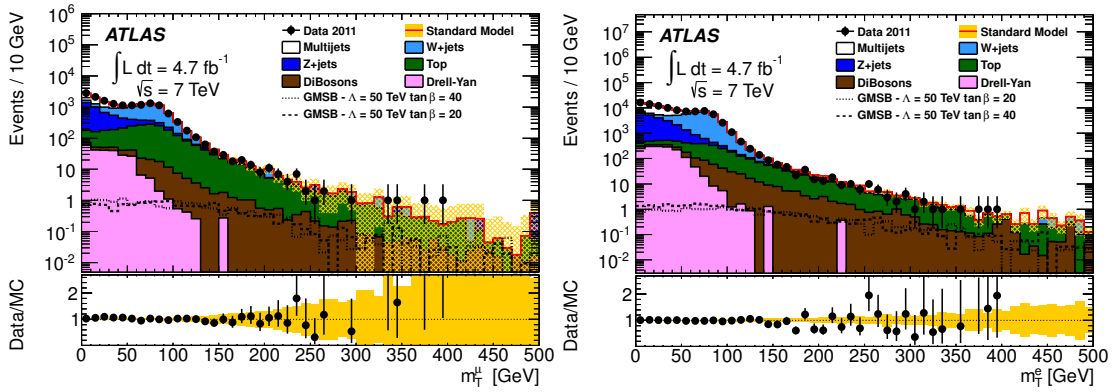

(a) m_{T}^{μ} distribution for the τ+μ final state. (b) m_{T}^{e} distribution for the τ+e final state.

Figure 6.4: Distribution of $m_{\text{T}}^{e,\mu}$ for the (a) τ+μ and (b) τ+e final states after all analysis requirements but the final requirement on m_{eff}. Data are represented by the points, with statistical uncertainty only. The SM prediction includes the data-driven corrections discussed in the text. The band centred around the total SM background indicates the uncertainty on the background expectation due to finite MC sample sizes. Also shown is the expected signal from the two GMSB benchmark points [163].

Table 6.6 contains a summary of the event selection for each of the four channels that are used in this analysis.

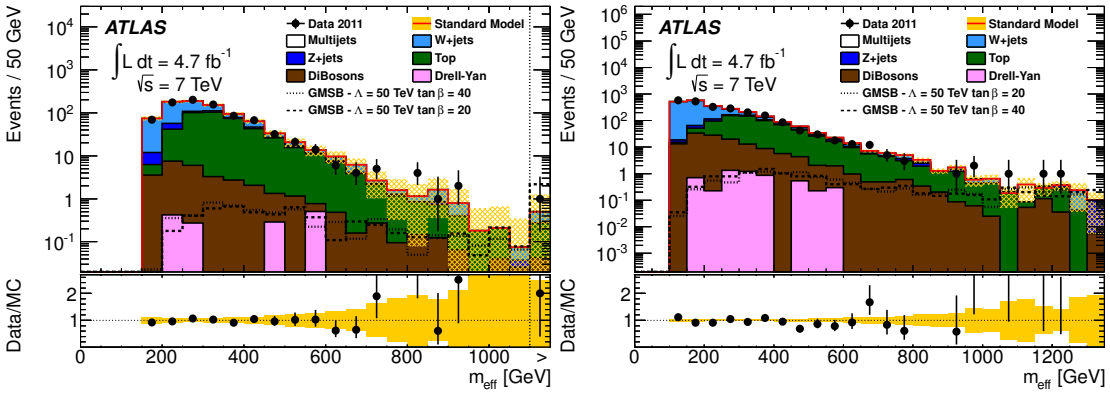

(a) m_{eff} distribution for the $\tau+\mu$ final state. (b) m_{eff} distribution for the $\tau+e$ final state.

Figure 6.5: Distribution of m_{eff} for the (a) $\tau+\mu$ and (b) $\tau+e$ final states after all analysis requirements. Data are represented by the points, with statistical uncertainty only. The SM prediction includes the data-driven corrections discussed in the text. The band centred around the total SM background indicates the uncertainty on the background expectation due to finite MC sample sizes. Also shown is the expected signal from the two GMSB benchmark points [163].

Table 6.6: Event selection for the four final states presented in this work. Numbers in parentheses are the minimal momenta required for the objects. Pairs of numbers separated by a slash denote different selection criteria imposed in different data-taking periods.

	1τ	2τ	$\tau+\mu$	$\tau+e$
Trigger	jet+$E_{\text{T}}^{\text{miss}}$ $p_{\text{T}}^{\text{jet}} > 75$ GeV $E_{\text{T}}^{\text{miss}} > 45/55$ GeV	jet+$E_{\text{T}}^{\text{miss}}$ $p_{\text{T}}^{\text{jet}} > 75$ GeV $E_{\text{T}}^{\text{miss}} > 45/55$ GeV	muon/muon+jet $p_{\text{T}}^{\mu} > 18$ GeV $p_{\text{T}}^{\text{jet}} > 10$ GeV	electron $p_{\text{T}}^{e} > 20/22$ GeV
N_{jet}	$\geq$2 jets (130, 30 GeV)	$\geq$2 jets (130, 30 GeV)	$\geq$1 jet (50 GeV)	
$E_{\text{T}}^{\text{miss}}$	$E_{\text{T}}^{\text{miss}} > 130/150$ GeV	$E_{\text{T}}^{\text{miss}} > 130/150$ GeV		
$N_{e,\mu}$	0	0	1 μ (20 GeV)	1 e (25 GeV)
N_{τ}	=1 medium (20 GeV) =0 additional loose	$\geq$2 loose (20 GeV)	$\geq$1 medium (20 GeV)	$\geq$1 medium (20 GeV)
Kinematic criteria	$\Delta\phi(\text{jet}_{1,2}, E_{\text{T}}^{\text{miss}}) > 0.3$ $E_{\text{T}}^{\text{miss}}/m_{\text{eff}} > 0.3$, $m_T > 110$ GeV $H_T > 775$ GeV	$\Delta\phi(\text{jet}_{1,2}, E_{\text{T}}^{\text{miss}}) > 0.3$ $m_T^{\tau_1} + m_T^{\tau_2} > 100$ GeV $H_T > 650$ GeV	$m_T^{\mu} > 100$ GeV $m_{\text{eff}} > 1000$ GeV	$m_T^{e} > 100$ GeV $m_{\text{eff}} > 1000$ GeV

6.6 Background estimation

In this section, the semi-data-driven techniques for estimating the background contributions in the signal region are described. This section will focus primarily on the 2τ final state, with the procedure used to estimate the multi-jet background described in section 6.6.1 and the procedure for the W, Z and top backgrounds described in section 6.6.2. I was solely responsible for the estimate of the multi-jet background, whilst a colleague from the University of Bonn was primarily responsible for the estimate of the W, Z and top backgrounds. I provided cross-checks for these studies. A summary of the background estimation techniques for the 1τ and $\tau + \ell$ final states is presented in sections 6.6.3 and 6.6.4, respectively. These sections are the work of other ATLAS colleagues, but are presented as they are relevant for the full combination of the four final states.

6.6.1 Estimation of the multi-jet background

As with the 2.05fb^{-1} analysis, the observed background yield is dominated by events in which jets have been misidentified as τ-leptons. A multi-jet enriched control region is defined by inverting the requirements designed to suppress this background, as discussed in section 6.5. This control region is used to normalise the multi-jet predictions from MC and to estimate jet fake rates, and the definition of this region closely follows that of the previous analysis. It is isolated by inverting the $\Delta\phi$ cut from the signal selection, requiring that the $E_{\mathrm{T}}^{\mathrm{miss}}$-vector points in the direction of one of the two leading jets. In order to further enrich the region with multi-jet events, an additional requirement on the variable $E_{\mathrm{T}}^{\mathrm{miss}}/m_{\mathrm{eff}}$ is used. The full list of requirements used to define this control region is:

1. Pre-selection, event cleaning and trigger requirements
2. Light lepton veto (no τ-lepton requirement)
3. $\Delta\phi(\mathrm{jet}_1, E_{\mathrm{T}}^{\mathrm{miss}})$ or $\Delta\phi(\mathrm{jet}_2, E_{\mathrm{T}}^{\mathrm{miss}}) < 0.3$
4. $E_{\mathrm{T}}^{\mathrm{miss}}/m_{\mathrm{eff}} < 0.4$

Figure 6.6 shows the distributions of $\Delta\phi$ between the two leading jets and the $E_{\mathrm{T}}^{\mathrm{miss}}$, for events surviving all of the signal selection requirements, up to and including the rejection of events containing light leptons. The shape of these two distributions is seen to be well described in MC, and the regions where $\Delta\phi < 0.3$ are dominated by the contribution from multi-jet events.

In order to determine a scale factor to correct for a possible mis-modelling of the normalisation applied to MC events, w_{QCD}, the number of events observed in the control

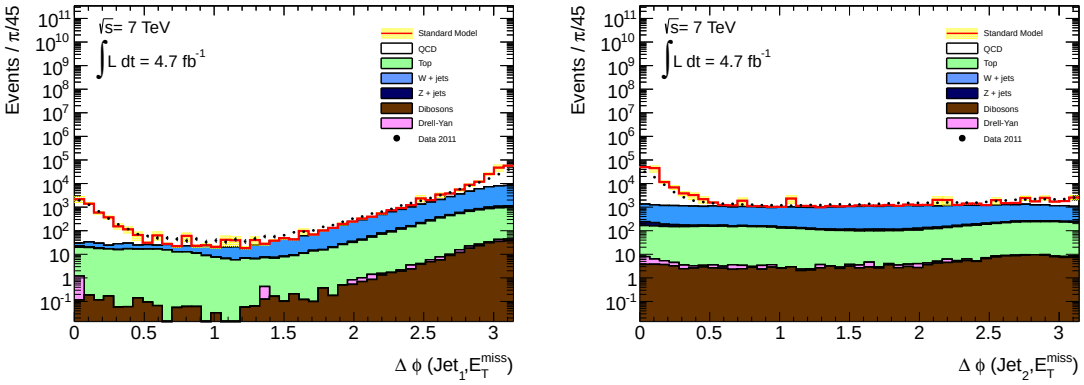

(a) (b)

Figure 6.6: Distributions of $\Delta\phi$ between the (a) leading and (b) sub-leading jet and the $E_{\mathrm{T}}^{\mathrm{miss}}$. All of the nominal signal selection up to and including the rejection of events containing a light lepton has been applied, but there is no requirement on τ-lepton multiplicity.

	Events
N_{QCD}^{QCD}	91153.10 ± 7752.31
$N_{QCD}^{\mathrm{nonQCD}}$	3902.26 ± 156.41
N_{QCD}^{data}	93713 ± 773.42

Table 6.7: The number of events and associated statistical uncertainty in the multi-jet control region for data (N_{QCD}^{data}), multi-jet MC (N_{QCD}^{QCD}) and non-multi-jet MC ($N_{QCD}^{\mathrm{nonQCD}}$).

region for both data and simulation are compared. A similar procedure was outlined in section 5.7.2 for the previous analysis, and w_{QCD} is calculated with equation 6.1. Unlike in the previous analysis there is no requirement on the τ-multiplicity for this calculation.

$$\omega_{QCD} = \frac{N_{QCD}^{\mathrm{data}} - N_{QCD}^{\mathrm{nonQCD}}}{N_{QCD}^{\mathrm{QCD}}} \ , \tag{6.1}$$

where N_{QCD}^{data} denotes the number of data events in the multi-jet control region, N_{QCD}^{QCD} is the number of MC multi-jet events, and $N_{QCD}^{\mathrm{nonQCD}}$ is the number of MC events for non-multi-jet processes. These numbers can be found in table 6.7. The value of ω_{QCD} is found to be 0.99 ± 0.09, and a comparison of the $E_{\mathrm{T}}^{\mathrm{miss}}/m_{\mathrm{eff}}$ distribution for the unscaled MC and data events in this region can be seen in figure 6.7. Several kinematic distributions in this control region can be seen in figure 6.8, and good agreement is observed between data and MC.

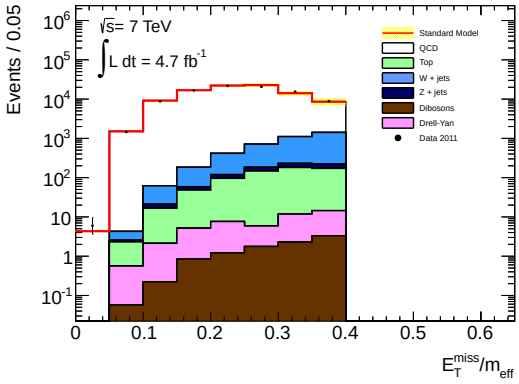

(a)

Figure 6.7: $E_{\mathrm{T}}^{\mathrm{miss}}/m_{\mathrm{eff}}$ in the multi-jet control region

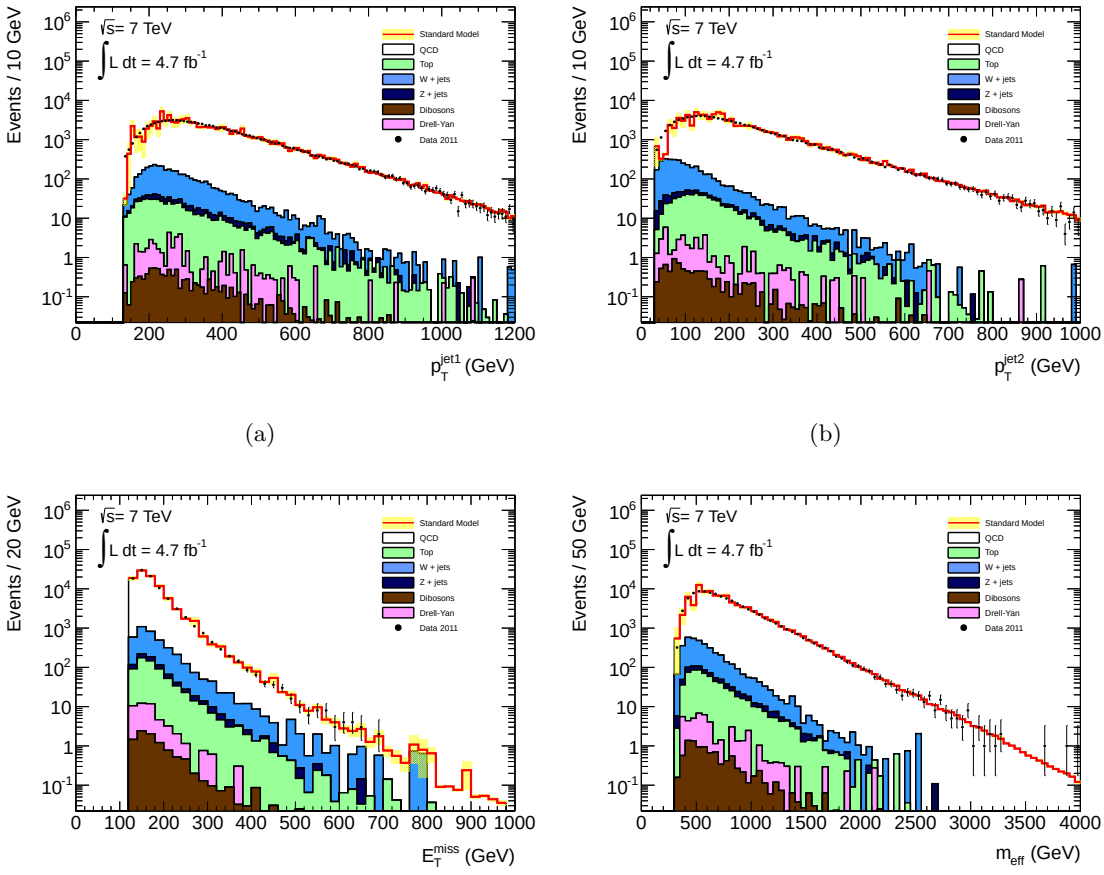

(a) (b)

(c) (d)

Figure 6.8: Kinematic variables in the multi-jet control region: the (a) leading and (b) sub-leading jet p_{T}, (c) the $E_{\mathrm{T}}^{\mathrm{miss}}$ and (d) the m_{eff}.

Due to the limited event yield available in the multi-jet simulated samples after requiring a reconstructed τ-lepton the approach used in the previous analysis for correcting the jet fake rate in MC can not be used, due to the large resulting statistical uncertainty.

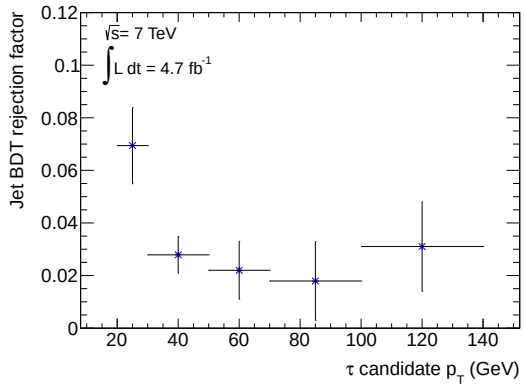

Figure 6.9: The rejection factor of the jet BDT requirement as function of the τ-candidate p_{T}. The final bin contains all τ-candidates with $p_{\mathrm{T}} \geq 100$ GeV

Instead, the rejection of hadronic jets due to the "loose" jet BDT is measured in data, and this is used to estimate the multi-jet contribution to the signal region. To do this, an "extra loose" level of τ-identification is constructed by removing the check on the jet BDT score from the "loose" τ-ID. The rest of the τ-ID remains unchanged. The signal selection is then repeated on the modified dataset, containing the "extra-loose" τ-candidates, and the contribution to the signal region is then scaled to correspond to the measured jet BDT rejection factor.

To do this in a data-driven way, the data events in the multi-jet control region that contain zero reconstructed "loose" τ-leptons, which are dominated by multi-jet events, are used. The events in this region that contain "extra loose" τ-candidates are identified, and a new region is defined for these events in which there is a single "extra loose" τ-candidate present. A second (disjoint) region is defined for the data events in the multi-jet control region in which there is one identified "loose" τ-candidate. The efficiency of the jet BDT rejection of fake τ-candidates from jets is then estimated, by comparing the number of data events in the 1 "loose" τ-candidate region and in the 1 "extra loose" τ-candidate region. This is possible because the only difference between these two regions is whether or not the τ-candidate passes the jet BDT requirement.

To estimate this rejection factor in data it is possible to take the ratio of the number of data events in the one "loose" τ-candidate region and in the "extra loose" one τ-candidate region, subtracting from both the non-multi-jet MC contribution to their respective region. This calculation results in a jet BDT rejection factor of 0.039 ± 0.009 per τ-candidate. To further refine this approach the rejection factor is calculated as a function of the p_{T} of the τ-candidate. This can be seen in figure 6.9.

	Events
$N_{0\tau}^{\mathrm{QCD}}$	81754.70 ± 6993.38
$N_{0\tau}^{\mathrm{nonQCD}}$	3005.37 ± 135.49
$N_{0\tau}^{\mathrm{data}}$	86888 ± 743.40
$N_{1\tau}^{\mathrm{QCD}}$	14406.90 ± 2617.82
$N_{1\tau}^{\mathrm{nonQCD}}$	951.00 ± 203.77
$N_{1\tau}^{\mathrm{data}}$	17712 ± 331.91

Table 6.8: Number of events in the "extra loose" 0 and 1τ regions. N^{QCD} corresponds to the number of multi-jet MC events, N^{nonQCD} to the number of non-multi-jet MC events and N^{data} to the number of events in data. The subscript corresponds to the number of "extra loose" τ-candidates required.

To estimate the multi-jet background in the signal region, the simulated multi-jet events with an "extra loose" τ-selection are allowed to propagate through the signal selection, with each event weighted to the appropriate p_{T}-dependent jet BDT rejection factor. This is applied once for each of the reconstructed τ-leptons in the event. After applying the measured jet BDT rejection factor, once per τ-candidate, there is an estimated 0.17 ± 0.15 multi-jet events in the signal region.

To validate the use of the "extra loose" τ-candidates, a comparison is made between MC and data for the 0 and 1 "extra loose" τ-candidate regions, where the "extra loose" selection is applied to both data and MC. The number of events in these regions can be seen in table 6.8, and the $E_{\mathrm{T}}^{\mathrm{miss}}/m_{\mathrm{eff}}$ distributions are shown in figure 6.10. Calculating ω_{QCD} from the "extra loose" τ-candidate regions (using equation 6.1) results in 1.03 ± 0.09. Several kinematic distributions in the 0 and 1 "extra loose" τ-candidate regions can be seen in figure 6.11.

As a further step of validation, a comparison is made between data and MC for several kinematic variables for the "loose" τ-ID selection, where the multi-jet contribution is replaced with the "extra loose" selection, scaled by the jet BDT rejection factor. This can be see in figure 6.12, and good agreement is observed between data and MC.

As a cross check to the jet BDT rejection technique, a study is performed in the same control region, but this time requiring that there is one reconstructed τ-candidate. The method used by the previous analysis is then applied to estimate the required correction to the jet fake rate in MC (as described in section 5.7.2). Figure 6.13 shows the $E_{\mathrm{T}}^{\mathrm{miss}}/m_{\mathrm{eff}}$

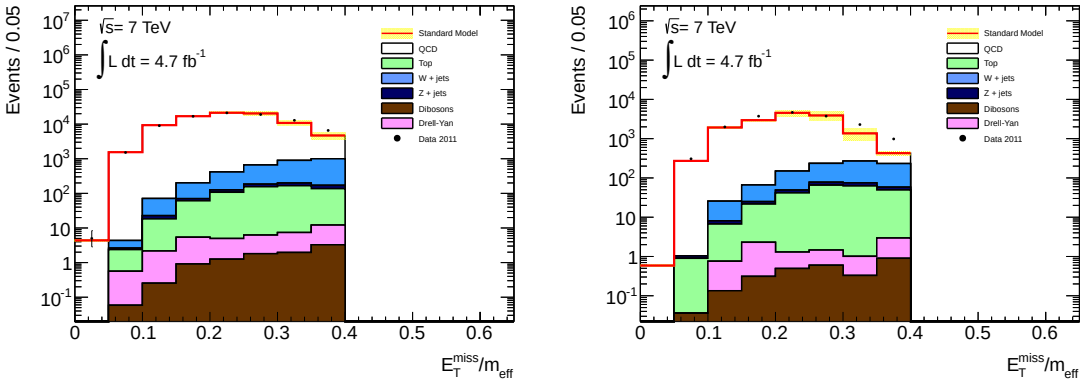

(a) (b)

Figure 6.10: $E_{\mathrm{T}}^{\mathrm{miss}}/m_{\mathrm{eff}}$ in the "extra loose" multi-jets control region, (a) inclusive or (b) 1 reconstructed τ-candidate.

	Events
$N_{1\tau}^{QCD}$	416.83 ± 139.20
$N_{1\tau}^{nonQCD}$	349.12 ± 40.20
$N_{1\tau}^{data}$	1026 ± 78.87

Table 6.9: Number of events in the 1τ sideband.

distributions in this regions, where the multi-jet contribution has been scaled by ω_{QCD}. The fake rate correction factor, f, is obtained from the 1τ region using the equation:

$$f = \frac{N_{1\tau}^{data} - N_{1\tau}^{nonQCD}}{\omega_{QCD} \cdot N_{1\tau}^{QCD}} \ , \tag{6.2}$$

The $E_{\mathrm{T}}^{\mathrm{miss}}/m_{\mathrm{eff}}$ distribution in the 1 τ-candidate region after this correction factor has been applied is shown in figure 6.13. The number of events in the 1τ region used to compute the correction factor are listed in table 6.9. This factor is found to be 1.62 ± 0.57. The limited multi-jet MC event yield available in the 1 τ-candidate region is responsible for the large uncertainty on this scale factor.

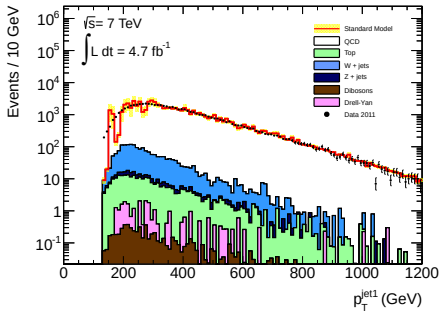

(a) $p_{\mathrm{T}}^{\mathrm{jet1}}$: 0 extra-loose τ sideband

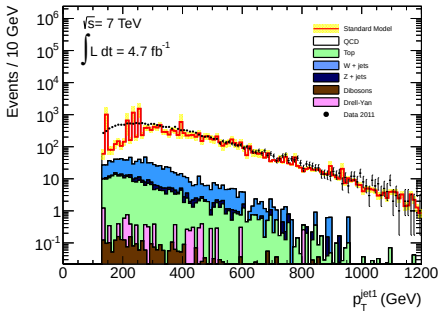

(b) $p_{\mathrm{T}}^{\mathrm{jet1}}$: 1 extra-loose τ sideband

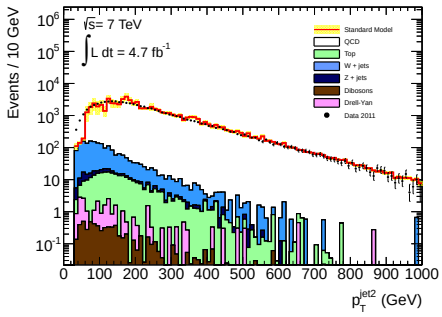

(c) $p_{\mathrm{T}}^{\mathrm{jet2}}$: 0 extra-loose τ sideband

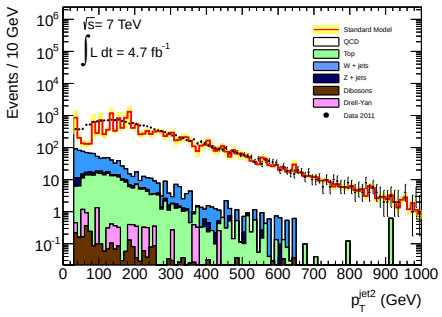

(d) $p_{\mathrm{T}}^{\mathrm{jet2}}$: 1 extra-loose τ sideband

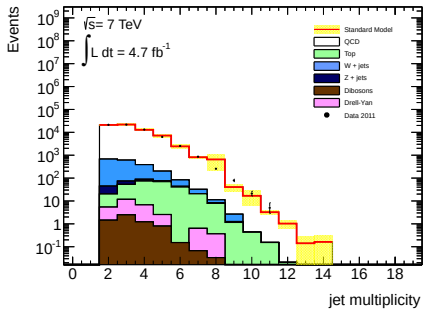

(e) Jet multiplicity: 0 extra-loose τ sideband

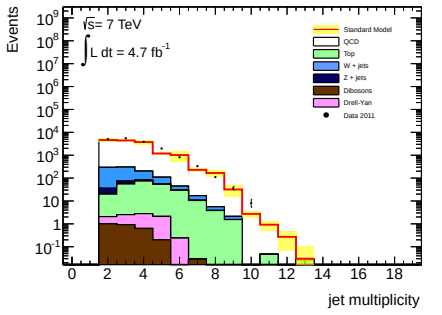

(f) Jet multiplicity: 1 extra-loose τ sideband

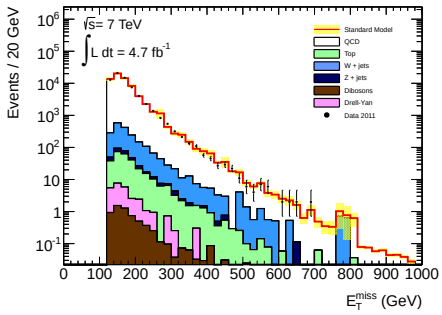

(g) $E_{\mathrm{T}}^{\mathrm{miss}}$: 0 extra-loose τ sideband

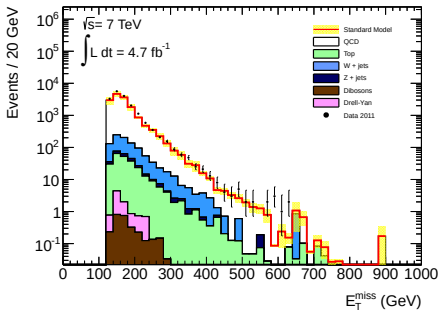

(h) $E_{\mathrm{T}}^{\mathrm{miss}}$: 1 extra-loose τ sideband

Figure 6.11: Kinematic variables in the 0 (left-handed column) and 1 (right-handed column) "extra loose" τ sideband of the multi-jet control region.

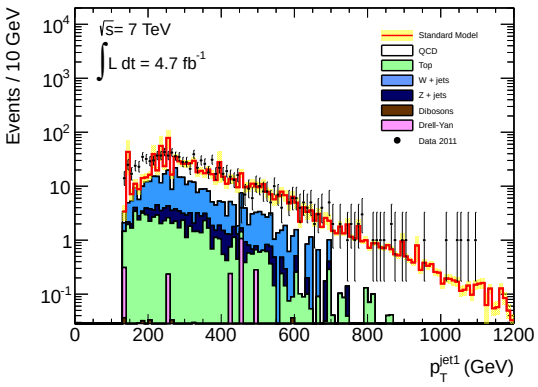

(a)

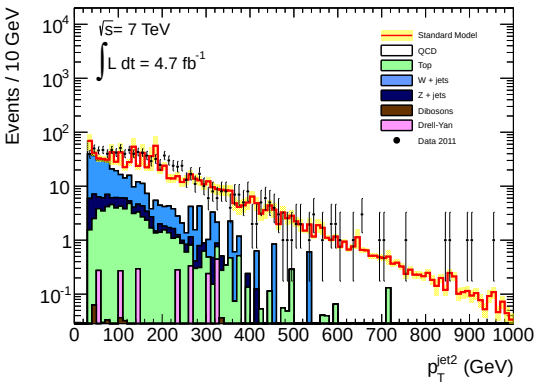

(b)

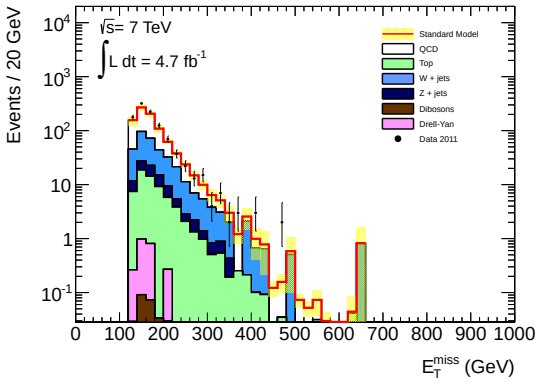

(c)

Figure 6.12: Validation plots for the jet BDT rejection method. Kinematic variables in the 1τ sideband, where the multi-jet contribution is the jet BDT scaled "extra loose" τ-candidate selection, and all other data and MC is with the standard "loose" τ-ID selection.

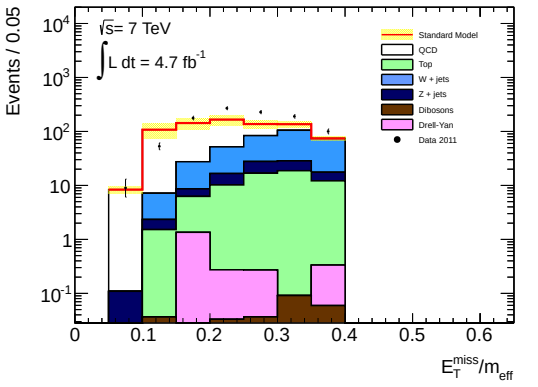

(a)

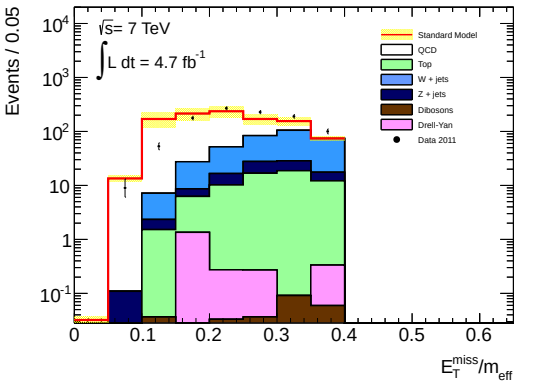

(b)

Figure 6.13: $E_{\mathrm{T}}^{\mathrm{miss}}/m_{\mathrm{eff}}$ in the 1τ sideband, (a) before and (b) after scaling.

6.6.2 Estimation of W/Z+jets and top backgrounds

Once all of the signal selection requirements have been applied, the dominant SM background contributions to the 2τ signal region are events from top and W/Z+jets production, and a data-driven estimation of these contributions is performed. The selection efficiency for the signal region and control regions will be different for each of these processes, and individual normalisation factors are computed by defining a separate control region for each background. For the $2.05\,\text{fb}^{-1}$ analysis the event yield was not sufficient to separate the $W+\text{jets}$ and top contributions, and a combined normalisation factor was calculated. These are treated separately for this analysis. The estimation of the $Z+\text{jets}$ contribution in the previous analysis was taken directly from the simulated samples, but for this analysis it is estimated using a semi-data-driven technique.

Three control regions have been defined for the estimation of these backgrounds, with each region being dominated by events from one of the three processes. When defining the control regions an effort is made to ensure that they have similar kinematic constraints to the signal region, and for this reason all of the nominal signal selection requirements, up to and including the $\Delta\phi$ requirement, are applied. At this stage the control regions are then defined, typically by inverting the selection requirement that is designed to suppress the background of interest. A small buffer region is included when inverting these requirements to ensure that events are not shifted across the decision boundary when variations due to systematic uncertainties are evaluated. The definition of the control regions can be found in table 6.10.

Background process	H_{T}	$m_{\text{T}}^{\tau_1} + m_{\text{T}}^{\tau_2}$	N_{bjet}
Top	< 550 GeV	≥ 100 GeV	≥ 1
W+jets	< 550 GeV	≥ 100 GeV	$= 1$
Z+jets	< 550 GeV	≤ 80 GeV	

Table 6.10: Definitions of the $W/Z+\text{jets}$ and top control regions for the 2τ analysis. All of the other requirements from the nominal selection, up to and including the $\Delta\phi$ requirement, are included.

For all of the control regions the H_{T} is required to be less than 550 GeV, to ensure that they are orthogonal to the signal region. This requirement also ensures that there is negligible signal contamination in these control regions. The $Z+\text{jets}$ region inverts the $m_{\text{T}}^{\tau_1} + m_{\text{T}}^{\tau_2}$ requirement designed to suppress it (including a 20 GeV buffer region), but

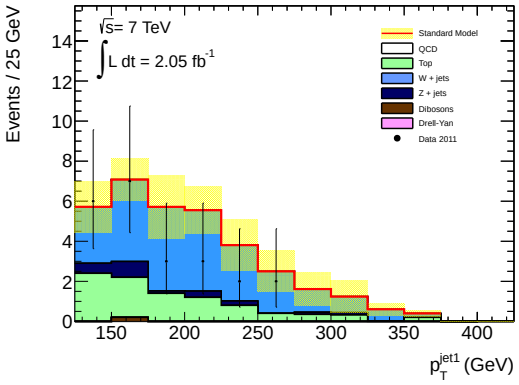

(a) W+jets control region

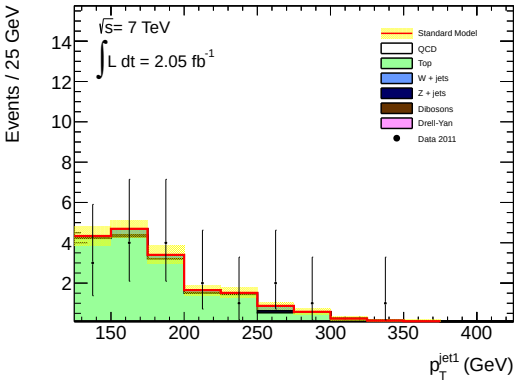

(b) Top control region

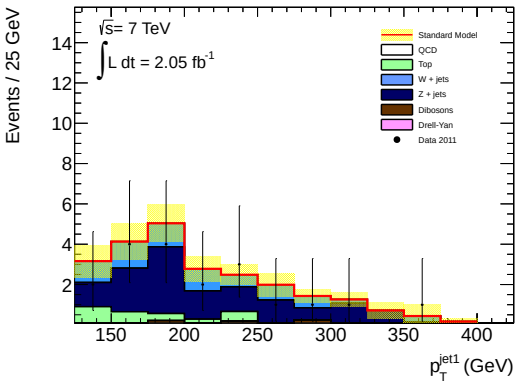

(c) Z+jets control region

Figure 6.14: The leading jet p_{T} in the (a) W+jets, (b) top, and (c) Z+jets control regions defined for the 2τ analysis. The dominance of a single background in each region is clearly visible.

this requirement is kept in place for the W + jets and top regions, to reduce the Z + jets contamination. These regions are divided using the b-tagging capabilities of the ATLAS detector, as the decay of top quarks will contain a b-quark in almost all cases and requiring at least one reconstructed b-jet leads to a relatively pure top control region.

The number of events for each of these control regions can be found in table 6.11. Each region is dominated by the appropriate background process, although a non-negligible contribution from the other processes still remains. The so-called "matrix method", described below, is used to simultaneously derive the normalisation factors in the three control regions. The leading jet p_{T} distributions in the three control regions are shown in figure 6.14.

To account for the cross-contamination of background samples in the three control regions the normalisation factors are calculated in a simultaneous way, via a matrix equa-

Control region	W+jets	Top	Z+jets	Other MC	Data
Top	1.07	16.47	0.28	0.08	18
W+jets	24.97	8.09	2.09	0.60	23
Z+jets	7.21	2.59	14.10	0.49	20

Table 6.11: Contributions from different background processes for the W, Z, and top control regions defined for the 2τ analysis.

tion:

$$\underbrace{\begin{pmatrix} N_{top}^{\text{data}} - N_{top}^{\text{QCD,data}} - N_{top}^{\text{MC,rest}} \\ N_{W}^{\text{data}} - N_{W}^{\text{QCD,data}} - N_{W}^{\text{MC,rest}} \\ N_{Z}^{\text{data}} - N_{Z}^{\text{QCD,data}} - N_{Z}^{\text{MC,rest}} \end{pmatrix}}_{\vec{N}} = \underbrace{\begin{pmatrix} N_{top}^{\text{top}} & N_{top}^{\text{W}} & N_{top}^{\text{Z}} \\ N_{W}^{\text{top}} & N_{W}^{\text{W}} & N_{W}^{\text{Z}} \\ N_{Z}^{\text{top}} & N_{Z}^{\text{W}} & N_{Z}^{\text{Z}} \end{pmatrix}}_{A} \underbrace{\begin{pmatrix} \omega_{top} \\ \omega_{W} \\ \omega_{Z} \end{pmatrix}}_{\vec{\omega}}, \tag{6.3}$$

where N_{CR}^{data} is the observed data events in the control region "CR", $N_{CR}^{\text{QCD,data}}$ is the data-driven multi-jet estimate and $N_{CR}^{\text{MC,rest}}$ is the sum of the remaining MC contributions in this control region (from backgrounds other than $t\bar{t}$, $W+\text{jets}$ or $Z+\text{jets}$). The small Drell-Yan contribution is included with the $Z+\text{jets}$ background as they share the same production process and MC generator, and the only difference is the invariant mass of the lepton pair. The MC prediction is used to obtain the values for the elements of matrix A, and the vector $\vec{\omega}$ (containing the normalisation factors) is obtained by inverting the matrix A, and multiplying this with $\vec{N}$:

$$\vec{\omega} = A^{-1}\vec{N} \tag{6.4}$$

This processes is repeated with all of the contributing parameters being varied within the range of their associated uncertainties, in order to calculate the uncertainties on each of the normalisation factors. Toy Monte Carlo is generated for this process, and the uncertainty on the normalisation factors is taken from the width of the associated distribution, as shown in figure 6.15. The normalisation factors and associated uncertainties obtained via this process are listed in table 6.12(a).

The matrix method also allows for the simultaneous evaluation of the correlation between each of the calculated normalisation factors, and these can be found in table 6.12(b). The W+jets and top events show significant anti-correlation, which is also true for W+jets and $Z+\text{jets}$ events. The top and $Z+\text{jets}$ events are almost fully uncorrelated. These anti-correlations are propagated to the estimation of the uncertainties on the SM back-

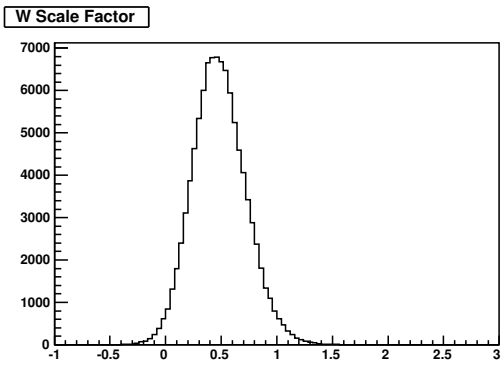

(a) $W +$ jets normalisation factor

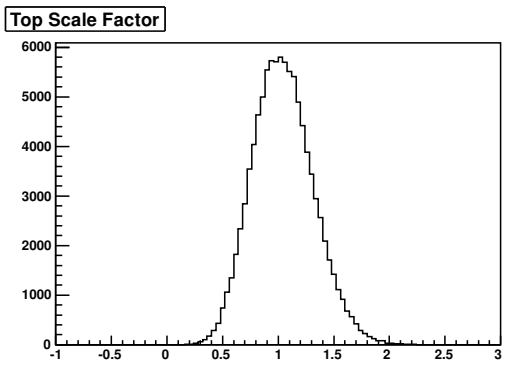

(b) Top normalisation factor

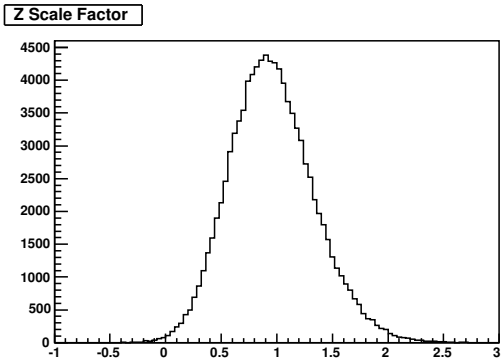

(c) $Z +$ jets normalisation factor

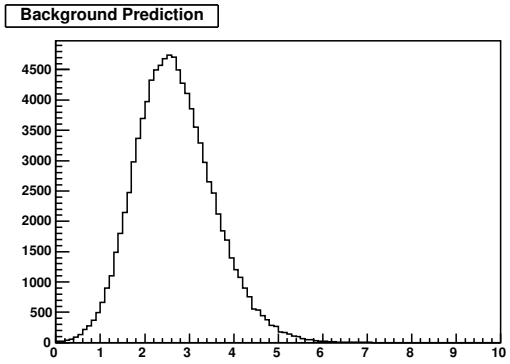

(d) Background expectation

Figure 6.15: Distributions of the computed normalisation factors (a-c) and in the background prediction (d). Each entry consists of one iteration of toy Monte Carlo with all input quantities varied randomly within their statistical uncertainties.

Table 6.12: (a) Measured normalisation factors for SM background contributions, and (b) correlations between the factors.

(a)

Background	Normalisation factor
W+jets	0.48 ± 0.24
Top	1.04 ± 0.27
Z+jets	0.96 ± 0.38

(b)

	W+jets	Top	Z+jets
W+jets	1	-0.41	-0.38
Top	-0.41	1	-0.02
Z+jets	-0.38	-0.02	1

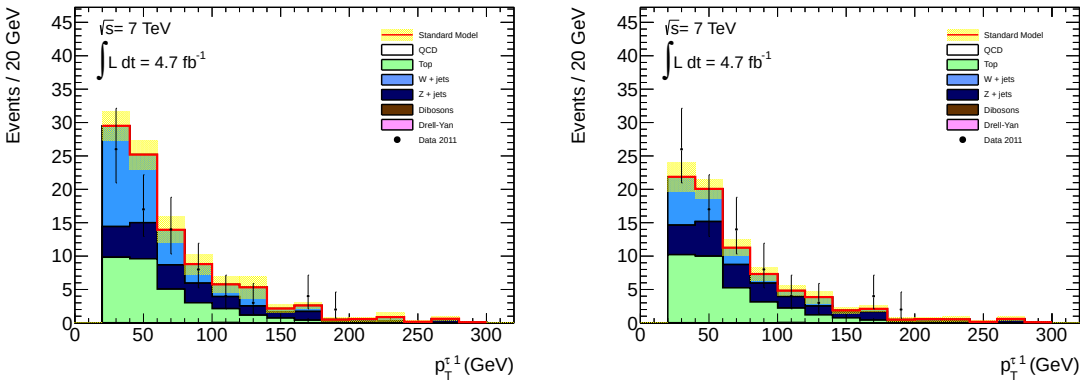

(a) Unscaled (b) Scaled

Figure 6.16: Leading τ-candidate p_{T} after the $\Delta\phi$ requirement, with and without the computed normalisation factors applied. An overall improvement of the data/MC agreement is visible.

grounds in the signal region by recalculating the estimated background for every set of toy Monte Carlo, whilst also varying the background prediction in the signal region within the associated uncertainty. After this process has been applied the expected SM contribution to the signal region is found to be $2.74 \pm 0.88^{\mathrm{stat}}$. Ignoring the anti-correlation results in a larger statistical uncertainty of 0.93. Figure 6.16 shows the leading τ-candidate p_{T} distribution, before and after the application of the normalisation factors.

Several studies are performed to test how robust the calculated normalisation factors are against changes in the analysis. A brief summary of these is presented in this section, and further details can be found in [163]. The true τ-lepton composition in the control and signal regions is studied to check that these are consistent. This is necessary to ensure that the normalisation factors calculated in the control regions can legitimately be applied to the events in the signal region. The factors are designed to correct a mis-modelling of the τ-fake rate and a different composition of true and fake τ-candidates would require a

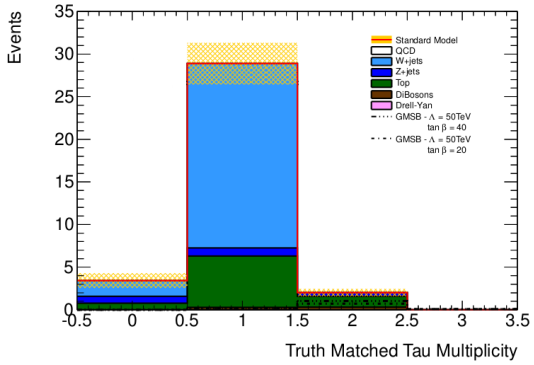

(a) W control region

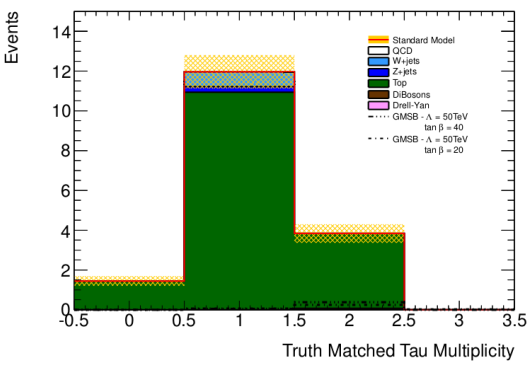

(b) Top control region

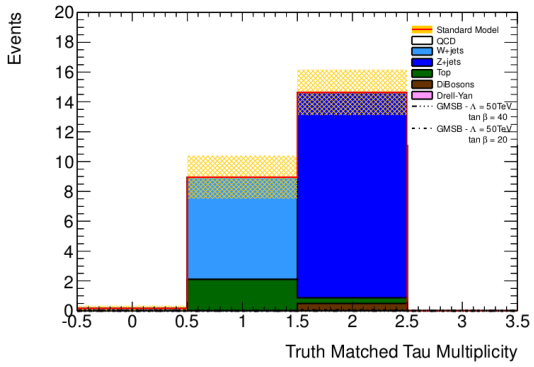

(c) Z control region

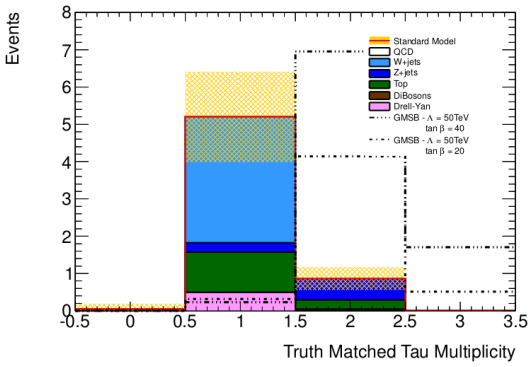

(d) Signal region

Figure 6.17: Number of reconstructed true τ-leptons per event in the W, top, and Z control regions (a-c) and in the signal region (d) for the 2τ analysis. Plots shown are for $\int \mathcal{L}\,\mathrm{dt} = 4.73\ \mathrm{fb}^{-1}$.

different normalisation factor. Figure 6.17 shows the the true composition of each of these regions.

As was the case for the $2.05\,\mathrm{fb}^{-1}$ analysis, most of the SM events passing the full selection contain one true and one fake τ-candidate. The signal region, and the W and top control regions are dominated by events containing one true τ-lepton ($\approx$75%). For the simulated top samples there are a small number of events with two true τ-candidates in both regions, and for $W+\mathrm{jets}$ there are a small number of events in the control region that contain no true τ-candidates, which is not observed in the signal region. These effects contribute well below 10% of events. For the simulated $Z+\mathrm{jets}$ sample in the Z control region all events contain two true τ-candidates, whilst in the signal region there is also a small number of Z events with only one true τ-candidate. These slight discrepancies are not large enough to invalidate the calculated normalisation factors. The full details of this study can be found in [163].

To check that the computed normalisation factors are independent of the control region definition, they are calculated for an H_{T} threshold of 550, 600 and 650 GeV. The calculated normalisation factors and resulting total SM background prediction in the signal region are listed in table 6.13, and good agreement is observed between the three regions.

	$H_{\mathrm{T}} < 550$ GeV	$H_{\mathrm{T}} < 600$ GeV	$H_{\mathrm{T}} < 650$ GeV
W+jets scaling:	0.48 ± 0.24	0.44 ± 0.22	0.49 ± 0.23
Top scaling:	1.04 ± 0.27	0.99 ± 0.26	1.00 ± 0.26
Z+jets scaling:	0.96 ± 0.38	0.92 ± 0.34	0.91 ± 0.35
SM contribution in signal region:	2.68 ± 0.88	2.51 ± 0.83	2.63 ± 0.85

Table 6.13: Obtained normalisation factors and SM background predictions by varying H_{T} threshold for the control regions. All of the values are robust against the changes.

6.6.3 1τ final state

This section will summarise the background estimation in the 1τ channel. Further details can be found in [163]. After the full signal selection requirements have been applied, the dominant SM backgrounds are top, W+jets, Z+jets and multi-jets events, with a small contribution from Drell-Yan and diboson production.

The W+jets and WZ contribution to the signal region is estimated by scaling the number of corresponding MC events observed in the signal region with the ratio of data to MC events in the W+jets control region. The definition of this, and all other control regions for the four analyses, can be found in table 6.16. The normalisation factors for W + jets and top samples are computed separately for events in which the τ-candidates are true τ-leptons and for those in which jets are misidentified as τ-leptons.

For the W+jets events with true τ-candidates, the charge asymmetry method [170, 171] is used to obtain the normalisation factor. To calculate the normalisation factor for the top events with true τ-candidates, the number of b-tagged data events in the top control region is fitted to a template from MC simulation. In the case of fake τ-candidates, the matrix method is used for both the W+jets and the top processes. The parameters in the normalisation factor vector $\vec{\omega}$ are ω_W^{fake}, ω_W^{true}, $\omega_{\mathrm{top}}^{\mathrm{fake}}$ and $\omega_{\mathrm{top}}^{\mathrm{true}}$. The fake τ dominated region is isolated by requiring that $m_{\mathrm{T}} > 110\,\mathrm{GeV}$, whilst the true τ dominated region defined by requiring $m_{\mathrm{T}} < 70\,\mathrm{GeV}$. The obtained values of $\omega_{\mathrm{top}}^{\mathrm{true}}$ from the matrix method and

from the template fit are in good agreement. The factor ω_W^{true} obtained from the charge asymmetry approach agrees within 2σ with the value obtained from the matrix method. A systematic uncertainty is assigned to account for the difference between the two ω_W^{true} values.

Top	$0.61 \pm 0.35^{\text{stat}} \pm 0.22^{\text{syst}}$
W+jets	$0.128 \pm 0.234^{\text{stat}} \pm 0.20^{\text{syst}}$
Z+jets	$0.22 \pm 0.22^{\text{stat}} \pm 0.13^{\text{syst}}$
Multi-jets	$0.17 \pm 0.04^{\text{stat}} \pm 0.11^{\text{syst}}$
Drell-Yan	< 0.36
Diboson	< 0.05
Total	$1.31 \pm 0.37^{\text{stat}} \pm 0.65^{\text{syst}}$

Table 6.14: Number of expected SM events in the signal region for the 1τ channel.

The Z+jets background is dominated by $Z \to \nu\nu$ events, where a jet is misidentified as a τ-lepton. The expected Z+jets contribution to the signal region is estimated from data by measuring the data/MC ratio from $Z \to \ell^+\ell^-$ decays, in the Z+jets control region (defined in table 6.16). The procedure for estimating the multi-jet background is consistent with the method used in the 2τ channel. A full breakdown of the contributions from individual processes to the signal region can be seen in table 6.14 [163].

6.6.4 $\tau + \ell$ final states

This section will summarise the background estimation in the τ+e and τ+μ final states, and further details can be found in [163]. For both final states the dominant SM backgrounds are top, W+jets and diboson events, whilst for the τ+e channel there are also non-negligible contributions from Z+jets and multi-jet events.

The contribution to the signal region from top production consists of events where the light lepton candidate is a true light lepton, but the τ-candidate can be either a true τ-lepton or a misidentified jet. The W + jets background, however, is dominated by events in which the τ-candidate is a misidentified jet. To account for this, the top control region is separated into a region dominated by true τ-candidates ($100\,\text{GeV} < m_{\text{T}}^{e,\mu} < 150\,\text{GeV}$), and a region dominated by fake τ-candidates ($50\,\text{GeV} < m_{\text{T}}^{e,\mu} < 100\,\text{GeV}$). The matrix method is then used to estimate the true and fake τ-candidate top and W+jets background contributions to the signal region.

The Z + jets background is found to be well described by simulation, and the signal region contribution is estimated directly from the MC samples. The multi-jet background

	τ+e	τ+μ
top	$1.41 \pm 0.27^{\text{stat}} \pm 0.84^{\text{syst}}$	$0.36 \pm 0.18^{\text{stat}} \pm 0.26^{\text{syst}}$
W+jets	$0.24 \pm 0.17^{\text{stat}} \pm 0.27^{\text{syst}}$	$0.27 \pm 0.21^{\text{stat}} \pm 0.14^{\text{syst}}$
Z+jets	$0.17 \pm 0.12^{\text{stat}} \pm 0.05^{\text{syst}}$	$0.05 \pm 0.05^{\text{stat}} \pm 0.01^{\text{syst}}$
QCD	$0.22 \pm 0.30^{\text{stat}}$	$0.01 \pm 0.01^{\text{stat+syst}}$
Drell-Yan	0	< 0.002
Diboson	$0.26 \pm 0.12^{\text{stat}} \pm 0.11^{\text{syst}}$	$0.11 \pm 0.04^{\text{stat}} \pm 0.02^{\text{syst}}$
Total	$2.31 \pm 0.40^{\text{stat}} \pm 1.40^{\text{syst}}$	$0.79 \pm 0.28^{\text{stat}} \pm 0.28^{\text{syst}}$

Table 6.15: Number of expected SM events in the signal region for the $\tau + \ell$ channels.

is comprised of events containing mis-identified prompt leptons. A comparison is made between the event yield with and without the lepton isolation requirement, and a data-driven estimate for the signal region contribution is obtained following the method described in [172]. The Drell-Yan and diboson contributions are estimated directly from the simulated samples. For both the $\tau + \ell$ channels, table 6.15 lists the contributions from the SM processes to the signal region, along with the associated systematic and statistical uncertainties.

Background	1τ	2τ	$\tau+\mu$	$\tau+e$
$t\bar{t}$	$\Delta(\phi_{\mathrm{jet}_{1,2}-\vec{p}_{\mathrm{T}}^{\,\mathrm{miss}}}) > 0.3\,\mathrm{rad}$ $m_{\mathrm{T}} < 70\,\mathrm{GeV}$ $E_{\mathrm{T}}^{\mathrm{miss}}/m_{\mathrm{eff}} > 0.3$ b-tag template fit	$\Delta(\phi_{\mathrm{jet}_{1,2}-\vec{p}_{\mathrm{T}}^{\,\mathrm{miss}}}) > 0.3\,\mathrm{rad}$ $m_{\mathrm{T}}^{\tau_1} + m_{\mathrm{T}}^{\tau_2} \geq 100\,\mathrm{GeV}$ $H_{\mathrm{T}} < 550\,\mathrm{GeV}$ $N_{b-\mathrm{tag}} \geq 1$	$30\ \mathrm{GeV} < E_{\mathrm{T}}^{\mathrm{miss}} < 100\ \mathrm{GeV}$ $50\,\mathrm{GeV} < m_{\mathrm{T}}^{e,\mu} < 150\,\mathrm{GeV}$ $N_{b-\mathrm{tag}} \geq 1$	
W+jets	$\Delta(\phi_{\mathrm{jet}_{1,2}-\vec{p}_{\mathrm{T}}^{\,\mathrm{miss}}}) > 0.3\,\mathrm{rad}$ $m_{\mathrm{T}} < 70\,\mathrm{GeV}$ $E_{\mathrm{T}}^{\mathrm{miss}}/m_{\mathrm{eff}} > 0.3$	$\Delta(\phi_{\mathrm{jet}_{1,2}-\vec{p}_{\mathrm{T}}^{\,\mathrm{miss}}}) > 0.3\,\mathrm{rad}$ $m_{\mathrm{T}}^{\tau_1} + m_{\mathrm{T}}^{\tau_2} \geq 100\,\mathrm{GeV}$ $H_{\mathrm{T}} < 550\,\mathrm{GeV}$ $N_{b-\mathrm{tag}} = 0$	$30\ \mathrm{GeV} < E_{\mathrm{T}}^{\mathrm{miss}} < 100\ \mathrm{GeV}$ $50\,\mathrm{GeV} < m_{\mathrm{T}}^{e,\mu} < 150\,\mathrm{GeV}$ $N_{b-\mathrm{tag}} = 0$	
Z+jets	2μ (20 GeV), $\lvert\eta\rvert < 2.4$ $\geq$2 jets (130, 30 GeV) $N_{b-\mathrm{tag}} = 0$	$\Delta(\phi_{\mathrm{jet}_{1,2}-\vec{p}_{\mathrm{T}}^{\,\mathrm{miss}}}) > 0.3\,\mathrm{rad}$ $m_{\mathrm{T}}^{\tau_1} + m_{\mathrm{T}}^{\tau_2} < 80\,\mathrm{GeV}$ $H_{\mathrm{T}} < 550\,\mathrm{GeV}$	MC-based normalisation	
Multi-jet	$\Delta(\phi_{\mathrm{jet}_{1,2}-\vec{p}_{\mathrm{T}}^{\,\mathrm{miss}}}) < 0.3\,\mathrm{rad}$ $E_{\mathrm{T}}^{\mathrm{miss}}/m_{\mathrm{eff}} < 0.3$	$\Delta(\phi_{\mathrm{jet}_{1,2}-\vec{p}_{\mathrm{T}}^{\,\mathrm{miss}}}) < 0.3\,\mathrm{rad}$ $E_{\mathrm{T}}^{\mathrm{miss}}/m_{\mathrm{eff}} < 0.4$	compare events with and without lepton isolation [172]	

Table 6.16: Definition of the background control regions (CRs) used to estimate the normalisation of background samples in the four final states: 1τ, 2τ, $\tau+\mu$ and $\tau+e$ [163].

6.7 Systematic uncertainties

Many of the systematic uncertainties have already been described in the context of the $2.05\,\mathrm{fb}^{-1}$ analysis. These include:

- jet and τ energy scale
- jet and τ energy resolution
- $E_{\mathrm{T}}^{\mathrm{miss}}$calculation
- event pile-up
- τ reconstruction efficiency
- τ fake rate
- signal and background MC predictions and cross-sections
- luminosity

The procedure for calculating the effect of the various sources of systematic uncertainty is consistent with the approach used in the previous analysis. The following section will focus on aspects of the systematic uncertainties that are different from the previous analysis.

6.7.1 Jet energy scale

The results of jet energy scale studies by the ATLAS Jet/EtMiss Combined Performance group are implemented in the `JESUncertaintyProvider` tool [152] which is employed in this analysis to rescale the energies of all jets in a correlated way. Additional corrections are taken into account for close-by jets. These are implemented in the `MultijetJESUncertaintyProvider` tool [152] which is used for jets in the region $|\eta| < 2.9$ where a sufficiently good double jet resolution is provided. Further details can be found in [154].

The fractional JES uncertainty in the central region is 2%–4% for jets with p_{T} less than 60 GeV, and it is 2%–2.5% for those with 60 GeV $< p_{\mathrm{T}} <$ 800 GeV. For jets with p_{T} greater than 800 GeV, the uncertainty is between 2.5%–4%. The uncertainty amounts to 7% and 3%, respectively, for jets with p_{T} less than 60 GeV or greater than 60 GeV in the end-cap region, where the central uncertainty is taken as a baseline and the uncertainty due to the intercalibration is added. For jets in the the forward region, a 13% uncertainty is assigned for jets with p_{T} less than 20 GeV [154].

6.7.2 Jet energy resolution

The agreement between the jet energy resolution in data and MC has been studied using the spread of the p_{T} imbalance in di-jet events and with different in-situ techniques, which are described in [154]. A tool, known as `JetEnergyResolutionProvider` [173], has been provided by the Jet/EtMiss Combined Performance Group which gives p_{T} and η dependent resolutions and uncertainties. When studying the variation due to the jet energy resolution all jets are smeared, uncorrelated and randomly with a Gaussian of mean 1, and a standard deviation provided by this tool. As with the jet energy scale, the modified jet energies are propagated to the $E_{\mathrm{T}}^{\mathrm{miss}}$ calculation.

6.7.3 Missing transverse energy

The calculation of the $E_{\mathrm{T}}^{\mathrm{miss}}$ takes the physics objects in the event as an input, and is therefore sensitive to variation in a large range of systematic uncertainties. There is also an effect on the $E_{\mathrm{T}}^{\mathrm{miss}}$ caused by uncertainties on "soft terms", which are the result of either objects below the reconstruction thresholds or energy depositions in the calorimeter which can not be related to physical objects. A scale uncertainty is evaluated for these soft terms by varying their magnitude by 6.5%, as recommended by the ATLAS Jet/EtMiss Combined Performance Group. A resolution uncertainty is also included by applying a smearing depending on the total deposited energy in the calorimeter.

6.7.4 *b*-tagging efficiencies

For the b-tagging used in this analysis, systematic uncertainties based on the efficiencies for tagging jets from c- and b-quarks as well as the mis-tag rate have been studied. The results are implemented in the `CalibrationDataInterface` tool [174], provided by the ATLAS Flavour Tagging Working Group, and used in this analysis.

6.7.5 Generator uncertainties

In order to quantify some of the generator uncertainties, alternative MC samples were used for some of the Standard Model backgrounds. For diboson production, a complete second sample (generated with `SHERPA`) has been used, with the results compared to the nominal `MC@NLO` sample. As the diboson contribution was estimated directly from MC, this is important to reduce the dependence on an accurate modelling of the events in the generator. For the top background, alternative `ALPGEN` samples are used to quantify generator effects.

Systematic	Total	Dibosons	W	Top	Z	Drell-Yan	Multi-jets
Jet energy resolution	-0.065	-0.249	-0.127	0.160	-0.226	-0.155	-0.088
Jet energy scale up	0.056	0.000	-0.094	-0.025	0.932	-0.127	-0.087
Jet energy scale down	-0.041	0.000	0.018	-0.062	-0.270	0.026	-0.100
τ energy scale up	0.103	0.000	0.110	0.094	0.257	-0.012	-0.102
τ energy scale down	-0.067	0.000	0.050	-0.108	-0.406	-0.020	-0.169
τ-ID	-0.011	0.101	-0.004	0.008	-0.020	-0.057	0.020
τ fake rate	0.007	0.000	-0.072	0.016	0.059	0.138	-0.090
b-tag up	-0.047	0.000	-0.034	-0.154	0.031	0.031	-0.002
b-tag down	0.051	0.000	0.013	0.228	-0.059	-0.059	0.010
Soft-terms resolution up	-0.010	0.000	-0.012	0.009	-0.024	-0.024	0.000
Soft-terms resolution down	-0.004	0.000	-0.018	0.019	-0.007	-0.007	0.000
Soft-terms scale up	0.001	0.000	-0.019	0.057	-0.025	-0.025	0.000
Soft-terms scale down	0.003	0.000	-0.017	0.013	0.020	0.020	0.000
Pile-up re-weighting	-0.137	0.298	-0.162	-0.098	0.094	-0.336	0.151
Generator: dibosons	0.013	2.988	0.031	0.001	-0.076	-0.076	0.000
Generator: $t\bar{t}$	0.048	0.000	0.030	0.113	0.016	0.016	0.000
Theory/Extrapolation	0.120	0.000	0.077	0.245	0.077	0.077	0.000
Total systematic uncertainty	0.246	3.015	0.274	0.409	0.974	0.427	0.303
Statistical uncertainty	0.320	0.615	0.598	0.412	0.705	1.076	0.150
Total uncertainty	0.403	3.077	0.657	0.581	1.202	1.158	0.338

Table 6.17: Breakdown of all systematic and statistical uncertainties for the 2τ channel.

6.7.6 Summary of the systematic uncertainties

All of the systematic uncertainties in the 2τ channel are summarised in table 6.17. The systematic uncertainty on the integrated luminosity is only included for the data events and the signal samples. For the background MC samples, only diboson production is calculated directly from the MC and would therefore be affected by this uncertainty, but other systematic uncertainties are significantly larger than 3.9% and therefore this contribution can be safely neglected.

For each background process the individual systematic uncertainties have been combined into a total systematic uncertainty. The method used for the combination was to average the "up" and "down" values of the systematic uncertainty. The τ energy scale and jet energy scale have been treated as fully correlated in the combination, as they are both related to the same detector effects and employ similar reconstructive approaches. For the final systematic uncertainty these values are all combined in quadrature.

The total systematic uncertainty is found to be 25%, slightly smaller than the 32% statistical uncertainty. This statistical uncertainty contains not only a contribution from the limited number of Monte Carlo events in the signal region, but also the uncertainties due to the limited event yield in both data and Monte Carlo in the various control regions. Table 6.18 contains a summary of the dominant systematic uncertainties and the statistical uncertainty for each of the four final states. Further details about the 1τ, $\tau+e$ and $\tau+\mu$

Source of uncertainty	1τ	2τ	$\tau+\mu$	$\tau+e$
CR to SR Extrapolation	27 %	12 %	26 %	29 %
Jet energy resolution	21 %	6.5 %	5.4 %	13 %
Jet energy scale	20 %	4.8 %	11 %	8.5 %
τ energy scale	10 %	8.5 %	0.3 %	4.3 %
Pile-up modelling	5.1 %	14 %	20 %	3.5 %
MC statistics	21 %	32 %	39 %	46 %

Table 6.18: Overview of the major systematic uncertainties and the MC statistical uncertainty for the background estimates in the four final states considered in this analysis.

final states can be found in [163].

6.8 Analysis results

6.8.1 2τ final state

The number of expected signal, background and data events at each stage of the 2τ signal selection process can be seen in table 6.19. The dominant SM processes in the signal region are W/Z+jets and top production, as was seen in the $2.05\,\text{fb}^{-1}$ analysis. There is also a small contribution from both diboson and multi-jet events. The total SM contribution to the signal region is expected to be $2.91 \pm 0.89^{\text{stat}} \pm 0.76^{\text{syst}}$. Distributions for the final two signal selection requirements on the $m_{\text{T}}^{\tau_1} + m_{\text{T}}^{\tau_2}$ and H_{T} are shown in figure 6.18, and good agreement is observed between data and MC.

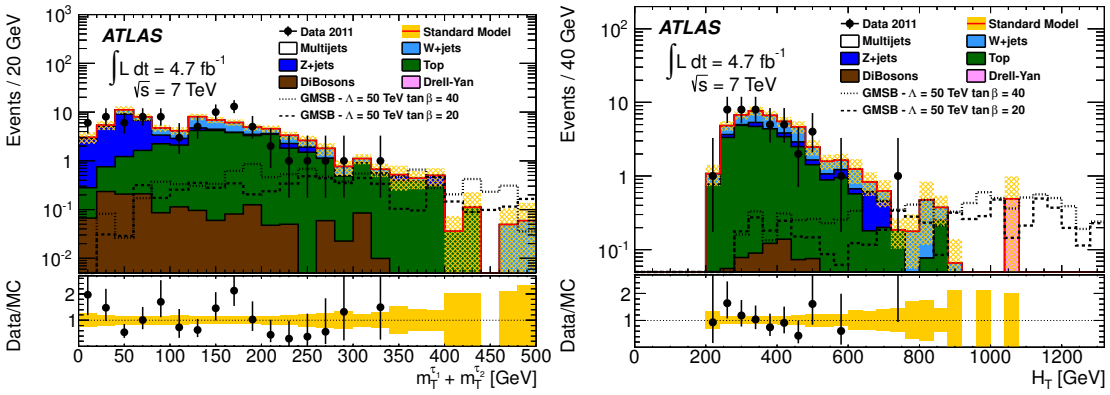

(a) $m_{\text{T}}^{\tau_1} + m_{\text{T}}^{\tau_2}$ distribution after the $\Delta\phi$ requirement

(b) H_{T} distribution after the $m_{\text{T}}^{\tau_1} + m_{\text{T}}^{\tau_2}$ requirement

Figure 6.18: (a) The $m_{\text{T}}^{\tau_1} + m_{\text{T}}^{\tau_2}$ distribution for the 2τ final state following the requirement on $\Delta\phi(\text{jet}_{1,2}, E_{\text{T}}^{\text{miss}})$, and (b) the H_{T} distribution after all other analysis requirements have been applied. Data are represented by the points, with statistical uncertainty only. The band centered around the total SM background indicates the statistical uncertainty on the estimated background expectation. Also shown is the expected signal from the two GMSB benchmark points [163].

A single event was observed in the signal region in data, a slight downward fluctuation from the expected value. As no excess above the SM expectation is observed, a 95% CL exclusion limit is set on the GMSB parameter space, following the procedure described in chapter 7. The exclusion plot obtained as a result of the 2τ analysis can be seen in figure 6.19. Due to the downward fluctuation, the 2τ final state results in the strongest individual exclusion limit of the four final states, with a lower bound of around 41 TeV set on Λ, independent of $\tan\beta$. The limit is strongest in the $\tilde{\tau}_1$ NLSP region, as expected. The

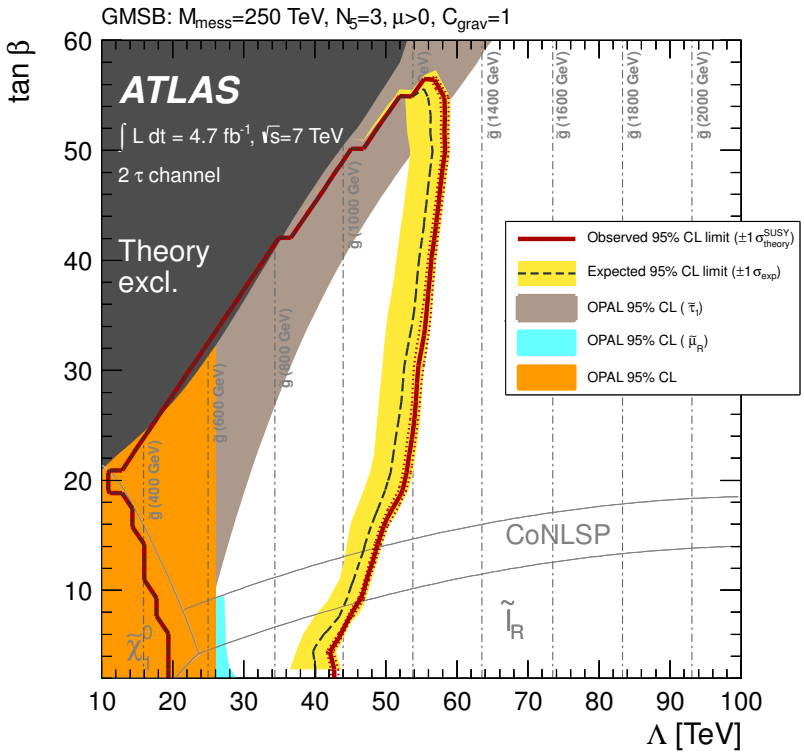

Figure 6.19: Expected and observed 95 % CL limits for the 2τ final state on the minimal GMSB model parameters Λ and $\tan\beta$. The dark grey area indicates the region which is theoretically excluded due to unphysical sparticle mass values. The different NLSP regions are indicated. In the co-NLSP region the $\tilde{\tau}$ and the $\tilde{\ell}$ are the NLSP. Additional model parameters are $M_{mess} = 250\,\text{TeV}$, $N_5 = 3$, $\mu > 0$ and $C_{grav} = 1$ [163].

event display for the single event observed in data can be seen in figure 6.20. For this event the leading and sub-leading τ-candidates have p_{T} of 129 GeV and 22 GeV, respectively. The two leading jets have p_{T} of 466 GeV and 131 GeV, and the $E_{\text{T}}^{\text{miss}}$ is 452 GeV.

In order to provide more information on the signal samples that are in the region of the 95% CL exclusion contour, table 6.20 shows the expected number of events and associated uncertainties for six points in this region. The acceptance, the efficiency, and the product of the two for the 2τ analysis can be found in figure 6.21. The region of parameter space to which the 2τ final state is the most sensitive is where the $\tilde{\tau}_1$ is the NLSP.

	Dibosons	Drell-Yan	Multi-jets	Top	W+jets	Z+jets	Full SM	Data	GMSB5020	GMSB5040
$E_{\mathrm{T}}^{\mathrm{miss}}$	724 ± 10	297 ± 14	$171\mathrm{k} \pm 23\mathrm{k}$	32414 ± 41	$206\mathrm{k} \pm 354$	$119\mathrm{k} \pm 675$	$5.29 \times 10^5 \pm 2.30 \times 10^4$	$8.22 \times 10^5 \pm 9.07 \times 10^2$	295 ± 3	295 ± 4
$p_{\mathrm{T}}^{\mathrm{jet1}}$	436 ± 8	217 ± 12	$142\mathrm{k} \pm 16\mathrm{k}$	21190 ± 37	$101\mathrm{k} \pm 154$	80474 ± 549	$3.46 \times 10^5 \pm 1.61 \times 10^4$	$3.92 \times 10^5 \pm 6.26 \times 10^2$	230 ± 3	234 ± 3
$p_{\mathrm{T}}^{\mathrm{jet2}}$	283 ± 7	142 ± 8	$142\mathrm{k} \pm 16\mathrm{k}$	19972 ± 36	52574 ± 98	36289 ± 359	$2.51 \times 10^5 \pm 1.61 \times 10^4$	$2.09 \times 10^5 \pm 4.58 \times 10^2$	219 ± 3	220 ± 3
Lepton veto	99 ± 4	113 ± 7	$140\mathrm{k} \pm 16\mathrm{k}$	10447 ± 27	33180 ± 79	35415 ± 359	$2.19 \times 10^5 \pm 1.61 \times 10^4$	$1.78 \times 10^5 \pm 4.22 \times 10^2$	50 ± 1	66 ± 2
1 τ	15 ± 1	7.16 ± 1.65	1140 ± 574	1464 ± 10	3477 ± 24	573 ± 23	6671 ± 575	6408 ± 80	25 ± 1	39 ± 1
2 τ	1.68 ± 0.24	0.49 ± 0.49	5.19 ± 0.87	36 ± 9	22 ± 11	26 ± 10	91 ± 17	85 ± 9	7.21 ± 0.54	13 ± 1
$\Delta\phi$	1.56 ± 0.23	0.49 ± 0.49	2.71 ± 0.83	33 ± 9	20 ± 10	24 ± 10	82 ± 17	79 ± 9	7.01 ± 0.54	12 ± 1
$m_{\mathrm{T}}^{\tau_1} + m_{\mathrm{T}}^{\tau_2}$	0.76 ± 0.15	0.49 ± 0.49	2.55 ± 0.83	28 ± 7	15 ± 8	3.33 ± 1.48	50 ± 11	43 ± 7	6.46 ± 0.50	11 ± 1
H_{T}	$.022 \pm .013 \pm .069$	$.49 \pm .49 \pm .21$	$.17 \pm .15 \pm .36$	$.76 \pm .31 \pm .31$	$1.11 \pm .67 \pm .30$	$.36 \pm .26 \pm .35$	$2.91 \pm 0.89 \pm 0.76$	1.00 ± 1.00	4.98 ± 0.45	8.66 ± 0.65

Table 6.19: Full signal selection summary table for the 2τ final state. For the $E_{\mathrm{T}}^{\mathrm{miss}}$ trigger requirement no MC scaling is applied. For all consecutive cuts up to and including the 1 τ requirement cut only the kinematic scale factors are applied. For all following requirements the full MC scaling is applied. For the final requirement on H_{T} the systematic uncertainty for all channels are given. The total MC prediction for the signal region is computed taking into account correlations between the different channels hence the uncertainties are different from the quadratic sum of the individual uncertainties.

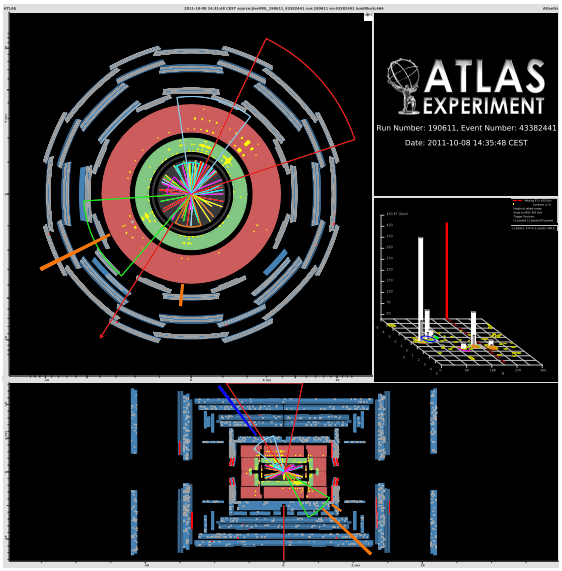

Figure 6.20: Event number 43382441 from run 190611, which was selected by the 2τ analysis. The leading and sub-leading jet p_{T} are 466 GeV and 131 GeV respectively. The leading τ-candidate p_{T} is 129 GeV and the sub-leading τ-candidate p_{T} is 22 GeV. The $E_{\mathrm{T}}^{\mathrm{miss}}$ is 452 GeV [163].

Λ	$\tan\beta$	Expected events	Stat. uncert.	Cross-section uncert.	Syst. uncert.
45	20	9.88	0.090	0.185	0.155
45	40	19.06	0.069	0.190	0.148
50	20	4.98	0.090	0.195	0.149
50	40	8.66	0.075	0.200	0.174
60	20	0.95	0.120	0.220	0.174
60	40	1.78	0.098	0.220	0.166

Table 6.20: Signal prediction and uncertainties in the 2τ analysis for six selected reference points from the GMSB grid around the expected exclusion contour.

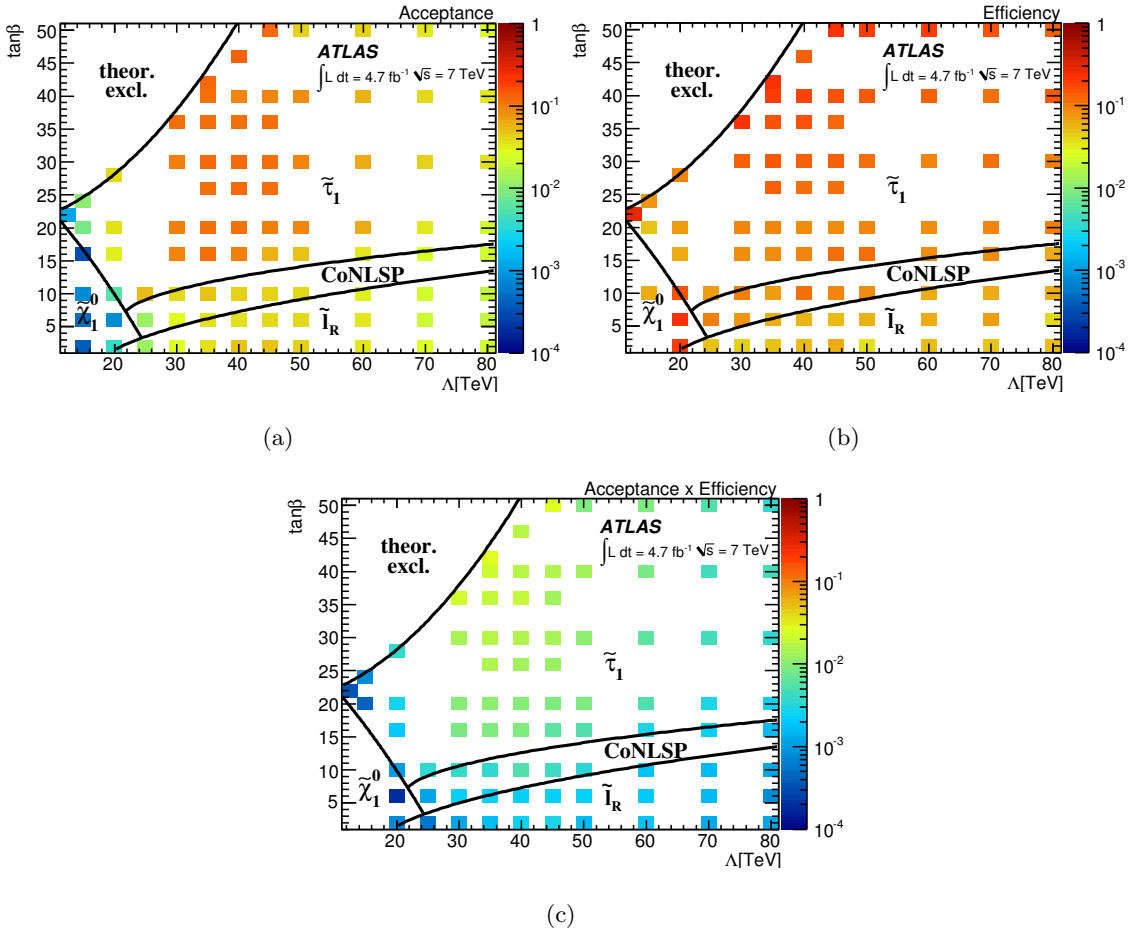

Figure 6.21: (a) The acceptance, (b) the efficiency, and (c) the acceptance times the efficiency for the 2τ analysis [163].

Λ	$\tan\beta$	Expected events	Stat. uncert.	Cross-section uncert.	Syst. uncert.
45	20	5.35	0.11	0.19	0.11
45	40	7.46	0.10	0.19	0.17
50	20	2.36	0.13	0.23	0.11
50	40	3.67	0.11	0.22	0.08
60	20	0.37	0.20	0.25	0.10
60	40	0.81	0.13	0.23	0.13

Table 6.21: Signal prediction and relative uncertainties in the 1τ final state for six selected reference points from the GMSB grid around the expected exclusion contour.

6.8.2 1τ final state

This section will summarise the results of the 1τ final state. I was not a member of the 1τ analysis team, and almost everything in this section is their work. My contribution was producing the exclusion limit plot shown in figure 6.22.

The expected SM contribution to the 1τ signal region is $1.31 \pm 0.37^{\text{stat}} \pm 0.65^{\text{syst}}$ events, comprised primarily of events due to top, W+jets or Z+jets production, with a smaller contribution from multi-jet events (with full detail given in table 6.23). Four events were observed in data in the signal region, slightly above the expected SM contribution. As no significant excess is observed above the SM expectation, 95% CL exclusion limits are set on the GMSB parameter space, and the observed exclusion is shown in figure 6.22. More information about the signal models in the region of the 95% CL exclusion contour, such as the expected number of signal events and associated uncertainties, can be found in table 6.21. Further discussion of the 1τ results can be found in [163].

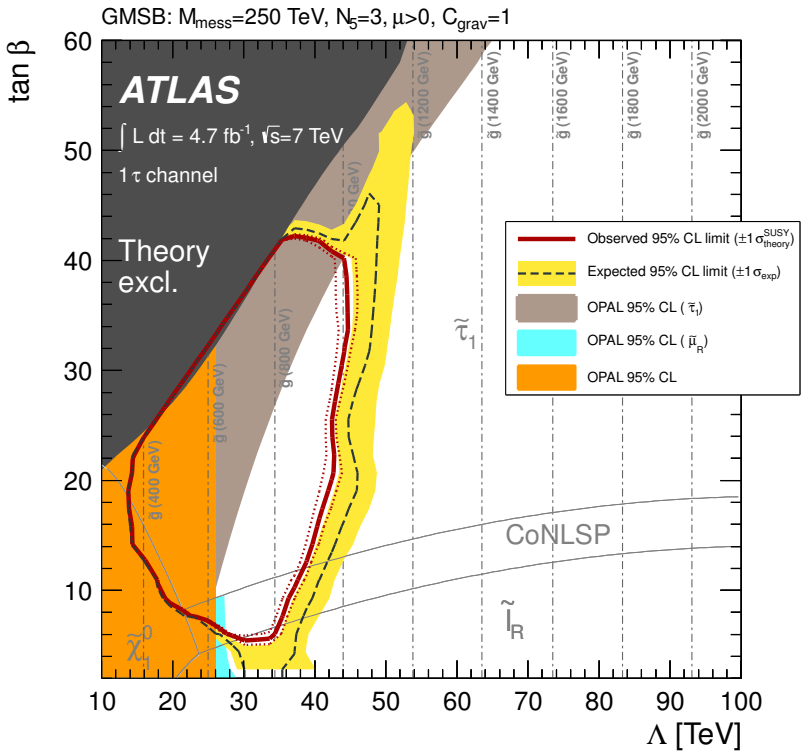

Figure 6.22: Expected and observed 95 % CL limits for the 1τ final state on the minimal GMSB model parameters Λ and $\tan\beta$. The dark grey area indicates the region which is theoretically excluded due to unphysical sparticle mass values. The different NLSP regions are indicated. In the co-NLSP region the $\tilde{\tau}_1$ and the $\tilde{\ell}_{\mathrm{R}}$ are the NLSP. Additional model parameters are $M_{mess} = 250\,\mathrm{TeV}$, $N_5 = 3$, $\mu > 0$ and $C_{grav} = 1$ [163].

		$\tau+\mu$ final state				$\tau+e$ final state			
Λ	$\tan\beta$	Expected events	Stat. uncert	Cross-section. uncert	Syst. uncert	Expected events	Stat. uncert	Cross-section uncert	Syst. uncert
45	20		0.13	0.18	0.11	8.28	0.09	0.30	0.17
45	40		0.11	0.18	0.08	8.84	0.1	0.42	0.14
50	20		0.12	0.19	0.16	4.21	0.09	0.26	0.11
50	40		0.12	0.20	0.10	4.12	0.11	0.34	0.16
60	20		0.15	0.23	0.09	1.23	0.11	0.22	0.16
60	40		0.15	0.25	0.09	0.94	0.14	0.35	0.14

Table 6.22: Signal prediction and relative uncertainties in the $\tau + \ell$ final states, for six selected reference points from the GMSB grid around the expected exclusion contours.

6.8.3 $\tau + \ell$ final states

As with the 1τ final state, I was not a part of the $\tau+\ell$ analysis team, and almost everything in this section is the work of ATLAS colleagues. My contribution was to produce the exclusion limit plots for both $\tau + \ell$ final states.

The final expected SM contribution to the $\tau+\mu$ signal region is $0.79\pm0.28^{\text{stat}}\pm0.39^{\text{syst}}$, and a single event was observed in data. A breakdown of the final SM expectation into individual processes can be found in table 6.23. Again, no excess above the SM expectation is observed and 95% CL exclusion limits are set on the GMSB parameter space. This can be found in figure 6.23(a). The expected number of events in the signal region for the GMSB models in the region of the 95% CL exclusion contour are listed in table 6.22, along with the relevant statistical, systematic and theory uncertainties.

For the $\tau+e$ final state the final expected SM contribution to the signal region is $2.31 \pm 0.40^{\text{stat}} \pm 1.40^{\text{syst}}$ events and three events are observed in data. As no significant excess is observed exclusion limits are again set on the GMSB $\Lambda - \tan\beta$ plane. This can be seen in figure 6.23(b). Table 6.23 lists the contributions from each of the SM processes to the signal region, along with the systematic and statistical uncertainties for each. As has been presented for the other final states, details of the GMSB signal models close to the 95% CL exclusion limit can be found in table 6.22. Figure 6.23(b) shows the observed exclusion limit for the $\tau+e$ final state.

A full summary of the results from each of the four final states can be found in table 6.23, including data, background and GMSB benchmark contributions to the signal regions.

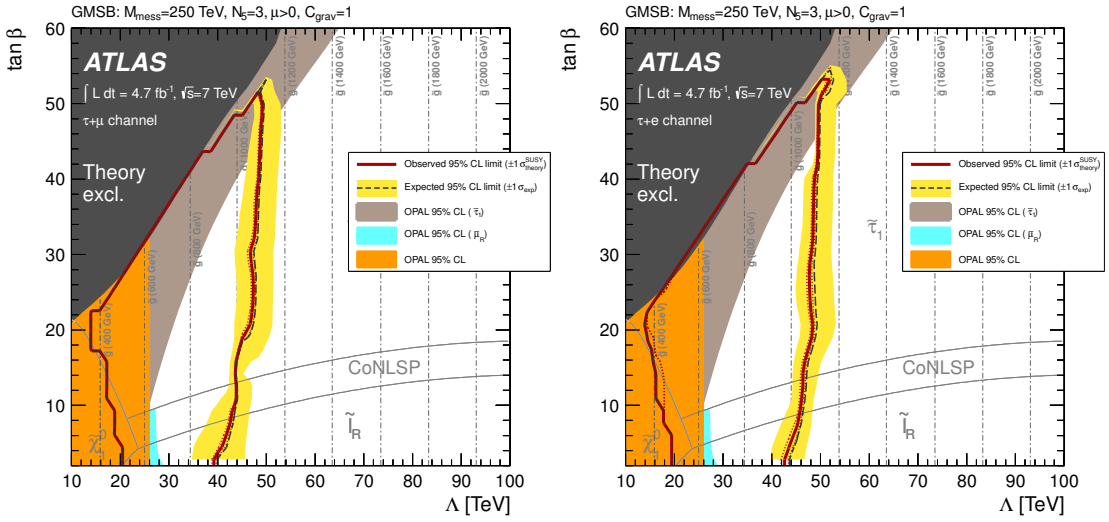

(a) $\tau+\mu$ (b) $\tau+e$

Figure 6.23: Expected and observed 95 % CL limits for the $\tau+\ell$ final states on the minimal GMSB model parameters Λ and $\tan\beta$. The dark grey area indicates the region which is theoretically excluded due to unphysical sparticle mass values. The different NLSP regions are indicated. In the co-NLSP region the $\tilde{\tau}_1$ and the $\tilde{\ell}$ are the NLSP. Additional model parameters are $M_{mess} = 250\,\text{TeV}$, $N_5 = 3$, $\mu > 0$ and $C_{grav} = 1$ [163].

–	1τ	2τ	$\tau+\mu$	$\tau+e$
Multi-jet	$0.17 \pm 0.04 \pm 0.11$	$0.17 \pm 0.15 \pm 0.36$	< 0.01	0.22 ± 0.30
W + jets	$0.31 \pm 0.16 \pm 0.16$	$1.11 \pm 0.67 \pm 0.30$	$0.27 \pm 0.21 \pm 0.13$	$0.24 \pm 0.17 \pm 0.27$
Z + jets	$0.22 \pm 0.22 \pm 0.09$	$0.36 \pm 0.26 \pm 0.35$	$0.05 \pm 0.05 \pm 0.01$	$0.17 \pm 0.12 \pm 0.05$
$t\bar{t}$	$0.61 \pm 0.25 \pm 0.11$	$0.76 \pm 0.31 \pm 0.31$	$0.36 \pm 0.18 \pm 0.26$	$1.41 \pm 0.27 \pm 0.84$
diboson	< 0.05	$0.022 \pm 0.013 \pm 0.069$	$0.11 \pm 0.04 \pm 0.02$	$0.26 \pm 0.12 \pm 0.11$
Drell-Yan	< 0.36	$0.49 \pm 0.49 \pm 0.21$	< 0.0015	< 0.0015
Total SM	$1.31 \pm 0.37 \pm 0.65$	$2.91 \pm 0.89 \pm 0.76$	$0.79 \pm 0.28 \pm 0.39$	$2.31 \pm 0.40 \pm 1.40$
GMSB5020	$2.36 \pm 0.30 \pm 0.60$	$4.94 \pm 0.45 \pm 0.74$	$2.48 \pm 0.30 \pm 0.39$	$4.21 \pm 0.38 \pm 0.46$
Data	4	1	1	3

Table 6.23: Expected background events and data yields in the four final states discussed. Where possible, the errors are separated in statistical and systematic. Also shown are the number of expected signal MC events for the GMSB5020 benchmark point.

7

Statistical analysis of the results

This chapter summarises the statistical analysis that is performed to produce the combined exclusion limits in the GMSB parameter space from the results obtained in chapter 6. In order to produce the strongest possible limits, a statistical combination of the four channels is performed. This is possible as all of the channels are orthogonal by construction. The CL_{s} method was first introduced in section 5.10, and this forms the foundation for the combination that is described here.

The ATLAS HistFitter package [175] was used throughout this process. It uses HistFactory (part of the RooStats [176] software) for the modelling of the likelihood and the RooStats frequentist calculator for the calculation of the CL_{s} and p-values. Whilst equation 5.14 describes the likelihood used for the analysis presented in chapter 5, and for each of the individual final states in the analysis presented in chapter 6, the combination of the four final states is performed by building a combined likelihood, given by:

$$\mathcal{L}_{\mathrm{combined}}(\mu, \boldsymbol{\theta}) = \mathcal{L}_{1\tau}(\mu, \boldsymbol{\theta}_{1\tau}) \times \mathcal{L}_{2\tau}(\mu, \boldsymbol{\theta}_{2\tau}) \times \mathcal{L}_{1\tau 1\mu}(\mu, \boldsymbol{\theta}_{1\tau 1\mu}) \times \mathcal{L}_{1\tau 1e}(\mu, \boldsymbol{\theta}_{1\tau 1e}) \ , \quad (7.1)$$

where each likelihood function follows the definition in equation 5.14. This combined likelihood is then used to calculate the CL_{s} and p-values.

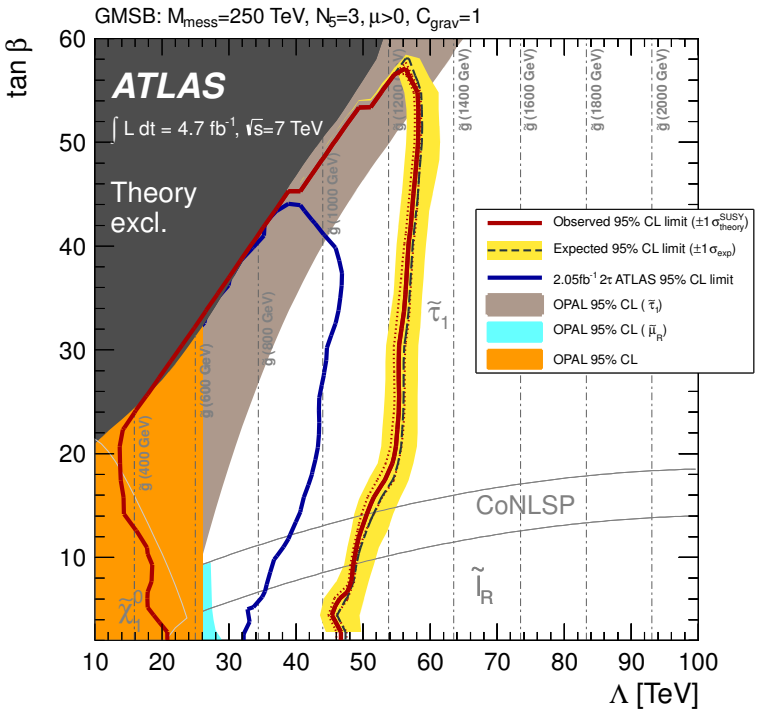

Figure 7.1: Expected and observed 95 % CL limits for the full combination of channels on the minimal GMSB model parameters Λ and $\tan\beta$. The dark grey area indicates the region which is theoretically excluded due to unphysical sparticle mass values. The different NLSP regions are indicated. In the co-NLSP region the $\tilde{\tau}$ and the $\tilde{\ell}$ are the NLSP. Additional model parameters are $M_{mess} = 250\,\text{TeV}$, $N_5 = 3$, $\mu > 0$ and $C_{grav} = 1$.

The 95% exclusion result for the full combination of all four channels is presented in figure 7.1. Observed and expected 95% exclusion contours (with $\pm 1\sigma$ bands) are produced for the results, calculated without including the uncertainties on the signal cross-sections. Additionally, the two contours for results obtained by increasing and decreasing the signal cross-section by the 1σ theory uncertainty are shown. The exclusion limits were calculated using 10^4 toy MC pseudo-experiments per grid point, and a full discussion of the procedure can be found in [158].

For each channel an upper limit is also set on the number of events from any signal model that would contribute events to the signal region. A set of exclusion hypothesis tests are performed, with varying values of the signal strength μ. An interpolation can then be performed to find while value of the signal strength corresponds to 95% exclusion.

The total SM prediction of $1.31 \pm 0.37^{\text{stat}} \pm 0.65^{\text{syst}}$ events in the 1τ signal region is compared with the observation of 4 events in the signal region for this channel. In the CL_{s} convention, these 4 observed events exclude at a 95% confidence level models resulting in

more than 7.86 observed signal events in the signal region, in addition to the expected SM background. The corresponding expected value, assuming the background only hypothesis, is 4.46 events. In the 2τ channel, given a total SM prediction of $2.91 \pm 0.89^{\text{stat}} \pm 0.76^{\text{syst}}$ events in the signal region compared with the observation of 1 event, the corresponding upper limits on the number of observed (expected) signal events for new physics are 3.19 (4.67). For the $\tau+\ell$ channels, the SM background is $0.79\pm0.28^{\text{stat}}\pm0.39^{\text{syst}}$, compared to 1 event observed in the signal region in the $\tau+\mu$ analysis, while this is $2.31\pm0.40^{\text{stat}}\pm1.40^{\text{syst}}$, compared with 3 observed events in the signal region for the $\tau + e$. The upper limit on observed (expected) signal events for new physics is therefore 3.66 (3.40) for the $\tau + \mu$ and 5.18 (4.62) for the $\tau + e$, respectively. These results can be found in table 7.1.

Using the observed (expected) number of data events and background expectations, an upper limit at 95% CL is placed on the cross-section times branching ratio times acceptance of new physics processes for each channel. These are found to be 1.67 (0.95) fb for the 1τ, 0.68 (0.99) fb for the 2τ, 0.78 (0.72) fb for the $\tau+\mu$ and 1.10 (0.98) fb for the $\tau+e$ final states, respectively. A summary of all of these results can be found in table 7.1. Figure 7.2 shows the CL_{s}, CL_{b}, and $CL_{\text{s+b}}$ p-values as a function of different signal strength values for each of the channels, taking the point GMSB5020 as a benchmark. The figure also shows the 1 and 2 σ variations around the background-only expected CL_{s} values. The 95% upper limit on the signal model is where the CL_{s} curve crosses the horizontal 5% line (in red). Note that there are 20 evaluations shown along the signal strength axis, although 100 are used when calculating the value.

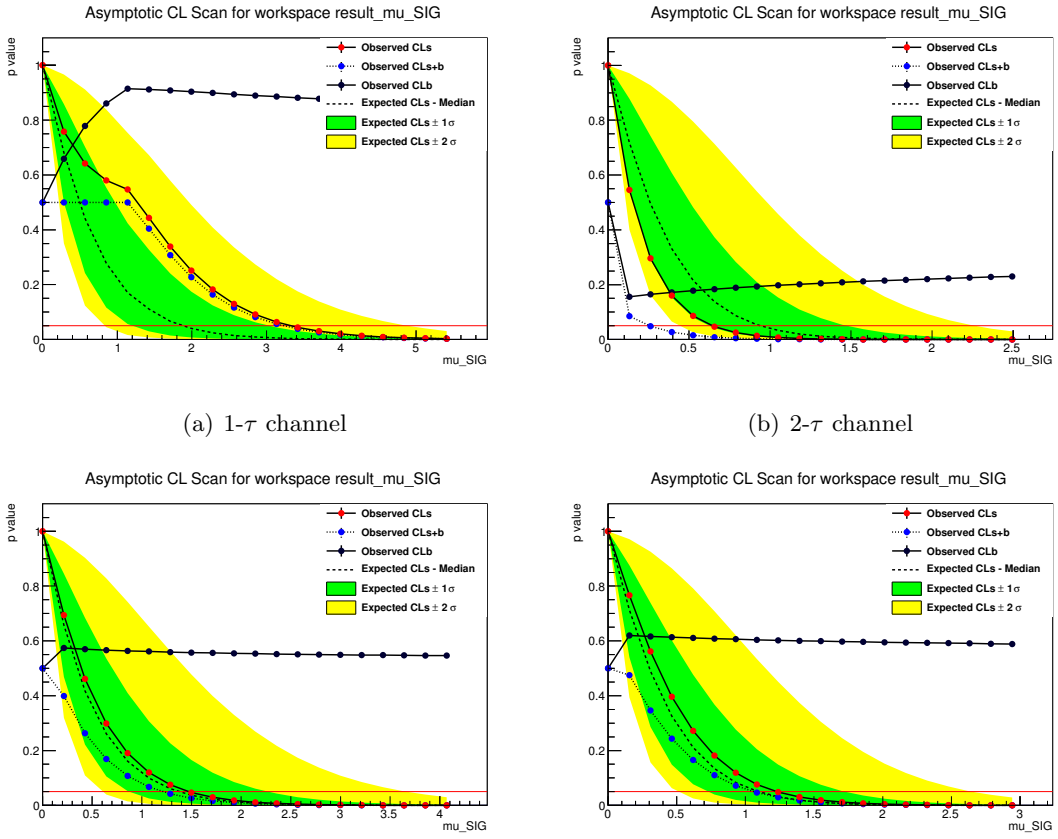

(a) 1-τ channel

(b) 2-τ channel

(c) $\tau + \mu$ channel

(d) $\tau + e$ channel

Figure 7.2: The CL_{s}, CL_{b}, and $CL_{\mathrm{s+b}}$ p-values as a function of different signal strength values for each of the channels, using the signal point $\Lambda = 50$ TeV, $\tan\beta = 20$. The 1 and 2 σ variations around the background-only expected CL_{s} values are shown in green and yellow, respectively. The 95% upper limit on the signal model is where the CL_{s} curve crosses the red horizontal 5% line.

–	1τ	2τ	$\tau+\mu$	$\tau+e$
Total background	$1.31 \pm 0.37 \pm 0.65$	$2.91 \pm 0.89 \pm 0.76$	$0.79 \pm 0.28 \pm 0.39$	$2.31 \pm 0.40 \pm 1.40$
Signal MC Events (GMSB5020)	$2.36 \pm 0.30 \pm 0.60$	$4.94 \pm 0.45 \pm 0.74$	$2.48 \pm 0.30 \pm 0.39$	$4.21 \pm 0.38 \pm 0.46$
Data	4	1	1	3
Obs (exp) limit on signal events	7.68 (4.46)	3.19 (4.67)	3.66 (3.40)	5.18 (4.62)
Obs (exp) limit on Cross-section (fb)	1.67 (0.95)	0.68 (0.99)	0.78 (0.72)	1.10 (0.98)

Table 7.1: Expected background events and data yields in the four final states discussed. The errors are separated into statistical and systematic, respectively. Also shown are the number of expected signal MC events for the GMSB5020 benchmark point and the 95 % CL limit on the number of observed (expected) signal events from any new physics scenario that can be set for each of the four final states, taking into account the observed events in data and the background expectations.

8 Conclusion

In this work two searches for supersymmetry in events containing hadronically decaying τ-leptons, jets, missing transverse momentum and zero or one light lepton have been presented. The first of these searches, presented in chapter 5 and published in [146], was performed using $2.05\,\text{fb}^{-1}$ of proton-proton collision data at $\sqrt{s} = 7\,\text{TeV}$ recorded with the ATLAS detector at the Large Hadron Collider, and focused exclusively on the 2τ final state. Three events are found in the ATLAS data, consistent with the SM background expectation of $5.3 \pm 1.3^{\text{stat}} \pm 2.2^{\text{sys}}$ and these results are used to set a model-independent 95 % CL upper limit of 5.9 events from new phenomena, corresponding to an upper limit on the visible cross section of 2.9 fb. A 95 % CL lower limit of 32 TeV is set on the GMSB breaking scale, Λ, independent of $\tan\beta$. This limit increases to 47 TeV for $\tan\beta = 37$. At the time these represented the most stringent tests in a large part of the considered GMSB parameter space. For this analysis I was directly involved in the signal selection and the definition of the background control regions, the process of estimating the multi-jet background, and also the statistical interpretation and the exclusion limit setting procedure.

The second analysis, using the full 2011 7 TeV p–p collision dataset of $4.7\,\text{fb}^{-1}$, was a search for supersymmetry in final states containing jets, $E_{\text{T}}^{\text{miss}}$, light leptons ($e/\mu$) and

hadronically decaying τ-leptons. No significant excess is found above the expected SM backgrounds. The results are used to set model-independent 95 % CL upper limits on the number of signal events from new phenomena and corresponding upper limits on the visible cross-section for the four different final states, all of which can be found in table 6.23. Limits on the model parameters are set for a minimal GMSB model, and the final limits from the analyses presented in chapters 5 and 6 are shown in figure 8.1.

A lower limit on the SUSY breaking scale Λ of 54 TeV is determined in the regions where the $\tilde{\tau}_1$ is the next-to-lightest SUSY particle ($\tan\beta > 20$) by statistically combining the result of the four analyses. The limit on Λ increases to 58 TeV for $\tan\beta$ between 45 and 55 . These results provide the most stringent test to date of GMSB SUSY breaking models in a large part of the considered parameter space. The observed 95 % CL limits in the GMSB parameter space, for both of the two analyses discussed in this thesis, are shown in figure 7.1. For this analysis I was directly involved in the 2τ final state, focusing again on the optimisation of the signal selection, the definition of the background control regions, and the multi-jet background estimation. I was also solely responsible for the combination of the four final states, the statistical interpretation and the exclusion limit setting procedure.

Further searches for this minimal GMSB model are possible with the 2012 dataset, where $\sqrt{s} = 8$ TeV. The GMSB production cross-section increases exponentially, and the increased centre-of-mass energy and integrated luminosity will provide scope for sensitivity over a large region of the parameter space. The possible discovery of the Higgs boson at $\sim$125 GeV will have implications for the searches for supersymmetry, and these constraints will have to be considered when designing future analyses. Minimal versions of GMSB models predict $m_H < 118$ GeV, if the SUSY particle masses lie below $\sim$2 TeV [177, 178]. Larger SUSY masses are possible within the GMSB framework, raising the 118 GeV limit for m_H, but masses exceeding 2 TeV destroy the naturalness of the theory, and can also push the SUSY mass spectra beyond the reach of the LHC [177].

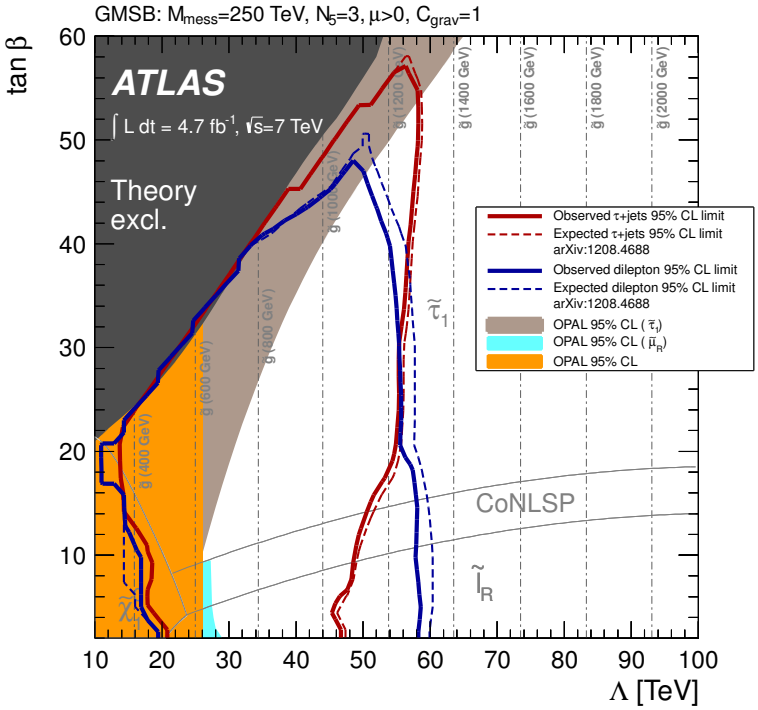

Figure 8.1: Expected and observed 95 % CL lower limits on the minimal GMSB model parameters Λ and $\tan\beta$ for the combination of the channels studied in this analysis and the one obtained in the ATLAS 2 lepton analysis reported in arXiv:1208.4688. For both analyses, the observed and expected limits lie within a 1σ uncertainty band. The dark grey area indicates the region which is theoretically excluded due to unphysical sparticle mass values. The different possible NLSP regions are indicated by the solid grey lines. The $\tilde{\tau}$ NLSP is the dominant contribution. In the CoNLSP region the $\tilde{\tau}$ and the $\tilde{\ell}$ are the NLSP. Additional model parameters are $M_{\text{mess}} = 250\,\text{TeV}$, $N_5 = 3$, $\mu > 0$ and $C_{\text{grav}} = 1$.

A

2.05fb^{-1} analysis: data and MC samples

This appendix details all of the simulated samples that are used for the analysis described in chapter 5. Table A.1 contains the details of the GMSB $\Lambda - \tan\beta$ grid, with particular focus on the benchmark points used during the analysis. The Standard Model samples can be found in tables A.2 (top), A.3 ($W+$jets), A.4 ($Z+$jets), A.5 (diboson), A.6 (multi-jet) and A.7 (Drell-Yan). For this analysis all data and MC samples are officially produced from ATLAS release 16 AODs, using the production tag `p601`.

Sample ID	Name	Generator	LO [pb]	NLO [pb]
137931	GMSB3020 ($\Lambda = 30, \tan\beta = 20$)	Herwig++	1.95	2.35
137940	GMSB4030 ($\Lambda = 40, \tan\beta = 30$)	Herwig++	0.41	0.45
137921–	GMSB grid	Herwig++	0.006	0.005
–137975	GMSB grid	Herwig++	15.8	21.7

Table A.1: The GMSB benchmark samples with sample ID, event generator, LO and NLO cross sections. The LO cross sections are taken from the generator, and the NLO cross sections are calculated using `PROSPINO`.

Sample ID	Name	Generator	NLO [pb]	k-factor	NNLO [pb]	No. of events
105200	$t\bar{t}$ semileptonic (T1)	MCAtNLOJimmy	79.99	1.117	89.35	14967040
105204	$t\bar{t}$ full hadronic	MCAtNLOJimmy	64.03	1.175	75.23	1198875
108340	t-channel $t \to e\nu$	MCAtNLOJimmy	7.12			299897
108341	t-channel $t \to \mu\nu$	MCAtNLOJimmy	7.12			299879
108342	t-channel $t \to \tau\nu$	MCAtNLOJimmy	7.10			299879
108343	s-channel $t \to e\nu$	MCAtNLOJimmy	0.47			299831
108344	s-channel $t \to \mu\nu$	MCAtNLOJimmy	0.47			299877
108345	s-channel $t \to \tau\nu$	MCAtNLOJimmy	0.47			299864
108346	single top Wt	MCAtNLOJimmy	14.59			899336

Table A.2: Used $t\bar{t}$ and single t Monte Carlo samples with their corresponding sample ID, event generator, NLO cross section and number of generated events. In the case of the $t\bar{t}$ MC samples applying the k-factor yields the NNLO cross sections.

Sample ID	Name	Generator	LO [pb]	k-factor	NNLO [pb]	No. of events
107680	WenuN0p	AlpgenJimmy	6921.6	1.20	8305.92	3455037
107681	WenuN1p	AlpgenJimmy	1304.3	1.20	1565.16	641361
107682	WenuN2p	AlpgenJimmy	378.3	1.20	453.95	3768265
107683	WenuN3p	AlpgenJimmy	101.4	1.20	121.72	1009641
107684	WenuN4p	AlpgenJimmy	25.9	1.20	31.04	249869
107685	WenuN5p	AlpgenJimmy	7.0	1.20	8.40	69953
107690	WmunuN0p	AlpgenJimmy	6919.6	1.20	8303.52	3466523
107691	WmunuN1p	AlpgenJimmy	1304.2	1.20	1565.04	641867
107692	WmunuN2p	AlpgenJimmy	377.8	1.20	453.39	3768893
107693	WmunuN3p	AlpgenJimmy	101.9	1.20	122.26	1009589
107694	WmunuN4p	AlpgenJimmy	25.8	1.20	30.90	254879
107695	WmunuN5p	AlpgenJimmy	6.9	1.20	8.30	69958
107700	WtaunuN0p	AlpgenJimmy	6918.6	1.20	8302.32	3416438
107701	WtaunuN1p	AlpgenJimmy	1303.2	1.20	1563.84	641809
107702	WtaunuN2p	AlpgenJimmy	378.2	1.20	453.82	3768750
107703	WtaunuN3p	AlpgenJimmy	101.5	1.20	121.81	1009548
107704	WtaunuN4p	AlpgenJimmy	25.6	1.20	30.77	249853
107705	WtaunuN5p	AlpgenJimmy	7.0	1.20	8.45	63692

Table A.3: Used $W+$jets Monte Carlo samples with their corresponding sample ID, event generator, LO cross section, and section, k-factor, NNLO cross section, and number of generated events.

Sample ID	Name	Generator	LO [pb]	k-factor	NNLO [pb]	No. of events
107650	ZeeN0p	AlpgenJimmy	668.3	1.25	835.40	6612265
107651	ZeeN1p	AlpgenJimmy	134.4	1.25	167.95	1333745
107652	ZeeN2p	AlpgenJimmy	40.54	1.25	50.68	404873
107653	ZeeN3p	AlpgenJimmy	11.16	1.25	13.95	109942
107654	ZeeN4p	AlpgenJimmy	2.88	1.25	3.60	29992
107655	ZeeN5p	AlpgenJimmy	0.83	1.25	1.04	8992
107660	ZmumuN0p	AlpgenJimmy	668.7	1.25	835.85	6619010
107661	ZmumuN1p	AlpgenJimmy	134.1	1.25	167.68	1334723
107662	ZmumuN2p	AlpgenJimmy	40.33	1.25	50.41	403886
107663	ZmumuN3p	AlpgenJimmy	11.19	1.25	13.99	109954
107664	ZmumuN4p	AlpgenJimmy	2.75	1.25	3.44	29978
107665	ZmumuN5p	AlpgenJimmy	0.77	1.25	0.96	9993
107670	ZtautauN0p	AlpgenJimmy	668.4	1.25	835.50	6618801
107671	ZtautauN1p	AlpgenJimmy	134.8	1.25	168.51	1334664
107672	ZtautauN2p	AlpgenJimmy	40.36	1.25	50.45	404853
107673	ZtautauN3p	AlpgenJimmy	11.25	1.25	14.06	109944
107674	ZtautauN4p	AlpgenJimmy	2.79	1.25	3.49	29982
107675	ZtautauN5p	AlpgenJimmy	0.77	1.25	0.96	9993
107710	ZnunuNp0	AlpgenJimmy	26.71	1.282	34.22	60485
107711	ZnunuNp1	AlpgenJimmy	451.4	1.282	578.54	864799
107712	ZnunuNp2	AlpgenJimmy	197.6	1.282	253.29	165454
107713	ZnunuNp3	AlpgenJimmy	59.89	1.282	76.75	128934
107714	ZnunuNp4	AlpgenJimmy	15.61	1.282	20.01	24986
107715	ZnunuNp5	AlpgenJimmy	4.17	1.282	5.34	6994

Table A.4: Used $Z+$jets Monte Carlo samples with their corresponding sample ID, event generator, LO cross section, k-factor, NNLO cross section, and number of generated events.

Sample ID	Generator	Final state	NLO [fb]	No. of events
105921	McAtNlo_JIMMY	$W^+W^- \to e\nu e\nu$	503.77	199960
105922	McAtNlo_JIMMY	$W^+W^- \to e\nu\mu\nu$	503.77	199960
105923	McAtNlo_JIMMY	$W^+W^- \to e\nu\tau\nu$	503.77	199966
105924	McAtNlo_JIMMY	$W^+W^- \to \mu\nu\mu\nu$	503.77	199956
105925	McAtNlo_JIMMY	$W^+W^- \to \mu\nu e\nu$	503.77	199961
105926	McAtNlo_JIMMY	$W^+W^- \to \mu\nu\tau\nu$	503.77	199960
105927	McAtNlo_JIMMY	$W^+W^- \to \tau\nu\tau\nu$	503.77	199966
105928	McAtNlo_JIMMY	$W^+W^- \to \tau\nu e\nu$	503.77	199958
105929	McAtNlo_JIMMY	$W^+W^- \to \tau\nu\mu\nu$	503.77	199957
105930	McAtNlo_JIMMY	$ZZ \to \ell\ell q\bar{q}$	523.54	24990
105931	McAtNlo_JIMMY	$ZZ \to \ell\ell\ell\ell$	24.68	99982
105932	McAtNlo_JIMMY	$ZZ \to \ell\ell\nu\nu$	150.33	99978
106036	McAtNlo_JIMMY	$ZZ \to 2\ell 2\tau$	24.68	24995
106037	McAtNlo_JIMMY	$ZZ \to 4\tau$	6.17	24991
113192	McAtNlo_JIMMY	$ZZ \to \tau\tau\nu\nu$	75.17	24996
113193	McAtNlo_JIMMY	$ZZ \to \tau\tau q\bar{q}$	261.77	24990
105940	McAtNlo_JIMMY	$W^+Z \to \ell\nu q\bar{q}$	1688.9	24989
105941	McAtNlo_JIMMY	$W^+Z \to \ell\nu\ell\ell$	159.24	24995
105942	McAtNlo_JIMMY	$W^+Z \to q\bar{q}'\ell\ell$	498.36	24992
106024	McAtNlo_JIMMY	$W^+Z \to \tau\nu\ell\ell$	79.62	24994
106025	McAtNlo_JIMMY	$W^+Z \to \ell\nu\tau\tau$	79.62	24992
106026	McAtNlo_JIMMY	$W^+Z \to \tau\nu\tau\tau$	39.81	24990
113190	McAtNlo_JIMMY	$W^+Z \to q\bar{q}'\tau\tau$	249.18	24987
105970	McAtNlo_JIMMY	$W^-Z \to \ell\nu q\bar{q}$	912.64	24993
105971	McAtNlo_JIMMY	$W^-Z \to \ell\nu\ell\ell$	86.05	99972
105972	McAtNlo_JIMMY	$W^-Z \to q\bar{q}'\ell\ell$	269.3	99968
106027	McAtNlo_JIMMY	$W^-Z \to \tau\nu\ell\ell$	43.02	24997
106028	McAtNlo_JIMMY	$W^-Z \to \ell\nu\tau\tau$	43.02	24993
106029	McAtNlo_JIMMY	$W^-Z \to \tau\nu\tau\tau$	21.51	24941
113191	McAtNlo_JIMMY	$W^-Z \to q\bar{q}'\tau\tau$	134.65	24989

Table A.5: Used diboson Monte Carlo samples with their corresponding their sample ID, event generator, final state, NLO cross section, and number of generated events.

Sample ID	Name	Generator	LO [pb]	No. of events
105009	J0	Pythia	9860800000.	16388258
105010	J1	Pythia	678180000.	7382565
105011	J2	Pythia	40982000.	2796084
105012	J3	Pythia	2192900.	2796879
105013	J4	Pythia	87701.	2793179
105014	J5	Pythia	2350.1	2790576
105015	J6	Pythia	33.61	2790601
105016	J7	Pythia	0.13744	1395025
105017	J8	Pythia	0.0000062	1353250

Table A.6: Used di-jet Monte Carlo samples with their corresponding sample ID, event generator, cross section and number of generated events.

Sample ID	Name	Generator	LO [pb]	k-factor	NNLO [pb]	No. of events
116250	ZeeNp0Mll10to40	AlpgenJimmy	3055.2	1.25	3819.00	999859
116251	ZeeNp1Mll10to40	AlpgenJimmy	84.92	1.25	106.15	299940
116252	ZeeNp2Mll10to40	AlpgenJimmy	41.40	1.25	51.75	499880
116253	ZeeNp3Mll10to40	AlpgenJimmy	8.38	1.25	10.48	149940
116254	ZeeNp4Mll10to40	AlpgenJimmy	1.85	1.25	2.31	39973
116255	ZeeNp5Mll10to40	AlpgenJimmy	0.46	1.25	0.58	9995
116260	ZmumuNp0Mll10to40	AlpgenJimmy	3054.9	1.25	3818.63	979869
116261	ZmumuNp1Mll10to40	AlpgenJimmy	84.87	1.25	106.09	299890
116262	ZmumuNp2Mll10to40	AlpgenJimmy	41.45	1.25	51.81	499864
116263	ZmumuNp3Mll10to40	AlpgenJimmy	8.38	1.25	10.48	149939
116264	ZmumuNp4Mll10to40	AlpgenJimmy	1.85	1.25	2.31	39988
116265	ZmumuNp5Mll10to40	AlpgenJimmy	0.46	1.25	0.58	9996
116270	ZtautauNp0Mll10to40	AlpgenJimmy	3055.1	1.25	3818.88	999865
116271	ZtautauNp1Mll10to40	AlpgenJimmy	84.93	1.25	106.16	299937
116272	ZtautauNp2Mll10to40	AlpgenJimmy	41.47	1.25	51.84	499886
116273	ZtautauNp3Mll10to40	AlpgenJimmy	8.36	1.25	10.45	149941
116274	ZtautauNp4Mll10to40	AlpgenJimmy	1.85	1.25	2.31	39984
116275	ZtautauNp5Mll10to40	AlpgenJimmy	0.46	1.25	0.58	9995

Table A.7: Used Drell-Yan Monte Carlo samples with their corresponding sample ID, event generator, LO cross section, k-factor, NNLO cross section, and number of generated events.

B

4.7fb^{-1} analysis: data and MC samples

This appendix details all of the simulated samples that are used for the analysis described in chapter 6. All of the data and Monte Carlo samples that were used in this analysis were centrally produced from ATLAS release 17 AODs, using production tag `p832`.

Sample ID	Name	Generator	NLO [pb]	k-factor	NNLO [pb]	No. of events
105200	$t\bar{t}$ semileptonic (T1)	MCAtNLOJimmy	79.01	1.146	90.57	14983835
105204	$t\bar{t}$ full hadronic	MCAtNLOJimmy	66.48	1.146	76.23	1199034
117360	t-channel $t \to e\nu$	AcerMCPythia	8.06	0.865	6.97	999295
117361	t-channel $t \to m\nu\nu$	AcerMCPythia	8.06	0.865	6.97	999948
117362	t-channel $t \to \tau\nu$	AcerMCPythia	8.05	0.855	6.97	998995
108343	s-channel $t \to e\nu$	MCAtNLOJimmy	0.47	1.064	0.50	299948
108344	s-channel $t \to m\nu\nu$	MCAtNLOJimmy	0.47	1.064	0.50	299998
108345	s-channel $t \to \tau\nu$	MCAtNLOJimmy	0.47	1.064	0.50	299899
108346	single top Wt	MCAtNLOJimmy	14.79	1.064	15.74	899694

Table B.1: Used $t\bar{t}$ and single t MC samples with their corresponding sample ID, event generator, NLO cross section and number of generated events. Applying the k-factor yields the NNLO cross sections.

Sample ID	Name	Generator	NLO [pb]	k-factor	NNLO [pb]	No. of events
105890	ttbarlnlnNp0	AlpgenJimmy	3.466	1.69	5.86	194499
105891	ttbarlnlnNp1	AlpgenJimmy	3.3987	1.69	5.74	159999
105892	ttbarlnlnNp2	AlpgenJimmy	2.1238	1.69	3.59	336897
117897	ttbarlnlnNp3	AlpgenJimmy	0.94698	1.69	1.60	148000
117898	ttbarlnlnNp4	AlpgenJimmy	0.33409	1.69	0.56	60000
117899	ttbarlnlnNp5	AlpgenJimmy	0.12753	1.69	0.22	25000
105894	ttbarlnqqNp0	AlpgenJimmy	13.764	1.77	24.36	647396
105895	ttbarlnqqNp1	AlpgenJimmy	13.608	1.77	24.09	652997
105896	ttbarlnqqNp2	AlpgenJimmy	8.4181	1.77	14.90	1145892
117887	ttbarlnqqNp3	AlpgenJimmy	3.7759	1.77	6.68	652495
117888	ttbarlnqqNp4	AlpgenJimmy	1.3361	1.77	2.36	118999
117889	ttbarlnqqNp5	AlpgenJimmy	0.50399	1.77	0.89	79997

Table B.2: Used $t\bar{t}$ samples with their corresponding sample ID, event generator, NLO cross section and number of generated events. Applying the k-factor yields the NNLO cross sections. Those samples are used for validation and systematics and replace the 105200 T1 sample of the MC@NLO production.

Sample ID	Name	Generator	LO [pb]	k-factor	FE	NNLO [pb]	No. of events
107680	WenuN0p	AlpgenJimmy	6930.5	1.196		8288.878	3458883
107681	WenuN1p	AlpgenJimmy	1305.3	1.196		1561.1388	2499645
107682	WenuN2p	AlpgenJimmy	378.13	1.196		452.24348	3768632
107683	WenuN3p	AlpgenJimmy	101.86	1.196		121.82456	1008947
107684	WenuN4p	AlpgenJimmy	25.68	1.196		30.71328	250000
107685	WenuN5p	AlpgenJimmy	6.99	1.196		8.36004	69999
144196	WenuNp1_susyfilt	AlpgenJimmy	1305	1.1955	0.005659	8.83	180899
144197	WenuNp2_susyfilt	AlpgenJimmy	378	1.1955	0.01652	7.47	134998
144198	WenuNp3_susyfilt	AlpgenJimmy	101.9	1.1955	0.03404	4.15	139999
144199	WenuNp4_susyfilt	AlpgenJimmy	25.7	1.1955	0.05639	1.73	75000
107690	WmunuN0p	AlpgenJimmy	6932.4	1.195		8284.218	3462942
107691	WmunuN1p	AlpgenJimmy	1305.9	1.195		1560.5505	2498593
107692	WmunuN2p	AlpgenJimmy	378.07	1.195		451.79365	3768737
107693	WmunuN3p	AlpgenJimmy	101.85	1.195		121.71075	1008446
107694	WmunuN4p	AlpgenJimmy	25.72	1.195		30.7354	254950
107695	WmunuN5p	AlpgenJimmy	7	1.195		8.365	70000
144200	WmunuNp1_susyfilt	AlpgenJimmy	1305	1.1955	0.005422	8.46	171000
144201	WmunuNp2_susyfilt	AlpgenJimmy	378	1.1955	0.016234	7.34	139900
144202	WmunuNp3_susyfilt	AlpgenJimmy	101.9	1.1955	0.033596	4.09	139899
144203	WmunuNp4_susyfilt	AlpgenJimmy	25.7	1.1955	0.056165	1.73	70000
107700	WtaunuN0p	AlpgenJimmy	6931.8	1.195		8283.501	3418296
107701	WtaunuN1p	AlpgenJimmy	1304.9	1.195		1559.3555	2499194
107702	WtaunuN2p	AlpgenJimmy	377.93	1.195		451.62635	3750986
107703	WtaunuN3p	AlpgenJimmy	101.96	1.195		121.8422	1009946
107704	WtaunuN4p	AlpgenJimmy	25.71	1.195		30.72345	249998
107705	WtaunuN5p	AlpgenJimmy	7	1.195		8.365	65000
144204	WtaunuNp1_susyfilt	AlpgenJimmy	1305	1.1955	0.008387	13.08	265000
144205	WtaunuNp2_susyfilt	AlpgenJimmy	378	1.1955	0.024476	11.06	204999
144206	WtaunuNp3_susyfilt	AlpgenJimmy	101.9	1.1955	0.050024	6.09	209900
144207	WtaunuNp4_susyfilt	AlpgenJimmy	25.7	1.1955	0.081906	2.52	104999

Table B.3: Used W+jets MC samples with their corresponding sample ID, event generator, LO cross section, and section, k-factor, NNLO cross section, and number of generated events.

Sample ID	Name	Generator	LO [pb]	k-factor	FE	NNLO [pb]	No. of events
107650	ZeeN0p	AlpgenJimmy	669.6	1.24345		832.61	6618284
107651	ZeeN1p	AlpgenJimmy	134.55	1.24345		167.31	1334897
107652	ZeeN2p	AlpgenJimmy	40.65	1.24345		50.55	2004195
107653	ZeeN3p	AlpgenJimmy	11.26	1.24345		14.00	549949
107654	ZeeN4p	AlpgenJimmy	2.84	1.24345		3.53	149948
107655	ZeeN5p	AlpgenJimmy	0.76	1.24345		0.95	50000
107660	ZmumuN0p	AlpgenJimmy	669.6	1.24345		832.61	6615230
107661	ZmumuN1p	AlpgenJimmy	134.55	1.24345		167.31	1334296
107662	ZmumuN2p	AlpgenJimmy	40.65	1.24345		50.55	1999941
107663	ZmumuN3p	AlpgenJimmy	11.26	1.24345		14.00	549896
107664	ZmumuN4p	AlpgenJimmy	2.84	1.24345		3.53	150000
107665	ZmumuN5p	AlpgenJimmy	0.76	1.24345		0.95	50000
107670	ZtautauN0p	AlpgenJimmy	669.6	1.24345		832.61	10613179
107671	ZtautauN1p	AlpgenJimmy	134.55	1.24345		167.31	3334137
107672	ZtautauN2p	AlpgenJimmy	40.65	1.24345		50.55	1004847
107673	ZtautauN3p	AlpgenJimmy	11.26	1.24345		14.00	509847
107674	ZtautauN4p	AlpgenJimmy	2.84	1.24345		3.53	144999
107675	ZtautauN5p	AlpgenJimmy	0.76	1.24345		0.95	45000
107710	ZnunuNp0	AlpgenJimmy	3572	1.2604	0.011091	49.93	54949
107711	ZnunuNp1	AlpgenJimmy	738.73	1.2604	0.6112	569.09	909848
107712	ZnunuNp2	AlpgenJimmy	222.91	1.2604	0.88158	247.68	169899
107713	ZnunuNp3	AlpgenJimmy	61.874	1.2604	0.96751	75.45	144999
107714	ZnunuNp4	AlpgenJimmy	15.635	1.2604	0.99205	19.55	309899
107715	ZnunuNp5	AlpgenJimmy	4.3094	1.2604	0.99854	5.42	189998

Table B.4: Used Z+jets MC samples with their corresponding sample ID, event generator, LO cross section, k-factor, NNLO cross section, and number of generated events.

Sample ID	Generator	Process	NLO [pb]	No. of events
105921	McAtNlo_JIMMY	$W^+W^- \to e\nu e\nu$	0.51	199949
105922	McAtNlo_JIMMY	$W^+W^- \to e\nu\mu\nu$	0.51	200000
105923	McAtNlo_JIMMY	$W^+W^- \to e\nu\tau\nu$	0.51	200000
105924	McAtNlo_JIMMY	$W^+W^- \to \mu\nu\mu\nu$	0.51	199000
105925	McAtNlo_JIMMY	$W^+W^- \to \mu\nu e\nu$	0.51	199949
105926	McAtNlo_JIMMY	$W^+W^- \to \mu\nu\tau\nu$	0.51	200000
105927	McAtNlo_JIMMY	$W^+W^- \to \tau\nu\tau\nu$	0.51	499676
105928	McAtNlo_JIMMY	$W^+W^- \to \tau\nu e\nu$	0.51	199950
105929	McAtNlo_JIMMY	$W^+W^- \to \tau\nu\mu\nu$	0.51	200000
105930	McAtNlo_JIMMY	$ZZ \to \ell\ell q\bar{q}$	0.270	25000
105931	McAtNlo_JIMMY	$ZZ \to \ell\ell\ell\ell$	0.026	99999
105932	McAtNlo_JIMMY	$ZZ \to \ell\ell\nu\nu$	0.077	99999
106036	McAtNlo_JIMMY	$ZZ \to 2\ell 2\tau$	1.695	25000
106037	McAtNlo_JIMMY	$ZZ \to 4\tau$	0.164	25000
113192	McAtNlo_JIMMY	$ZZ \to \tau\tau\nu\nu$	0.514	24950
113193	McAtNlo_JIMMY	$ZZ \to \tau\tau q\bar{q}$	0.928	25000
105940	McAtNlo_JIMMY	$W^+Z \to \ell\nu q\bar{q}$	0.090	100000
105941	McAtNlo_JIMMY	$W^+Z \to \ell\nu\ell\ell$	0.28	100000
105942	McAtNlo_JIMMY	$W^+Z \to q\bar{q}'\ell\ell$	0.086	25000
106024	McAtNlo_JIMMY	$W^+Z \to \tau\nu\ell\ell$	0.082	25000
106025	McAtNlo_JIMMY	$W^+Z \to \ell\nu\tau\tau$	0.043	199950
106026	McAtNlo_JIMMY	$W^+Z \to \tau\nu\tau\tau$	0.047	25000
113190	McAtNlo_JIMMY	$W^+Z \to q\bar{q}'\tau\tau$	0.045	25000
105970	McAtNlo_JIMMY	$W^-Z \to \ell\nu q\bar{q}$	0.0234	200000
105971	McAtNlo_JIMMY	$W^-Z \to \ell\nu\ell\ell$	0.0129	25000
105972	McAtNlo_JIMMY	$W^-Z \to q\bar{q}'\ell\ell$	0.0065	25000
106027	McAtNlo_JIMMY	$W^-Z \to \tau\nu\ell\ell$	0.2568	199949
106028	McAtNlo_JIMMY	$W^-Z \to \ell\nu\tau\tau$	0.1397	200000
106029	McAtNlo_JIMMY	$W^-Z \to \tau\nu\tau\tau$	0.0386	200000
113191	McAtNlo_JIMMY	$W^-Z \to q\bar{q}'\tau\tau$	0.1348	199950

Table B.5: Used diboson MC samples with their corresponding sample ID, event generator, final state, NLO cross section, and number of generated events.

Sample ID	Generator	Process	NLO [pb]	No. of events
125950	Sherpa	Ztoee2JetsEW2JetsQCD15GeVM40	0.44702	199999
125951	Sherpa	Ztomm2JetsEW2JetsQCD15GeVM40	0.44585	181200
125952	Sherpa	Ztott2JetsEW2JetsQCD15GeVM40	0.44445	199899
125956	Sherpa	Ztoee2JetsEW2JetsQCD15GeVM07to40	0.47727	100000
125957	Sherpa	Ztomm2JetsEW2JetsQCD15GeVM07to40	0.47712	100000
125958	Sherpa	Ztott2JetsEW2JetsQCD15GeVM07to40	0.46924	99900
128810	Sherpa	WWlnulnu	2.9832	1999697
128811	Sherpa	WZlllnu	0.36164	299950
128812	Sherpa	WZlllnuLowMass	1.0209	299949
128813	Sherpa	ZZllll	0.26622	100000
128814	Sherpa	ZZllnn	0.23838	349900
143062	Sherpa	WZlnnn	0.71868	100000
143063	Sherpa	WZqqnn	1.4249	99900
143064	Sherpa	Wtolnu2JetsEW1JetQCD	24.537	99900
143065	Sherpa	Ztonunu2JetsEW1JetQCD	1.3368	99999

Table B.6: Used alternative diboson MC samples for validation and systematics with their corresponding sample ID, event generator, final state, NLO cross section, and number of generated events.

Sample ID	Name	Generator	LO [pb]	No. of events
105009	J0	Pythia	12030000000	999997
105010	J1	Pythia	807266000	999993
105011	J2	Pythia	48048000	999999
105012	J3	Pythia	2192900	999992
105013	J4	Pythia	87701	989992
105014	J5	Pythia	2350.1	999987
105015	J6	Pythia	33.61	999974
105016	J7	Pythia	0.13744	998955
105017	J8	Pythia	0.000006	998948

Table B.7:]

Used dijet MC samples with their corresponding sample ID, event generator, cross section and number of generated events.

Sample ID	Name	Generator	LO [pb]	k-factor	NNLO [pb]	No. of events
116250	ZeeNp0Mll10to40	AlpgenJimmy	3054.7	1.24345	3798.37	994949
116251	ZeeNp1Mll10to40	AlpgenJimmy	84.91	1.24345	105.58	299998
116252	ZeeNp2Mll10to40	AlpgenJimmy	41.19	1.24345	51.22	999946
116253	ZeeNp3Mll10to40	AlpgenJimmy	8.35	1.24345	10.38	149998
116254	ZeeNp4Mll10to40	AlpgenJimmy	1.85	1.24345	2.30	40000
116255	ZeeNp5Mll10to40	AlpgenJimmy	0.46	1.24345	0.57	10000
116260	ZmumuNp0Mll10to40	AlpgenJimmy	3054.9	1.24345	3798.62	999849
116261	ZmumuNp1Mll10to40	AlpgenJimmy	84.78	1.24345	105.42	300000
116262	ZmumuNp2Mll10to40	AlpgenJimmy	41.13	1.24345	51.14	999995
116263	ZmumuNp3Mll10to40	AlpgenJimmy	8.34	1.24345	10.37	150000
116264	ZmumuNp4Mll10to40	AlpgenJimmy	1.87	1.24345	2.33	39999
116265	ZmumuNp5Mll10to40	AlpgenJimmy	0.46	1.24345	0.57	10000
116270	ZtautauNp0Mll10to40	AlpgenJimmy	3054.8	1.24345	3798.49	999649
116271	ZtautauNp1Mll10to40	AlpgenJimmy	84.88	1.24345	105.54	299999
116272	ZtautauNp2Mll10to40	AlpgenJimmy	41.28	1.24345	51.33	498899
116273	ZtautauNp3Mll10to40	AlpgenJimmy	8.35	1.24345	10.38	150000
116274	ZtautauNp4Mll10to40	AlpgenJimmy	1.83	1.24345	2.28	39999
116275	ZtautauNp5Mll10to40	AlpgenJimmy	0.46	1.24345	0.57	10000

Table B.8: Used Drell-Yan MC samples with their corresponding sample ID, event generator, LO cross section, k-factor, NNLO cross section, and number of generated events.

Sample ID	Λ [TeV]	$\tan\beta$	σ [pb]	Sample ID	Λ [TeV]	$\tan\beta$	σ [pb]
137915	10	2	552.595	137942	40	40	0.546
137916	10	5	552.996	137943	40	46	1.814
137917	10	10	552.960	142568	45	2	0.184
137918	10	15	552.166	142569	45	5	0.208
137919	10	20	661.116	142570	45	10	0.213
137920	10	21	659.621	142571	45	15	0.214
143061	12	21	312.079	142572	45	20	0.215
143055	15	2	106.275	142573	45	25	0.218
143056	15	5	109.792	142574	45	30	0.223
143057	15	10	102.786	142575	45	35	0.233
143058	15	15	100.390	142576	45	40	0.256
143059	15	20	99.823	142577	45	50	1.327
143060	15	23	100.555	137944	50	2	0.093
137921	20	2	21.666	137945	50	5	0.109
137922	20	5	22.427	137946	50	10	0.112
137923	20	10	21.964	137947	50	15	0.113
137924	20	15	21.795	137948	50	20	0.114
137925	20	20	21.846	137949	50	30	0.118
137926	20	27	22.994	137950	50	40	0.133
137927	30	2	2.212	137951	50	50	0.248
137928	30	5	2.344	137952	60	2	0.028
137929	30	10	2.339	137953	60	5	0.035
137930	30	15	2.337	137954	60	10	0.037
137931	30	20	2.346	137955	60	15	0.038
137932	30	30	2.458	137956	60	20	0.038
137933	30	36	3.207	137957	60	30	0.040
142558	35	2	0.882	137958	60	40	0.044
142559	35	5	0.951	137959	60	50	0.060
142560	35	10	0.956	137960	70	2	0.011
142561	35	15	0.958	137961	70	5	0.014
142562	35	20	0.963	137962	70	10	0.015
142563	35	25	0.974	137963	70	15	0.015
142564	35	30	1.000	137964	70	20	0.016
142565	35	35	1.073	137965	70	30	0.016
142566	35	40	1.546	137966	70	40	0.018
142567	35	42	2.962	137967	70	50	0.022
137934	40	2	0.389	137968	80	2	0.0046
137935	40	5	0.427	137969	80	5	0.0063
137936	40	10	0.433	137970	80	10	0.0070
137937	40	15	0.434	137971	80	15	0.0072
137938	40	20	0.436	137972	80	20	0.0073
137939	40	25	0.442	137973	80	30	0.0076
137940	40	30	0.452	137974	80	40	0.0084
137941	40	36	0.484	137975	80	50	0.0101

Table B.9: List of MC samples for SUSY signal. All samples are generated using Herwig++. Four out of six parameters defining the GMSB points are the same for all samples: $M_{\text{mess}} = 250$ TeV, $N_5 = 3$, sign(μ) = +, and C_{grav}. The parameters Λ and $\tan\beta$ are varied as shown in the table.

C

BDT input variables for τ-ID

This section details the range of tracking and calorimeter variables that are used in the BDT discriminants [141].

Track radius ($R_{\mathbf{track}}$): the p_{T} weighted track width, associated to the cluster:

$$R_{texttrack} = \frac{\sum_{i}^{\Delta R_i<0.4} p_{T,i}\Delta R_i}{\sum_{i}^{\Delta R_i<0.4} p_{T,i}}$$

where i runs over all tracks associated to the τ-candidate, and $p_{T,i}$ is the p_{T} of the track.

Leading track momentum fraction ($f_{\mathbf{track}}$):

$$f_{\mathrm{track}} = \frac{p_{T,i}^{\mathrm{track}}}{p_T^{\tau}}$$

where $p_{T,i}^{\mathrm{track}}$ is the p_{T} of the leading core track and p_T^{τ} is the p_{T} of the τ-candidate (calibrated at EM energy scale).

Core energy fraction ($f_{\mathbf{core}}$):

$$f_{\mathrm{core}} = \frac{\sum_{i\in\{\mathrm{all}\}}^{\Delta R_i<0.1} E_{T,i}}{\sum_{j\in\{\mathrm{all}\}}^{\Delta R_j<0.4} E_{T,j}}$$

where i runs over all cells associated to the τ-candidate in the region $\Delta R < 0.1$ and j runs over all cells in the region $\Delta R < 0.4$. ΔR_i corresponds to the distance between a cell and the axis of the τ-candidate. $E_{T,i}$ is the transverse energy of the cell, calibrated at the EM scale.

Number of isolation tracks ($N^{\mathbf{iso}}_{\mathbf{track}}$): the number of tracks is the isolation annulus, defined as the region $0.2 < \Delta R < 0.4$ from the τ-candidate axis.

Calorimetric radius ($R_{\mathbf{Cal}}$): The width of the shower in the electromagnetic and hadronic calorimeter, weighted with the E_T of each calorimeter element.

$$R_{\mathrm{Cal}} = \frac{\sum_{i\in\{\mathrm{all}\}}^{\Delta R_i<0.4} E_{T,i}\Delta R_i}{\sum_{i\in\{\mathrm{all}\}}^{\Delta R_i<0.4} E_{T,i}}$$

where i runs over cells in all layers of the EM and hadronic calorimeters.

Ring isolation ($f_{\mathbf{iso}}$):

$$f_{\mathrm{iso}} = \frac{\sum_{i\in\{\mathrm{EM0-2}\}}^{0.1<\Delta R<0.2} E_{T,i}}{\sum_{j\in\{\mathrm{EM0-2}\}}^{\Delta R<0.4} E_{T,j}}$$

where i runs over cells in the first three layers of the EM calorimeter in the region $0.1 < \Delta R < 0.2$ from the axis of the τ-candidate and j runs over EM cells in the wide cone.

Cluster mass ($m_{\mathbf{eff.\ clusters}}$): the invariant mass computed from the clusters associated to the seed jet. To minimise the effect of pileup, only the first N leading E_T clusters are considered.

$$m_{\mathrm{eff.\ clusters}} = \sqrt{\left(\sum_{\mathrm{clusters}} E\right)^2 - \left(\sum_{\mathrm{clusters}} \boldsymbol{p}\right)^2}$$

Track mass ($m_{\mathbf{tracks}}$): the invariant mass of the associated tracks, including both core and isolation tracks.

Transverse flight path significance ($S_T^{\mathbf{flight}}$): the decay length significance of the secondary vertex in the transverse plane (only for 3-prong candidates):

$$S_T^{\mathrm{flight}} = \frac{L_T^{\mathrm{flight}}}{\delta L_T^{\mathrm{flight}}}$$

where L_T^{flight} is the reconstructed signed decay length, and $\delta L_T^{\mathrm{flight}}$ core tracks are used for the secondary vertex fit.

Leading track IP significance ($S_{\textbf{lead track}}$): the impact parameter significance of the leading track of the τ-candidate.

$$S_{\text{lead track}} = \frac{d_0}{\delta d_0}$$

where d_0 is the distance of closest approach of the track to the reconstructed primary vertex in the transverse plane, and δd_0 is the estimated uncertainty.

First 3 leading clusters energy ratio ($f_{3\textbf{lead clusters}}$): the ratio of the energy of the first three leading clusters over the total energy of all clusters associated to the τ-candidate.

Maximum ΔR ($\Delta R_{\textbf{max}}$): the maximal ΔR between a core track and the axis of the τ-candidate.

Electromagnetic fraction ($f_{\textbf{EM}}$): the fraction of the τ-candidate's E_T deposited in the EM calorimeter

$$f_{\text{EM}} = \frac{\sum_{i\in\{\text{EM0}-2\}}^{\Delta R_i<0.4} E_{T,i}}{\sum_{j\in\{\text{all}\}}^{\Delta R_j<0.4} E_{T,j}}$$

where $E_{T,i/j}$ is the transverse energy deposited in cell i/j. i runs over the cells in the first three layers of the EM calorimeter and j runs over the cells in all of the layers.

TRT HT fraction ($f_{\textbf{HT}}$): the ratio of high-threshold to low-threshold hits in the TRT, for the leading p_{T} core track.

$$f_{\text{HT}} = \frac{\text{High-threshold TRT hits}}{\text{Low-threshold TRT hits}}$$

Electrons likely than pions to produce high-threshold hits in the TRT and therefore this can be used in the electron BDT.

Hadronic track fraction ($f_{\textbf{Had}}^{\textbf{track}}$): the ratio of the hadronic E_T to the p_{T} of the leading track.

Maximum strip E_T ($E_{T,\textbf{max}}^{\textbf{strip}}$): the maximum E_T deposited in a cell in the pre-sampler layer of the EM calorimeter, which is not associated with that of the leading track.

Hadronic radius ($R_{\textbf{Had}}$): the E_T weighted shower width in the hadronic calorimeter.

$$R_{\text{Had}} = \frac{\sum_{i\in\{\text{Had,EM3}\}}^{\Delta R_i<0.4} E_{T,i}\Delta R_i}{\sum_{i\in\{\text{Had,EM3}\}}^{\Delta R_i<0.4} E_{T,i}}$$

where i runs over cells associated to the τ-candidate in the hadronic calorimeter and third layer of the EM calorimeter.

Bibliography

[1] S. L. Glashow. Partial-symmetries of weak interactions. *Nuclear Physics*, 22(4):579 – 588, 1961. 1, 3

[2] F. Englert and R. Brout. Broken symmetry and the mass of gauge vector mesons. *Phys. Rev. Lett.*, 13:321–323, Aug 1964. 3, 11

[3] P. Higgs. Broken symmetries and the masses of gauge bosons. *Phys. Rev. Lett.*, 13:508–509, Oct 1964.

[4] G. S. Guralnik, C. R. Hagen, and T. W. B. Kibble. Global conservation laws and massless particles. *Phys. Rev. Lett.*, 13:585–587, Nov 1964. 3, 11

[5] S. Weinberg. A model of leptons. *Phys. Rev. Lett.*, 19:1264–1266, Nov 1967. 3

[6] A. Salam. Weak and electromagnetic interactions. In Nils Svartholm, editor, *Elementary particle theory*, pages 367–377. Almquist & Wiksell, 1968. 1, 3

[7] G. Aad et al. Observation of a new particle in the search for the Standard Model Higgs boson with the ATLAS detector at the LHC. *Phys.Lett.*, B716:1–29, 2012. 1, 12

[8] CMS Collaboration. Observation of a new boson at a mass of 125 GeV with the CMS experiment at the LHC. *Phys.Lett.*, B716:30–61, 2012. 1

[9] J.M. Butterworth, B.E. Cox, and J. R. Forshaw. WW scattering at the CERN LHC. *Phys.Rev.*, D65:096014, 2002. 1

[10] H. Miyazawa. Baryon number changing currents. *Prog. Theor. Phys.*, 36 (6):1266–1276, 1966. 2, 4

[11] P. Ramond. Dual theory for free fermions. *Phys. Rev.*, D3:2415–2418, 1971.

[12] Y. A. Gol'fand and E. P. Likhtman. Extension of the algebra of poincare group generators and violation of p invariance. *JETP Lett.*, 13:323–326, 1971.

[13] A. Neveu and J. H. Schwarz. Factorizable dual model of pions. *Nucl. Phys.*, B31:86–112, 1971.

[14] A. Neveu and J. H. Schwarz. Quark model of dual pions. *Phys. Rev.*, D4:1109–1111, 1971.

[15] J.L. Gervais and B. Sakita. Field theory interpretation of supergauges in dual models. *Nucl. Phys.*, B34:632–639, 1971.

[16] D. V. Volkov and V. P. Akulov. Is the neutrino a Goldstone particle? *Phys. Lett.*, B46:109–110, 1973.

[17] J. Wess and B. Zumino. A Lagrangian model invariant under supergauge transformations. *Phys. Lett.*, B49:52, 1974.

[18] J. Wess and B. Zumino. Supergauge transformations in four-dimensions. *Nucl. Phys.*, B70:39–50, 1974. 2, 4

[19] F.J. Hasert et al. Search for elastic muon-neutrino electron scattering. *Physics Letters B*, 46(1):121 – 124, 1973. 3

[20] F.J. Hasert et al. Observation of neutrino-like interactions without muon or electron in the gargamelle neutrino experiment. *Physics Letters B*, 46(1):138 – 140, 1973.

[21] F.J. Hasert et al. Observation of neutrino-like interactions without muon or electron in the gargamelle neutrino experiment. *Nuclear Physics B*, 73(1):1 – 22, 1974. 3

[22] E. D. Bloom, D. H. Coward, H. DeStaebler, J. Drees, G. Miller, L. W. Mo, R. E. Taylor, M. Breidenbach, J. I. Friedman, G. C. Hartmann, and H. W. Kendall. High-energy inelastic $e - p$ scattering at 6° and 10°. *Phys. Rev. Lett.*, 23:930–934, Oct 1969. 3

[23] M. Breidenbach, J. I. Friedman, H. W. Kendall, E. D. Bloom, D. H. Coward, H. DeStaebler, J. Drees, L. W. Mo, and R. E. Taylor. Observed behavior of highly inelastic electron-proton scattering. *Phys. Rev. Lett.*, 23:935–939, Oct 1969. 3

[24] C. N. Yang and R. L. Mills. Conservation of isotopic spin and isotopic gauge invariance. *Phys. Rev.*, 96:191–195, Oct 1954. 4

[25] H. Fritzsch, M. Gell-Mann, and H. Leutwyler. Advantages of the color octet gluon picture. *Physics Letters B*, 47(4):365 – 368, 1973. 4

[26] H. Fritzsch and M. Gell-Mann. Current algebra: Quarks and what else? *eConf*, C720906V2:135–165, 1972. 4

[27] J. Gross, D and F. Wilczek. Ultraviolet behavior of non-abelian gauge theories. *Phys. Rev. Lett.*, 30:1343–1346, Jun 1973. 7

[28] H. D. Politzer. Reliable perturbative results for strong interactions? *Phys. Rev. Lett.*, 30:1346–1349, Jun 1973. 7

[29] J. et al. Beringer. Review of particle physics. *Phys. Rev. D*, 86:010001, Jul 2012. 8, 13, 40, 50

[30] C. S. Wu, E. Ambler, R. W. Hayward, D. D. Hoppes, and R. P. Hudson. Experimental test of parity conservation in beta decay. *Phys. Rev.*, 105:1413–1415, Feb 1957. 8

[31] The LEP Collaboration. The LEP Electoweak Working Group. `http://lepewwg.web.cern.ch/LEPEWWG/`, Sept 2012. 8

[32] Y. Nambu. Axial vector current conservation in weak interactions. *Phys. Rev. Lett.*, 4:380–382, Apr 1960. 11

[33] J. Goldstone. Field theories with superconductor solutions. *Il Nuovo Cimento (1955-1965)*, 19:154–164, 1961. 10.1007/BF02812722.

[34] J. Goldstone, A. Salam, and S. Weinberg. Broken symmetries. *Phys. Rev.*, 127:965–970, Aug 1962. 11

[35] L. Alvarez-Gaume and J. Ellis. Eyes on a prize particle. *Nature Physics*, 7:2–3, 2011. 11

[36] S. P. Martin. A Supersymmetry primer. In G. L. Kane, editor, *Perspectives on Supersymmetry*, page 1, 1998. 12, 13, 14, 15, 16, 17, 18, 19, 20, 22

[37] S. Weinberg. Implications of dynamical symmetry breaking. *Phys. Rev.*, D13:974–996, 1976. 12

[38] E. Gildener. Gauge symmetry hierarchies. *Phys. Rev.*, D14:1667, 1976.

[39] S. Weinberg. Implications of dynamical symmetry breaking: An addendum. *Phys. Rev.*, D19:1277–1280, 1979.

[40] L. Susskind. Dynamics of spontaneous symmetry breaking in the Weinberg- Salam theory. *Phys. Rev.*, D20:2619–2625, 1979. 12

[41] N. Jarosik, C. L. Bennett, J. Dunkley, B. Gold, M. R. Greason, M. Halpern, R. S. Hill, G. Hinshaw, A. Kogut, E. Komatsu, D. Larson, M. Limon, S. S. Meyer, M. R. Nolta, N. Odegard, L. Page, K. M. Smith, D.N. Spergel, G. S. Tucker, J. L. Weiland, E. Wollack, and E. L. Wright. Seven-year Wilkinson Microwave Anisotropy Probe (WMAP) observations: Sky maps, systematic errors, and basic results. *The Astrophysical Journal Supplement Series*, 192(2):14, 2011. 13

[42] S. Dimopoulos and H. Georgi. Softly broken supersymmetry and SU(5). *Nucl. Phys.*, B193:150, 1981. 15

[43] E. Witten. Dynamical breaking of supersymmetry. *Nucl. Phys.*, B188:513, 1981.

[44] M. Dine, W. Fischler, and M. Srednicki. Supersymmetric technicolor. *Nucl. Phys.*, B189:575, 1981. 19

[45] S. Dimopoulos and S. Raby. Supercolor. *Nucl. Phys.*, B192:353, 1981.

[46] N. Sakai. Naturalness in supersymmetric GUTS. *Zeit. Phys.*, C11:153, 1981. 15

[47] R.K. Kaul and P. Majumdar. Cancellation of quadratically divergent mass corrections in globally supersymmetric spontaneously broken gauge theories. *Nucl. Phys.*, B199:36, 1982. 15

[48] D. I. Kazakov. Beyond the Standard Model (In Search of Supersymmetry). *ArXiv High Energy Physics - Phenomenology e-prints*, December 2000. 15, 16, 19

[49] S. Dimopoulos, S. Raby, and F. Wilczek. Supersymmetry and the scale of unification. *Phys. Rev.*, D24:1681–1683, 1981. 15

[50] L. E. Ibanez and G. G. Ross. Low-energy predictions in supersymmetric grand unified theories. *Phys. Lett.*, B105:439, 1981.

[51] M. B. Einhorn and D. R. T. Jones. The weak mixing angle and unification mass in supersymmetric SU(5). *Nucl. Phys.*, B196:475, 1982.

[52] W. J. Marciano and G. Senjanovic. Predictions of supersymmetric grand unified theories. *Phys. Rev.*, D25:3092, 1982.

[53] C. Giunti, C. W. Kim, and U.W. Lee. Running coupling constants and grand unification models. *Mod. Phys. Lett.*, A6:1745–1755, 1991.

[54] J.R. Ellis, S. Kelley, and D.V. Nanopoulos. Probing the desert using gauge coupling unification. *Phys. Lett.*, B260:131–137, 1991.

[55] U. Amaldi, W. de Boer, and H. Furstenau. Comparison of grand unified theories with electroweak and strong coupling constants measured at LEP. *Phys. Lett.*, B260:447–455, 1991.

[56] P. Langacker and M.-X. Luo. Implications of precision electroweak experiments for M(t), rho(0), sin**2-Theta(W) and grand unification. *Phys. Rev.*, D44:817–822, 1991. 15

[57] P. Fayet. Supersymmetry and weak, electromagnetic and strong interactions. *Phys. Lett.*, B64:159, 1976. 15

[58] P. Fayet. Spontaneously broken supersymmetric theories of weak, electromagnetic and strong interactions. *Phys. Lett.*, B69:489, 1977.

[59] G. R. Farrar and P. Fayet. Phenomenology of the production, decay, and detection of new hadronic states associated with supersymmetry. *Phys. Lett.*, B76:575–579, 1978.

[60] P. Fayet. Relations between the masses of the superpartners of leptons and quarks, the goldstino couplings and the neutral currents. *Phys. Lett.*, B84:416, 1979. 15

[61] H. Goldberg. Constraint on the photino mass from cosmology. *Phys. Rev. Lett.*, 50:1419, 1983. 15

[62] J.R. Ellis, J.S. Hagelin, D.V. Nanopoulos, K.A. Olive, and M. Srednicki. Supersymmetric relics from the big bang. *Nucl. Phys.*, B238:453–476, 1984. 15

[63] P. B. Pal. Dirac, Majorana, and Weyl fermions. *American Journal of Physics*, 79:485–498, May 2011. 16

[64] L. Hall, J. Lykken, and S. Weinberg. Supergravity as the messenger of supersymmetry breaking. *Phys. Rev. D*, 27:2359–2378, May 1983. 18

[65] Sanjeev K. S. and H. A. Weldon. Analysis of the supersymmetry breaking induced by n = 1 supergravity theories. *Physics Letters B*, 126(34):215 – 219, 1983.

[66] I. Affleck, M. Dine, and N. Seiberg. Dynamical supersymmetry breaking in supersymmetric qcd. *Nuclear Physics B*, 241(2):493 – 534, 1984. 18

[67] M. Dine, A. E. Nelson, Y. Nir, and Y. Shirman. New tools for low-energy dynamical supersymmetry breaking. *Phys.Rev.*, D53:2658–2669, 1996. 19

[68] M. Dine and W. Fischler. A phenomenological model of particle physics based on supersymmetry. *Phys. Lett.*, B110:227, 1982.

[69] L. Alvarez-Gaume, M. Claudson, and M. B. Wise. Low-energy supersymmetry. *Nucl. Phys.*, B207:96, 1982.

[70] S. Dimopoulos and S. Raby. Supercolor. *Nucl. Phys.*, B192:353, 1981.

[71] C. R. Nappi and B. A. Ovrut. Supersymmetric extension of the SU(3)×SU(2)×U(1) model. *Phys. Lett.*, B113:175, 1982.

[72] M. Dine and A. E. Nelson. Dynamical supersymmetry breaking at low-energies. *Phys. Rev.*, D48:1277–1287, 1993.

[73] M. Dine, A. E. Nelson, and Y. Shirman. Low-energy dynamical supersymmetry breaking simplified. *Phys.Rev.*, D51:1362–1370, 1995. 19

[74] PROSPINO2. `http://www.thphys.uni-heidelberg.de/~plehn/index.php?show=prospino`, Sept 2012. 21, 42

[75] T. Sven Pettersson and P Lefvre. The Large Hadron Collider: conceptual design. oai:cds.cern.ch:291782. Technical Report CERN-AC-95-05 LHC, CERN, Geneva, Oct 1995. 23

[76] O. S. Brning, P. Collier, P. Lebrun, S. Myers, R. Ostojic, J. Poole, and P. Proudlock. *LHC Design Report*. CERN, Geneva, 2004. 23, 24

[77] CERN the European Organisation for Nuclear Research. `http://public.web.cern.ch/public/Welcome.html/`, Sept 2012. 25

[78] ATLAS Collaboration. The ATLAS Experiment at the CERN Large Hadron Collider. *JINST*, 3:S08003, 2008. 24, 27, 29

[79] The CMS Collaboration. The CMS experiment at the CERN LHC. *Journal of Instrumentation*, 3(08):S08004, 2008. 24

[80] The LHCb Collaboration. The LHCb detector at the LHC. *Journal of Instrumentation*, 3(08):S08005, 2008. 24

[81] The ALICE Collaboration. The ALICE experiment at the CERN LHC. *Journal of Instrumentation*, 3(08):S08002, 2008. 24

[82] The LHCf Collaboration. The LHCf detector at the CERN Large Hadron Collider. *Journal of Instrumentation*, 3(08):S08006, 2008. 24

[83] The TOTEM Collaboration. The TOTEM experiment at the CERN Large Hadron Collider. *Journal of Instrumentation*, 3(08):S08007, 2008. 24

[84] ATLAS Collaboration. Performance of the ATLAS Trigger System in 2010. *Eur. Phys. J. C*, 72:1849, 2012. 26, 28, 36, 38, 70

[85] The ATLAS Collaboration. ATLAS public luminosity results. `https://twiki.cern.ch/twiki/bin/view/AtlasPublic/LuminosityPublicResults/`, Sept 2012. 26

[86] ATLAS Collaboration. Luminosity determination in pp collisions at $\sqrt{s} = 7$ TeV using the ATLAS detector in 2011. Technical Report ATLAS-CONF-2011-116, CERN, Geneva, Aug 2011. 27, 64, 100

[87] ATLAS Collaboration. Luminosity Determination in p–p Collisions at sqrt(s)=7 TeV Using the ATLAS Detector at the LHC. *Eur. Phys. J.*, C71:1630, 2011. 26, 27, 64, 100, 116

[88] The ATLAS Collaboration. *ATLAS detector and physics performance: Technical Design Report, 1.* Technical Design Report ATLAS. CERN, Geneva, 1999. Electronic version not available. 27, 29, 32, 33, 34

[89] The ATLAS Collaboration. *ATLAS detector and physics performance: Technical Design Report, 2.* Technical Design Report ATLAS. CERN, Geneva, 1999. Electronic version not available. 27

[90] ATLAS Collaboration. *Expected performance of the ATLAS experiment: detector, trigger and physics.* CERN, Geneva, 2009. 28, 29, 31, 32, 34, 45, 48

[91] S Haywood, L Rossi, R Nickerson, and A Romaniouk. *ATLAS inner detector: Technical Design Report, 2.* Technical Design Report ATLAS. CERN, Geneva, 1997. 28, 29, 32

[92] The ATLAS Collaboration. The ATLAS collaboration website. `http://atlas.ch/`, Sept 2012. 30, 32, 36

[93] N. Wermes and G Hallewel. *ATLAS pixel detector: Technical Design Report*. Technical Design Report ATLAS. CERN, Geneva, 1998. 31

[94] The ATLAS Collaboration. *ATLAS calorimeter performance: Technical Design Report*. Technical Design Report ATLAS. CERN, Geneva, 1996. 32

[95] The ATLAS Collaboration. *ATLAS liquid-argon calorimeter: Technical Design Report*. Technical Design Report ATLAS. CERN, Geneva, 1996. 32, 33

[96] The ATLAS Collaboration. *ATLAS muon spectrometer: Technical Design Report*. Technical Design Report ATLAS. CERN, Geneva, 1997. distribution. 34, 35

[97] P. Jenni, M. Nessi, M. Nordberg, and K. Smith. *ATLAS high-level trigger, data-acquisition and controls: Technical Design Report*. Technical Design Report ATLAS. CERN, Geneva, 2003. 36

[98] The ATLAS Collaboration. *ATLAS level-1 trigger: Technical Design Report*. Technical Design Report ATLAS. CERN, Geneva, 1998. 36

[99] S. Weinberg. New approach to the renormalization group. *Phys. Rev. D*, 8:3497–3509, Nov 1973. 40

[100] G. 't Hooft. Dimensional regularization and the renormalization group. *Nuclear Physics B*, 61(0):455 – 468, 1973. 40

[101] A. De Roeck and R.S. Thorne. Structure Functions. *Prog.Part.Nucl.Phys.*, 66:727–781, 2011. 40

[102] T Sjostrand, S Mrenna, and P Skands. PYTHIA 6.4 Physics and Manual. *JHEP*, 0605:026, 2006. 40, 41

[103] The ATLAS Collaboration. New ATLAS event generator tunes to 2010 data. Technical Report ATL-PHYS-PUB-2011-008, CERN, Geneva, Apr 2011. 41

[104] ATLAS Collaboration. Charged Particle Multiplicities in pp Interactions at $\sqrt{s} = 0.9$ and 7 TeV in a Diffractive Limited Phase Space Measured with the ATLAS Detector at the LHC and a New PYTHIA6 Tune. ATLAS-CONF-2010-031, July 2010. `http://cdsweb.cern.ch/record/1277665`. 41

[105] ATLAS Collaboration. ATLAS Tunes for PYTHIA6 and PYTHIA8 for MC11. ATLAS-PHYS-PUB-2011-009, July 2011. https://cdsweb.cern.ch/record/1363300. 41

[106] A. Sherstnev and R. S. Thorne. Parton Distributions for LO Generators. *Eur. Phys. J.*, C55:553, 2008. 41

[107] M. L. Mangano, M. Moretti, F. Piccinini, R. Pittau, and A. D. Polosa. ALPGEN, a generator for hard multiparton processes in hadronic collisions. *JHEP*, 0307:001, 2003. 41

[108] J. Pumplin, D.R. Stump, J. Huston, H.L. Lai, Pavel M. Nadolsky, et al. New Generation of Parton Distributions with Uncertainties from Global QCD Analysis. *JHEP*, 0207:012, 2002. 41

[109] J.M. Butterworth, J. R. Forshaw, and M.H. Seymour. Multiparton interactions in photoproduction at HERA. *Z.Phys.*, C72:637, 1996. 41

[110] G. Corcella, I. G. Knowles, G. Marchesini, S. Moretti, K. Odagiri, et al. HERWIG 6: An event generator for hadron emission reactions with interfering gluons (including supersymmetric processes). *JHEP*, 0101:010, 2001. 41

[111] S. Frixione and B. R. Webber. Matching NLO QCD Computations and Parton Shower Simulations. *JHEP*, 0206:029, 2002. 42

[112] S. Frixione, P. Nason, and B. R. Webber. Matching NLO QCD and Parton Showers in Heavy Flavor Production. *JHEP*, 0308:007, 2003.

[113] S. Frixione, E. Laenen, P. Motylinski, and B. R. Webber. Single-top production in MC@NLO. *JHEP*, 0603:092, 2006. 42

[114] P. M. Nadolsky, H. L. Lai, Q. H. Cao, J. Huston, J. Pumplin, et al. Implications of CTEQ global analysis for collider observables. *Phys. Rev.*, D78:013004, 2008. 42

[115] H.-L. Lai, M. Guzzi, J. Huston, Z. Li, P. M. Nadolsky, J. Pumplin, and C.-P. Yuan. New Parton Distributions for Collider Physics. *Phys. Rev. D*, 82(7):074024, October 2010. 42

[116] H. Baer, F. E. Paige, S. D. Protopescu, and X. Tata. ISAJET 7.69: A Monte Carlo Event Generator for pp, $\bar pp$, and $e^=e^-$ Reactions. *ArXiv High Energy Physics - Phenomenology e-prints*, December 2003. 42

[117] M. Bahr et al. Herwig++ Physics and Manual. *Eur. Phys. J.*, C58:639–707, 2008. 42

[118] W. Beenakker, R. Hopker, M. Spira, and P. M. Zerwas. Squark and Gluino Production at Hadron Colliders. *Nucl. Phys.*, B492:51, 1997. 42

[119] W. Beenakker, M. Kramer, T. Plehn, M. Spira, and P. M. Zerwas. Stop Production at Hadron Colliders. *Nucl. Phys.*, B515:3, 1998.

[120] W. Beenakker, M. Klasen, M. Kramer, T. Plehn, M. Spira, et al. The Production of Charginos, Neutralinos and Sleptons at Hadron Colliders. *Phys. Rev. Lett.*, 83:3780, 1999.

[121] M. Spira. Higgs and SUSY Particle Production at Hadron Colliders. *ArXiv High Energy Physics - Phenomenology e-prints*, November 2002.

[122] T. Plehn. Measuring the MSSM Lagrangean. *Czech. J. Phys.*, 55:B213, 2005. 42

[123] A. Kulesza and L. Motyka. Threshold resummation for squark-antisquark and gluino-pair production at the LHC. *Phys. Rev. Lett.*, 102:111802, 2009. 42

[124] A. Kulesza and L. Motyka. Soft gluon resummation for the production of gluino-gluino and squark-antisquark pairs at the LHC. *Phys.Rev.*, D80:095004, 2009.

[125] W. Beenakker, S. Brensing, M. Kramer, A. Kulesza, E. Laenen, et al. Soft-gluon resummation for squark and gluino production. *JHEP*, 0912:041, 2009.

[126] W. Beenakker, S. Brensing, M. Kramer, A. Kulesza, E. Laenen, et al. Squark and gluino production. *Int. J. Mod. Phys.*, A26:2637–2664, 2011. 42

[127] M. Krämer, A. Kulesza, R. van der Leeuw, M. Mangano, S. Padhi, T. Plehn, and X. Portell. Supersymmetry production cross sections in pp collisions at sqrt{s} = 7 TeV. *ArXiv e-prints*, June 2012. 42

[128] S. Jadach, Z. Was, R. Decker, and Johann H. Kuhn. The Tau Decay Library TAUOLA, Version 2.4. *Comput. Phys. Commun.*, 76:361, 1993. 42

[129] P. Golonka et al. The Tauola-Photos-F Environment for the TAUOLA and PHOTOS Packages, Release II. *Comput. Phys. Commun.*, 174:818, 2006. 42

[130] E. Barberio and Z. Was. PHOTOS - a Universal Monte Carlo for QED Radiative Corrections: Version 2.0. *Comput. Phys. Commun.*, 79:291, 1994. 42

[131] The ATLAS Collaboration. *ATLAS Computing: Technical Design Report*. CERN, Geneva, 2005. 43

[132] ATLAS Collaboration. The ATLAS Simulation Infrastructure. *Eur. Phys. J.*, C70:823, 2010. 43, 44

[133] SUSY Tools. `https://twiki.cern.ch/twiki/bin/view/AtlasProtected/SUSYD3PDSnippets`, 2011. SUSYTools-00-00-34. 44, 50

[134] ATLAS Collaboration. Electron performance measurements with the ATLAS detector using the 2012 LHC in proton-proton collision data. *Eur. Phys. J.*, C 72:1909, 2012. 45, 46

[135] ATLAS Collaboration. Measurement of the $W \to l\nu$ and $Z/\gamma \to ll$ production cross section in Proton-Proton collisions at $\sqrt(s) = 7\,\text{TeV}$ with the ATLAS detector. *JHEP*, 1012:060, 2010. 47

[136] ATLAS Collaboration. Searches for supersymmetry with the ATLAS detector using final states with two leptons and missing transverse momentum in $\sqrt{s} = 7$ TeV Proton-Proton collisions. *Phys. Lett.*, B709:137, 2012. 47

[137] M. Cacciari, G. P. Salam, and G. Soyez. The anti-kt jet clustering algorithm. *JHEP*, 0804:063, 2008. 48, 49, 50

[138] ATLAS Collaboration. Jet energy measurement with the ATLAS detector in proton-proton collisions at $\sqrt{s} = 7$ TeV. Technical Report arXiv:1112.6426. CERN-PH-EP-2011-191, CERN, Geneva, Dec 2011. 48

[139] ATLAS Collaboration. Commissioning of the ATLAS high-performance b-tagging algorithms in the 7 TeV collision data. ATLAS-CONF-2011-102, Jul 2011. `http://cdsweb.cern.ch/record/1369219`. 49

[140] ATLAS Collaboration. Measurement of the b-tag efficiency in a sample of jets containing muons with 5 fb^{-1} of data from the ATLAS detector. ATLAS-CONF-2012-043, Mar 2012. `http://cdsweb.cern.ch/record/1435197`. 49

[141] ATLAS Collaboration. Performance of the Reconstruction and Identification of Hadronic Tau Decays with ATLAS. ATLAS-CONF-2011-152, Nov 2011. `http://cdsweb.cern.ch/record/1398195`. 51, 52, 53, 54, 55, 56, 57, 58, 59, 81, 82, 99, 100, 176

[142] The ATLAS Collaboration. Determination of the tau energy scale and the associated systematic uncertainty in proton-proton collisions at $\sqrt{s} = 7$ TeV with the ATLAS detector at the LHC in 2011. Technical Report ATLAS-CONF-2012-054, CERN, Geneva, Jun 2012. 52

[143] A. Hoecker, P. Speckmayer, J. Stelzer, J. Therhaag, E. von Toerne, H. Voss, M. Backes, T. Carli, O. Cohen, A. Christov, D. Dannheim, K. Danielowski, S. Henrot-Versille, M. Jachowski, K. Kraszewski, A. Krasznahorkay, Jr., M. Kruk, Y. Mahalalel, R. Ospanov, X. Prudent, A. Robert, D. Schouten, F. Tegenfeldt, A. Voigt, K. Voss, M. Wolter, and A. Zemla. TMVA - Toolkit for Multivariate Data Analysis. *ArXiv Physics e-prints*, March 2007. 52, 54

[144] R. Brun. ROOT an object oriented data analysis framework. *Nuclear Instruments and Methods in Physics Research Section A: Accelerators, Spectrometers, Detectors and Associated Equipment*, 389(1-2):81–86, April 1997. 54

[145] ATLAS Collaboration. Performance of missing transverse momentum reconstruction in proton-proton collisions at 7 TeV with ATLAS. *Eur. Phys. J.*, C72:1844, 2012. 60

[146] ATLAS Collaboration. Search for events with large missing transverse momentum, jets and at least two tau leptons in 7 TeV proton-proton collision data with the ATLAS detector. *Phys.Lett.B*, 714:180, 2012. 62, 88, 93, 96, 104, 105, 106, 107, 111, 112, 113, 114, 162

[147] The ATLAS Collaboration. Expected performance of the ATLAS detector in GMSB models with tau final states. Technical Report ATL-PHYS-PUB-2009-089, CERN, Geneva, Nov 2009. 65

[148] Georges Aad et al. Search for squarks and gluinos using final states with jets and missing transverse momentum with the ATLAS detector in $\sqrt{s} = 7$ TeV proton-proton collisions. *Phys.Lett.*, B710:67–85, 2012. 71

[149] G. Cowan, K. Cranmer, E. Gross, and O. Vitells. Asymptotic formulae for likelihood-based tests of new physics. *Eur. Phys. J.*, C71:1554, 2011. 74

[150] Search for neutral MSSM Higgs bosons decaying to $\tau^+\tau^-$ pairs in proton-proton collisions at sqrt(s)=7TeV with the ATLAS detector. ATLAS-CONF-2011-132, Sep 2011. 81, 92

[151] ATLAS Collaboration. Jet energy scale and its systematic uncertainty in proton-proton collisions at $\sqrt{s}$ = 7 TeV in ATLAS 2010 data. ATLAS-CONF-2011-032, Mar 2011. https://cdsweb.cern.ch/record/1337782. 98

[152] The ATLAS Collaboration. Jet uncertainties 2011. https://twiki.cern.ch/twiki/bin/viewauth/AtlasProtected/JetUncertainties2011, Sept 2012. 98, 144

[153] ATLAS Collaboration. Jet energy resolution and selection efficiency relative to track jets from in-situ techniques with the ATLAS detector using proton-proton collisions at a center of mass energy $\sqrt{s}$ = 7 TeV. ATLAS-CONF-2010-054, Jul 2010. https://cdsweb.cern.ch/record/1281311. 98

[154] G. Aad, B. Abbott, J. Abdallah, A. A. Abdelalim, A. Abdesselam, O. Abdinov, B. Abi, M. Abolins, H. Abramowicz, H. Abreu, and et al. Jet energy measurement with the ATLAS detector in proton-proton collisions at $\sqrt{s}$=7 TeV. *European Physical Journal C*, 73:2304, March 2013. 98, 144, 145

[155] Z. Sullivan. Fully differential W-prime production and decay at next-to-leading order in QCD. *Phys.Rev.*, D66:075011, 2002. 100

[156] H. L. Lai et al. Uncertainty Induced by QCD Coupling in the CTEQ Global Analysis of Parton Distributions. *Phys.Rev.*, D82:054021, 2010. 101

[157] ATLAS Collaboration. Search for supersymmetry in final states with jets, missing transverse momentum and one isolated lepton in $\sqrt{s}$ = 7 TeV p–p collisions using $1fb^{-1}$ of ATLAS data. 2011. accepted for publication in Physical Review D. 102

[158] A. L. Read. Presentation of Search Results: The CL_s technique. *J. Phys.*, G28:2693, 2002. 108, 110, 158

[159] CERN. *1st Workshop on Confidence Limits*, Geneva, 2000. CERN. 108

[160] The ATLAS Collaboration. Combination package. https://svnweb.cern.ch/trac/atlasgrp/browser/Physics/SUSY/Analyses/Combination/, Sept 2012. 108

[161] ATLAS Collaboration. Constraining the gauge-mediated supersymmetry breaking model in final states with two leptons, jets and missing transverse momentum with the ATLAS experiment at $\sqrt{s}$ = 7 TeV. ATLAS-CONF-2011-156, Nov 2011. https://cdsweb.cern.ch/record/1398247. 111, 113

[162] ATLAS Collaboration. Search for supersymmetry with jets, missing transverse momentum and at least one hadronically decaying tau lepton in proton-proton collisions at $\sqrt{s} = 7$ TeV with the ATLAS detector. *Phys.Lett.B*, 714:197, 2012. 112

[163] The ATLAS Collaboration. Search for supersymmetry in events with large missing transverse momentum,jets, and at least one tau lepton in 7 TeV proton-proton collision data with the ATLAS detector. *The European Physical Journal C*, 72:1–22, 2012. 115, 123, 124, 125, 138, 139, 140, 141, 143, 147, 148, 149, 151, 152, 153, 154, 156

[164] The ATLAS Collaboration. Improved luminosity determination in $p - p$ collisions at $\sqrt{s} = 7$ TeV using the ATLAS detector at the LHC. Technical Report ATLAS-CONF-2012-080, CERN, Geneva, Jul 2012. 116

[165] A. D. Martin, W. J. Stirling, R. S. Thorne, and G. Wat. Parton Distributions for the LHC. *Eur. Phys. J.*, C63:189, 2009. 118

[166] M. Botje, J. Butterworth, A. Cooper-Sarkar, A. de Roeck, J. Feltesse, S. Forte, A. Glazov, J. Huston, R. McNulty, T. Sjostrand, and R. Thorne. The PDF4LHC Working Group Interim Recommendations. *ArXiv e-prints*, January 2011. 118

[167] The ATLAS Collaboration. Expected electron performance in the ATLAS experiment. Technical Report ATL-PHYS-PUB-2011-006, CERN, Geneva, Apr 2011. 119

[168] The ATLAS Collaboration. Muon reconstruction efficiency in reprocessed 2010 LHC proton-proton collision data recorded with the ATLAS detector. Technical Report ATLAS-CONF-2011-063, CERN, Geneva, Apr 2011. 119

[169] G. Aad, T. Abajyan, B. Abbott, J. Abdallah, S. Abdel Khalek, A. A. Abdelalim, O. Abdinov, R. Aben, B. Abi, M. Abolins, and et al. Further search for supersymmetry at $\sqrt{s} = 7$ TeV in final states with jets, missing transverse momentum, and isolated leptons with the ATLAS detector. *Phys. Rev. D*, 86(9):092002, November 2012. 123

[170] ATLAS Collaboration. Measurement of the inclusive $w^{\pm}$ and z/γ^* cross sections in the e and μ decay channels in p–p collisions at $\sqrt{(}s) = 7\,\mathrm{TeV}$ with the ATLAS detector. *Phys. Rev.*, D 85:072004, 2012. 140

[171] ATLAS Collaboration. Measurement of the charge asymmetry in top quark pair

production in p–p collisions at $\sqrt(s) = 7\,\text{TeV}$ using the ATLAS detector. *Eur. Phys. J.*, C 72:2039, 2012. 140

[172] ATLAS Collaboration. Measurement of the top quark-pair production cross section with ATLAS in p–p collisions at $\sqrt{s} = 7$ TeV. *Eur. Phys. J.*, C 71:1577, 2011. 142, 143

[173] The ATLAS Collaboration. Jet energy resolution provider. `https://twiki.cern.ch/twiki/bin/viewauth/AtlasProtected/JetEnergyResolutionProvider/`, Sept 2012. 145

[174] The ATLAS Collaboration. Btagging calibration data interface. `https://twiki.cern.ch/twiki/bin/viewauth/AtlasProtected/BTaggingCalibrationDataInterface/`, Sept 2012. 145

[175] The ATLAS Collaboration. Histfitter package. `https://twiki.cern.ch/twiki/bin/viewauth/AtlasProtected/SusyFitter/`, Sept 2012. 157

[176] L. Moneta, K. Cranmer, G. Schott, and W. Verkerke. The RooStats project. In *Proceedings of the 13th International Workshop on Advanced Computing and Analysis Techniques in Physics Research. February 22-27, 2010, Jaipur, India.*, February 2010. 157

[177] M. Adeel Ajaib, Ilia Gogoladze, Fariha Nasir, and Qaisar Shafi. Revisiting mGMSB in Light of a 125 GeV Higgs. *Phys.Lett.*, B713:462–468, 2012. 163

[178] A. Albaid. Higgs boson mass in GMSB with messenger-matter mixing. *Nuclear Physics B Proceedings Supplements*, 233:51–57, December 2012. 163